Doctoral Thesis

Ultrafast Magnetization Dynamics in Multilayered Films Down to Few-cycle Regime

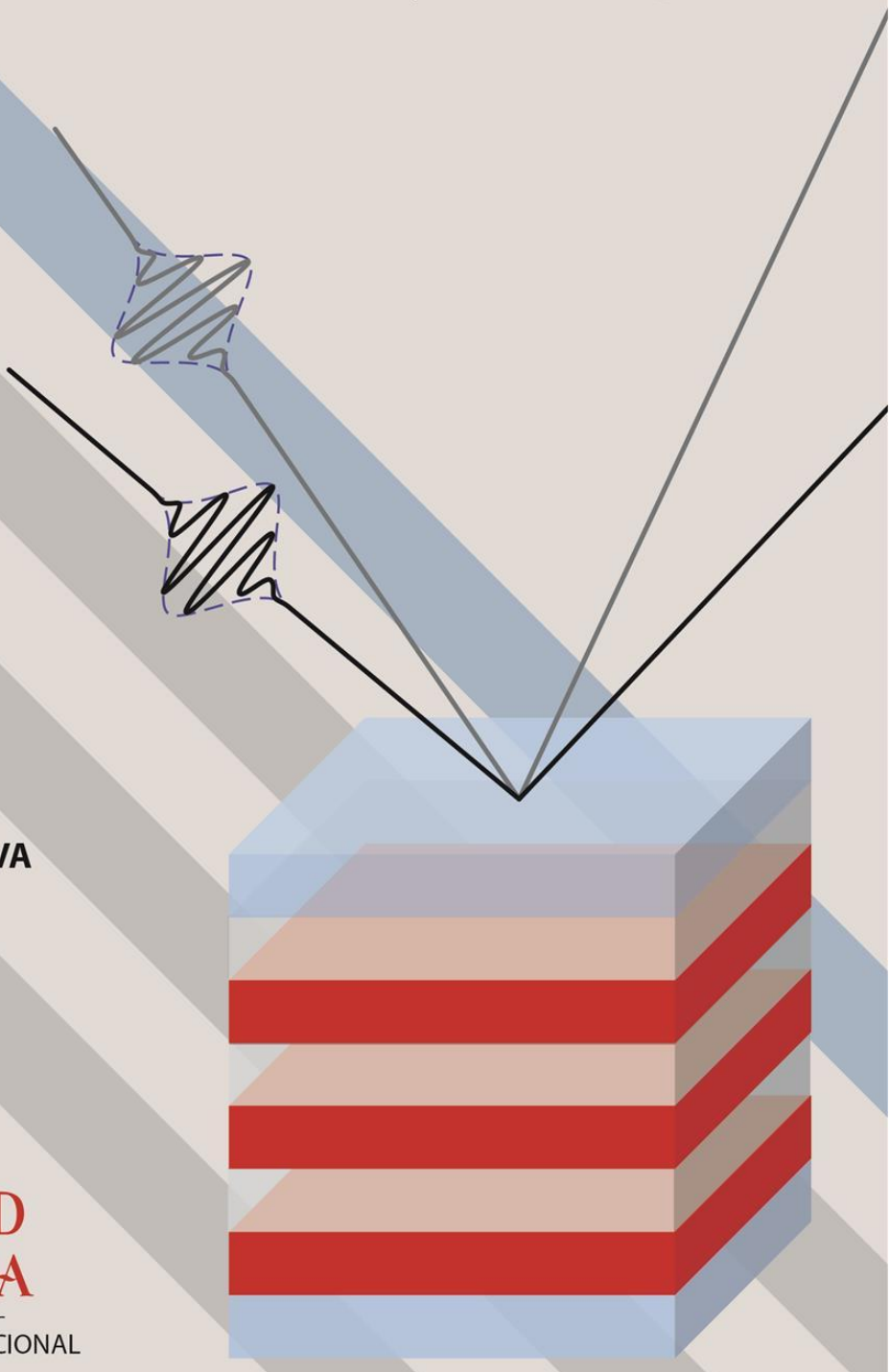

ANA SOFIA VIEIRA SILVA

VNiVERSiDAD D SALAMANCA

CAMPUS DE EXCELENCIA INTERNACIONAL

October 2020

Ana Sofia Vieira Silva

Ultrafast Magnetization Dynamics in Multilayered Films Down to the Few-cycle Regime

VNiVERSiDAD D SALAMANCA

CAMPUS DE EXCELENCIA INTERNACIONAL

Tutor: Dr Íñigo Juan Sola

Director: Dr. David Navas

Codirector: Dr Helder Crespo

Dr Íñigo Juan Sola

Thesis submitted to the Escuela de Doctorado "Studii Salamantini" of the Universidad de Salamanca in partial fulfilment of the requirements for the degree *of Doctor en Física Aplicada y Tecnología*

Universidad de Salamanca

Octubre 2020

DAVID NAVAS OTERO, Investigador Ramón y Cajal, Instituto de Ciencia de Materiales de Madrid, ICMM-CSIC,

HELDER MANUEL PAIVA REBELO CEREJO CRESPO, Professor Auxiliar do Departamento de Física e Astronomia da Faculdade de Ciências da Universidade do Porto,

ÍÑIGO JUAN SOLA LARRAÑAGA, Profesor Titular del Departamento de Física Aplicada de la Universidad de Salamanca,

CERTIFICAN:

Que la presente memoria titulada “Ultrafast Magnetization Dynamics in Multilayered Films Down to Few-cycle Regime" ha sido realizada bajo su dirección por Ana Sofia Vieira Silva

Y para que conste, AUTORIZAN su presentación firmando la presente en

Salamanca, 9 de Octubre de 2020.

To my mother and father,

To my sister and brother,

To my niece and nephew.

À minha mãe e ao meu pai,

À minha irmã e ao meu irmão,

À minha sobrinha e ao meu sobrinho.

“Life is too short to be little.”

Benjamin Disraeli

Acknowledgements

Over the last five years, many people contributed in many different ways in my journey to conclude this thesis, and others on a much longer time-scale, whom without their help, this would not be possible.

I want first to express my gratitude to my supervisors for all their support, and mostly patience. I feel very privileged to have not only one, but three amazing supervisors.

To David Navas, my supervisor, I want to thank him very much for giving me the incredible opportunity to do a PhD in this research area, for all the encouragement transmitted since day one, his dedication, teachings, and friendship.

To Helder Crespo, my co-supervisor, I want to express my gratitude for the amazing experience of working in the Femtolab, his contagious enthusiasm, and all he taught me about lasers and much more (as cinema).

To Íñigo Sola, my many thanks for accepting to be my tutor and co-supervisor, for all his help in Salamanca and constant availability whenever I needed it, for his kindness, and every pinch of salt in our result discussions.

I would like to acknowledge Gleb Kakazei and Sergiy Bunyaev, from IFIMUP; for all the help with VNA-FMR measurements and the enlightening discussions about the results.

I want to thank Carlos Garcia, from the Universidad Técnica Federico Santa María, Chile, for providing the CoFeB/Pd-based multilayer set of samples and fruitful collaboration.

To David Schmool, my degree advisor, my gratitude for introducing me to the fascinating field of ultrafast magnetization dynamics.

Many thanks also to Francisco Carpinteiro, Fernando, and Pedro Cruz for all their help and technical support in the lab, to Isabel Alves for her constant availability to help with paperwork and logistics, and to Armanda Sá for helping with grants paperwork.

A very especial thanks to all the incredible people who shared with me the Femtolab and helpe me: Miguel Miranda, Miguel Mike, Francisco Chico, Cledson, Bejamin, Warein, Tiagos (Pinto e Magalhães), José Iglesias, José Chibaca, Ana Miguel, Tiago Gomes, Simão Sá, Rodrigo, Tânia Ribeiro, Rosa Romero and Paulo Guerreiro. Thanks for the long hours in the lab, it was truly enjoyable, and all the shared teachings.

To all my IFIMUP/DFA colleagues many thanks for all the shared experiences, all the smiles, breaks, lunchs and dinners, namely Arlete, Célia, Aurélio, José Miguel, Paz, André Pereira, Margarida Maia, João Horta, Gonçalo, Cátia, Paulinha, Suellen, Catarina, Sofia, Viviane, Francisca, Ludgero, Luís Guerra, Pedro Machado, Pedro Rodrigues, Rui Costa and Rui Vilarinho. I'm glad to have worked with you and to have you as friends.

Thanks to the members of the “JollyField Running Club” for all the miles running and laughing (Ana Pires, André Pereira, Cláudio Gomes, Fernando Maia, Herder Crespo, Joana Silva, Paula Quitério, Rodrigo Ferreira, Pedro Jorge and Sofia Ferreira-Teixeira).
To Fernanda Mendes, I want to express my gratitude for never giving up on me and be by my side all over these years through this journey.
Anita, my dear ‘little sis’, many thanks for all the help, support, patience, and incentive, and without you, it would have been much harder to get through this journey. Janana, we don’t need words, my twin, thanks for all the support since the cradle. Ivone, my dear “big sis” thanks for your beautiful friendship over all the years, your kindness and support. Dear Becas and Claúdio, I want to thank you for your sweet friendship and to for being by my side all these years, you are like family to me. My dear Su, thanks for so many smiles and tears shared with a tight hug, and your support even at distance. Debby gata, many thanks for welcoming me so well when I arrived at the home and for all the support.
Many thanks to my dear friends, Hugo, Mini e Dee, Marco e Xana, Suzie, Joana (Wally), Rui e Susana, Zé Manel, who, over the years, have been by my side and shared so many significant moments.
I would like to thank my family support. Quero agradecer à minha família, titó Regina, tia São e tio Adelino, tio Helder, e às primas Ana Raquel, Luisinha e Tininha.
Last but not least, I would like to thank my loved ones. Uma palavra especial de agradecimento aos meus queridos pais, Maria Isabel e José, à minha irmã Rute, à minha sobrinha Constança, ao meu sobrinho Salvador e ao meu ‘irmão’ José, pelo vosso apoio incondicional e sempre presente, sem qual seria impossível chegar até aqui. Vocês são a minha inspiração, a minha força.

Resumen

Multicapas de películas ultrafinas basadas en la aleación de CoFeB y con anisotropía magnética perpendicular (PMA) constituyen unos sistemas muy prometedores para diferentes aplicaciones tecnológicas como, por ejemplo, memorias no volátiles de bajo consumo energético y alta velocidad. Sin embargo, y antes de poderlas utilizar en ninguna aplicación tecnológica, es necesario comprender la dinámica de sus propiedades magnéticas.

Con la intención de poder realizar estudios dinámicos de las propiedades magnéticas en este tipo de materiales, un objetivo de esta tesis doctoral fue el desarrollo de un montaje compacto y versátil de medidas magnetoópticas resueltas en tiempo (TR-MO). Nuestro montaje TR-MO ha sido diseñado para su uso en diferentes configuraciones magnetoópticas y con diferentes fuentes láser. El equipo de TR-MO ha sido usado para investigar las propiedades estáticas y dinámicas de las multicapas [CoFeB(t_{CoFeB})/Pd]$_N$. En primer lugar, investigamos la respuesta magnética del sistema multicapa cuando fijamos el número de bicapas en N = 5 y el espesor de la película de CoFeB se modificó entre 1 y 5 Å. A continuación, hemos investigado los casos en los que se varía N entre 3 y 15 bicapas para muestras con un espesor de la capa de CoFeB (t_{CoFeB}) de 3 y 4 Å. Además, se han estudiado otras estructuras, conocidas como "*Exchange spring magnets*", y donde las multicapas [CoFeB($t_{CoFeB} = 3$ Å)/Pd]$_5$ constituyen el sistema magnéticamente duro y con PMA, mientras que la capa de Co es la parte magnética blanda con anisotropía en el plano de la muestra y un espesor (t_{Co}) que se modificó entre 0 y 25 Å. Estos estudios han sido complementados con medidas en el campo de las frecuencias empleando la espectroscopia VNA-FMR (*Resonancia Ferromagnética basada en un Analizador de Redes*).

En el último capítulo de esta tesis doctoral, enfocamos nuestro trabajo a estudiar la posibilidad de modificar y manipular el magnetismo de una muestra mediante el campo eléctrico de la luz. De este modo, nuestro montaje TR-MO ha sido diseñado para ser capaz de emplear pulsos ultracortos en el régimen de pocos ciclos, con duraciones menores de 5 fs, y obtenidos mediante la técnica de post-compresión en fibra hueca rellena de gas. Se presentan resultados preliminares, empleando dichos pulsos ultracortos con su fase portadora-envolvente (CEP) estabilizada, que confirman que el proceso de desimanación del sistema de multicapas considerado se ve afectado directamente por el campo eléctrico de la luz.

Palabras clave: dinámica de magnetización ultrarrápida; multicapas de películas ultrafinas; espectroscopia de pulsos de pocos ciclos.

Abstract

CoFeB-based multilayer ultrathin films with perpendicular magnetic anisotropy (PMA) are promising for different emerging technological applications such as nonvolatile memories with low power consumption and high-speed performance. However, and before being able to use them in any technological application, it is necessary a deep understanding of its magnetic dynamical behavior.

In order to can perform studies of the dynamical properties in this kind of ferromagnetic materials, an aim of this thesis was the development of a compact and versatile Time-Resolved Magneto-Optical (TR-MO) setup. Our TR-MO setup was designed to be used in different magneto-optical configurations and with different laser sources.

The TR-MO system was used for studying the static and dynamical properties of [CoFeB(t_{CoFeB})/Pd]$_N$ multilayers ultrathin films. Firstly, the magnetic response was investigated when the CoFeB layer thickness (t_{CoFeB}) was ranged between 1 and 5 Å and keeping constant number of bilayers (N = 5). Afterwards, we investigated the system with N ranging between 3 and 15 bilayers for the set of samples with t_{CoFeB} = 3 and 4 Å. In addition, we also studied exchange spring structures, where the [CoFeB($t_{CoFeB} = 3$ Å)/Pd]$_5$ multilayers system is the hard-magnetic part with PMA, while a thin Co layer is the soft-magnetic one with an in-plane anisotropy and a thickness (t_{Co}) ranging between 0 and 25 Å. These studies were complemented by measurements in the frequency domain using Vector Network Analyzer based Ferromagnetic Resonance (VNA-FMR) spectroscopy.

In the last chapter of this thesis, we focused our work on studying the possibility to directly modify and manipulate the magnetism of a sample by the electric-field of light. Therefore, our TR-MO setup was designed to be able to use the few-cycle pulses of our hollow-fiber compressor with a temporal duration of sub-5-fs. The preliminary results using these pulses with the carrier phase envelope (CEP) stabilized are presented, confirming that the ultrafast demagnetization of these multilayer systems is affected by the electric-field of light directly.

Keywords: ultrafast magnetization dynamics; multilayers ultrathin films; few-cycle pulses spectroscopy.

Resumo

Multicamadas baseadas em filmes ultrafinos de CoFeB são promissoras para diferentes tecnologias emergentes tais como memórias não voláteis com baixo consumo de energia e elevada velocidade de desempenho. No entanto, e antes de ser possível usá-los em qualquer aplicação, é necessário compreender profundamente o seu comportamento dinâmico magnético.

Com o propósito de poder realizar estudos dinâmicos das propriedades magnéticas neste tipo de materiais, um objectivo desta tese foi o desenvolvimento de uma montagem compacta e versátil para medidas magneto-ópticas resolvidas no tempo (TR-MO). A nossa montagem TR-MO foi desenhado para ser usada em diferentes configurações magneto-ópticas e com diferentes fontes laser.

O sistema TR-MO foi usado para estudar as propriedades estáticas e dinâmicas das multicamadas [CoFeB(t_{CoFeB})/Pd]$_N$. Em primeiro lugar, investigamos a resposta magnética do sistema multicamada quando fixamos o número de bicamadas em N = 5 e variamos a espessura do filme de CoFeB entre 1 e 5 Å. Em seguida, foram investigados os caso em que N foi variado de entre 3 e 15 bicamadas para amostras com uma espessura de CoFeB (t_{CoFeB}) de 3 e 4 Å. Além disso, foram estudadas outras estruturas, conhecidas como "*exchange spring magnets*", e onde as multicamadas [CoFeB($t_{CoFeB} = 3$ Å)/Pd]$_5$ constituem um sistema magneticamente duro e com PMA, enquanto que um filme de Co é a parte magnética macia com anisotropia no plano da amostra e com espessura (t_{Co}) a variar entre 0 e 25 Å. Estes estudos foram complementados com medidas no domínio das frequências usando la espectroscopia VNA-FMR (*Ressonância Ferromagnética baseada num Analisador de Redes*).

No último capítulo desta tese de doutoramento, focamos o nosso trabalho o estudo na possibilidade de modificar e manipular o magnetismo de uma amostra pelo campo eléctrico da luz. Por esse motivo, o nosso sistema TR-MO foi concebido para ser capaz de usar impulsos ultracurtos no regime de poucos ciclos, com uma duração de sub-5-fs, e obtidos pela técnica de pós-compressão numa fibra-oca cheia de gás. Apresentam-se resultados preliminares, usando estes impulsos ultracurtos com a fase da portadora (CEP) estabilizada, que confirmam que o processo de desmagnetização do sistema de multicamadas considerado é afectado directamente pelo campo eléctrico da luz.

Palavras-chave: dinâmica de magnetização ultra-rápida; multicamadas de filmes ultra-finos; espectroscopia com impulsos de poucos ciclos.

Contents

Abbreviations

All Optical Switching	AOS
Autocorrelation	AC
Brillouin Light Scattering	BLS
Carrier-Envelope Offset	CEO
Carrier-Envelope Phase	CEP
Charged Coupled Device	CCD
Chirped-Pulse Amplification	CPA
Coplanar Waveguide	CPW
Double-Chirped Mirrors	DCM
Ferromagnetic	FM
Ferromagnetic Resonance	FMR
Ferromagnetic Resonance Force Microscopy	FMRFM
Frequency-Resolved Optical Gating	FROG
Full-Width at Half-Maximum	FWHM
Fused Silica	FS
Group Delay Dispersion	GDD
Hollow-Core Fiber	HCF
Kerr Lens Mode-Locking	KLM
Landau-Lifshitz-Gilbert	LLG
Magnetic Circular Birefringence	MCB
Magnetic Circular Dichroism	MCD
Magnetic Tunnel Junctions	MTJs
Magneto-Optical Kerr Effect	MOKE
Multiphoton Intrapulse Interference Phase Scan	MIIPS
Neutral Density	ND
Nuclear Magnetic Resonance	NMR
Optically induced Spin Transfer	OISTR
Periodic Boundary Conditions	PBC
Periodically-Polled Lithium Niobate Crystal	PPNL
Perpendicular Magnetic Anisotropy	PMA
Pulse-inductive Microwave Magnetometry	PIMM
Scanning Electron Microscopy	SEM
Second Harmonic Generation	SHG
Self-Phase Modulation	SPM
Spectral Phase Interferometry for Direct Electric-Field Reconstruction	SPIDER
Spin–Orbit	SO
Spin-Polarized Low-Energy Electron Microscopy	SPLEEM
Spin-Transfer Torque Magnetic Random Access Memories	STT-MRAM
Superconducting Quantum Interference Device	SQUID
Third-Order Dispersion	TOD
Three-Temperature Model	3TM
Time-Bandwidth Product	TBP

Time-Dependent Density Functional Theory	TDDFT
Time-Resolved Magneto-Optical	TR-MO
Time-Resolved Magneto-Optical Kerr Effect	TR-MOKE
Time-Resolved Second Harmonic Generation	TR-SHG
Two-dimension	2D
Two-Magnon Scattering	TMS
Two-Temperature Model	2TM
Vector Network Analyzer - Ferromagnetic Resonance	VNA-FMR
Vibrating Sample Magnetometer	VSM
Body Centered Cubic	bcc
Face Centered Cubic	fcc
Extreme Ultraviolet	XUV
X-ray Absorption Spectroscopy	XAS

Chapter 1

Introduction

1.1. Nanomagnetism and Technology

Magnetism is a phenomenon that fascinated humankind from ancient times, but the first historical mention was about 600 BC by Thales of Miletus [1]. Since these early times, it has inspired inventions that greatly benefit humankind, from its use in surgery [2] to the compass for navigation [3].

The modern magnetism has its origin in the 19th century, with the research works by Oersted, Ampère, Gauss, Biot-Savart, Faraday, Lorentz, and Maxwell, which formed the basis of magnetostatics and magnetodynamics [4] and led to more sophisticated inventions such as electro-motors, generators, and transformers, that have become the foundation of our technological society [5].

Since then, the magnetism research has discovered several fundamental phenomena and contributed for many modern-day technologies in the electromagnetics industry, in health science, and, more recently, in miniaturized solid-state devices, including magnetic data storage and memory devices [4]. The demand of the new technologies creates the need for new materials with properties different from the ones to achieve in a single material in the bulk [4].

Nanomagnetism is the research area dedicated to the study the nanoscale magnetic objects, including isolated nanoparticles, nanodots, nanowires, thin films, and multilayers, and macroscopic samples that contain nanoscale particles, as well their properties and applications [6]. It is a very dynamic field, with several major advances in a range of areas, from fundamental scientific discovery to new applications and devices, due to the versatility of the magnetic behavior in nanoscale systems, such as hard disc drives and magnetic sensors, among others [7]–[9].

In our days, with the invention of new magnetic materials, magnetic nanostructures are being developed in a range of multidisciplinary fields in one, two, and three dimensions [10], to invent faster, smaller, more energy-efficient technologies [11] for our daily life use. The different magnetic properties in nanoscale compared to macroscopic materials, arising from the fact that nanoscopic dimensions are comparable to characteristic magnetic lengths, and also from broken translation symmetry [12]. Moreover, exploiting

the dynamical magnetic properties over various time scales may give rise to desirable material properties [4].

In two dimension (2D), single- or multi-layered magnetic structures, the thickness is of the order of some characteristic magnetic length-scale, which leads to monodomain magnetic states in the vertical direction. In these cases, complex and useful magnetic behaviour is possible by exploiting interfacial effects between layers [10], such as effects of spin-orbit coupling and symmetry breaking at the interface between a magnet and nonmagnet are of particular interest and importance [11].

In this thesis, the magnetization dynamics of CoFeB/Pd-based multilayers ultrathin films from the magnetization precession and damping to the ultrafast demagnetization were studied.

In this chapter, we start by introducing the thin films with perpendicular magnetic anisotropy (PMA) (section 1.2), and we give an overview of the CoFeB ultrathin films with PMA (sub-section 1.2.1). In the following two sections, we make a brief introduction to the basic concepts in magnetism, which are relevant for this thesis. In section 1.3, the different energy contributions that come into play when describing the magnetization's static or dynamic behavior in a ferromagnetic thin film sample. In section 1.4, we describe the equation of motion governing the magnetization dynamics and damping contributions. A brief reference to the methods to investigate the magnetization dynamics depending on the time scales of various dynamical magnetic processes is done in section 1.5. The laser-induced magnetization dynamics is overviewed in section 1.6. In the end, the scope of this thesis is presented.

1.2. Thin Films with Perpendicular Magnetic Anisotropy (PMA)

With the development of the fabrication and characterization techniques, thin films, with well-controlled and improved physical and chemical properties, has become one of the most active areas of several research fields. The use of thin films was already reported during the middle bronze age (more than 5000 years ago) when the Egyptians produced thin gold layers (thickness < 300 nm) for decorative and optical applications [13]. Since them, thin films are a key factor for important developments in all areas of engineering and applied science [14]. In particular, the quickly development of thin films has occurred in parallel with the progress of the electronic devices miniaturization such as the Cu thin layers used for the electrical connection among billions of transistors in a silicon integrated-circuit [13], [15].

Other common applications include transparent conductive oxide and absorber layers in solar cells, catalytic layers for toxic-gas sensing, corrosion-, friction and wear-protective

layers for the automotive and airplane areas, on eyeglasses to correct vision, minimize ultraviolet light transmission, and provide scratch resistance, and even as antibacterial and gas barriers for food packaging [14]–[17]. Regarding the magnetic applications [16], thin films have been usually suggested for data storage [18]–[20] and magnetic sensors [21], [22].

In 1950's, researchers had already recognized the enormous technological potential of thin magnetic films for use as sensors and information storage devices [23]. Louis Néel [24] pointed out the importance of the surface in leading to modified switching fields, the role of finite thickness in modifying the domain structure of a thin ferromagnetic film and the role of interface roughness in mediating interlayer dipole coupling [23].

Since the mid-70s of the 20th century [25], [26], materials with perpendicular magnetic anisotropy (PMA) have been studied for a large diversity of applications including, but not limited to, perpendicular recording media [19], [20], [25], [26], patterned magnetic media [27], [28], high-density spin-transfer torque magnetic random access memories (STT-MRAM) [29]–[31] and more recently in skyrmion-based devices [32]–[34] and synthetic antiferromagnets for biomedical applications [35]–[37].

PMA in thin films can be usually achieved though different strategies which can be summarized in a simple way by the following two approaches:

1) Materials with large magnetocrystalline anisotropy energy such as CoCr-based alloys, with well-oriented c-axis and hexagonal close-packed crystal structure (hcp) [26], [38], [39], well as alloys exhibiting L10-ordering (FePt and FePd) [40]–[42] or L11 CoPt films [43], [44].

2) Multilayer thin films or superlattices with a high surface anisotropy energy contribution. These multilayers are formed by alternating ultrathin layers which generates a large number of interfaces. The alternating ultrathin layers are usually formed by two ferromagnetic materials, such as Co/Ni [45]–[47] and CoFe/Ni [48], or by the combination of nonmagnetic/ferromagnetic bilayers such as in Co/Pt [49]–[51], Co/Pd [52] or CoFe/Pt [53] multilayers.

1.2.1. CoFeB-based Ultrathin Films with PMA

Among different materials showing this last alternative, CoFeB-based thin films have received great attention since in 2010 when Ikeda *et al.* [31] demonstrated that this alloy in contact with an MgO layer can show PMA. Then, this alloy can be used in perpendicular Magnetic tunnel junctions (MTJs) devices [31], [54], [55]. It was demsotrated that this behaviour can be achieved when the CoFeB layer is thin enough and the CoFeB/MgO interfacial anisotropy contribution [31], [55], [56] overcomes the volumetric terms of the

anisotropy energy (including for example the magneto-crystalline, shape and/or magnetoelastic terms) [57].

The efficient achievement of PMA in crystalline CoFeB films, usually, requires bcc CoFeB with (0 0 1) orientation (perpendicular to the film plane) and a MgO/CoFeB interface [31], [56], [58]. Since the crystalline phase of CoFeB film does not form naturally at room temperature, heat treatments, as *in situ* heating during the deposition or post-annealing, are frequently employed to convert the amorphous film into the required crystalline texture needed [59], [60]. Nevertheless, in the case of films with oxide interfaces, the heat processes can originate oxidation or migration (of boron and oxygen), with consequences for the magnetic properties of these films [61]–[63].

Therefore, multilayer systems with PMA based on amorphous CoFeB with noble metal as spacing layers have been also reported [64]–[66]. In comparison with the crystalline CoFeB films, the amorphous systems shows several advantages that make them excellent candidates for spin-transfer torque applications [67]:

• First of all, the amorphous CoFeB alloys show high spin polarization (up to 65%), higher than crystalline CoFeB film [68], and than Co, Fe, and Ni (around 45%) [69].

• An amorphous thin layer does not exhibit grain boundaries, which should decrease the pinning site density that slows down the magnetization reversal, and consequently, an enhancement of the speed of the spin switching can occur, a desirable feature for high-speed spin-transfer torque devices [67]. Furthermore, amorphous layers could establish very smooth interfaces that would diminish the attenuation of the electron spin during transfer through interfaces, which is beneficial for the high tunneling magneto resistance [70], [71], when employed in magnetic tunneling junctions.

• Comparing with crystalline CoFeB film interfaced with an oxide layer (e.g., MgO), the multilayer system with amorphous CoFeB and the noble metal spacing layers (of e.g., Pd or Pt) removes the possibility of oxidation and diffusion, which, as above mentioned, influences the magnetic properties of the films [67].

• In the CoFeB films, the presence of B atoms, with a smaller radius than Co an Fe atoms, results in a high glass-forming capability [72] and, therefore, the amorphous structure is expected to have high stability, even under heating, when compared with rare earth-transition metal amorphous films (e.g., TbFeCo and GdFeCo) [73]–[76].

• Additionally, the PMA could easily occur in amorphous CoFeB films in any substrate without further heat treatment, making the fabrication process more straightforward and less expensive [67].

In conclusion, the development of nonmagnetic/ferromagnetic superlattices, with high surface anisotropy energy and using CoFeB-based alloys as the ferromagnetic element, have received great attention and several works have been focused on the optimization

of the PMA by using different materials for the capping and/or buffer layers [77], including Ta [78], [79], Hf [80], [81], Mo [82], [83], Ru [84], [85], V [84], Nb [85], Pt [86], [87], Pd [64], [65], [67] and Au [88].

Regarding the system studied in this thesis, it was also in 2010 when PMA in CoFeB/Pd was first demonstrated in bilayers by Fowley *et al.* [65] as well as in multilayers by Jung *et al.* [89]. Moreover, literature has reported that the effective anisotropy energy depends on the thickness of magnetic (t_{CoFeB}) and non-magnetic (t_{Pd}) layers as well as on the number of bilayers (N) [66], [67], [89]–[91].

Regarding the dynamical properties, the CoFeB alloys can be growth with a low damping parameter (α) [31], [92]. Since damping determines the temporal performance of magnetic devices such as the time-scale for magnetization reversal or spin-transfer-torque (STT) switching, α is a key parameter for the development of several technological applications.

1.3. Energy Contributions in Ferromagnets

The magnetic response of a ferromagnetic sample is determined by the interplay between the different contributions to its total or effective free magnetic energy density (K_{eff}). Then, the sample magnetization will be oriented in such a way, that the total free magnetic energy density of the ferromagnetic system should be reduced. The most significant contributions to K_{eff} in ferromagnetic thin films, such as exchange, Zeeman, magneto-crystalline anisotropy, shape anisotropy, surface anisotropy and magneto-elastic anisotropy energies, are summarized below. In our description, we have considered a continuum model where the magnetization $\boldsymbol{M}$ is be given by the total of the magnetic moments ($\sum_i \boldsymbol{m}_i$) divided by the sample volume (V):

$$\boldsymbol{M} = \frac{1}{V}\sum_i \boldsymbol{m}_i. \tag{1.1}$$

Exchange Energy

The exchange interaction is responsible for the aligning of spins as parallel or antiparallel to each other [5]. This contribution originates from the Coulomb interaction between electrons in combination with the Pauli exclusion principle, which declares that two fermions cannot be in the same state, and results in a difference in energy for the parallel and antiparallel alignment of the spins of two atoms. Using the Heisenberg model, the exchange interaction is described by [93]:

$$E_{exc} = -\sum_{i,j}^{N} J_{ij}\left(\boldsymbol{S}_i.\boldsymbol{S}_j\right) = -2\sum_{i<j}^{N} J_{ij}\left(\boldsymbol{S}_i.\boldsymbol{S}_j\right) \tag{1.2}$$

where J_{ij} is the exchange integral and $\boldsymbol{S}_{i,j}$ are spin operators of atoms *i* and *j*. If $J_{ij} > 0$, E_{exc} reaches a minimum when the spins are parallel like in samples with ferromagnetic ordering. If $J_{ij} < 0$, the lowest energy state results from antiparallel spins. As the Heisenberg model is isotropic, the exchange interaction term does not depend on the direction of the magnetization relative to the material crystal structure.

In addition, and as the value of J_{ij} decreases rapidly with increasing the distance between the atoms, the summation in Eq. (1.2) may be limited to the nearest neighbors only [94]. Under this assumption, a value of the exchange integral $J_{ij} = J$ can be derived from the Weiss classical molecular field theory:

$$J = \frac{3kT_c}{2zS(S+1)} \tag{1.3}$$

where T_c is the Curie temperature, z is the number of nearest neighbors and S is the magnitude of the spin. By replacing the summation in Eq. (1.2) by an integral over the volume of the ferromagnetic sample (V), or making the transition to a (classical) continuum representation, the exchange energy density is given by [95]

$$K_{exc} = \frac{A}{V}\int dV(\nabla \boldsymbol{m}^2) \tag{1.4}$$

where $\boldsymbol{m} = \boldsymbol{M}/M_{sat}$ is the reduced or normalized magnetization, $\boldsymbol{M}$ is the magnetization vector, and M_{sat} is the saturation magnetization value. A is the exchange stiffness constant, which has the dimension [energy/length] and is related to J by

$$A = nJS^2/a, \tag{1.5}$$

where a is the lattice constant, S is the magnitude of the spin and n is a factor depending on the crystal structure [96]. n is equal to 1 for the simple cubic lattice, 2 for the bcc lattice, and 4 for the fcc lattice [6].

Then, the exchange interaction is the origin of spontaneous long-range ordering in ferromagnetic materials.

Shape Anisotropy Energy

The shape anisotropy energy arises from the magnetic field generated by the ferromagnet itself and it is also known as stray field energy, magnetostatic energy or demagnetization field energy. It is originated by the dipolar interaction between the magnetic moments. As

each magnetic moment interacts with the dipolar field generated by the rest of magnetic moments, it is a non-local energy contribution and shows a long-ranged interaction.
The demagnetizing field, $\boldsymbol{H}_{dem}$, can be determined from Maxwell's equation. The Gauss's law for the magnetic flux density $\boldsymbol{B}$ is given by:

$$\nabla.\boldsymbol{B} = \nabla.(\boldsymbol{H}_{dem} + 4\pi\boldsymbol{M}) = 0. \tag{1.6}$$

and the $\boldsymbol{H}_{dem}$ can be defined as divergence of the magnetization:

$$\nabla.\boldsymbol{H}_{dem} = -\nabla.4\pi\boldsymbol{M}. \tag{1.7}$$

Then, the corresponding energy density can be described by [97]

$$K_{dem} = \frac{1}{8\pi}\int_{all\ space}\boldsymbol{H}_{dem}^2 dV = -\frac{1}{2}\int_{sample}\boldsymbol{M}.\boldsymbol{H}_{dem}dV \tag{1.8}$$

In contrast to the exchange interaction energy, which only depends on the nearest neighbors, K_{dem} is characterized by the entire sample.
In general, the demagnetizing field $\boldsymbol{H}_{dem}$ of a sample, with an arbitrarily shaped, may be approximate by [93]:

$$\boldsymbol{H}_{dem} = -\bar{\bar{N}}\boldsymbol{M}. \tag{1.9}$$

where $\bar{\bar{N}}$ is the demagnetization factor and it is tensor function of the sample shape. Then, the energy density can be expressed as

$$\boldsymbol{K}_{dem} = -\frac{1}{2}\bar{\bar{N}}\boldsymbol{M^2}. \tag{1.10}$$

As it was commented, $\bar{\bar{N}}$ depends on the sample shape and it can be easily calculated for an ellipsoid uniformly magnetized but difficult for any other geometry.
Then, $\bar{\bar{N}}$ is just a diagonal matrix $\begin{pmatrix} N_x & 0 & 0 \\ 0 & N_y & 0 \\ 0 & 0 & N_z \end{pmatrix}$ for an ellipsoidal shape. Moreover, $\bar{\bar{N}}$ should fulfill the condition that the sum of the demagnetizing factors along the three orthogonal axes of an ellipsoid is a constant:

$$N_x + N_y + N_z = 4\pi \tag{1.11}$$

In particular, and for the development of this thesis, we are interested in studying infinite thin film homogeneously magnetized and with the z-axis pointing perpendicular to the film

plane. This geometry corresponds to the limit case of an oblate ellipsoid with $x = y = \infty \gg z$ and one obtains $N_x = N_y = 0$ and $N_z = 4\pi$. According to this, the xy-plane is an easy-plane of magnetization, the z -axis is a hard magnetization axis, and the shape anisotropy energy density is described by:

$$\boldsymbol{K}_{dem} = -2\pi M_{sat}^2. \tag{1.12}$$

Magneto-crystalline Anisotropy Energy

In general, the energy of a ferromagnet depends on the direction of the magnetization relative to the crystallographic axes of the sample. As it was already described, the shape anisotropy term is based on the dipolar interactions and depends on the sample shape but it has no dependence on the crystallographic axes. This dependence of the anisotropy energy on the crystal lattice is explained by the spin-orbit interaction, which couples the spin system to the orientation of the crystalline orbitals [5]. The spins energy is connected to its orientation concerning the crystal lattice and its symmetry. The anisotropy energy is approximately $10 - 100$ times smaller than the exchange energy [5], but it is of considerable importance as it breaks the spatial isotropy.

The most common types of magneto-crystalline anisotropies are cubic and uniaxial. For cubic crystals structure, such as found in iron and nickel, the energy density of the **cubic magneto-crystalline anisotropy** is given by [95]

$$K_{cryst} = k_1\left(m_x^2 m_y^2 + m_y^2 m_z^2 + m_z^2 m_x^2\right) + k_2 m_x^2 m_y^2 m_z^2 + \ldots \tag{1.13}$$

where m_i are the components of the normalized magnetization $\boldsymbol{m}$ referring to the cubic axes of the lattice. k_1 , k_2 , ... are the magnetic anisotropy constants. These for a particular material at a particular temperature are constants. They are expressed in erg/cm^3 (cgs) that can be converted to J/m^3 (SI) by dividing by 10. k_1 and k_2 are the anisotropy constants of first and second order. Third and higher orders terms are negligibly small [95]. While positive values of the anisotropy constants indicate that this direction is an easy magnetization axis, negative values show that the plane perpendicular to this direction is the easy magnetization plane.

A **uniaxial magneto-crystalline anisotropy** which can arise in crystals that exhibit hexagonal or tetragonal symmetry.

For example, Cobalt has a hexagonal close-packed (hcp) structure at room temperature. The hexagonal crystallographic c-axis is the direction of easy magnetization, and all directions in the basal plane are found to be equally hard. Then, the anisotropy energy

depends on the angle (θ) between the M_{sat} vector and the c-axis, and Its energy density is described by

$$K_{cryst} = k_1 sin^2(\theta) + k_2 sin^4(\theta) + \cdots \quad (1.14)$$

where k_1 and k_2 are the uniaxial anisotropy constants. Usually, $k_1 \gg k_2$ and the contribution of k_2 is negligible. For $k_1 > 0$, the c-axis becomes a so-called easy axis, i.e. the energy is minimal when the magnetization is aligned in parallel. For $k_1 < 0$, the c-axis is a hard axis and the magnetization tends to align in the plane perpendicular to it. Uniaxial anisotropies can be very strong, reaching 10^7 J/m^3 for rare earth transition metal permanent magnets [95].

Surface Magneto-crystalline Anisotropy Energy

Apart from the previous contributions which can be suggested as volume anisotropies, an extra anisotropic energy term applied only to the surface magnetization could be considered. It was introduced in 1954 by Louis Néel [24], who pointed out that the proportion of atoms on the surface or interface of a thin film is much higher when compared to the bulk material. Then the surface magneto-crystalline anisotropy becomes relevant in thin films and multilayers. This effect, which is negligible in bulk samples, is attributed to the reduced symmetry of the atomic environment of surface atoms concerning the interior or bulk atoms of the material. The surface anisotropy in films is manifest as a uniaxial anisotropy term which depends on the angle between the magnetization and the normal to the film surface, and given as:

$$K_{sur} = -k_s cos^2\theta, \quad (1.15)$$

where k_s is the surface anisotropy constant and it expressed in erg/cm^2 (cgs). Then, the contribution of this term could be significant for thin films and it can even dominate and control the magnetization response in ultrathin layers (< 1 nm).

Magneto-elastic Anisotropy Energy

One of the consequences of the spin-orbit interaction is the phenomenon of magnetostriction, in which the sample size changes if the direction of the magnetization is altered. Strain in a ferromagnet changes the magneto-crystalline anisotropy and may alter the direction of the magnetization, which is the ‘inverse’ of the previous effect. As the spin moments are coupled to the lattice via the orbital electrons, if the lattice is changed

by a strain the distances between the magnetic atoms are altered and hence the interaction energies are modified. This effect produces a magnetic anisotropy contribution, the so-called magnetoelastic anisotropy and it can be significant for nanostructured thin films [57].

The density energy associated with this effect can, for an elastically isotropic medium with isotropic magnetostriction, be written as [57]

$$K_{elas} = -k_{me} cos^2\theta \ , \tag{1.16}$$

with $k_{me} = -\frac{3}{2}\lambda\sigma = -\frac{3}{2}\lambda E\varepsilon$, where k_{me} is the magneto-elastic anisotropy constant, σ is the stress, which is related to the strain, ε, by the elastic modulus E via $\sigma = E\varepsilon$. The magnetostriction constant λ depends on the orientation and can be positive or negative. The angle θ measures the direction of the magnetization relative to the direction of uniform stress.

Strain in thin films can be induced by several sources from thermal strain, associated with differences in thermal expansion coefficients, to intrinsic strain brought about by the nature of the deposition process and strain due to non-matching lattice parameters of adjacent layers [57].

When the magneto-elastic term does not depend on the magnetic layer thickness (t) and is constant across the sample thickness, it can be identified as an extra volumetric contribution However, and in particular for thicker samples, the magneto-elastic term is not constant across t anymore, and this term should be considered as a surface contribution [57].

Zeeman Energy

The interaction of the magnetization ($\boldsymbol{M}$) and the external field ($\boldsymbol{H}_{ext}$) is known as the Zeeman energy [5]. When an external magnetic field $\boldsymbol{H}_{ext}$ is applied, the magnetization $\boldsymbol{M}$ suffers a torque that makes all the magnetic moments align in the direction of such field. The magnetization will align with the external field if the other energy contributions (described above) were overcome. In particular, if one wants to align a magnetic material in the hard direction the Zeeman interaction has to overcome the spin-orbit interaction which determines the magneto-crystalline anisotropy [5]. The Zeeman energy density is described by [95]

$$K_{zee} = -\int \boldsymbol{M}.\boldsymbol{H}_{ext}\ dV \tag{1.17}$$

K_{zee} is minimized as soon as the sample magnetization is aligned in the direction of the external applied magnetic field.

Summing up the different contributions, we can now determine the total or effective free energy density as

$$K_{eff} = K_{exc} + K_{dem} + K_{cryst} + K_{sur} + K_{elas} + K_{zee}. \quad (1.18)$$

From the minimization of the effective free energy density (Eq. (1.18)), the direction of the sample magnetization or the equilibrium angle of the magnetization can be determined. Moreover, we should note that in thin films, such as the samples studied along this thesis, the effective magnetic anisotropy energy density could be phenomenologically separated in [57]:

$$K_{eff} = K_{vol} + (2K_{sur}/t) \quad (1.19)$$

where K_{vol} (erg/cm^3) is the bulk anisotropy energy density operating uniformly throughout the film thickness and K_{sur} is an energy per unit area localized (erg/cm^2) at the surface. This relation only represents a weighted average of the magnetic anisotropy energy of the interface atoms and the inner atoms of a magnetic layer of thickness t. The pre-factor 2 accounts the magnetic layer to be bounded by two identical interfaces [57].
A quantitative measure of the strength of the effective magnetic anisotropy energy is the anisotropy field, H_{eff}, which is the applied magnetic field needed to saturate the magnetization of a sample in the hard magnetic direction [57], [98]. The energy per unit volume needed to saturate a material in a particular direction follows the equation [57], [98]:

$$K_{eff} = \int_0^{M_{sat}} H(M)dM \quad (1.20)$$

which corresponds to the area between the $M(H)$ curve and the M-axis of the hysteresis loops. In the first-order approximation, Eq. (1.20) can be described by:

$$K_{eff} = \frac{1}{2}\left(H_{eff} \times M_{sat}\right) \quad (1.21)$$

Considering the simplest case, when the magnetic sample shows a uniaxial anisotropy, such as hcp Co, the uniaxial anisotropy energy density is the energy needed to saturate the magnetization in the basal plane minus that needed to saturate along the c-axis (which is essentially zero, by comparison). Then, the magnetic anisotropy energy density is the area between the magnetization curves in different crystallographic directions.

As it will be described in sub-section 3.7.1, H_{eff} is experimentally obtained from the fitted data of the measurements performed to study the magnetization dynamics, and these values will be used to determine the different contributions to the effective anisotropy energy.

1.3.1. Hysteresis Loops

Ferromagnets are characterized by a non-zero spontaneous magnetization even without the application of a magnetic field. The magnetization of ferromagnetic materials is not a linear function of the applied magnetic field, and its magnetic curves present a hysteretic behavior. Figure 1.3 shows a typical hysteresis loop for a ferromagnetic material.
The increasing of the applied magnetic field until the saturation field H_{sat} leads the material to be magnetized to the saturation magnetization M_{sat}. From this point, the magnetic field increase does not further affect the magnetization since all the magnetic moments are aligned entirely into the direction of the applied field.

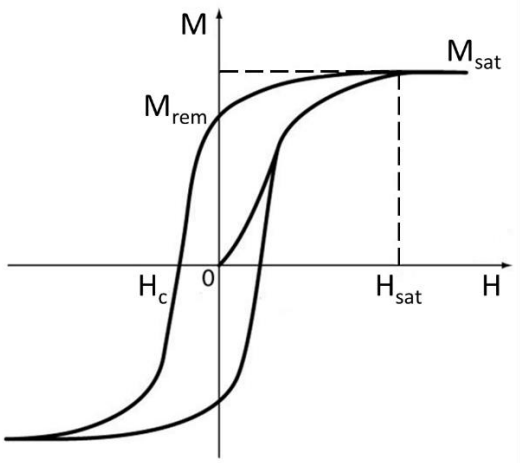

Figure 1.1: Schematic represents the magnetic hysteresis loop of a ferromagnetic material. From Reference [99].

When the applied field is reduced to zero from the positive values, the material retains some magnetization, the so-called remanent magnetization M_{rem}. To obtain a zero magnetization and leads it to switch in the opposite direction, the applied field must continue to be reduced towards negative values. The critical field needed for magnetization changes sign is the coercive field H_c. From a general point of view, the parameters M_{sat}, H_{sat}, M_{rem} and H_c can be used to characterize the magnetic behavior of a ferromagnetic material.

1.4. Magnetization Dynamics

1.4.1. Magnetization Precession

In 1935 Landau and Lifshitz [100] proposed a model for the description of the magnetization dynamics using an equation that shows the magnetization precession. A phenomenological damping term was later introduced by Gilbert [101], [102] in the Landau–Lifshitz equation to explain the dynamical magnetization precession and subsequent alignment of magnetization along the effective field direction [103].

Landau-Lifshitz Equation

The equation of motion for the dynamics of a single spin can be derived from quantum mechanics [103], and expressed as:

$$\frac{d}{dt}\langle \boldsymbol{S} \rangle = \frac{g\mu_B}{\hbar}\langle \boldsymbol{S} \rangle \times \boldsymbol{B} \tag{1.22}$$

where $\boldsymbol{S}$ denotes spin and $\boldsymbol{B}$ the magnetic field, the multiplicative term corresponds to the gyromagnetic ratio $\gamma = g\mu_B/\hbar$, μ_B is the Bohr magneton, g is the gyromagnetic factor for a free electron and $\hbar$ is reduced Planck´s constant.
The motion equation of one spin can be generalized for the case of a sample with homogeneous magnetization. In this macrospin model, the magnetization vector, $\boldsymbol{M}$, is defined by a uniform distribution of spins in the sample, and it is express as:

$$\boldsymbol{M} = -\frac{g\mu_B}{\hbar}\langle \boldsymbol{S} \rangle \tag{1.23}$$

Therefore, the equation of the magnetization motion in presence of an external magnetic field is given by

$$\frac{d\boldsymbol{M}}{dt} = -\gamma \boldsymbol{M} \times \boldsymbol{H} \tag{1.24}$$

Eq. (1.24) is known as the Landau–Lifshitz (LL) equation, and this is generalized by using the effective magnetic field $\boldsymbol{H}_{eff}$ in the place of the external magnetic field $\boldsymbol{H}$. According to Eq. (1.18) and (1.20), the effective magnetic field is composed of the exchange field ($\boldsymbol{H}_{exc}$), the demagnetizing field ($\boldsymbol{H}_{dem}$), the crystallography anisotropy field ($\boldsymbol{H}_{cryst}$), the magnetoelastic anisotropy field ($\boldsymbol{H}_{elas}$) and the external applied magnetic field ($\boldsymbol{H}_{ext}$):

$$\boldsymbol{H}_{eff} = \boldsymbol{H}_{exc} + \boldsymbol{H}_{dem} + \boldsymbol{H}_{cryst} + \boldsymbol{H}_{elas} + \boldsymbol{H}_{ext} \tag{1.25}$$

The LL model considers that the total magnetic moment is connected to the total angular momentum, which is subject to a torque, and results in a precessional motion. It thus implies that $\boldsymbol{M}$ precesses around the $\boldsymbol{H}_{eff}$ in a circular orbit as shown in Figure 1.4 (a) for infinite duration and with an angular frequency $\omega_L = \gamma H_{eff}$, known as the Larmor precession frequency. However, this behaviour does not correspond to the experimental observations, where the precession amplitude of magnetization decreases with time, until $\boldsymbol{M}$ is aligned with the direction of the minimal energy or the $\boldsymbol{H}_{eff}$ direction (see Figure 1.4 (b)). Therefore, a dissipative effect was considered in order to describe the real magnetization dynamics, and a damping term or a phenomenological dissipation term was included in the LL equation [100]:

$$\frac{d\boldsymbol{M}}{dt} = -\gamma \boldsymbol{M} \times \boldsymbol{H}_{eff} + \frac{\lambda}{M_{sat}^2} \boldsymbol{M} \times \left(\boldsymbol{M} \times \boldsymbol{H}_{eff}\right) \tag{1.26}$$

with the phenomenological damping constant $\lambda > 0$ that should have the dimension of a frequency. We should point out that Eq. (1.26) conserves the magnitude of the magnetization according to the micromagnetic constraint $|\boldsymbol{M}| = M_{sat}$ [104].

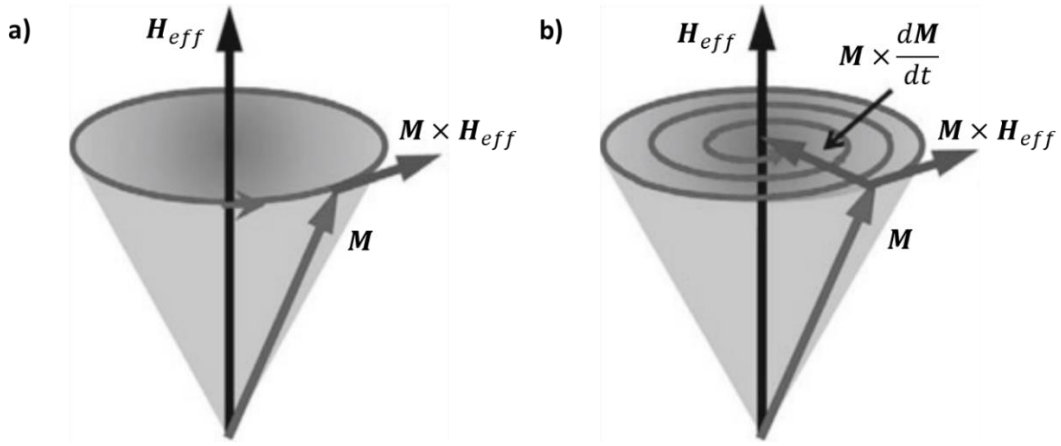

Figure 1.2: Precession of magnetization about the applied bias field **a)** without damping and **b)** with damping. From [103].

Landau-Lifshitz-Gilbert (LLG) Equation

However, the most often employed equation of motion is the so-called Landau-Lifshitz-Gilbert (LLG) equation. It consists of the same precessional term as in the LL equation (Eq. 1.24) but combined with a different damping term.

In 1955, Gilbert [101], [102] modeled a 'viscous' damping, depending on the time derivative of the magnetization and considering a phenomenological dissipation term. Gilbert applied a thermodynamical approach in the following form:

$$\frac{\alpha}{M_{sat}}\left(\boldsymbol{M}\times\frac{d\boldsymbol{M}}{dt}\right) \tag{1.27}$$

where α is the dimensionless Gilbert damping. This term determines how fast the energy of the magnetization precession is dissipated from the system.
Including this term in Eq. (1.24), the LLG equation [101], [102] is described by:

$$\frac{d\boldsymbol{M}}{dt} = -\gamma\boldsymbol{M}\times\boldsymbol{H}_{eff} + \frac{\alpha}{M_{sat}}\left(\boldsymbol{M}\times\frac{d\boldsymbol{M}}{dt}\right) \tag{1.28}$$

As in the LL model, the magnitude of the magnetization is also conserved in the LLG equation, and Eq. (1.28) can show an appearance similar to that of the LL equation (Eq. 1.23) [5]:

$$\frac{d\boldsymbol{M}}{dt} = -\frac{\gamma\mu_0}{1+\alpha^2}\boldsymbol{M}\times\boldsymbol{H}_{eff} + \frac{\gamma\mu_0\alpha}{M_{sat}(1+\alpha^2)}\boldsymbol{M}\times\left(\boldsymbol{M}\times\boldsymbol{H}_{eff}\right) \tag{1.29}$$

One can see the mathematical equivalence between Eq. (1.29) and Eq. (1.26) when assuming

$$\gamma_{LL} = \frac{\gamma_{Gilb}\mu_0}{1+\alpha^2} \quad ; \quad \lambda = \frac{\gamma_{Gilb}\mu_0 M_{sat}}{1+\alpha^2} \tag{1.30}$$

The two equations, albeit mathematically equivalent, do not lead to the same magnetization dynamics for infinitely high damping. The LLG equation results in $(d\boldsymbol{M})/(dt) \to 0$ for $\alpha \to \infty$. In contrast, the LL equation results in $(d\boldsymbol{M})/(dt) \to \infty$ for $\lambda \to \infty$ [104]. Therefore, only the LLG equation predictes a behavior with physical meaning for large damping values. In summary, we would like to restate that the damping term is phenomenological, i.e. it was specifically introduced to reproduce the experimental observation in the best conceivable way. Nevertheless, the processes of energy dissipation in ferromagnets are numerous and complicated and can be only approximately described by a single damping parameter [104]. An overview of contributions to energy dissipation, and therefore to α, is given in section 1.4.

Smit & Beljers Resonance Equation

The easier way to determine the frequency of the magnetic precession is related to the derivatives of the total energy density K_{eff}, and it can be deduced by using the ansatz

after Smit & Beljers [105]. Similar approach was also found simultaneously and independently by Suhl [106] as well as by Gilbert [101].

To derive the general expression for the resonance frequency, first we must derive the Landau-Lifshitz equation in a more appropriate system of coordinates. Under the condition that the magnitude of the magnetization does not change, we can choose the spherical coordinate system. Thus, $\boldsymbol{H}_{eff}$ in spherical coordinates is given by:

$$\boldsymbol{H}_{eff} = -\frac{1}{\mu_0}\left(\frac{\partial K_{eff}}{\partial r}\boldsymbol{e}_r + \frac{\partial K_{eff}}{\partial \theta}\boldsymbol{e}_\theta + \frac{1}{M_{sat} sin\theta}\frac{\partial K_{eff}}{\partial \phi}\boldsymbol{e}_\phi\right) \tag{1.31}$$

where θ and ϕ are the polar and azimutal angles, respectively (see Figure 1.5). In this coordinate system, the magnetization is given by $\boldsymbol{M} = M_{sat}\boldsymbol{e}_r$, where M_{sat} is the saturation magnetization. The infinitesimal change in the magnetization vector can be expressed as $d\boldsymbol{M}$ =$M_{sat}\left(dr\boldsymbol{e}_r + d\theta\boldsymbol{e}_\theta + sin\theta d\phi\boldsymbol{e}_\phi\right)$.

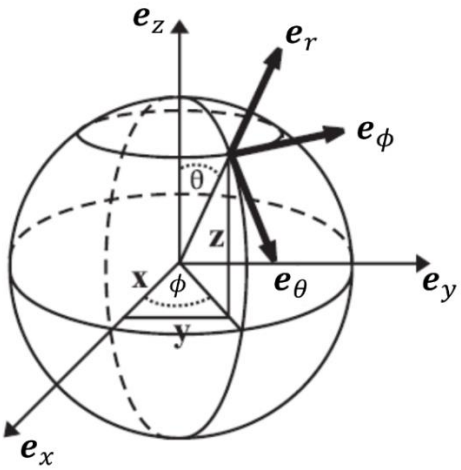

Figure 1.3: Spherical coordinates used during the derivation of the Smit and Beljers resonance formula. From [107].

The left- and right-hand side in the Landau Lifshitz equation (Eq. (1.24)) can be written as:

$$\frac{d\boldsymbol{M}}{dt} = M_{sat}\frac{d\theta}{dt}\boldsymbol{e}_\theta + M_{sat} sin\theta \frac{d\phi}{dt}\boldsymbol{e}_\phi \tag{1.32}$$

$$\boldsymbol{M} \times \boldsymbol{H}_{eff} = \frac{1}{\mu_0 sin\theta}\frac{\partial K_{eff}}{\partial \phi}\boldsymbol{e}_\theta - \frac{\partial K_{eff}}{\partial \theta}\boldsymbol{e}_\phi, \tag{1.33}$$

respectively, which leads to the Landau-Lifshitz equation in spherical coordinates:

$$\frac{d\theta}{dt} = -\frac{\gamma}{M_{sat}sin\theta}\frac{\partial K_{eff}}{\partial \phi} \tag{1.34}$$

$$\frac{d\phi}{dt} = -\frac{\gamma}{M_{sat}sin\theta}\frac{\partial K_{eff}}{\partial \theta}. \tag{1.35}$$

These are nonlinear equations in spherical coordinates. As there is not an exact analytical solution, we must find perturbative solutions around the equilibrium position, assuming small deviations of both θ and ϕ around the equilibrium positions θ_0 and ϕ_0, respectively. Therefore, the free energy density K_{eff}can be expanded in a Taylor series, and considering only first-order terms, we obtain:

$$K_{eff}(\theta,\phi) = K_{eff}(\theta_0,\phi_0) + \frac{1}{2}\left(K_{eff\_\theta\theta}\theta^2 + K_{eff\_\theta\phi}\theta\phi + K_{eff\_\phi\phi}\phi^2\right) \tag{1.36}$$

The equations of motion for the polar and azimuthal angle of the magnetization become:

$$\frac{d\theta}{dt} = -\frac{\gamma}{M_{sat}sin\theta}\left(K_{eff\_\theta\phi}\theta + K_{eff\_\phi\phi}\phi\right) \tag{1.37}$$

$$\frac{d\phi}{dt} = -\frac{\gamma}{M_{sat}sin\theta}\left(K_{eff\_\theta\theta}\theta + K_{eff\_\theta\phi}\phi\right) \tag{1.38}$$

The θ and ϕ, which satisfy the previous sets of equations, are given by the small harmonic oscillations around the equilibrium values, θ_0 and ϕ_0:

$$\delta\theta \approx \theta - \theta_0 = A_\theta e^{i\omega t} \tag{1.39}$$

$$\delta\phi \approx \phi - \phi_0 = A_\phi e^{i\omega t} \tag{1.40}$$

where A_θ and A_ϕ are the amplitude of the precession. The previous solutions are incorporated into Eq. (1.37) and Eq. (1.38) to derive the following set of equations:

$$\left(\frac{\gamma K_{eff\_\theta\phi}}{M_{sat}sin\theta} - i\omega\right)\theta + \frac{\gamma K_{eff\_\theta\theta}}{M_{sat}sin\theta}\phi = 0 \tag{1.41}$$

$$\frac{\gamma K_{eff\_\theta\theta}}{M_{sat}sin\theta}\theta + \left(\frac{\gamma K_{eff\_\theta\phi}}{M_{sat}sin\theta} + i\omega\right)\phi = 0 \tag{1.42}$$

The non-trivial solution to the homogeneous system given by the previous equations exists only when the following condition is satisfied:

$$\omega = \frac{\gamma}{M_{sat}sin\theta}\sqrt{\frac{\partial^2 K_{eff}}{\partial\theta^2}\frac{\partial^2 K_{eff}}{\partial\phi^2} + \left(\frac{\partial^2 K_{eff}}{\partial\theta\partial\phi}\right)}\Bigg|_{\theta=\theta_0,\phi=\phi_0} \tag{1.43}$$

This is the so-called Smith-Beljers equation. It is interesting to note that the frequency of precession of the magnetization is given by the partial derivatives of the free magnetic energy with respect to the polar and azimuthal angles of the magnetization in their equilibrium values. This representation is therefore very practical since the resonance condition can be directly evaluated from the relevant free energy density of a magnetic system in conjunction with the equilibrium conditions:

$$K_\theta = \frac{\partial K_{eff}}{\partial \theta}\Big|_{\theta=\theta_0} = 0 \qquad \text{and} \qquad K_\phi = \frac{\partial K_{eff}}{\partial \phi}\Big|_{\phi=\phi_0} = 0. \qquad (1.44)$$

1.4.2. Magnetization Damping Contributions

In the previous section, we introduced the phenomenological or effective Gilbert damping parameter. As it was previously commented, damping determines the temporal performance of magnetic devices. Then, materials with low α have been suggested for high speed spintronic devices, such as in STT-based systems with low switching and power consumption minimization [30], [108], as well as in Magnetic tunnel junctions (MTJs) with high signal-to-noise ratio [31], and in magnonic devices [109]. On the other hand, systems, with high α values, have been suggested for spin pumping and inverse spin Hall effect applications [110]–[112]. Therefore, understanding the behaviour of the α parameter is of particular importance.

However, this unique parameter contains contributions from a variety of processes involved in the dissipation of energy to the non-magnetic degrees of freedom and they are distinguished between intrinsic and extrinsic contributions [113]. In most cases, the energy is transferred to the lattice resulting in heating it and creating phonons [70]. This contribution is an intrinsic term that depends on the spin-orbit coupling. However, extrinsic processes, such as for example the two-magnon scattering [104], should be also considered.

Next, we will focus our attention on describing the main published results of the damping parameter for the CoFeB alloy.

Intrinsic Term

Regarding the intrinsic term or Gilbert damping, it is generally assumed that each material should show a particular $\alpha_{Gilbert}$ which is constant with the resonance frequency but shows composition and temperature dependence [113], [114]. In particular and in connection with the material studied along this thesis, a Gilbert damping as small as $\alpha_{Gilbert} = 0.004$ has been reported for CoFeB [115]–[117]. In addition, Devolder *et al.* [92]

studied the correlation between $\alpha_{Gilbert}$ and the g-factor (g) in CoFeB thin films as a function of the alloy composition and annealing conditions. As it was expected in transition metals [118], the dependence $\alpha_{Gilbert} \approx (g-2)^2$ was reported.

Extrinsic Terms

Among different contributions, we will introduce few of the main processes that can contribute for the extrinsic term of α_{eff}:

Inhomogenety Contribution

The inhomogeneity contribution is based on the local variations of the magnetization and the magnetic anisotropy field. This effect can be caused by structural defects and/or thickness variations [113]. Then, it should be constant with the resonance frequency but, for example, should depend on the sample composition, thickness and materials used for the capping and/or buffer layers [92].

Two-magnon Contribution

The two-magnon scattering (TMS) contribution provides an additional magnetic relaxation channel based on the annihilation of a uniform precession magnon (wave vector k = 0) and the creation of a magnon with $k \neq 0$ [119]. Although the total number of magnons is kept constant in this process, all the spins in the generated $k \neq 0$ magnon are not parallel, the total magnetization is reduced and leads to an additional term in α_{eff} [120]. In particular, Liu et al. [115] performed out-of-plane angular dependence FMR measurement of CoFeB thin films and they reported that the damping mechanism depends on the layer thickness. It was suggested that α_{eff} is mainly governed by the Gilbert damping in thicker (≥ 4 nm) CoFeB films, while inhomogeneous broadening and two-magnon scattering are the main factors for films thinner than 2 nm.

Spin-pumping Contribution

The spin-pumping effect is a phenomenon where spin current generated by the precession of magnetization in ferromagnetic layers is injected and relaxed in adjacent non-magnetic metal layer [121], [122]. Spin-pumping was first suggested by Berger [123], and it was experimentally confirmed by Mizikami *et al.* [124], [125] that the damping of non-magnetic/magnetic/non-magnetic trilayers depends on the non-magnetic material. Large damping parameters were determined when non-magnetic materials with a stronger spin-orbit coupling, such as Pt and Pd, were used. In particular, Iihama *et al.* [78] investigated the damping parameter of Ta/CoFeB/MgO and Ta/CoFeB/Ta thin films using

all-optical pump-probe method and it was suggested that the enhancement of α_{eff} is caused by the spin pumping effect at the Ta/CoFeB interfaces.

Eddy currents Contribution

When a magnetic field varies with time within a conductor, eddy currents are induced as well as an opposite magnetic field. Therefore, magnetization precession in a ferromagnet placed on top of a coplanar waveguide (CPW) induces ac currents both in the ferromagnet and the CPW, giving rise to two contributions to magnetic damping:

a) Any change in the magnetization of a ferromagnetic material induces eddy currents. These eddy currents generate a magnetic field in the ferromagnet that tends to oppose the original change and provides a damping mechanism (α_{eddy}) [126], [127].

b) Moreover, the generated eddy currents also affect the waveguide and an extra damping mechanism, known as radiative damping (α_{rad}), should be considered [128], [129].

1.5. Methods for Investigating Magnetization Dynamics

The time scale for magnetization dynamics, depending on the processes involved, varies from several nanoseconds (ns) to femtoseconds (fs). The time scales (τ) are determined by the interaction energies (E) via Heisenberg relation $\tau = h/E$ [4].

Figure 1.4 is presented several mechanisms involved in the magnetization dynamics with their characteristic time scales. The fundamental exchange interaction is fastest process, occurring within 10fs. The spin–orbit coupling and spin-transfer torque occur in the time scale of 10 fs – 1ps. Laser-induced ultrafast demagnetization (addressed in the following section) occurs within few hundreds of fs, and the following fast remagnetization full covers the time scale of 1 – 10ps. The magnetic writing, which is done via reversal of spins, has a time scale of few ps to few hundreds of ps, whereas vortex core switching occurs from few tens of ps to ns time scale. The precession of magnetization occurs within few ps to few hundreds of ps whereas the associated damping occurs from sub-ns to tens of ns time scale. The spin waves in ferromagnetic material can propagate in a time scale from few hundreds of ps to tens of ns time scale before it dies out. The slowest process is the domain wall motion, which has the time scale from few ns to hundreds ms.

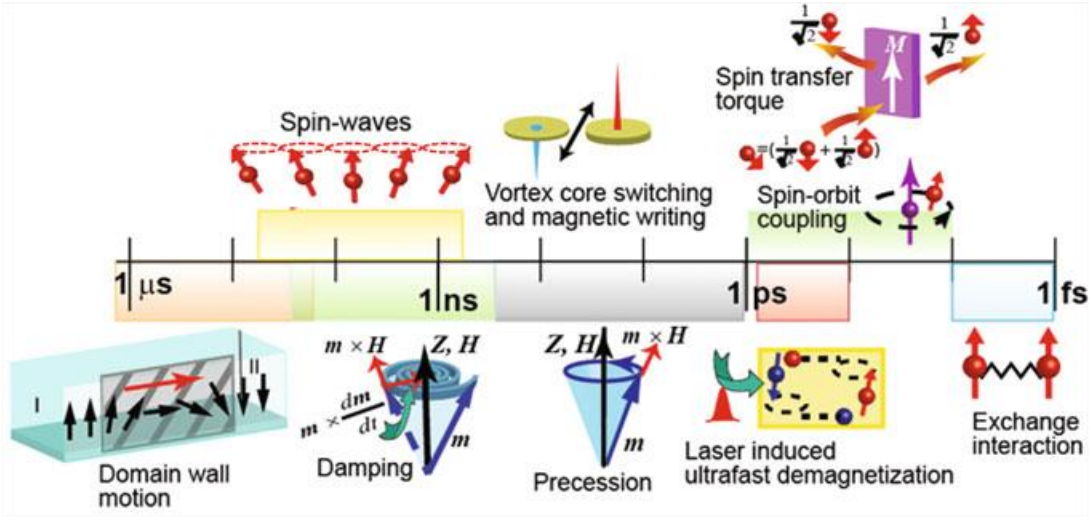

Figure 1.4: Time scales of various dynamical magnetic processes. From Reference [103].

In order to be able investigate the magnetization dynamics, from a fundamental perspective and for applications at these timescales, several techniques in the frequency, wave-vector, and time domains have been developed in the last decades [103]. Techniques, such as Ferromagnetic Resonance Force Microscopy (FMRFM) [130], [131], Spin-Polarized Low-Energy Electron Microscopy (SPLEEM) [132], Ferromagnetic Resonance (FMR) spectroscopy [133], [134], Brillouin Light Scattering (BLS) spectroscopy [135], [136], or Pulse-inductive microwave magnetometry (PIMM) [137], [138], allow the access to mechanisms on a time scale from several picoseconds up to nanoseconds. However, processes that occur on a shorter time scales (up to picoseconds) can only be studied by time-resolved methodologies such as the Time-Resolved Magneto-Optical Kerr Effect (TR-MOKE) or Time-Resolved Second Harmonic Generation (TR-SHG) [139], which are based on the stroboscopic principle using ultrashort laser pulses in a pump-probe scheme [140] (see subsection 3.5.1.). Slower processes such as magnetization precession can be accessed also by time-resolved spectroscopy [141], [142].

During this thesis, our work has used the two following methods: 1) The Ferromagnetic Resonance (FMR), on the frequency-domain, and it described in section 3.6.2) The Time-Resolved Magneto-Optical Kerr Effect (TR-MOKE) on time-domain and with a high temporal resolution, it is described in section 3.5 and our experimental setup is detailed described in Chapter 4.

1.6. Laser-induced Ultrafast Magnetization Dynamics

With the emergence of the ultrafast laser technology in the 1980s and 1990s, and the capability of producing sub-picosecond light puses, a whole new research field started in magnetism: the ultrafast magnetism or femtomagnetism. These ultrashort pulses are used in a pump-probe scheme (see subsection 3.5.1) to control and observe magnetism on a femtosecond timescale.

Ultrafast Demagnetization

The first demonstration of the possibility of manipulating the magnetization using fs laser pulses was performed by Beaurepaire et al. in 1996 [143]. A nickel thin film was demagnetized in a sub-picosecond time scale after being excited with a 60 fs laser pulse followed by magnetization recovery on a longer time scale (see Figure 1.5 (a)). Subsequent research after this first observation, confirms this finding in Nickel [139], and on other materials such as Fe [144] and Co [145] confirmed the generality of the effect in magnetic metals. In the following years it was observed and study as well in a wide range of magnetic materials, such magnetic semiconductors [146], dielectrics [147] and half-metals [148]. Since then, the ultrafast demagnetization receveid a lot of attention, and an intense research was carried out from both fundamental and experimental point of view [140], [149], [150].

From the first observation of this phenomenon some questions about the mechanism and processes involved, particulary the ultrashort excitation leads to a complex, strongly non-equilibrium state, were raised. Several models envolving different mechanisms had being propose to explain the ultrafast demagnetization dynamics, and continues an open debate.

The three-temperature model (3TM), based on rate equations, which is an extension of the two-temperature model (2TM) [151], was used to described phenomenologically the sub-ps demagnetization by Beaurepaire et al. The model assumes that the system consists of three thermalized reservoirs for exchanging energy, namely the electron, lattice, and spin subsystems. In 3TM, heat capacities and temperatures are assigned to the reservoirs of electron (*e*), spin (*s*), and lattice/phonons (*l*): (C_e;T_e), (C_s;T_s), and (C_l;T_l), respectively, and coupling constants between electron–spin, spin–lattice, and charge–lattice are defined as G_{es}, G_{sl}, and G_{el}. (Figure 1.5 (b)), which describe the rate of energy exchange between the participating subsystems. By exchanging heat, spins come to an equilibrium temperature with electron and lattice. Therefore, the lattice temperature changes, and also does the magnetocrystalline anisotropy, which is a function of lattice

temperature. The ultrafast change in magnetocrystalline anisotropy acts as an effective pulsed field and triggers the precession of magnetization [4].

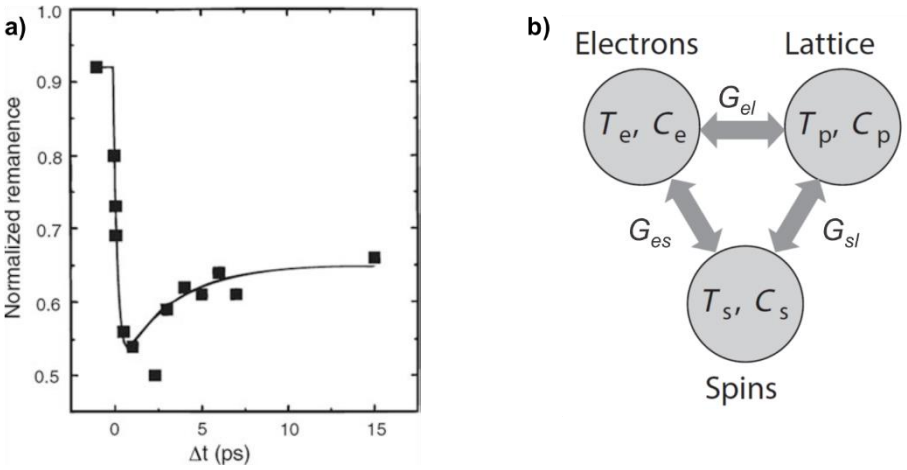

Figure 1.5: (a) Ultrafast demagnetization measurement on a 20nm thick Ni film and using a 60fs laser pulse. From Reference [143]. (b) The three-temperature model (3TM), the magnetic film is divided into three subsystems: the electron, phonon or lattice, and the spin reservoirs. Each one described by a temperature $T_{e,l,s}$ and a heat capacity $C_{e,l,s}$, and $G_{el,es,sl}$ are the coupling constants between them. From Reference [152].

In 2000, Zhang and Hübner [153] proposed a model based on the **direct interaction between photons and spins**, as a cooperative effect in the presence of both an external laser field and the internal spin–orbit coupling that smears out singlet and triplet states allowing for optically induced spin flips. In 2009, Bigot et al. [154] proposed a similar microscopic mechanism in which a laser-field-induced time-dependent modification of the spin–orbit interaction was taken into account, such effect leading to a coherent interaction between the pump photons and the spins [103].

Koopmans *et al*. proposed that during ultrafast demagnetization, phonon-mediated Elliot-Yafet spin-flip scattering [155], [156] is responsible for the spin angular momentum transfer to the lattice, the so-called **microscopic three temperature model** (M3TM) [157], [158]. As in the case of the 3TM, it is derived three coupled differential equations for the electron, spin and lattice temperatures. The derivation of the equations starts from microscopic Hamiltonians, giving a better insight in the underlying mechanisms. In this model, the spin angular momentum is dissipated (locally) to the lattice by a spin flip upon electron-phonon scattering.

Battiato *et al.* [159], [160], proposed completely different model based on the **superdiffusive spin transport** mechanism, which attributes the demagnetization to a non-local transfer of angular momentum. In this model, the ultrafast demagnetization

results from the spin-dependent transport of charge carriers out of a ferromagnetic layer instead of spin flips. In multilayer systems, Rudolf *et al*. [161] showed that the ultrafast magnetization enhancement in metallic multilayers is driven by a superdiffusive spin current, and Eschenlohr *et al.* [162] declared the ultrafast spin transport as key to femtosecond demagnetization.

In 2013, Mueller *et al.* [163], proposed a model based on **eletron-eletron mediated Elliot-Yafet spin-flip scattering**. It is dynamical model for Elliott-Yafet-type spin-flip scattering in ferromagnets that combines Boltzmann scattering dynamics (including a material specific density of states) with a Stoner model for itinerant electrons [163].

Other models like **atomistic Landau-Lifshitz-Gilbert and Landau-Lifshitz-Bloch approaches** [164]–[166], despite the differences in microscopic interpretation produce a very similar ultrafast magnetization dynamics profile to the one M3TM gives, assuming as well that the angular momentum is dumped into the lattice.

Interesting developments in ab initio calculations had been made using many-body cluster calculations [167] and time-dependent density functional theory (TDDFT) [168] considering **spin orbit - induced spin-flip scattering.**

All optical Switching (AOS)

In 2007, in another pioneering work, Stanciu *et al.* [169] demonstrated a complete reversal of the magnetization using only a single 40 fs laser pulse without any external magnetic field in a ferrimagnetic amorphous GdFeCo alloy (Figure 1.6 (a)), which was called all optical magnetic switching (AOS).

The discovery of AOS is an important outcome of the ultrafast optical research and had an enormous impact on the field of magnetism, partly due to its potential to be used in future magnetic memory devices. The complete optical switching of the magnetization was achieved at a timescale of tens of picoseconds [170], which is a huge increase in writing speed and could be used to write magnetic information in spintronic devices at an unprecedented speed and with high energy efficiency.

AOS is heat driven and can be achieved with light pulses of any polarization above a certain fluence threshold [171], [172], and mechanism through which occurs is reasonably well understood in GdFeCo and involves the sublattice dynamics of its ferrimagnetic structure [172], [173].

In 2014, Mangin *et al* [174] shown that, apart from ferrimagnetic RE-TM alloys, AOS also occur in artificial ferrimagnetic systems that have compensation temperatures but are RE-free, magnetic multilayers and heterostructures. Lambert *et al* [175] demonstrated that helicity dependent AOS is also possible in ferromagnetic thin films such as [Co/Pt]

multilayers and granular L10 FePt in a C matrix. Figure 1.6 (b) the results for a [Co (0.4 nm) / Pt (0.7 nm)]3 multilayer where the final state of the magnet is dependent on the helicity of the light.

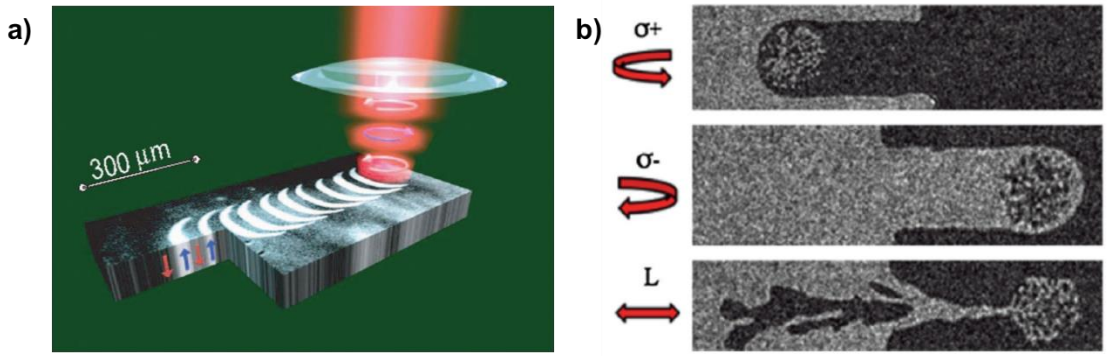

Figure 1.6: All-optical switching. (a) Scanning a laser beam across the sample and simultaneously modulating its polarization between left- and right-circular pulses yields a magnetic bit pattern in an amorphous Gd-Fe-Co alloy. From Reference [169]. (b) Magneto-optical images of a [Co (0.4 nm) / Pt (0.7 nm)]$_3$ multilayer, where sweeping a pulsed laser source with circular polarization determines the final state's magnetic orientation. From Reference [175].

Ultrafast laser induced processes are driven mainly by spin-orbit and exchange interactions, and it is possible that interfacial and intersublattice exchange interactions and interfacial spin-orbit interactions play a crucial role in AOS, while the details processes still unclear [11]. For further information on topic, one can refer to [150], [176], [177].

Ultrafast Coherent Magnetism

How fast can the magnetization of a magnetic medium to be changed? The fastest control of the magnetic state should occur through coherent excitation with a light field [153], [154], [168], [178], which implies a direct interaction between the spin system of the material and the laser field itself [179].

In the visible region, Bigot et al. [154] proposed coherent excitation of ferromagnetism and a mechanism to explain the coherent signals extract from the demagnetization curves with the pump and probe pulses polarizations parallel and cross, which are only present during the laser pulse interaction with the sample, for a Ni and a $CoPt_3$ thin films. In 2013, C. Vicario et al. [180], reported a coherent, phase-locked coupling between a high-field single-cycle THz transient, where the B-field amplitude reaches the Tesla range, and the magnetization dynamics of ferromagnetic Co films.

In 2019, F. Siegrist *et al.* [181] showed how the magnetic properties of a ferromagnetic layer stack could be manipulated directly by the electric-field of light, with a reduction of the magnetic response time by two orders of magnitude, by combining simultaneously attosecond transient extreme ultraviolet (XUV) absorption spectroscopy detection (attosecond XAS) with attosecond time-resolved magnetic circular dichroism (attosecond MCD). It was the first experimental evidence of the electric-field of light induced coherent transfer of spin and orbital angular momentum in space and time caused by the interplay of few-cycle optical excitation and the spin–orbit (SO) interaction in magnetic and non-magnetic multilayers [181]. The initial femtoseconds of the coherent spin-dynamics can be explained by the optically induced spin transfer (OISTR) effect recently introduced by Dewhurst *et al.* [182], whose the theoretical work predicted that few-cycle optical excitation can directly redistribute spins between different magnetic sublattices in a multicomponent magnetic material, without change the total magnetization of the material [183]. OISTR is the fastest and most efficient process to manipulate macroscopic magnetization since it does not rely on secondary mechanisms to dissipate angular momentum [184], and is particularly interesting from both a fundamental and an experimental point of view [183].

Since the initial work of F. Siegrist *et al.* [181], other works have shown the coherent interaction between the light-wave and spin system and confirming the OISTR effect in different materials. Hofherr *et al.* [183], in their work, provide experimental evidence of a direct, ultrafast, and coherent spin transfer between two magnetic subsystems of an alloy of Fe and Ni. Willems *et al.* [184] show that OISTR from Pt to Co emerges as a dominant mechanism in the ultrafast magnetization dynamics of a CoPt alloy, in which two processes lead to an increased demagnetization: enhanced spin-flips mediated by SO coupling and optically driven spin transport from Pt *5d* minority electrons to the Co *3d* states. P. Tengdin *et al.* [185] demonstrate the first direct optical manipulation of the magnetic moment of an individual element in a half-metallic Heusler material. Steil *et al.* [186] investigated experimentally and theoretically the efficiency of the OISTR process for half and full Heusler compounds.

With the advance of the light electric-filed control of magnetism, a whole new research field is open, the ultrafast coherent magnetism on femtosecond and attosecond regimes.

1.7. Scope of this Thesis

This introductory chapter is concluded by presenting the scope of this thesis and providing a broad outline of the following 7 chapters. In this thesis, the static and dynamic magnetic behaviour of CoFeB/Pd-based multilayers with perpendicular magnetic anisotropy and

exchange spring structures were studied. A versatile Time-Resolved Magneto-Optical (TR-MO) system was developed and used to investigate the dynamic magnetic behavior of the multilayers structures on time-domain. Our TR-MO setup was designed with the main goal of being able to access the ultrafast coherent magnetization regime with few-cycle visible pulses (sub-5-fs pulse duration).

The present PhD Thesis is organized as follows. **Chapter 2** aims to present the tools used, from the point of view of ultrafast optics, in the development of our pump-probe experimental apparatus operating in the femtosecond regime. **Chapter 3** presents a general description of the experimental techniques employed to investigate the static and dynamical response of the ferromagnetic samples studied in this thesis. **Chapter 4** describes our TR-MO setup which can be used in different configurations and with different light sources allowing us to perform the ultrafast magnetization dynamics measurements reported in Chapters 5, 6 and 7. Our ultimate goal was the development of a TR-MO system with sub-5-fs temporal resolution pulses. **Chapter 5** presents the study of the dynamical properties of [CoFeB(t_{CoFeB})/Pd]$_N$ multilayer ultrathin films, ranging the CoFeB layer thickness (t_{CoFeB}) between 1 and 5 Å with a number of bilayers N = 3, as well as for the set of samples with t_{CoFeB} = 3 and 4 Å and N ranged between 3 and 15. **Chapter 6**: presents the study of the magneto dynamical behavior of exchange spring structures, where the CoFeB/Pd-based multilayer system (hard part), with t_{CoFeB} = 3 Å and N = 5, is magnetically coupled with a Co layer (soft part) with a thickness ranging between 0 and 25 Å. **Chapter 7** presents the preliminary results of our pump probe setup based on pulses compressed by the gas-filled hollow-core fiber technique, with a temporal duration of sub-5-fs (few-cycle regime), which was developed to access and control the magnetic properties directly by the electric-field of light. **Chapter 8** concludes this thesis with a general summary.

Chapter 2

Ultrashort Light Pulses

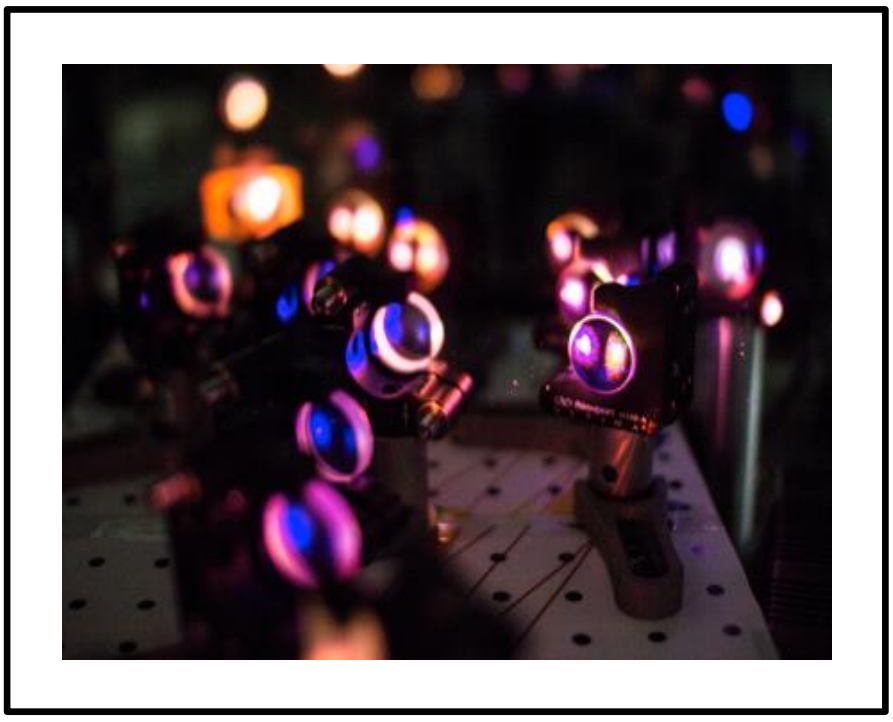

Chapter 2

Ultrashort Light Pulses

2.1. Introduction

This chapter aims to present the tools used, from the point of view of ultrafast optics, in the development of our pump-probe experimental apparatus operating in the femtosecond regime.

The advent of laser sources capable of producing sub-ps light pulses launched a whole new field of ultrafast (or femtosecond) magnetism. Ultrashort laser pulses are used in a pump-probe scheme to manipulate and observe magnetism on a femtosecond (fs) timescale, much faster than the typical timescales of magnetization dynamics in magnetic materials, something that cannot be achieved by any other technique.

This chapter gives a brief introduction to the generation and propagation of ultrashort laser pulses and to the techniques used to measure and compress them. Firstly, a description of ultrashort laser pulses is presented, followed by the dispersion effect due to their propagation in a medium and how to compensate it. We then introduce the basic concepts of ultrashort pulse generation, with emphasis on laser sources based on Ti:sapphire technology. The last sections are devoted to a brief introduction to nonlinear optics, followed by the diagnostic technique (dispersion scan) used in the present work, which allows the measurement and the compression of these ultrafast events.

2.2. Ultrashort Laser Pulses

Ultrashort laser pulses are laser pulses with durations of a few picoseconds (10^{-12} s) or less. Besides their ultrashort durations, these pulses have a broad spectrum. Therefore, it is important to acknowledge the relationship between the pulse duration and the spectral bandwidth when considering the generation and application of ultrashort pulses.

An ultrashort pulse can be described either in the time or spectral domain. The general time and frequency Fourier transforms of a pulse can be expressed in terms of the time-dependent electric field, $E(t)$, where $\tilde{E}(\omega)$ is its Fourier transform. The chosen conventions for the direct Fourier transform and inverse Fourier transform are,

$$\tilde{E}(\omega) = \int_{-\infty}^{+\infty} E(t) e^{-i\omega t} dt \qquad (2.1)$$

$$E(t) = \frac{1}{2\pi}\int_{-\infty}^{+\infty} E(\omega)e^{i\omega t}d\omega. \quad (2.2)$$

The duration and spectral bandwidth of a pulse can then be calculated with standard statistical definitions [187],

$$\langle \Delta t \rangle = \frac{\int_{-\infty}^{+\infty} t|E(t)|^2 dt}{\int_{-\infty}^{+\infty}|E(t)|^2 dt} \quad (2.3)$$

$$\langle \Delta \omega^2 \rangle = \frac{\int_{-\infty}^{+\infty} \omega^2|\tilde{E}(\omega)|^2 d\omega}{\int_{-\infty}^{+\infty}|\tilde{E}(\omega)|^2 d\omega} \quad (2.4)$$

It can be shown that the relationship between the duration and spectral bandwidth of the laser pulse are related by the following inequality

$$\langle \Delta t \rangle \langle \Delta \omega \rangle \geq \frac{1}{2} \quad (2.5)$$

This relationship, which leads to the quantum-mechanical time-energy uncertainty principle, has several important consequences in the field of ultrashort light pulses. Eq. (2.5) shows that one cannot have an arbitrarily short pulse without a broad spectrum and vice-versa. A broad-spectrum is a necessary, but not sufficient condition to have a short pulse. In fact, for a given broad-spectrum, we may have a relatively longer pulse than expected due to the existence of a non-constant spectral phase.

The product of pulse duration and spectral bandwidth is known as the **time-bandwidth product (TBP)**, which tells us how compressed a pulse is, i.e., how close the actual pulse is from the shortest pulse obtainable for a given spectrum. From the experimental point of view, full-width at half-maximum (FWHM) quantities are easier to measure; the Fourier inequality is then usually written as:

$$\Delta t \Delta \nu \geq K \quad (2.6)$$

where $\Delta\nu$ is the frequency bandwidth measured at FWHM, with $\nu = \omega/2\pi$, Δt is the FWHM pulse duration, and K is a number of the order of unity which depends on the temporal pulse shape. Table 2.1 presents K values for some symmetrical pulse shapes; for other pulse shapes see Reference [188]. If the equality is reached, one speaks about a Fourier-transform-limited pulse or simply a transform-limited pulse.

One can also express the minimum temporal duration of a pulse for a given spectrum with $\Delta\lambda$ (nm) at FWHM and central wavelength λ_0 (nm), with c (m/s) the speed of light:

$$\Delta t \geq K \frac{{\lambda_0}^2}{\Delta\lambda . c} \tag{2.7}$$

Shape	$\boldsymbol{E(t)}$	TBP
Gaussian	$exp[-(t/t_0)^2/2]$	0.441
Exponential function	$exp[-(t/t_0)/2]$	0.140
Hyperbolic secant	$1/\ cosh(t/t_0)$	0.315
Rectangle	-	0.892
Cardinal sine	$sin^2(t/t_0)/(t/t_0)^2$	0.336
Lorentzian function	$[1\ +\ (t/t_0)^2]^{-1}$	0.142

Table 2.1: Values of K for various pulse shapes in the inequality $\Delta\nu\Delta t \geq K$, when $\Delta\nu$ and Δt are full-width at half-maximum quantities [187]

In the **time domain**, an ultrashort optical pulse consists of a real-valued oscillating electric field, but the mathematical description can be simplified if a complex representation is used (at the spatial origin, x = 0):

$$E(t) = A(t)e^{i\omega_0 t} \tag{2.8}$$

where $A(t)$ is the complex amplitude envelope, and ω_0 is the carrier frequency, usually chosen to be close to the center of gravity of the spectrum. In this representation, the rapidly oscillating part of the electric field can be separated from the slowly varying envelope $A(t)$. The complex electric field can be further decomposed:

$$E(t) = |E(t)|\ e^{-i\phi_0}e^{-i\phi(t)}e^{i\omega_0 t} \tag{2.9}$$

Here $|E(t)|$ is referred to as the electric field envelope, or pulse amplitude, which in turn is the square-root of the pulse intensity, $I(t)$. The pulse intensity determines the pulse profile as well as its duration which is commonly given by its full-width at half-maximum (FWHM); $\phi(t)$ is the temporal phase and ϕ_0 is the absolute phase, which relates the position of the carrier wave to the temporal pulse envelope. For this reason, ϕ_0 is also called the carrier-envelope phase (CEP).

If the temporal phase $\phi(t)$ changes with time, the oscillation period of the electric field also becomes a function of time. In this case, the variation of $\phi(t)$ in time gives rise to a varying frequency and is described by the **instantaneous frequency** $\omega_{inst}(t)$ given by

$$\omega_{inst}(t) = \omega_0 - \frac{d\phi(t)}{dt} \tag{2.10}$$

If $\frac{d\phi}{dt} \neq 0$ then the field has chirp (i.e., the carrier frequency of the pulse varies in time) and so the pulse has a time-dependent instantaneous frequency and is said to be "chirped" (see Figure 2.1).

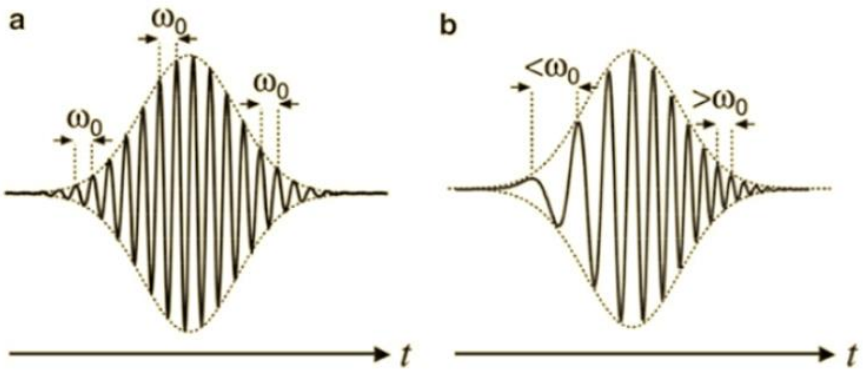

Figure 2.1: (a) Unchirped pulse; (b) chirped pulse showing the variation of instantaneous frequency. From Reference [189].

For many purposes, namely when calculating the effect of dispersion, it is more advantageous to represent a pulse in the **frequency domain** rather than in the time domain. One can write:

$$\tilde{E}(\omega) = \left|\tilde{E}(\omega)\right| e^{-i\varphi(\omega)} \tag{2.11}$$

where $\varphi(\omega)$ is the spectral phase. It should be noticed that the temporal electric field $E(t)$ can be regarded as a superposition of monochromatic waves with frequency ω, spectral amplitude $\left|\tilde{E}(\omega)\right|$, and phase $\varphi(\omega)$.
The effect of the spectral phase on the temporal profile of the pulse is described in the following section.

2.3. Dispersion

2.3.1. Dispersive Media

To obtain ultrashort pulses a broad bandwidth is necessary, which presents considerable technical challenges. The different spectral components of the pulses travel at different phase velocities through air, glass, or any other transparent media (see Figure 2.2). They suffer the effects of dispersion, i.e., a different refractive index for every frequency/wavelength, leading to pulse distortion that increases the temporal pulse

duration. The pulse broadens with time, but from energy conservation, its time integrated intensity remains constant [187]. The shortest the pulse, the broader its spectrum, and the harder it is to keep the pulse short.

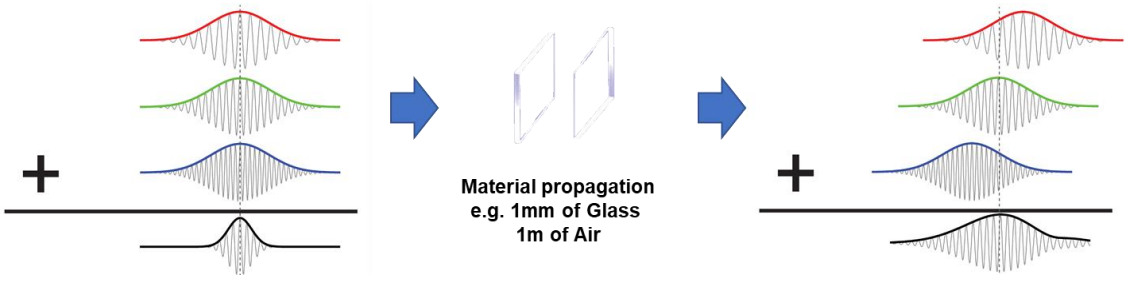

Figure 2.2: A schematic of a pulse stretched in time after passed through a dispersive media, the instantaneous frequency varies in time. When the dispersion of the material is normal (positive), longer wavelengths will travel faster.

The effects of pulse propagation in a dispersive medium can be studied particularly well in the frequency domain. For ultrashort pulses, the spectral phase is generally expressed as Taylor series expansion around ω_0, the central frequency, as:

$$\varphi(\omega) = \varphi(\omega_0) + \frac{d\varphi}{d\omega}(\omega - \omega_0) + \frac{1}{2!}\frac{d^2\varphi}{d\omega}(\omega - \omega_0)^2 + \frac{1}{3!}\frac{d^3\varphi}{d\omega}(\omega - \omega_0)^3 + \cdots \qquad (2.12)$$

When $\varphi(\omega)$ is constant or a linear function of ω , the pulse is said to be transform-limited (TL). The first term of $\varphi(\omega)$ is the Carrier-Envelope Phase (CEP), $\varphi(\omega_0)$, also known as Carrier-Envelope Offset (CEO) or absolute phase. Conceptually, it is a constant phase offset that does not influence the temporal profile of an ultrashort pulse. With the advent of few-cycle pulses, and highly nonlinear effects, this phase can be extremely important since the maximum field intensity of a few-cycle pulse depends on the CEP. The next term in Eq. (2.12) is the group-delay, t_g, given by

$$t_g = \frac{d\varphi}{d\omega} \qquad (2.13)$$

and it represents the time taken for a wave packet at a given frequency/wavelength to traverse an optical element. If $t_g(\omega)$ is constant for all ω, the effect in the spectral domain is a translation in time of the ultrashort pulse; otherwise, the pulse will suffer distortions due to higher-order dispersion. If we consider higher-order terms, we see that they imply a non-constant group-delay, i.e, a frequency dependent group-delay which naturally leads to the distortion of the original pulse.

Higher-order terms of the expansion are important for ultrafast optics because they are responsible for temporal pulse broadening and distortion. The quadratic term of the expansion is the first that leads to a deformation of the pulse envelope, usually called group delay dispersion (GDD), which can be expressed not only as a value referring to a central frequency, but also as a function of frequency

$$GDD(\omega) = \frac{d^2\varphi(\omega)}{d\omega^2}. \tag{2.14}$$

Other higher order phase terms can be described similarly, i.e., third-order dispersion (TOD)

$$TOD(\omega) = \frac{d^3\varphi(\omega)}{d\omega^3}, \tag{2.15}$$

as well as fourth-order dispersion, etc.

Figure 2.3 shows an initial gaussian pulse (capable of supporting a TL 5 fs duration) affected by a group-delay (GD) of 20 fs, a group-delay dispersion (GDD) of 20 fs^2 and a third-order dispersion of 80 fs^3 [190]. The group-delay translates into a shift of the pulse in time, the GDD broadens the pulse in time and the TOD gives rise to temporal broadening together with pre/post-pulses depending on the negative/positive sign of the TOD.

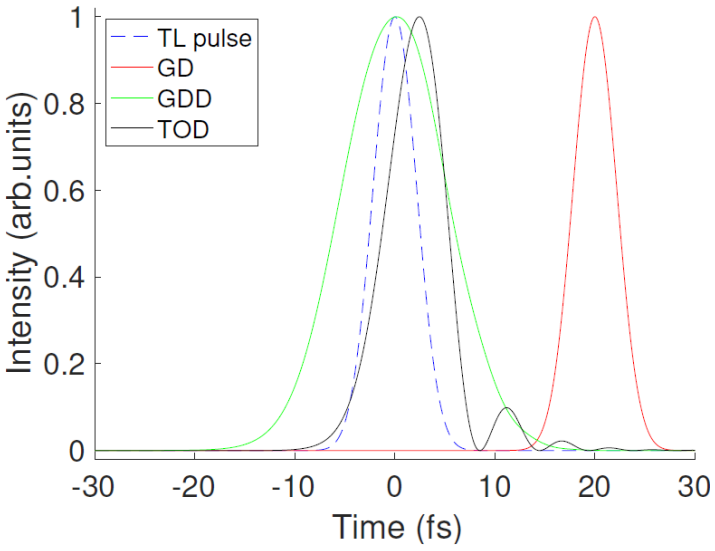

Figure 2.3: A gaussian pulse capable of supporting a TL duration of 5 fs affected by group-delay (20 fs), group-delay dispersion (20 fs^2) and third-order dispersion (80 fs^3). From Reference [190].

2.3.2. Dispersion Compensation

Dispersion compensation can be achieved in many ways. Some strategies, among the most common like gratings and prisms, are based on geometrical optical path length manipulation. Other strategy relies on both the path length manipulation as well as in the modulation of the refractive index of the medium or the phase introduced by engineered optical elements, e.g., chirped mirrors.

Gratings and Prism Compressors

The first technique for pulse compression introducing negative dispersion was based on diffraction gratings [191]. It makes use of pair of reflection gratings, the first to spatially separate the different spectral components of the pulses and lead them to travel different lengths, the second to compensate the spatial dispersion and recombine the pulses. This technique allows to compress pulses down to ~30 fs [192]. It is widely used since it can introduce a high amount of negative dispersion. Nevertheless, the method presents disadvantages, namely that the compressor has high losses, and only the first diffraction order is used. In chirped pulse amplification (described in subsection 2.4.2), it is extensively used as often the material dispersion alone is not sufficient to stretch the pulses enough to prevent damage.
In the case of a prism compressor [193], an advantage is that the losses are usually much lower (especially if they can be used at Brewster's angle). However, almost all prisms are less dispersive than gratings, which means larger distances between prisms are needed to provide enough spatial separation between the different spectral components. The total system GDD is compensated by orienting the prisms making the light travel through either more or less glass. Furthermore, since the light has to go through glass, there is intrinsic material dispersion that limits the amount of total negative dispersion that can be reached [194]. There is also the possibility of unwanted nonlinear effects due to propagation in the prism material. Several schemes exist that are more suited for amplifiers [194], [195] and combinations of prisms and gratings are also commonly used, as this enables compensating both the GDD and TOD.

Chirped Mirror Compressors

Another way for dispersion compensation was invented more recently [196]. This new strategy involves the creation of special dielectric mirrors. These so-called chirped mirrors, are specifically designed in such a way that the reflection phase compensates for material dispersion [196]. Figure 2.4 illustrates the working concept of chirped mirrors.

Different wavelengths penetrate different depths into the multilayer structure, where longer wavelengths travel a long distance inside the stack compared to shorter wavelengths, before being reflected. By varying the thickness of the layers that each have alternating refractive indices, results in a custom mirror design with a phase curve that matches a given target, e.g., a glass, and the achieved reflectivity is usually very high (typically more than 99% over their operation bandwidth).

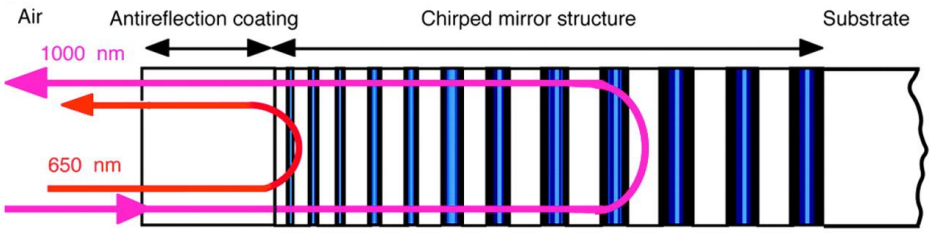

Figure 2.4: Structure of a chirped mirror, showing layers of different thickness and of alternating refractive indices, where the different wavelengths penetrate and are reflected at different depths into the multilayer stack. From Reference [197].

Double-chirped mirrors (DCM), usually designed and manufactured in matched pairs, present an anti-reflection coating and an extra layer structure [198], [199] that act as an impedance matching from air to the chirped structure itself. Such design results in very broad bandwidths and minimal residual dispersion oscillations.

Another chirped mirror scheme uses a single mirror design to be used at two different incident angles (double angle mirrors), to provide an overall negative dispersion with fewer ripples (compared to regular DCMs) over a broad wavelength range [200].

Chirped mirrors provide a fixed dispersion and are normally used in conjunction with a pair of glass wedges to fine-tune the dispersion.

In this thesis, we use the latter method to compensate for the dispersion of our experimental apparatus (see Chapter 4).

2.4. Generation

2.4.1. Mode-locked Lasers

Ultrashort pulses are usually generated by a mode-locked laser. A short pulse is formed by constructive interference when many longitudinal modes are synchronized in phase in a laser resonator. In a laser cavity, many longitudinal modes oscillate with different frequencies within the range supported by the gain medium, ideally as many as possible.

First studied by Moulton [201], Ti:sapphire is the most used gain medium for ultrashort lasers due to its broad gain bandwidth, amongst other important characteristics. If these modes oscillate with a random relative phase, the laser oscillator generates continuous wave light (CW operation). However, if the modes are phase-locked to each other, they will interfere constructively (see Figure 2.5) at certain times, resulting in a train of potentially short pulses, the so-called mode-locking regime.

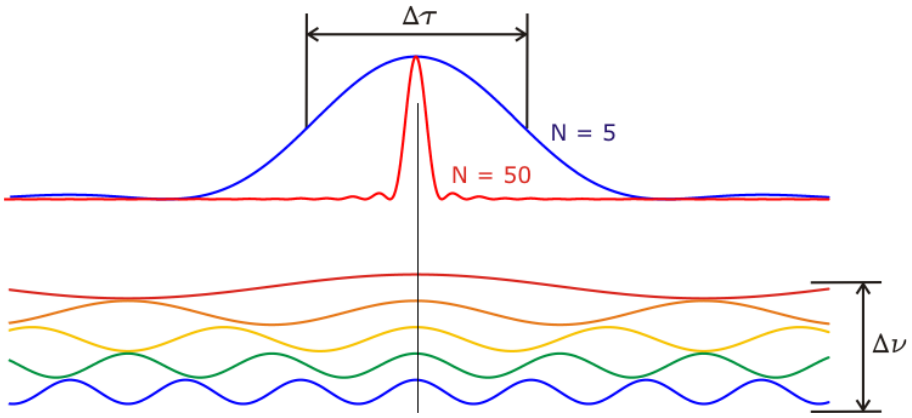

Figure 2.5: Simplified schematic of a superposition of resonator modes. While a mode number of 5 results in a long pulse duration (blue), pulses with a spectral width of 50 modes are much shorter (red). The gain bandwidth determines the shortest duration obtainable for the pulses. From Reference [202]

A gain medium with a broad gain bandwidth is necessary to generate ultrashort pulses but this is not enough. It is also required to favor the broad bandwidth pulsed operation over the CW operation. There are different methods to achieve mode-locking operation. In the lasers based on Ti:sapphire technology, the most common is the Kerr lens mode-locking (KLM) method, which effectively results in an intensity-dependent loss mechanism. The KLM technique makes use of the optical Kerr effect to establish a phase relation between adjacent laser modes without the need for external modulation (passive mode-locking). This is a simple way to consider Kerr lensing, which will occur if there is enough intensity in the crystal. Since the Kerr effect depends non-linearly on the intensity, the Kerr lens, due to self-focusing in the laser crystal, only occurs for short pulses in the cavity [203]. If this mechanism is introduced into the cavity the mode-locked operation will be favored, eventually, only phase-locked modes will survive in the cavity. In mode-locked Ti:sapphire lasers based on the Kerr lens effect, sub-10-fs pulses can routinely be generated.

2.4.2. Chirped-Pulse Amplification

The chirped-pulse amplification (CPA) technique, introduced by Strickland and Mourou [204] (Nobel prize in Physics 2018), is one of the main techniques to produce ultrashort pulses with high-energy and femtosecond durations. By using such a technique, it is possible to obtain pulses with durations of the order of 20–100 fs with energies from hundreds of microjoules up to several tens of joules (as in the recent Petawatt lasers).
Figure 2.6 shows a schematic of a chirped-pulse amplification-based laser system. In the pulse amplification, high instantaneous intensities are reached that could easily damage the pulse and the laser gain medium itself. The solution is to chirp the pulse (i.e., stretch it in time), hence reducing its intensity. The pulse can then be safely amplified.

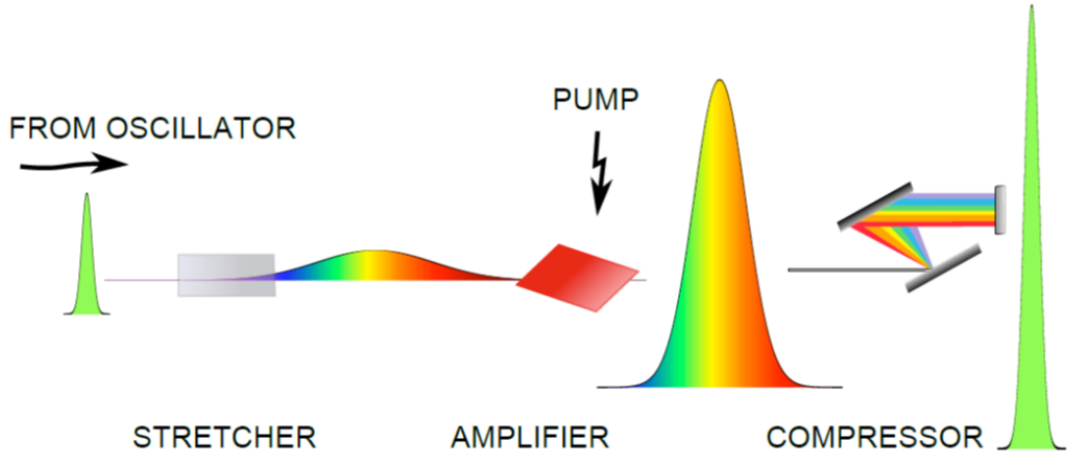

Figure 2.6: Simplified schematic of a chirped-pulse amplification-based laser system. From Reference [205].

In a CPA-based laser system, the pulse is stretched using a dispersive system (a grating stretcher or another dispersive device), typically to durations ranging from a few picoseconds up to several nanoseconds. After amplification, a second set of gratings and/or prisms is used to recompress the pulse, typically to 20-30 fs durations.
The amplified pulse duration is longer than the seed one since its spectral bandwidth is reduced due to the gain-narrowing effect during the amplification process [206].
Our CPA-based Ti:sapphire laser amplifier is described in section 4.4. The time-domain magnetization dynamics studies presented in chapters 5 and 6 were performed with our Time-Resolved Magneto-Optical Kerr Effect (TR-MOKE) system based on our amplifier laser source.

2.4.3. Spectral Broadening in a Hollow-Core Fiber

The spectral broadening and pulse post-compression with a hollow-core gas-filled fiber were first introduced by Nisoli *et al.* [207]. This technique is composed of two steps: i) nonlinear spectral broadening and ii) broadband dispersion compensation [207]–[210] (Figure 3.1).

In the first step, the laser pulse spectrum is broadened inside a gas-filled hollow-core fiber (HCF) mainly by self-phase modulation (SPM) due to the time-dependent optical Kerr effect. Other effects must be taken into account as well, such as plasma effects from the gas ionization and the linear dispersion [205]. The nonlinear propagation of the pulses leads to spectral broadening, which allows generating shorter pulses since a larger spectral bandwidth becomes available. The dynamics of spectral broadening in hollow-core fibers can be very complex, and the output of such systems is very sensitive to the input parameters [205].

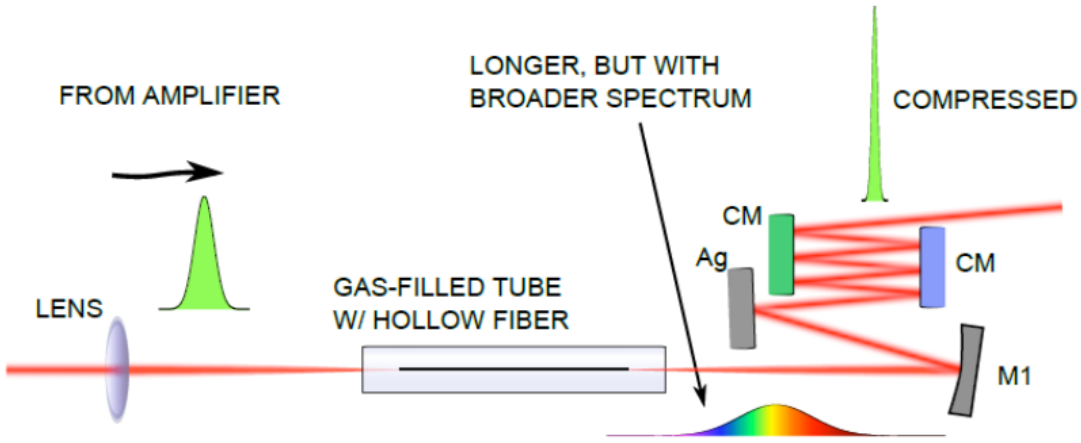

Figure 2.7: Simplified schematic of a hollow-core fiber compressor. From Reference [205]

As the pulse spectrum broadens during nonlinear propagation along the hollow fiber, the pulse itself acquires a chirp due to SPM as well as due to dispersion in the gas and optical windows of the chamber containing the hollow fiber. This leads us to the second step, where the acquired chirp needs to be compensated for in order to obtain pulses with the shortest possible temporal duration. For this purpose, one employs a dispersion compensation stage, normally composed of broadband chirped mirrors.

A standard 1 m long hollow-core fiber with a diameter of 250 micrometers and placed in a static pressure chamber with 1 atm of Argon, is a quite typical configuration of HCF compressor in terms of fiber parameters and nominal gas pressure.

The hollow-core-fiber chirped-mirror compressor used in this thesis work is described in sub-section 4.5.1.

2.5. Brief Review of Relevant Nonlinear Optical Effects

In this section, we will present a brief introduction to the nonlinear optics effects relevant to the work in this thesis. The Magneto-Optical Kerr Effect will be described in chapter 3, as well as its application as a tool to probe the magnetic properties and magnetization dynamics of the matter.

Nonlinear optics describes the phenomena that arise from the modification of the optical properties of a medium induced by the presence of light. The response of the medium to the applied optical field depends in a nonlinear way on the strength of the optical field. Typically, this behavior is observed only at very high light intensities, such as short laser pulses, which durations imply high peak intensities, enough to modify the optical properties of a material system.

Let us consider the case for an anisotropic medium. The nonlinear dependence of the electric polarization, $\boldsymbol{P}$, of an electric field with high intensity, can be expressed as power series in $\boldsymbol{E}$ [211]:

$$\boldsymbol{P} = \epsilon_0\left(\boldsymbol{\chi}^{(1)}\boldsymbol{E} + \boldsymbol{\chi}^{(2)}\boldsymbol{EE} + \boldsymbol{\chi}^{(3)}\boldsymbol{EEE} + \cdots\right) \tag{2.16}$$

where $\boldsymbol{\chi}^{(1)}$ is linear susceptibility, $\boldsymbol{\chi}^{(2)}$ and $\boldsymbol{\chi}^{(3)}$ are the second- and third-order nonlinear susceptibilities, respectively, and ϵ_0 is the permittivity of free space. $\boldsymbol{\chi}^{(1)}$, $\boldsymbol{\chi}^{(2)}$, and $\boldsymbol{\chi}^{(3)}$ are second-, third- and fourth-rank tensors, respectively. On the right side of Equation (2.16), the first term is linear polarization, the second term, third term, and so on are high-order nonlinear polarizations. The most relevant effect of nonlinear terms is that the electric polarization vector can be expressed as a product of more than one electric field, and consequently, light in newer frequencies can be generated [190]. For more extended information on nonlinear phenomena, one may see [211]–[213].

Second Harmonic Generation

In the second harmonic generation (SHG) effect, governed by second-order susceptibility $\chi^{(2)}$, two photons with an angular frequency ω propagating through a non-centrosymmetric media (i.e., the material do not display an inversion symmetry) combine to give rise to a single photon with twice the original frequency (2ω) (Figure 2.8).

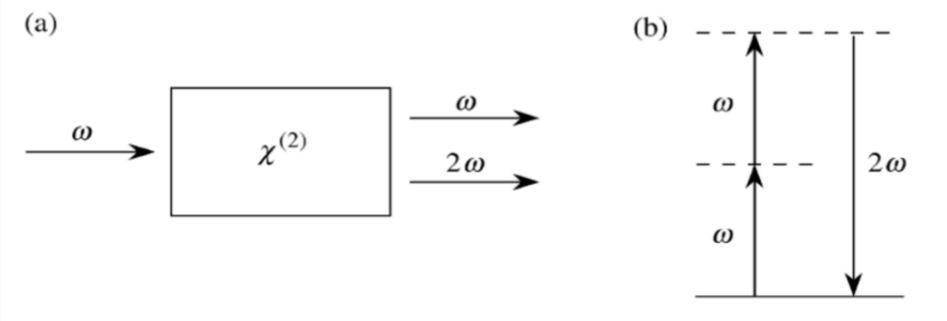

Figure 2.8: (a) Geometry of second-harmonic generation. (b) Energy-level diagram describing second-harmonic generation. From Reference [212].

Let us consider the propagation in a SHG crystal. In a dipole approximation of the electron-photon interaction, the second-order susceptibility $\chi^{(2)}$ is a third-order tensor, which the components correspond to the several possible orientations of the crystal axis and the light polarization [187]. The nonlinear polarization induced in the material can be written as

$$P_i(2\omega) = \epsilon_0 \sum_{j,k} \chi^{(2)}_{ijk} E_j(\omega) E_k(\omega). \tag{2.17}$$

If both waves propagate through the medium with the same phase velocity, occurring phase-matching between them, maximum second-harmonic conversion efficiency can be achieved. However, due to dispersion, both waves do not usually propagate with the same velocity.

The intensity of the SHG, assuming monochromatic plane waves, can be given by

$$I(2\omega, L) = \frac{2\omega^2 \chi^2_{eff} L^2}{n_{2\omega} n^2_{\omega} c^3 \epsilon_0} \left(\frac{sin(\Delta k L/2)}{\Delta k L/2}\right)^2 I^2(\omega) \tag{2.18}$$

where L is the length of the medium (SHG crystal) length, χ^2_{eff} is the effective nonlinear susceptibility for the considered wavelengths, and $\Delta k = k(2\omega) - 2k(\omega)$ is the phase mismatch. For the second harmonic conversion efficiency to be maximum, Δk must be zero. The most common method for achieve phase matching makes use of birefringent materials, in which the ordinary and extraordinary index surfaces for the fundamental and second harmonic frequencies cross one another [187]. More specifically, uniaxial crystals (e.g., BBO, KDP) can be used, where the refractive index, $n(\theta)$, can be change through the angle between propagation and the crystal optical axis, θ [190]. For a uniaxial crystal, $n(\theta)$ is given by

$$\frac{1}{n^2(\theta)} = \frac{cos^2(\theta)}{n_o^2} + \frac{sin^2(\theta)}{n_e^2} \tag{2.19}$$

where n_o and n_e are the refractive indices along the ordinary and extraordinary axes of the crystal. The refractive index (as a function of θ), in this case, can be tuned and the phase mismatch, for SHG, becomes $\Delta k = k(\theta, 2\omega) - 2k(\omega)$, where Δk can be minimized or set to zero for a given value of θ [190].

One can encountered different situations depending on the birefringent crystal: in positive crystals, like quartz, $n_e > n_o$, while in negative crystals, like calcite, $n_e < n_o$. For type I phase matching, the two mixing photons have the same polarization direction, while in type II they are orthogonally polarized [187]. Both types of phase matching are possible in positive and negative uniaxial crystals [214].

Self-Phase Modulation

The self-phase modulation (SPM) is a third-order nonlinear effect, in which an intense pulse transitorily modifies the medium refractive index through the optical Kerr effect, which changes the temporal phase of that pulse. Consequently, this can lead to the spectral broadening of the optical pulse, characterized by a refractive index, $n(I)$, time dependent on the beam intensity, I.

Let us consider the propagation of an optical pulse. The electric field of the pulse can be written as

$$E(z,t) = A(z,t)e^{i(kz-\omega t)} \tag{2.20}$$

where $A(z,t)$ is the slowly-varying envelope of the pulse. The nonlinear refractive index of the medium is given by

$$n(I) = n_0 + n_2 I(t) \tag{2.21}$$

where $I(t) = 2n_0\epsilon_0 c|A(z,t)|^2$ and n_2 is the nonlinear refractive index.

As the pulse intensity $I(t)$ is a time dependent quantity, it modulates the refractive index seen by the pulse, which determines the amount of phase acquired by the pulse during propagation, $\phi_{\mathrm{SPM}} = \frac{2\pi z}{\lambda_0} n(I)$, where λ_0 is the carrier wavelength, and z is the propagation length [190]. The radial instantaneous frequency is given by

$$\omega(t) = \omega_0 - \frac{d\phi_{SPM}}{dt} \tag{2.22}$$

The effect of SPM on an initially TL pulse translates into a broadening of the pulse spectrum, as new frequencies are generated (see Figure 2.9) during propagation in the

nonlinear medium. Figure 2.9 shows the simulation of SPM for a gaussian pulse with 25 fs of pulse duration, propagation length of 50 cm in fused silica, and pulse intensity of 10 GW/cm^2 [190].

The time-varying nonlinear phase shift gives rise to time-varying frequency shifts away from the initial carrier frequency [214]. The SPM process, for a medium with n_2 positive, gives rise to red shifts, and new low frequencies are created in the leading edge of the pulse envelope, and new high frequencies are created in the trailing edge [214]. These new frequencies are not synchronized but are still created inside the original pulse envelope [187]. The SPM itself is not a dispersive effect, however, the transparent material in which the pulse propagates is dispersive, and therefore the frequencies are further chirped along the propagation [187].

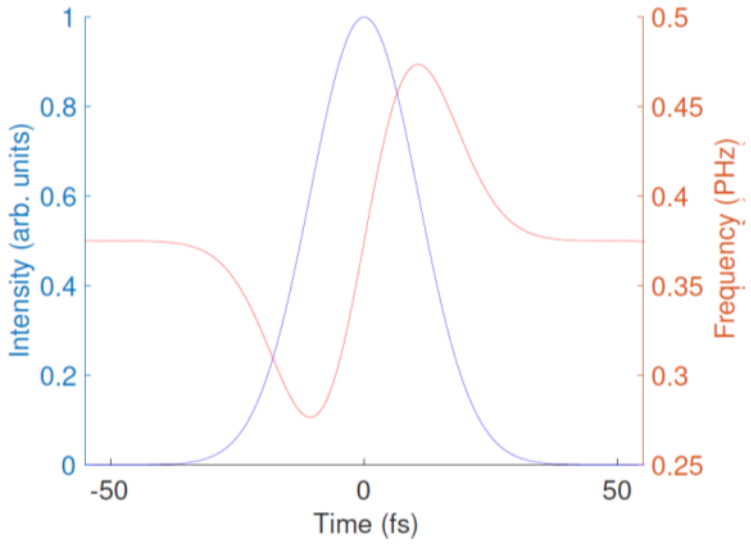

Figure 2.9: Simulation of SPM (without dispersion) with a gaussian pulse. The pulse temporal profile (blue) remains unchanged while the range of frequencies get broadened as evidenced by the variation of the instantaneous frequency $f = \omega(t)/2\pi$ with time (red). From Reference [190].

Since it opens the way to a spectral broadening of a light pulse, SMP has been (and still is) the very basis of the optical post-compression technique used for producing ultrashort light pulses less than 10 fs in duration in the visible spectral range [187].

2.6. Pulse Characterization

The time-domain waveform and pulse width are key parameters in any study involving ultrashort optical pulses since they determine the timescale of the excitation, the intensity, and hence the interaction regime, as well as the achievable temporal resolution. Therefore, a precise knowledge of the optical pulse duration is fundamental. There are

several techniques for ultrashort pulse characterization, from autocorrelation (AC) [215], which can only provide an estimate of the pulse duration, to methods capable of retrieving the complete field (amplitude and phase) of the pulses, such as frequency-resolved optical gating (FROG) [216], spectral phase interferometry for direct electric-field reconstruction (SPIDER) [217], or Multiphoton Intrapulse Interference Phase Scan (MIIPS) [218].
In this thesis work, it was used a more recent technique called dispersion-scan (d-scan), introduced in the following subsection, to characterize the ultrashort laser pulses.

2.6.1. The d-scan Technique

The d-scan technique [219]–[222] is a recent method for the simultaneous measurement and compression of ultrashort pulses. Let us briefly introduce the principle of d-scan.
We already saw that an ultrashort laser pulse can be described by its complex spectral amplitude:

$$\tilde{E}(\omega) = \left|\tilde{E}(\omega)\right| e^{-i\varphi(\omega)}. \tag{2.23}$$

To fully characterize $\tilde{E}(\omega)$, it is necessary to determine two quantities: its amplitude, $\left|\tilde{E}(\omega)\right|$, and spectral phase, $\varphi(\omega)$.
When a pulse goes through a dispersive medium, the electric field acquires an additional phase, $\rho(\omega)$, and one can write:

$$\tilde{E}(\omega) = \left|\tilde{E}(\omega)\right| e^{-i\varphi(\omega)} e^{-i\rho(\omega)}. \tag{2.24}$$

When the pulse goes through a SHG crystal, a second harmonic field, $\tilde{E}_{SHG}(\omega)$, will be generated. One can use a simple model to write down the second harmonic electric field $\tilde{E}_{SHG}(\omega)$ using the following steps [11]:

$$\tilde{E}(\omega) \xrightarrow{\mathcal{F}^{-1}} E(t) \xrightarrow{\times E(t)} E^2(t) \xrightarrow{\mathcal{F}} \tilde{E}_{SHG}(\omega) \longrightarrow \left|\tilde{E}_{SHG}(\omega)\right|^2 = S_{SHG}(\omega) \tag{2.25}$$

So, one can write the spectral intensity of the second harmonic, $S_{SHG}(\omega)$, as a function of the glass thickness z as:

$$S_{SHG}(\omega, z) = A\left|\int_{-\infty}^{+\infty}\left(\int_{-\infty}^{+\infty}\left|\tilde{E}(\Omega)\right| e^{-izk(\Omega)} e^{i\Omega t} d\Omega\right)^2 e^{-i\omega t} dt\right|^2 \tag{2.26}$$

where A is a constant, which contains all the omitted constants, Ω represents the frequency of the second Fourier transform, $S_{SHG}(\omega, z)$ is the spectral intensity of the SHG measured by the spectrometer as a function of z, $n(\Omega)$ is either given by the manufacturer of the glass wedges, calculated using Sellmeier equations, or measured, $\left|\tilde{E}(\Omega)\right|$ is the fundamental spectrum, as measured by a spectrometer.

The experimental implementation of d-scan (Figure 2.10) consists in measuring the SHG spectrum of the pulse (or the spectrum of another nonlinear process) while the dispersion is varied via the insertion of the glass wedges around the point of maximum compression (minimum pulse duration). As a result, a spectrally resolved SHG trace as a function of wedge insertion (dispersion) is obtained.

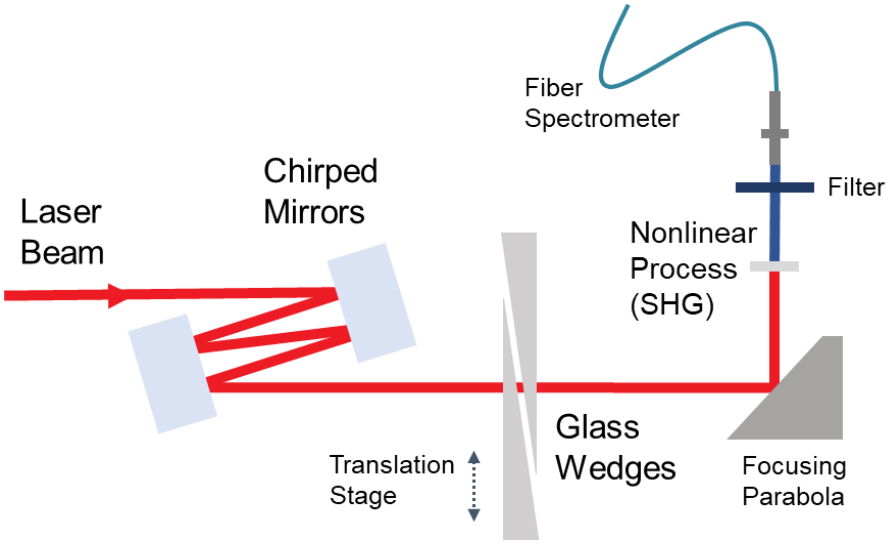

Figure 2.10: Simplified schematic of the experimental setup of the d-scan. Adapted from Reference [220].

An iterative algorithm applies phases to the fundamental spectrum and simulates the SHG process to recreate the measured trace. From this retrieved phase, the pulse can be reconstructed in the time domain. The retrieval of the complete electric field of the pulses is performed with the iterative numerical algorithm described in detail in [219], [220], [223]. Figure 2.11 presents the result of the d-scan measurement of the laser oscillator in our laboratory that provides the seed pulses for our CPA system.

In this work, d-scan was used to measure both the pump and probe pulses of our TR-MOKE system directly at the plane of the sample.

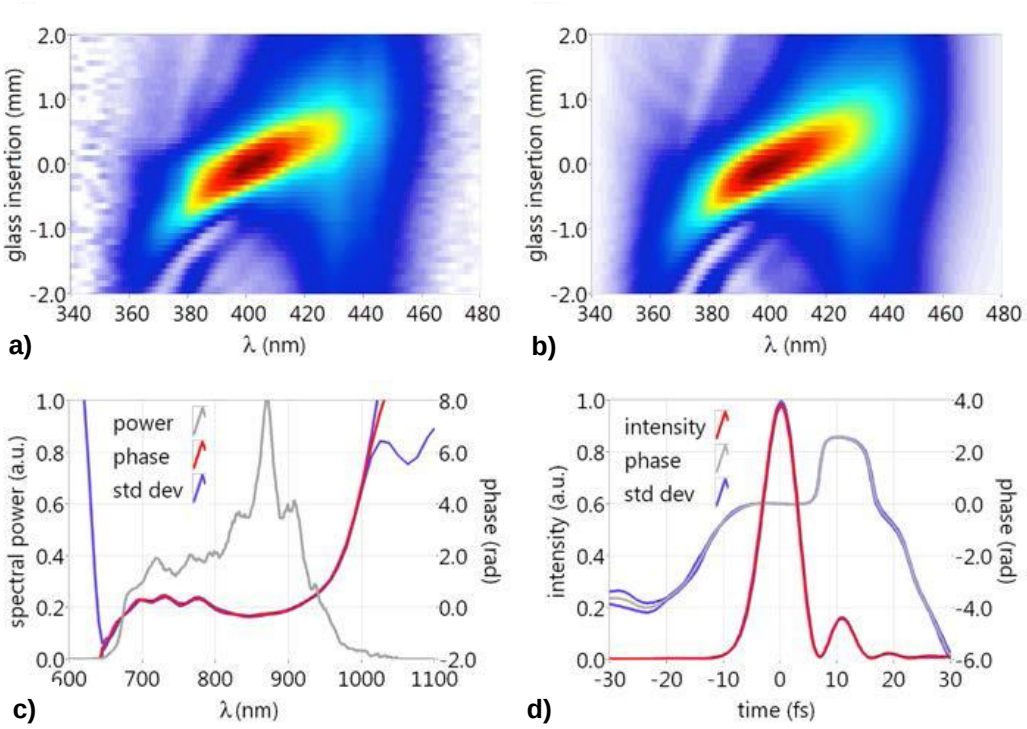

Figure 2.11: Temporal characterization of an ultrafast oscillator with the d-scan technique [219]. Measured (a) and retrieved (b) d-scan traces for the pump pulse; retrieved pump pulse in the spectral (c) and temporal (d) domains. From Reference [219].

2.7. Summary

The main ultrafast optics tools needed to develop our pump-probe apparatus in the femtosecond regime were reviewed. State-of-the-art ultrafast optical methods were used in our time-resolved magneto-optical system (see chapter 4). These methods permit the delivery of ultrashort laser pump and probe sub-5-fs carrier-envelope phase (CEP) stabilized pulses, at the sample plane, to manipulate and observe the ultrafast magnetization dynamics at unprecedented temporal resolutions from all-optical setups.

Chapter 3

Experimental Techniques

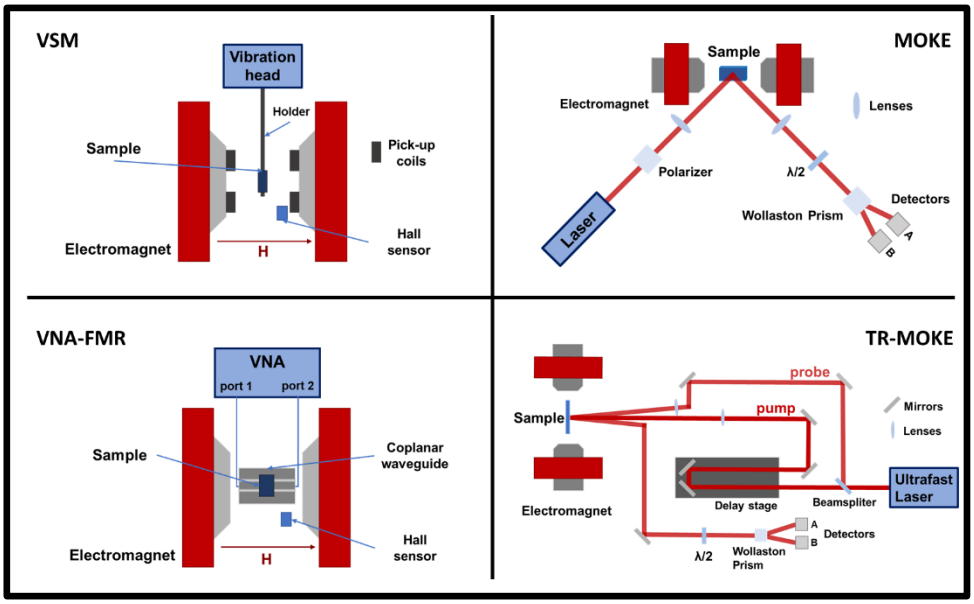

Chapter 3

Experimental Techniques

3.1. Introduction

In order to investigate the magnetic properties and magnetization state of a material, several techniques have been developed during the last decades [224]. Each method relies on different principles of measurement and can be classed in various categories, e.g. static (or quasi-static) methods and dynamic methods capable of resolving the time-dependent magnetic properties of the materials.

Static characterization techniques, such as the Vibrating Sample Magnetometry (VSM), Superconducting Quantum Interference Device (SQUID), and Nuclear Magnetic Resonance spectroscopy (NMR), or magneto-optical techniques, employing the Faraday effect or the Kerr effect (MOKE), among others, are usually used to observe the magnetic properties on longer time scales. On the other hand, dynamic characterization techniques (see section 1.5) are employed to determine the magnetic response on shorter time scales, between the nanosecond and femtosecond (or even attosecond) ranges. Techniques working in the frequency-domain (like Ferromagnetic Resonance Spectroscopy) or in the time-domain (Time-Resolved Magneto-Optical (TR-MO) spectroscopies) are commonly employed.

In this chapter, we presented a general description of the experimental techniques employed to investigate the static and dynamic response of the ferromagnetic samples studied in this thesis. Although we did not fabricate the samples in our laboratory, the sample preparation is briefly introduced and discussed in section 3.2.

In the next two sections (3.3 and 3.4), we introduce two static characterization techniques used to study the magnetic properties of the samples: Vibrating Sample Magnetometer (VSM) and Magneto-Optical Kerr Effect (MOKE) magnetometer. The VSM working principle and general setup are described in section 3.3. In the case of the MOKE magnetometry, the theory behind the different configurations and a standard experimental apparatus are described in section 3.4.

The last sections are devoted to the two techniques we have used to understand the magnetization dynamics behavior of the samples under study (3.5 and 3.6). Firstly, the Time-Resolved Magneto-Optical Spectroscopy (in the time domain) is presented in section 3.5. The pump-probe technique is introduced and followed by a generic

description of a time-resolved magneto-optical Kerr effect (TR-MOKE) setup. Finally, the Ferromagnetic Resonance (FMR) spectroscopy (in the frequency domain) is introduced in section 3.6. In addition, the vector network analyzer based ferromagnetic resonance (VNA-FMR) technique, which has also been used in this thesis, is briefly described (3.6.2). In section 3.7, a comparison between TR-MO and VNA-FMR is made. Finally, the analysis of the data provided by both techniques is summarized at the end of this chapter.

3.2. Sample Preparation

In this section, we briefly describe the samples used in this thesis as well as the employed fabrication techniques. First, we present the well-ordered line and antidot arrays of Permalloy (Py). Both samples have been used for the development and improvement of our time-resolved magneto-optical system (chapter 4) in the longitudinal MOKE configuration and based on the oscillator laser source (see sub-section 4.3.1), as well as on the amplifier (see sub-section 4.4.1). The 25 nm thick Py line array and 10 nm thick Py antidot arrays were growth on Si substrates. They were prepared by combining laser interference lithography (IL), ion beam sputtering deposition (IBS) and liftoff techniques (for more details, see Reference [225]). Templates, with controlled feature sizes and periodicities, were obtained by IL. The antireflective coating WIDE–8B (_80-nm-thick) and a negative resist tone TSMR-IN027 (≈ 200-nmthick) were spin-coated onto (100) Si substrates and exposed using a Lloyd's mirror interferometer with a He:Cd laser (λ = 325 nm) as the light source. After a single (for the line array) or a double exposure (for the antidot array), the resist was post-baked at 110º C and developed in AZ726 MIF. Then, 5-nm Ti seed layer, 10 nm thick Py film, and a 3 nm Ti capping layer were deposited sequentially by IBS at room temperature and with the base pressure below 1×10−8 Torr. Finally, ferromagnetic line and antidot arrays were achieved after a liftoff process by immersing the sample in 1-methyl-2pyrrolidinone (NMP) at 120º C.

Figure 3.1 shows the scanning electron microscopy (SEM) images of both nanostructures. While the 25 nm thick Py line array has a periodicity of 465 nm and a line width of 260 nm (Figure 3.1 a)-c)), the 10 nm thick Py antidot array shows a square lattice symmetry with a periodicity of 2050 nm and a hole diameter of 1380 and 1200 nm, along the x- and y-axis respectively (Figure 3.1 d)-f)). These two samples were prepared at Departamento de Química-Física from the Universidad del País Vasco (UPV/EHU, Spain) by Dr. C. Redondo and Dr. R. Morales.

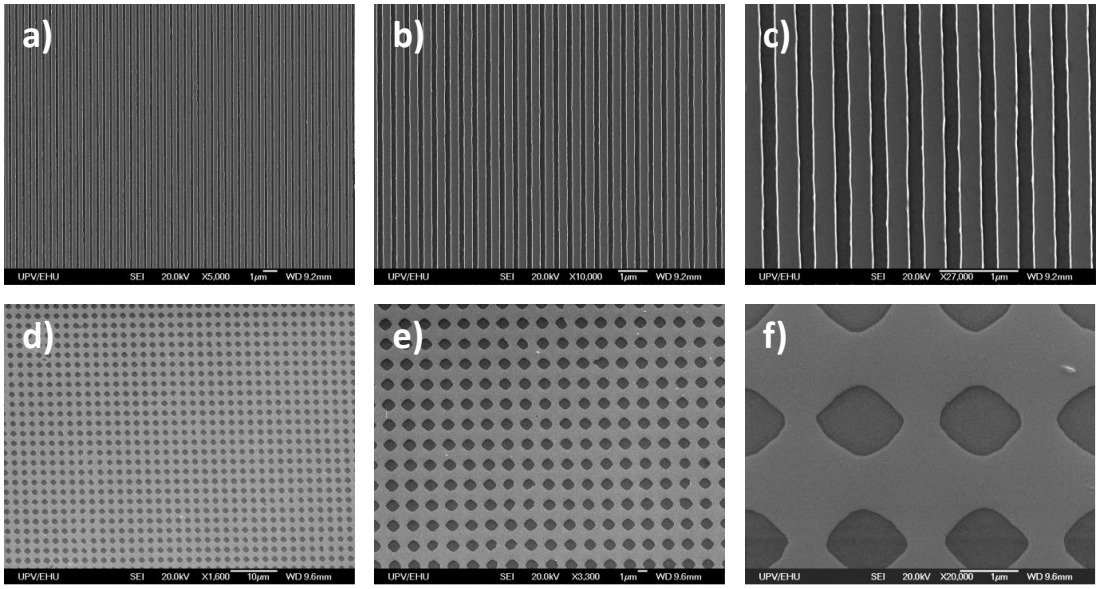

Figure 3.1: SEM images of (a-c) the 25 nm thick Py line array and (d-f) 10 nm thick antidot array at different magnifications.

Next, we describe the preparation of the CoFeB-based multilayers ultrathin films studied in this thesis (chapters 5, 6 and 7).

A Ta(20 Å) / Pd(20 Å) seed bilayer, [CoFeB (t_{CoFeB}) / Pd (10 Å)]$_N$ and a 50 Å Pd capping layer were deposited sequentially on thermally oxidized Si(100) substrates using confocal dc magnetron sputtering at ambient temperature in a chamber with a base pressure below (0.02×10^{-8}) Torr. Layers were deposited using an Ar working gas pressure of 5 mTorr. The CoFeB layers were sputtered from a stoichiometric target 40-40-20 at. %. Both Pd and Co were sputtered under the same experimental conditions. We studied the following different configurations of CoFeB/Pd-based multilayer systems (see Figure 3.2):

- The CoFeB layer thickness (t_{CoFeB}) was varied between 1 and 5 Å, while the number of bilayers (N) was fixed to 5 (Figure 3.2 (a)). Within the study of this set of samples, we wanted to determine the range of CoFeB layer thickness where thin films show perpendicular magnetic anisotropy (PMA). Results are presented and discussed in Chapter 5.

- We confirmed that the CoFeB/Pd-based multilayer show PMA for t_{CoFeB} = 3 and 4 Å. Then, we studied the PMA as a function of the number of bilayers (N) which ranged between 3 and 15 (Figure 3.2 (a)). Results of the studies performed in these second set of multilayers are presented and discussed in Chapter 5.

- Finally, the CoFeB/Pd-based multilayer system with PMA was magnetically coupled to a Co layer with in-plane magnetic anisotropy. In these exchange spring structures (see Figure 3.2 (b)), the CoFeB/Pd-based multilayer system is the hard-magnetic part with t_{CoFeB} = 3 Å and N = 5, while the Co layer is the soft-magnetic one. The Co thickness was varied between 0 and 25 Å. In Chapter 6, the results on this set of samples are presented and discussed.

A detailed description of the fabrication process can be found in Reference [90]. These sets of samples were prepared at Departamento de Física and Centro Científico Tecnológico de Valparaíso-CCTVal from the Universidad Técnica Federico Santa María (Valparaíso, Chile) by Dr. C. Garcia.

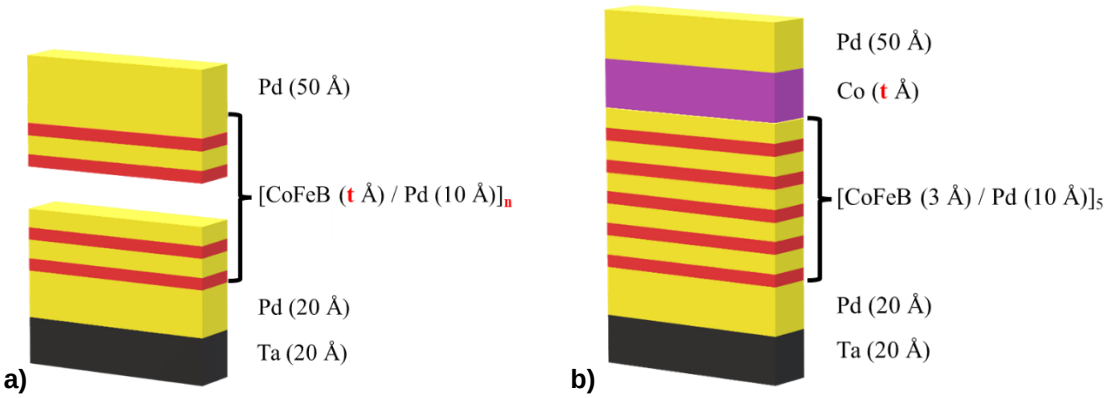

Figure 3.2: A schematic of the multilayer systems studied. **a)** Different configurations are described: when the number of bilayers CoFeB/Pd were fixed (N = 5) and t_{CoFeB} ranged from 1 to 5 Å; when t_{CoFeB} was fixed to 3 and 4 Å and N ranged between 3 and 15. **b)** an exchange spring structure based on the CoFeB/Pd multilayer system with a Co layer which thickness was varied from 0 to 25 Å.

3.3. Vibrating Sample Magnetometer (VSM)

A Vibrating Sample Magnetometer (VSM) has been used to measure the magnetic moment of a given magnetic material as a function of the external magnetic field. From the hysteresis loops, we have determined the coercivity, the saturation magnetic moment and the remanence of the material. VSM was firstly developed by Simon Foner at the Lincoln laboratories [226], [227]. Its good performance, simplicity of operation, and versatility make the VSM one of the most common methods used in the characterization of magnetic materials. Nowadays, commercial VSMs reach sensitivities as low as 10^{-6} emu and can operate at different temperature ranges.

3.3.1. VSM Working Principle

The working principle of the VSM is very simple and based on the Faraday's law of electromagnetic induction. The sample, placed in a homogenous magnetic field, will be magnetized by the alignment of the magnetic domains, or the individual magnetic spins, along the field direction. A magnetic dipole moment, proportional to the product of the sample susceptibility times the applied field, will be induced in the sample. The magnetic dipole moment of the sample will create a magnetic field around the sample, i.e. the magnetic stray field.

As the sample is made to undergo a sinusoidal oscillatory motion at a frequency (f), an alternating voltage with the same frequency will be induced in the pick-up coils due to the harmonic vibration of the sample in the homogenous magnetic field. As the magnetized sample is moved up and down, the magnetic stray field will change as a function of time. The alternating magnetic field will induce an electric field/current in the pick-up coils according to the Faraday's Law of Induction:

$$V_{coil} = \frac{d\Phi}{dt} = \frac{d\Phi}{dz} . \frac{dz}{dt} \propto f.A.m \tag{3.1}$$

where V_{coil} is the voltage in the pick-up coil, $\frac{d\Phi}{dt}$ is the magnetic flux, $\frac{dz}{dt}$ is the position along the vibration direction, f is the vibration frequency, A is the sample area and m is the magnetic moment. The induced voltage (or current) in the pick-up coil is proportional to the magnetic moment of the vibrating sample. The relationship between the induced magnetic flux density of the sample and the external applied magnetic field is the hysteresis loop.

3.3.2. VSM Setup

Figure 3.3 shows a typical VSM system. The sample is suspended from the vibration head by a non-magnetic rigid rod. A loudspeaker membrane, attached to the other end of the rod, provides the vibration frequency of the sample motion. Sample should be placed at the center of the pick-up coils in a region where the DC external magnetic field, produced by an electromagnet, is homogeneous.

As mentioned previously, the electrical signal detected in the pick-up coils (see Eq. (3.1)) is proportional to (i) the frequency and amplitude of the sinusoidal motion; (ii) the magnetic response of the sample to the applied magnetic field; (iii) a geometrical factor that considers the surface area of the pick-up coils and their distance from the sample. The

induced voltage in the pick-up coils is amplified and phase-sensitive-detected using a lock-in amplifier, which extracts the signal at the frequency of the sample vibration.

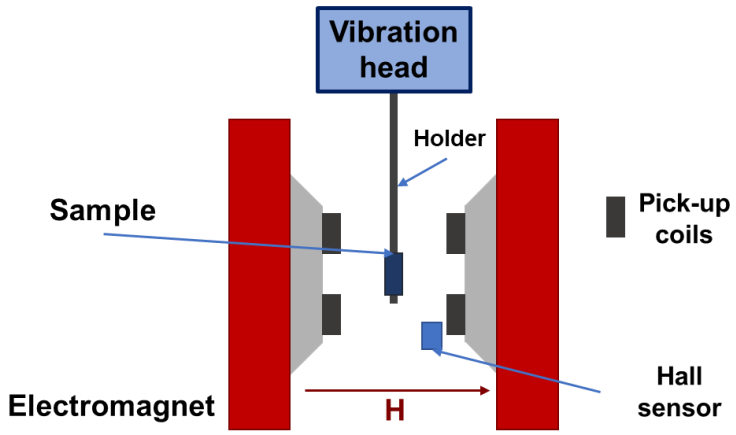

Figure 3.3: A simple schematic of VSM system.

In particular, the VSM measurements, presented in this thesis were performed using a KLA-Tencor EV7 VSM with the external magnetic field applied along or perpendicular to the sample plane for the in-plane or perpendicular (out-of-plane) measurements, respectively. All measurements were performed under ambient conditions, at the Instituto de Ciencia de Materiales de Madrid, ICMM-CSIC.

3.4. Magneto-Optical Kerr Effect (MOKE) magnetometer

The Magneto-Optical Kerr Effect (MOKE) was discovered in 1877 by John Kerr [228] who observed changes in the polarization state and/or intensity of polarized light upon its reflection from a magnetic sample. Since them, MOKE spectroscopy has been a very suitable tool to probe the magnetic properties of different materials. Moreover, it has been demonstrated that MOKE is a very sensitive technique and allows studying very small amounts of material such as thin films and magnetic nanostructures. Even monolayers of magnetic materials have been investigated [229]. As the name suggests, it is a way of measuring magnetism with light. Typical measurements performed with MOKE are the hysteresis loops, but this effect can be used as well for time-domain magnetization dynamics studies (see section 3.5).

3.4.1. MOKE Introduction

The magneto-optical (MO) effects result from the interaction between light and magnetized matter. A medium magnetically ordered or submitted to an external magnetic field induces changes on the properties of the electromagnetic waves that pass through or are reflected by that medium. In general, most MO effects are due to electron energy level splitting caused by the magnetic field/magnetization (the Zeeman effect) [230].

The oldest MO phenomenon is the Faraday effect, discovered in 1845 and named after his discoverer Michael Faraday [231]. In this effect, changes in the polarization state of light, such as rotation of the plane of polarization, are observed when polarized light passes through a magnetized material. MOKE shows the same effect when the electromagnetic wave is reflected by a magnetized material.

The polarization of light can change by the interaction with a magnetized medium, due to, for example, magnetic circular birefringence (MCB) or magnetic circular dichroism (MCD) effects. Linearly polarized light can be seen as consisting of the superposition of left- and right-circularly polarized light. The MCB effect results in a rotation of the plane of polarization of linearly polarized light, since in a magnetized medium, the refractive indexes for left- and right-handed circularly polarized light are different [230]. On the other hand, MCD translates itself in a change of the polarization state, from linear to elliptical. This effect occurs when the magnetized medium exhibits absorption, and the absorption coefficients of the left- and right-handed circularly polarized light are different [230].

Therefore, the Faraday effect (MCB and MCD in transmission) and MOKE (MCB and MCD in reflection) are classified as linear magneto-optic effects, i.e., linear (or more precisely, odd) in magnetization and consequently changing sign upon the reversal of magnetization [232].

As shown in Figure 3.4, MOKE results in a rotation of the polarization plane and a change in the ellipticity of the incident light when it is reflected by a magnetized material.

In MOKE, three different configurations are usually identified, and they are designated as longitudinal, polar and transversal (see Figure 3.5), according to the orientation of the magnetization concerning the direction of the wave propagation and the normal to the sample surface.

In the polar configuration, magnetization is perpendicular to the sample surface and parallel to the plane of the incidence light. Reflected light shows a rotation of the polarization plane and a change in the ellipticity of the incident light. This configuration is only sensitive to changes in the out-of-plane component of the magnetization, and polarized light should reach the sample in normal incidence. The polar MOKE is mostly used to characterize thin films with perpendicular magnetic anisotropy (PMA).

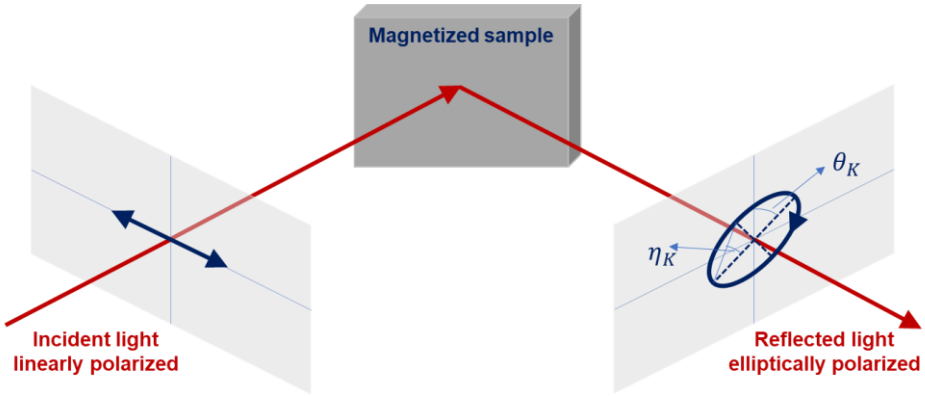

Figure 3.4: A schematic illustration of the magneto-optical Kerr effect: the incident linearly polarized light has its polarization angle rotated (Kerr rotation θ_k) and becomes elliptically polarized (Kerr ellipticity η_k) after being reflected by a magnetized material.

In the longitudinal configuration, the magnetization lies in the sample plane and parallel to the plane of incidence light. As in the polar configuration, the reflected light shows a rotation of the polarization plane and a change in the ellipticity of the incident light.
In the transversal configuration, the magnetization lies in the sample plane, but is perpendicular to the plane of incidence of light. In this case, changes in the intensity and phase of the polarized light are observed when light is reflected from the magnetic sample.

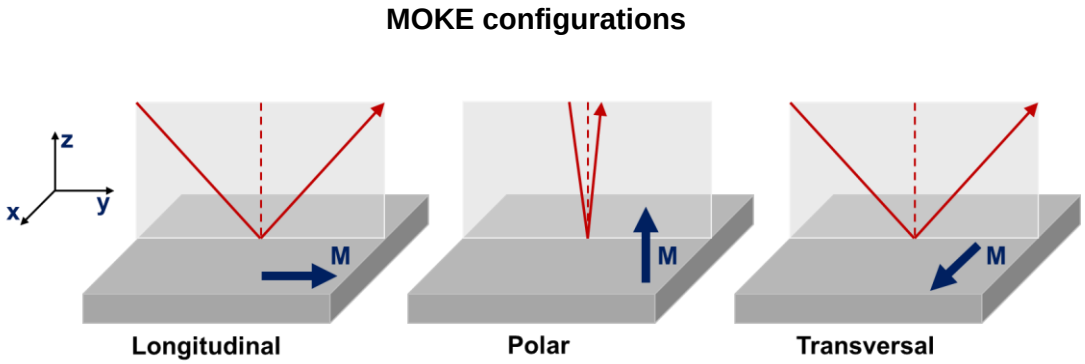

Figure 3.5: The different MOKE configurations: Longitudinal, Polar and Transversal.

Throughout this thesis, we have mainly worked with samples showing perpendicular magnetic anisotropy. Therefore, our measurements have been mainly performed using the polar configuration unless we indicate that the measurements were made in the longitudinal configuration. In the following, we will introduce the origin of the MOKE effect and analyze it for the polar configuration.

From a microscopic point of view, MOKE is originated by the coupling between the spin angular momentum and the orbital angular momentum, i.e. spin-orbit coupling. Phenomenologically, one can describe the MOKE effect through the dielectric permittivity tensor $\boldsymbol{\epsilon}$ of the medium in which the interaction between the light and the magnetization occurs. The three diagonal elements of this tensor are identical in an optically isotropic or highly symmetric material (e.g. cubic). However, in cubic ferromagnets, the symmetry is broken due to the magnetization.

In the case of the interaction of light with a ferromagnetic material, in which the magnetization and the incident light are both perpendicular to the plane of the magnetic material, i.e. parallel to the z-axis, there is a non-zero off-diagonal element which couples the x- and y-components of the optical $\boldsymbol{E}$ field. The dielectric tensor for this case only has two independent elements and is given by

$$\boldsymbol{\epsilon} = \begin{pmatrix} \epsilon_{xx} & i\epsilon_{xy} & 0 \\ -i\epsilon_{xy} & \epsilon_{xx} & 0 \\ 0 & 0 & \epsilon_{xx} \end{pmatrix} \tag{3.2}$$

In a linear approximation, the off-diagonal elements $\pm\epsilon_{xy}$ are the only ones dependent on the magnetization [233] and lead to the magnetization-dependent rotation of the reflected polarization. Using the cylindrical coordinates defined by $\boldsymbol{e}_- = \frac{1}{\sqrt{2}}(\boldsymbol{e}_x - i\boldsymbol{e}_y)$, $\boldsymbol{e}_+ = \frac{1}{\sqrt{2}}(\boldsymbol{e}_x + i\boldsymbol{e}_y)$, and $\boldsymbol{e}_z = \boldsymbol{e}_z$, the tensor (3.2) can be expressed in a diagonalized form:

$$\boldsymbol{\epsilon}' = \begin{pmatrix} \epsilon_{xx} - i\epsilon_{xy} & 0 & 0 \\ 0 & \epsilon_{xx} + i\epsilon_{xy} & 0 \\ 0 & 0 & \epsilon_{xx} \end{pmatrix} \tag{3.3}$$

We see that the dielectric constants are different for the left- ($\boldsymbol{e}_-$) and right-handed ($\boldsymbol{e}_+$) circularly polarized light, i.e. $\epsilon_\pm = \epsilon_{xx} \pm i\epsilon_{xy}$. Since ϵ_{xy} is linearly dependent on M_z in this case, we can obtain the change in M_z by taking the difference between right- and left-handed circularly polarized light, which is equal to $\epsilon_+ - \epsilon_- = 2i\epsilon_{xy}$.

Then, we can consider that linearly polarized light is formed by the combination of left- and right-handed circularly polarized light. Due to the different dielectric constants, the originally linearly polarized light will experience a rotation (Kerr rotation θ_k) and gain an ellipticity (Kerr ellipticity η_k) after being reflected by a magnetic material. The complex rotation angle of the light, proportional to the out-of-plane component of the magnetization, M_z, is given by

$$\Phi_k = \theta_k + i\eta_k. \tag{3.4}$$

In terms of the dielectric tensor components and for a magnetized medium in the polar configuration ($\boldsymbol{k} \parallel \boldsymbol{M} \parallel \boldsymbol{e}_z$), it is obtained that $\Phi_k \sim \epsilon_{xy}/\epsilon_{xx} \sim M$. Thus, by measuring the polarization change of the light along the direction of the magnetization (z -direction in the above case) yields to a complex rotation Φ_k proportional to the out-of-plane component of the magnetization, M_z.

A analytical description of the Kerr-rotation angle for an arbitrary magnetization direction and arbitrary angle of incidence for p- and s-polarized light can be found in Reference [234].

3.4.2. MOKE Setup

A generic longitudinal MOKE setup is presented in Figure 3.6. A polarizer is used to ensure that the incident light beam is linearly polarized. The beam is focused on the sample plane using a lens. After reflection from the magnetic sample, the diverging beam is collimated/focused by a second lens before passing through a half-wave plate and an analyzer (a Wollaston prism).

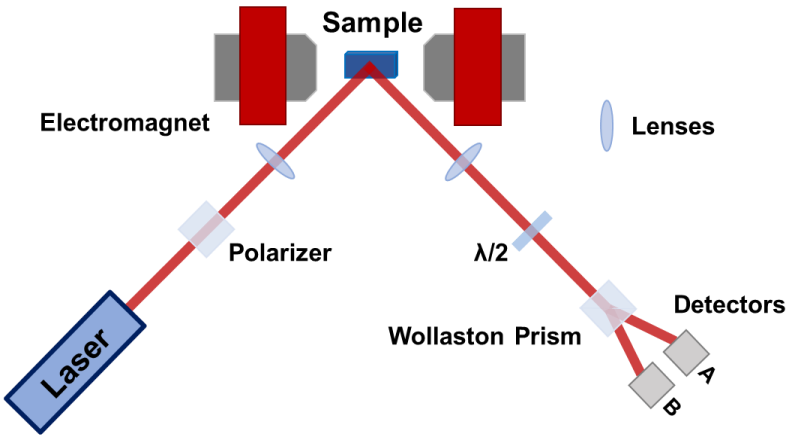

Figure 3.6: A simple schematic of longitudinal-MOKE setup.

The Wollaston prism splits the two orthogonally (s and p) polarized components of the laser beam, and two amplified photodetectors measure their corresponding intensities. The half-wave plate should be rotated to equalize both components with the resulting difference between them being a null signal. This zeroing procedure is performed before the start of the measurement. The difference between s and p components is proportional to the sine of the rotation angle of the polarized light. When the magnitude of the applied magnetic field is changed, the polarized light shows a different angle rotation related to changes in the sample magnetization. A detailed description of this balanced detection is

presented in sub-section 4.6.1, as well as the signal acquisition system we used with the ultrashort pulsed laser (sub-section 4.6.2).

3.5. Time-Resolved Magneto-Optical Spectroscopy

So far, we have discussed techniques that allow studying the static magnetic properties of matter. With the intention of being able to access the dynamic magnetic behaviors, other approaches are needed. One powerful alternative is the Time-resolved magneto-optical (TR-MO) spectroscopy, which is based on a stroboscopic principle using a pump-probe technique with magneto-optical effects.

3.5.1. Pump-probe Technique

From a general point of view, one way to access fast processes is by using a very short flashing light to freeze the process and get its image at the chosen moment. By taking several images at different consecutive moments, it is possible to reconstruct the dynamics of the process.

The pump-probe technique is based on this idea and has been used to study the dynamical response of different processes. In this technique, an intense ultrashort pulse (pump) induces the dynamic of the process while a much weaker laser pulse (probe) is used to observe the behavior of the system at the chosen moment. By precisely controlling the time delay between both pulses, one can recover the dynamical response of the process.

In the study of ultrafast magnetization dynamics, ultrashort laser pulses in the femtosecond (fs) time regime are usually used as the pump pulses to induce the dynamics in the samples under study; sampling or splitting these pulses is usually used to obtain the weaker probe pulses. The temporal resolution of the technique is directly related to the pulse width of the individual laser pulses used in the experiment and is normally in the few tens of fs range (30 – 100 fs).

The measurements are performed by monitoring changes in the intensity and/ or polarization state of the probe light (reflected or transmitted by the sample) as a function of the time delay in respect to the pump pulse. Figure 3.7 presents a schematic of the principle behind the pump-probe method.

Pump-probe systems can be classified as degenerate, when both pump and probe beams have the same spectral bandwidth and/or frequency, or non-degenerate when the pump and probe beams have different spectral bandwidths.

In the case of the degenerate pump-probe, there are some issues to consider and related to the pump contamination of the probe signal. One of these issues, the so-called coherent artifact, is an interference between the pump and the probe beams that can give rise to a temporal oscillation of the measured probe [235], [236]. Others sources of contamination can be: i) the diffraction from the transient grating produced by intense light in materials [236], and as a consequence, part of the pump beam is reflected in the same direction as the probe beam and both contributions reach the detectors; ii) the pump scattering on the sample surface and other components of the setup, which substantially decreases the signal-to-noise ratio. In addition, other nonmagnetic artifacts should be considered, namely: i) the state blocking or dichroic bleaching, which consists on the transient saturation of an optical transition by the pump pulse; ii) and the generation of nonequilibrium electron distributions that can be introduced by the transient hot-electron distribution generated in the sample by the pump pulse [237].

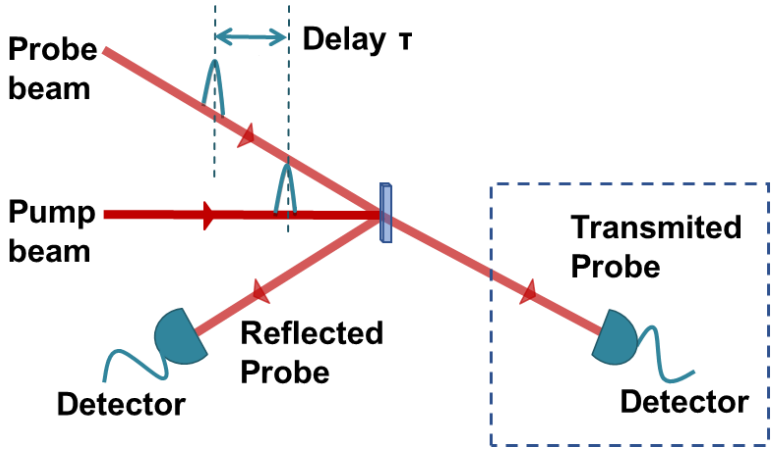

Figure 3.7: A simple illustration of the pump-probe technique in reflection measurements. The dashed blue square shows the setup to perform transmission measurements.

Although a degenerate system presents the aforementioned issues, it is possible to overcome them by implementing several measures (see sub-section 4.2.1).
Our all-optical pump-probe system is a degenerate one, which has the advantage to reach ultrashort pulses of only a few femtoseconds at the sample plane (see section 4.5), which cannot be achieved with non-degenerate schemes.

3.5.2. Time-Resolved MOKE (TR-MOKE)

In our implementation of the TR-MO spectroscopy, a pump-probe technique (sub-section 3.4.1), combined with femtosecond laser pulses, has been used to obtain the temporal

resolution, while a static magnetic field is used to control the initial magnetic state of the sample.

The proper design of such experiment should have into account several issues, like the choice of the laser source (according to the pulse energy, repetition rate and the temporal duration of the pulse), the system temporal resolution (limited by the pulse temporal width and the delay-stage minimum step), the dispersion compensation, and the detection and acquisition systems. For more details on these choices, see Reference [238] for general consideration and chapter 4 for our TR-MO system.

In the following, we will describe a Time-Resolved Magneto-Optical Kerr Effect (TR-MOKE) system, as it was the technique that we have setup and developed for this thesis. A schematic of a degenerate polar TR-MOKE setup is presented in Figure 3.8.

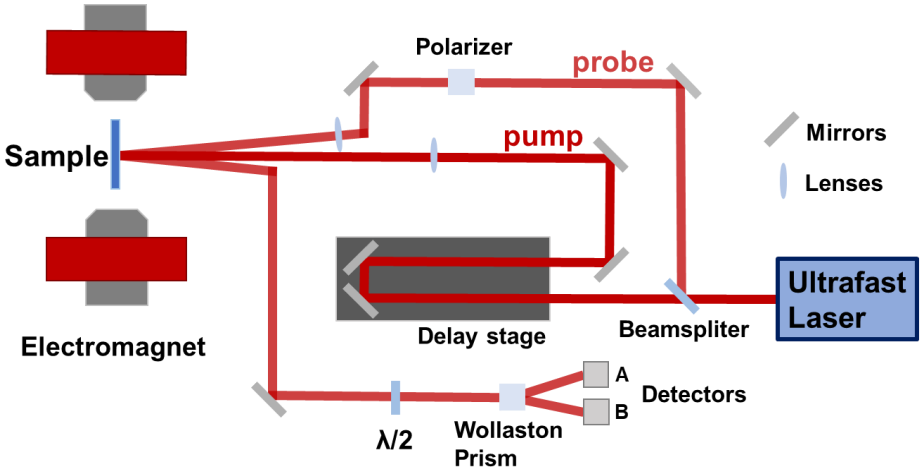

Figure 3.8: A simple schematic of a TR-MOKE setup, in the Polar configuration.

From a general point of view, the output laser pulses are passed through a beamsplitter that usually reflects <10% of the pulse energy. The reflected beam is used as the probe pulse, while the transmitted part of the pulse energy is used as the pump pulse.

The pump (or the probe) pulse is sent through a mechanical delay line to control its path length concerning the fixed path of the other beam. The final outcome is the fine control of the time delay between the pump and probe pulses.

To set the polarization of the probe beam, a polarizer cube is placed in the probe beam path. A combination polarizer and a half-wave plate can be introduced to control the probe beam polarization as well as the beam intensity, not represented in Figure 3.6. In addition, the pump beam polarization can be controlled also by positioning a polarizer in the pump beam optical path. Furthermore, a quarter-wave plate can be used to change/control the polarization of the pump and/or probe beams from linear to circular.

The sample is mounted inside the gap of an electromagnet (see Figure 3.8) and a cryostat/oven can be also used, depending on the experiment.
The polarized light of the probe beam hits the sample and is reflected. The reflected probe beam passes through a half- and/or a quarter-wave plate (in Figure 3.6 only the half-wave plate is represented), which can be used as an analyzer for rotation angle and ellipticity measurements, respectively.
Like in standard MOKE measurements, a Wollaston prism is used to split the two orthogonally polarized components of the pulsed beam (s and p).
The intensities of both components are measured using two amplified photodetectors for successive time delay positions.
The polarization rotation angle or Kerr angle is in the order of a few mdeg for most of the ferromagnetic transition metals. Such a small change in the polarization plane, either rotation or ellipticity, of the reflected probe pulse could be detected by different techniques. The simplest scheme for polarization analysis is known as the crossed polarizer. This approach consists of two polarizers placed before and after the sample with roughly perpendicular optical axes. Other options are based on the balanced photodiodes method, also named polarization balanced bridge, or on the use of modulation techniques, in which the intensity or the polarization of light is modulated and recorded with a lock-in amplifier in a heterodyning sheme.
Although data acquisition depends on the repetition rate of the chosen laser [238], lock-in amplifiers and/or boxcar integrators (in particular for kHz-laser sources) have normally been used individually or in combination.
Regarding our TR-MOKE system, developed at the Institute of Physics for Advanced Materials, Nanotechnology and Photonics (IFIMUP) of the University of Porto, a detailed description is presented in chapter 4, where the detection and acquisition systems are discussed in depth (see section 4.6).

3.6. Ferromagnetic Resonance Spectroscopy

The Ferromagnetic Resonance (FMR) Spectroscopy is a well-established and versatile experimental technique for the high-frequency characterization of ferromagnetic materials. In particular, the Vector Network Analyzer based Ferromagnetic Resonance (VNA-FMR) is widely used to analyze several magnetic parameters like the effective damping, interlayer exchange coupling, magnetic anisotropies, and demagnetization field in magnetic thin films and nanostructures [239]–[241]. In this thesis work, we have used the VNA-FMR technique to characterize the samples in the frequency domain and the results are presented in chapters 5 and 6.

3.6.1. Ferromagnetic Resonance

The initial theory of FMR absorption was given in 1948 by Charles Kittel [134]. He derived the expression for the FMR frequency by taking into account the external magnetic field and internal magnetic parameters. Experimentally, FMR was observed two years earlier (1946) by Griffiths [133], who performed a measurement analogous to the Purcell–Torrey–Pound nuclear resonance experiment [242].

In FMR experiments, a strong enough static uniform external field $\boldsymbol{H}_{ext}$ is applied to a ferromagnetic (FM) material to define the initial magnetization direction. In addition, the magnetization equilibrium state is excited by a weak rf-magnetic field with a microwave frequency, ω, and applied perpendicularly to the static magnetic field, $\boldsymbol{H}_{rf}\,(t) = \boldsymbol{H}.e^{i\omega t}$. The resonant absorption process occurs when the angular frequency of the $\boldsymbol{H}_{rf}$ equals the frequency of the magnetization precession of the FM material.

In the study by Griffith [133], it was found that the ferromagnetic resonance frequency (ω_{res}) is quite higher than the expected Larmor frequency (ω_L), given by the equation $\omega_L = \gamma \boldsymbol{H}_{eff}$, under the same effective field. The explanation of this anomaly was given by Kittel [134] who highlighted the importance of considering the dynamical coupling due to the demagnetizing field. In this case, the resonance condition for a plane surface is described by [134]

$$\omega_{res} = \gamma\sqrt{\boldsymbol{B}.\boldsymbol{H}_{ext}} \tag{3.5}$$

where γ is the gyromagnetic ratio and $\boldsymbol{B}$ is the magnetic induction at the sample.

3.6.2. Cavity-based Ferromagnetic Resonance

In the cavity-based FMR technique, also referred to as conventional or classic FMR, the sample is placed in a resonant microwave cavity. A Klystron or a Gunn diode provides microwave radiation with a fixed frequency (typically 1 ~ 80 GHz), which is coupled via a waveguide into the cavity and creating a standing microwave field [103], [104]. The sample is placed into a maximum of the magnetic field component of the standing microwave field, acting as the pumping field. Different pumping geometries may be realized for various sample positions depending upon the type of the cavity used.

In a typical experiment, the microwave frequency is kept constant. At the same time, an electromagnet provides an external magnetic field, which is swept while the power reflected by the cavity is monitored using a microwave diode [103]. When the resonance condition is satisfied, there is a strong increase in the absorbed power by the sample from the microwave radiation. Then, this reduction of the reflected power is a measure of the

imaginary part of the complex susceptibility χ, where $\chi = \chi' + i\chi''$, or alternately, is proportional to the out-of-phase microwave susceptibility χ''. The out-of-phase microwave susceptibility χ'' has a Lorentzian line shape and reaches a maximum for ω_{res} (see Figure 3.9) [104].

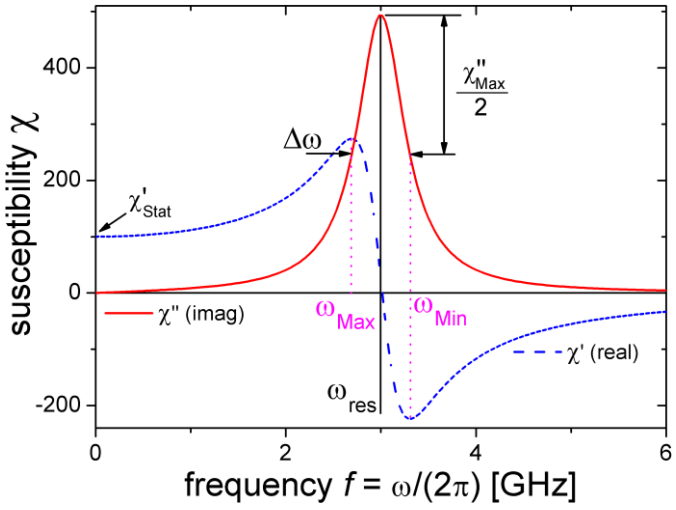

Figure 3.9: The real (dashed blue line) and imaginary (solid red line) parts of the complex susceptibility. The imaginary part has a Lorentzian line shape. From Reference [104].

In order to enhance the signal-to-noise ratio, the external magnetic field can be modulated (typically to 100 ~ 200 Hz), which allows the use of lock-in detection [104]. The measured signal is proportional to the field derivative $d\chi''/dH$. The resonance field (H_{res}) corresponds to the zero crossing of the $d\chi''/dH$, and the FMR linewidth is given by the field interval between the two extrema of $d\chi''/dH$. By measuring the resonance linewidth (half width at half maximum), $\Delta H(\omega)$ as a function of microwave frequency ω, the damping parameter (α) of a ferromagnetic material can be determined by [103]

$$\Delta H(\omega) = \alpha \frac{2\omega}{\gamma}. \tag{3.6}$$

3.6.3. Vector Network Analyzer Ferromagnetic Resonance (VNA-FMR)

As mentioned before, the FMR microwave cavity has been one of the most often used techniques to study magnetization dynamics. However, it is limited to a single resonance frequency.

On the other hand, Vector network analyzer based Ferromagnetic Resonance (VNA-FMR), or broadband Ferromagnetic Resonance [243], measurements can be performed

as a function of the applied magnetic field and over a wide frequency band (up to few tens of GHz). A coplanar waveguide (CPW) is used to create the oscillating field which excites the magnetization precession [240].

Figure 3.10 shows a diagram of a VNA-FMR system, which consists of a coplanar waveguide (CPW), the magnetic sample placed faced down on the CPW, an electromagnet that produces the static magnetic field and the VNA itself. The CPW induces a transversal rf-field on the sample. Usually, measurements are carried out by sweeping the frequency in the desired range with a fixed magnetic field, and signals are recorded by the VNA. Then, the sequence is repeated for different applied magnetic fields.

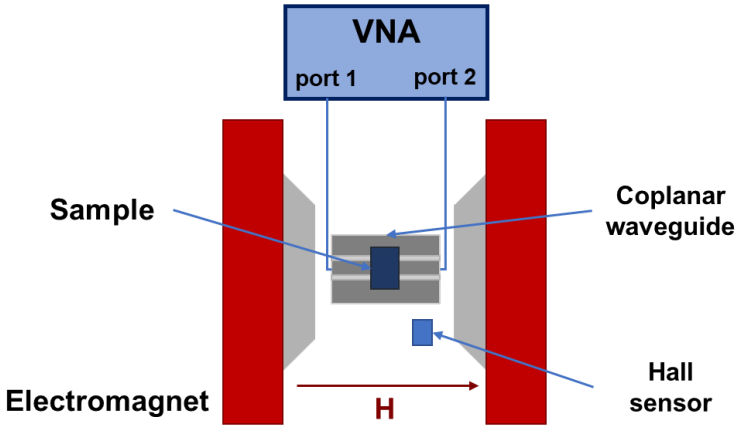

Figure 3.10: A schematic of VNA-FMR system. The sample is mounted on top of the CPW.

The VNA device is used to apply a sinusoidal electromagnetic wave $V_1\, sin(\omega t)$ with amplitude V_1 to the CPW (using port 1), which generates the microwave driving field. Then, the VNA device receives in port 2 the measurements of the amplitude V_2 and the phase of the signal $V_2\, sin(\omega t)$ transmitted from the CPW after the interaction with the sample. The measured signal is then compared to the original output signal and the resulting complex voltage ratio is:

$$S_{21} = \frac{V_2}{V_1} \tag{3.7}$$

Therefore, the VNA compares the incoming and the outgoing signals concerning their amplitude and phase, allowing us to measure the absorption of the sample as a function of frequency. Again, both the ω_{res} and the linewidth can be determined from the VNA-FMR measurements. However, the linewidth obtained in the VNA-FMR measurements is a frequency linewidth, which may not directly correspond to the field linewidth obtained in

the classic FMR measurements. The connection between the field linewidth and the frequency linewidth will be described in Section 3.7.1.

The measurements presented in this thesis were performed using a home-made VNA-FMR system which uses a commercial VNA device (Anritsu 37247D), at the Institute of Physics for Advanced Materials, Nanotechnology and Photonics (IFIMUP) of the University of Porto. This system can operate over a frequency range up to 20 GHz and has a resolution that depends on the range of the working frequencies. In measurements that span up to 20 GHz, a resolution of a few MHz is achieved.

3.7. Comparison of VNA-FMR and TR-MO Methods

In this section, we briefly address the advantages and disadvantages of using VNA-FMR and TR-MO methods to investigate the magnetization dynamics of ferromagnetic nanostructured materials.

In the frequency-domain, FMR is a well stablished and widely used technique for the high-frequency characterization of magnetic thin films [239]. Although the conventional FMR measurements are very sensitives, measurements are performed and limited to a fixed frequency because the magnetic samples are placed in a high frequency resonant cavity working at its own resonant frequency.

On the contrary, the VNA-FMR technique has the advantage that the microwave excitation frequency can be swept at an external fixed bias field conserving this way the domain state of the sample during the measurement. This aspect is an essential feature to study the dynamic behavior of small ferromagnetic elements [239]. In addition, the VNA-FMR technique has also been greatly useful in investigating the collective magnetization dynamics in magnetic nanostructures, and spin-wave modes in periodically patterned magnetic nanostructures [103].

On the other hand, the TR-MO techniques with high temporal resolution, usually only limited by the laser pulse width, gives access to several process related to the ultrafast magnetization dynamics, including ultrafast demagnetization, relaxation mechanisms, and various nonlinear effects like carrier and phonon dynamics, as well as the study of precessional switching in ferromagnetic thin films and patterned structures. [103].

Moreover, the TR-MO methods can reach temporal resolutions that can allow studying dynamical processes in the THz regime [149], [244]. No other techniques can reach this temporal resolution (VNA-FMR can achieve up to few tens of GHz) and this is of great importance for the development of spintronic devices based on antiferromagnetic materials [245], [246]. In addition, we should also highlight that the magnetic damping parameter is measured directly in the time domain, and is therefore more reliable [247],

and the magnetization dynamics can be access on different time scales [140], [149] in the TR-MO methods. Other advantage of time-resolved methods over frequency-domain techniques is the capability to measure spin precession even for large damping [11].
Since the TR-MO techniques can be highly localized due to the focused laser spot, the area sample probed is significantly smaller than the probe area in frequency domain-based techniques, this avoids the issues as variations and inhomogeneities related to larger areas [103].
However, TR-MO methods show some limitations and disadvantages. In particular, these techniques usually require expensive equipment and maintenance. Moreover, the TR-MO signals are so low that very sensitive and non-trivial optical alignments are required, which it is always a limitation from the experimental point of view.
The application of one or the other experimental technique, or their use together, will depend on the system under study and the information one intends to obtain from the spin dynamics investigation.

3.7.1. VNA-FMR and TR-MOKE Measurements and Data Analysis

Data Analysis of the Resonance Frequency

As it was described in section 3.6.3, the measured signal in our VNA-FMR setup is the complex S_{21} parameter as a function of the external magnetic field over a frequency range up to 20 GHz. In particular, we have studied the imaginary part of the S_{21} parameter as a function of the external magnetic field and an example of the measured VNA-FMR spectra is shown in Figure 3.11 (a). Then, the imaginary part of the S_{21} parameter, for each applied magnetic field, has been fitted (see Figure 3.11 (b)) using the equation [248]:

$$U = A + \frac{B\left(\left({f_{res}}^2 - f^2\right)\cos(\varphi) + \Delta f_{res} f \sin(\varphi)\right)}{\Delta {f_{res}}^2 f^2 + \left({f_{res}}^2 - f^2\right)^2} \tag{3.8}$$

where A and B are real scaling and the complex offset parameters, respectively, φ is the phase shift adjustment in degrees, f is the frequency, f_{res} is the resonance frequency and Δf_{res} is the resonance linewidth. Therefore, both the resonance frequency, f_{res}, and the resonance linewidth, Δf_{res}, have been determined.
In a general, the FMR spectrum of a thin film depends significantly on the presence of different anisotropies, such as the magnetocrystalline, shape, magnetoelastic and surface contributions, and it can be described through the following equations or Kittel equations [134], [78], [249]:

$$f_{res} = \frac{\gamma}{2\pi}\sqrt{H_1 \times H_2} \tag{3.9}$$

with $$H_1 = H\cos(\theta_0 - \theta_H) + H_{eff}\cos^2(\theta_0) \tag{3.9 (a)}$$

and $$H_2 = H\cos(\theta_0 - \theta_H) + H_{eff}\cos(2\theta_0) \tag{3.9 (b)}$$

where $(\gamma/2\pi) = (g\mu_B/h)$ is the gyromagnetic ratio, g is the g-factor, μ_B is the Bohr magneton, h is Planck´s constant, H is the external applied DC magnetic field and H_{eff} is the effective anisotropy field, θ_H is the angle of the external applied magnetic field and θ_0 is the equilibrium angle of the sample magnetization. The equilibrium angle θ_0 is calculated using the energy equilibrium relationship obtained from $(\partial F/\partial\theta_0) = 0$, where F is the free energy (described in section 1.3):

$$H\sin(\theta_H - \theta_0) = \frac{1}{2}H_{eff}\sin(2\theta_0) \tag{3.10}$$

When thin films are saturated and $\theta_H = \theta_0$, Eq. (3.9) can be reduced to [134]:

for in-plane geometry $$f_{res} = \frac{\gamma}{2\pi}\sqrt{H \times (H - H_{eff})} \tag{3.11 (a)}$$

for perpendicular geometry $$f_{res} = \frac{\gamma}{2\pi}(H + H_{eff}) \tag{3.11 (b)}$$

These last equations have been used to fit the data of the VNA-FMR measurements in the in-plane and perpendicular configurations, respectively (see black line in Figure 3.11 (a)).

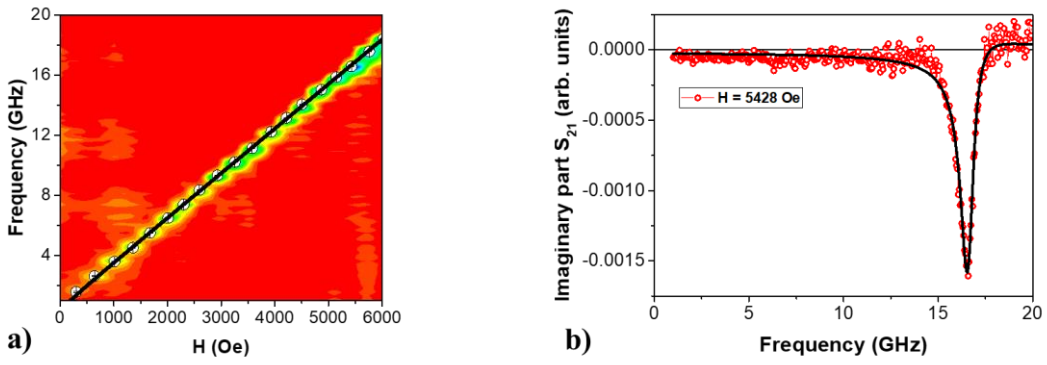

Figure 3.11: a) VNA-FMR spectra of [CoFeB (5 Å) / Pd (10 Å)]$_5$ multilayer stack with the external magnetic field applied in the sample plane, the black line correspond to the fit using Eq. (3.11 (a)), the open symbols correspond to the resonance frequency determined by Eq.(3.8) used to fit the resonance peak for each field measured. **b)** the resonance peak for an applied field H = 5428 Oe for the same multilayer stack, the black line is the fit using Eq. (3.8).

On the other hand, the magnetization in the TR-MOKE measurements usually shows a sudden drop within the first picosecond after the pump pulse and a fast recovery (remagnetization) within a few picoseconds, followed by a clear oscillation, or precession, during a slower magnetization recovery (Figure 3.12 (a)), which is characterized by the ferromagnetic resonance frequency (f_{res}) and the damping parameter α.

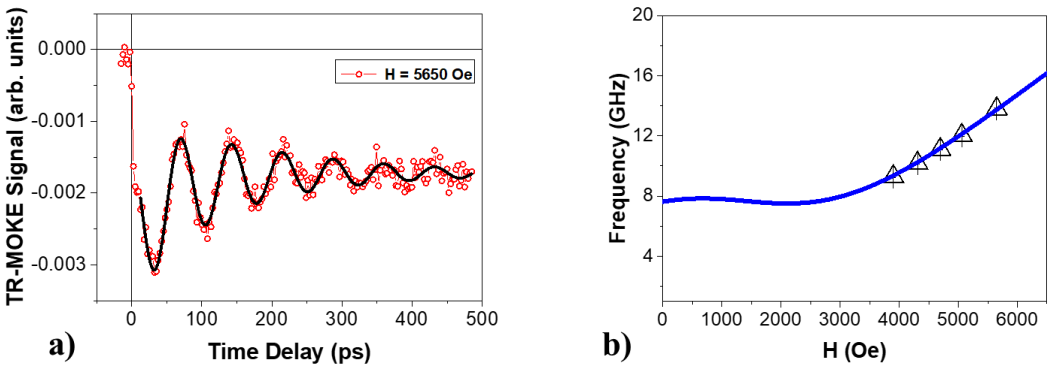

Figure 3.12: a) TR-MOKE curve of [CoFeB (3 Å) / Pd (10 Å)]$_5$ multilayer stack under an applied magnetic field of 5650 Oe, with a fluence of around 2mJ/cm^2, the magnetization precession fitted (black line) using Eq. (3.12) The FMR spectrum of the same multilayer (open symbols are the f_{res} obtain by Eq. (3.12) for five different magnetic fields applied with an angle θ_H = 78º) fitted (blue line) using the set Eq. (3.9) and the Eq. (3.10).

These precessional processes can be fitted using a damped-harmonic function superposed with an exponential decay background [249], [250]:

$$\theta = \theta_0 + A \times e^{-t/t_0} + B \times \sin(2\pi f_{res}\, t + \varphi) \times e^{-t/\tau} \qquad (3.12)$$

where θ_0 and A are the background magnitudes and t_0 is the background recovery time. The final term represents the precessional motion where B, f_{res}, φ and τ are the amplitude, frequency, phase, and relaxation time, respectively. Therefore, the resonance frequency (f_{res}) can be determined and its field-dependence fit (f_{res} vs. H) can be performed through the set of Eq. (3.9) and (3.10) [78], [249].

From the fits of the data of the VNA-FMR and TR-MOKE measurements, we can determine the gyromagnetic ratio $(\gamma/2\pi)$, the g-factor g, and the effective anisotropy field H_{eff}. The use of both techniques in our studies allows us to compare and complete the information for our sets of samples.

Data Analysis of the Damping Parameter

The damping parameter (α) can be extracted from the frequency linewidths (Δf_{res}) in the VNA-FMR spectra. However, it was experimentally observed that the measured values of Δf_{res} are broadened by extrinsic contributions which affect the calculations of the damping parameter (described in sub-section 1.5.2) [104]. Then, we have used the Δf_{res} to determine an apparent damping by the relationship [104]:

$$\alpha_{app} = \frac{\Delta f_{res}}{\left(\frac{\gamma}{2\pi}\right)(2H+H_{eff})} \tag{3.13}$$

where $(\gamma/2\pi) = (g\mu_B/h)$ is the gyromagnetic ratio, g is the g-factor, μ_B is the Bohr magneton, h is Planck´s constant, H is the external applied DC magnetic field and H_{eff} is the effective anisotropy field.

From the pump-probe measurements, α_{app} can be determined using [249]:

$$\alpha_{app} = \frac{1}{2\pi \times f_{res} \times \tau} \tag{3.14}$$

where f_{res} is the resonance frequency and τ is the relaxation time.

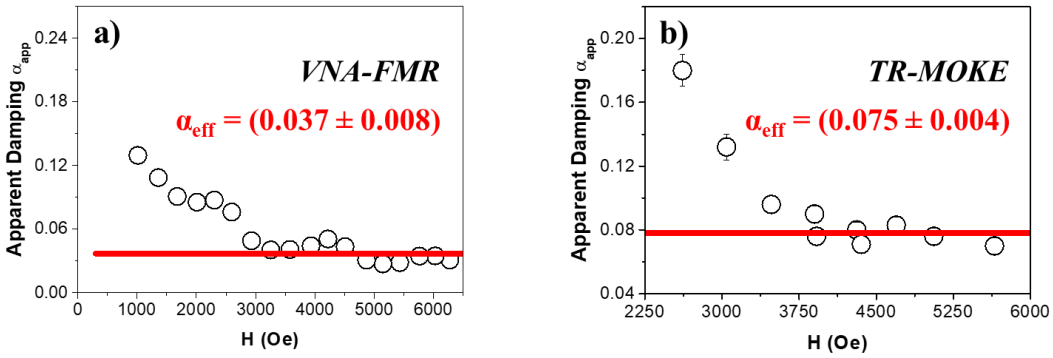

Figure 3.13: The apparent damping α_{app} (black symbols) as a function of the external applied magnetic field for **a)** [CoFeB (5 Å) / Pd (10 Å)]$_5$ multilayer stack determined by Eq. (3.13) from VNA-FMR measurements and **b)** [CoFeB (3 Å) / Pd (10 Å)]$_5$ multilayer stack determined by Eq. (3.14) from TR-MOKE measurements The red solid lines are the average of α_{app} for large applied fields and correspond to the α_{eff} .

Although α_{app} and the intrinsic damping may be different, we should note that α_{app} , in these both situations, should be an upper limit for the intrinsic or Gilbert damping ($\alpha_{Gilbert}$) for large applied external magnetic fields and when α_{app} reaches a constant value. Then,

we have assumed that this constant value is the effective damping α_{eff} . Figures 3.13 (a) and (b) show the α_{app} and α_{eff} obtained for [CoFeB (5 Å) / Pd (10 Å)]$_5$ multilayer stack from VNA-FMR data and [CoFeB (3 Å) / Pd (10 Å)]$_5$ multilayer stack from TR-MOKE data, respectively.

Another method that has been usually used to determine the damping parameter from FMR measurements is based on the linear relationship between the field swept linewidth (ΔH) and the resonance frequency (f_{res}) [251]:

$$\Delta H = \Delta H_0 + \frac{4\pi\alpha f_{res}}{\gamma} \tag{3.16}$$

where ΔH_0 corresponds to ΔH at f_{res} = 0 and is a measure of the inhomogeneity term, and the damping parameter (α) is the slope of this curve and is formed by the sum of the different contributions to α (described in section 1.5.2). Since our VNA-FMR measurements show the resonance linewidth (Δf_{res}) instead of the field swept linewidth (ΔH), we should use the identity [248], [252]:

$$\Delta f_{res} = \Delta H \left.\frac{\partial f_{res}(H)}{\partial H}\right|_{H=H_{res}} \tag{3.17}$$

in combination with the Kittel equations [134] (Eqs. (3.10.a)) and (3.10.b)). Here, the following conversions have been used [248], [252]:

for in-plane geometry

$$\Delta H = (\Delta f_{res}) \Big/ \left((\gamma/2\pi)\sqrt{1 + \left(\frac{\gamma H_{eff}}{4\pi f_{res}}\right)^2} \right) \tag{3.18 (a)}$$

and for perpendicular geometry

$$\Delta H = (\Delta f_{res})/(\gamma/2\pi). \tag{3.18 (b)}$$

In summary, the previous data analysis have been used to obtain the different magnetic dynamical properties, such as the gyromagnetic ratio, the g-factor, the effective field and the damping parameter, for [CoFeB (t Å) / Pd (10 Å)]$_N$ multilayer stacks and [CoFeB (3 Å) / Pd (10 Å)]5 / Co (t Å) exchange spring structure. These studies will be presented in Chapters 5 and 6, respectively.

3.3. Summary

In this chapter, we have presented the main magnetic characterization techniques which have been used for the development of this thesis. For the static characterization, we have described two magnetometry techniques, namely VSM and MOKE. Based on the MOKE magnetometer, the analyses of the dynamical properties have been carried out using TR-MOKE spectroscopy. Femtosecond laser pulses allow us to use the magneto-optic effects in a pump-probe scheme confirming that magnetism can be successfully manipulated and observed on an ultrashort timescale. To complete our studies of the magnetization dynamics, in the frequency-domain, we have also addressed FMR spectroscopy.

Chapter 4

Time-Resolved Magneto-Optical System

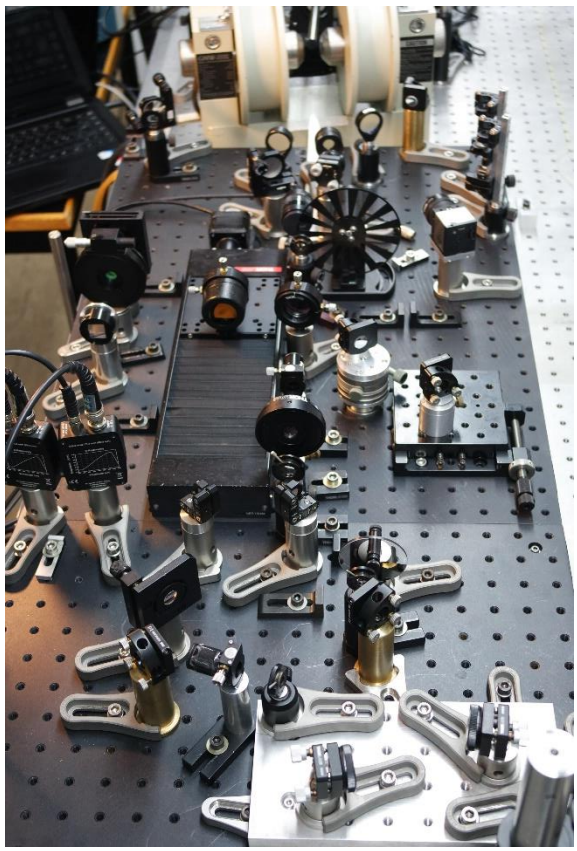

Chapter 4

Time-Resolved Magneto-Optical System

4.1. Introduction

Our time-resolved (TR) magneto-optical (MO) system to study ultrafast magnetization dynamics was built as a compact and very versatile setup. It was designed in such a way that measurements could be performed using the different and complementary laser sources available in our lab, as well in different geometries of reflection or transmission using magneto-optical Kerr or Faraday effects, respectively.

In summary, this chapter describes our TR-MO setup which can be used in different configurations and with different light sources allowing us to perform the ultrafast magnetization dynamics measurements reported in Chapters 5, 6 and 7.

Our ultimate goal was the development of a TR-MO system with sub-5-fs temporal resolution pulses. In order to achieve these few-cycle pulses on the sample plane, we developed a degenerate pump-probe setup based on our home-built ultra-broadband hollow-fiber chirped-mirror compressor. Independently of the laser source used, our setup has been implemented in a degenerate configuration, which presents additional challenges. Therefore, the setup implementation went through several stages, as described along the following sections. We considered several aspects, like the optical components, the laser sources, the dispersion compensation, pulse characterization, signal detection and acquisition scheme, among others.

In section 4.2, our pump-probe setup is firstly introduced. The general optical scheme, shown in sub-section 4.2.1, describes the optical components, the beam spot sizes, the laser fluence estimation, and other relevant specifications.

In the following sections (4.3, 4.4 and 4.5), the setup is addressed according to the laser source used. In each section, advantages and disadvantages of each laser source are presented, as well as the different aspects related to the setup, like the dispersion compensation, the involved magneto-optical effects, and respective configurations.

The signal detection and acquisition schemes are explained in section 4.6, starting with the balanced detection (sub-section 4.6.1) followed by our particular acquisition system (sub-section 4.6.2).

4.2. Degenerate Magneto-Optical Pump-Probe Setup

Our degenerated pump-probe system is based on a commercial Ti:sapphire laser amplifier (Femtolasers Compact Pro CE-phase) delivering sub-30-fs laser pulses (approximately 40 nm bandwidth centered at 800 nm) with 1 mJ of energy at a repetition rate of 1 kHz and with carrier-envelope phase (CEP) stabilization, seeded by a CEP-stabilized ultrafast oscillator (Femtolasers Rainbow CEP). The oscillator generates pulses with sub-7-fs duration, a spectral bandwidth centered at 800 nm, a repetition rate of 78 MHz and an energy per pulse up to 5 nJ, with 2 nJ available for experiments. In addition, the laser amplifier pulses can be further post-compressed in a home-built state-of-the-art hollow-core fiber and chirped-mirror compressor [208], [219]–[222]. In theory, the hollow-fiber compressor can generate pulses with sub-4-fs duration, a broadband spectral bandwidth (450-1050 nm), a repetition rate of 1 kHz and an energy per pulse of ~200 µJ. The design of our degenerated pump-probe system allows using any of these three systems (oscillator, amplifier or hollow-fiber compressor) as the laser source. In addition, measurements in both reflection and transmission geometries can be performed. We can carry out measurements in reflection, using the magneto-optical Kerr effect (both in longitudinal, transversal and polar configurations), as well as in transmission through the Faraday effect for the study of ultrafast magnetization dynamics in magnetic materials.

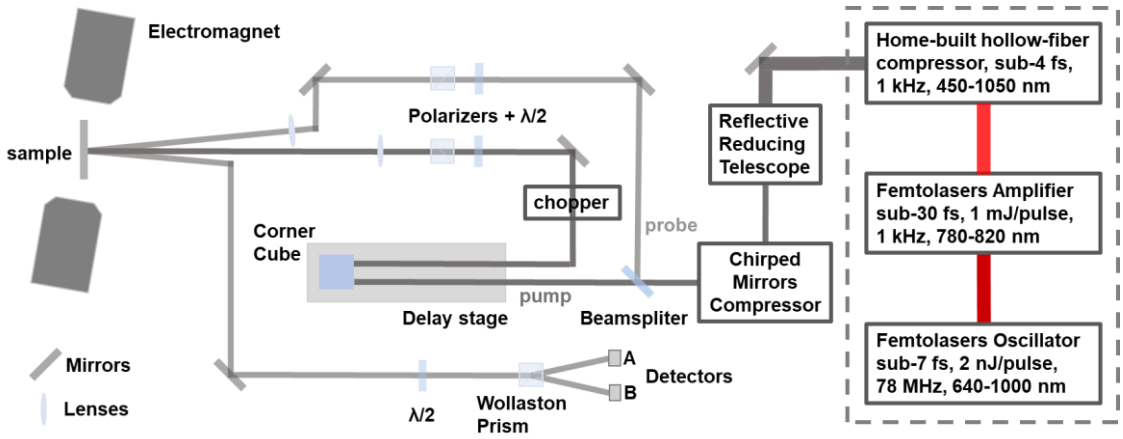

Figure 4.1: Schematic of our pump-probe apparatus, in a polar MOKE configuration, with the possibility of using any of the laser sources available (grey dashed rectangle).

We would like to note that the use of the setup with a different laser source implies only the change of few optical components and minor alignments. Moreover, the conversion of the setup for different MOKE configurations (or even in the Faraday geometry) can be

easily implemented by changing the incidence angle of the probe and/or its path to the detectors and rearranging the position of the electromagnet with respect to the sample.

4.2.1. General Optical Scheme

The laser pulses are passed through a home-built reflective telescope, based on Reference [253] (see Figure 4.2), to reduce the diameter of the beam before sending the pulses through a chirped-mirror compressor (see Figure 4.1).
These chirped mirrors are capable of compensating, up to high-order, the material dispersion introduced by the air paths and the optical components (beamsplitter, lenses, wave-plates, and polarizers) that pulsed beams cross on their way to the sample under study (see section 2.2). We should note that the election of the light source affects the required set of chirped mirrors.

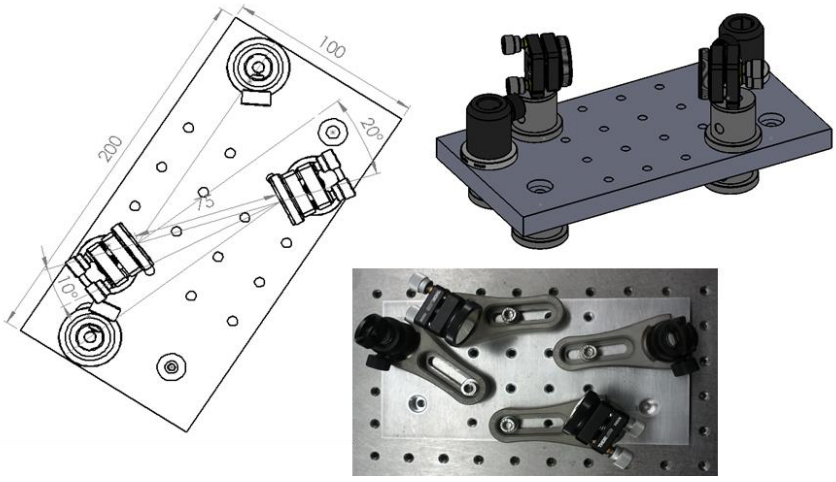

Figure 4.2: Two diagrams and an image of the home-made reflective telescope.

We used a reflective telescope that, unlike refractive telescopes based on lenses, does not introduce any positive dispersion. Therefore, and since the total amount of positive dispersion to be compensated has been reduced, a smaller number of pair reflections (bounces) are needed on the chirped mirrors, which leads to less wavefront distortion and losses in the laser beam. The replacement of the refractive telescope by a reflective one should also decrease the power losses due to the absorption and scattering in the material of the lenses, but more importantly, it enables a high-quality focus without the chromatic aberrations that would be introduced by the lenses.

After the chirped mirrors, a broadband beamsplitter reflects 0.7% of the pulse energy, which is used as the probe pulse, while the transmitted part (99.3%) of the pulse energy is used as the pump pulse (Figure 4.1).

To control both the probe beam polarization and intensity, a combination of a polarizer cube and a half-wave plate was introduced. Furthermore, a polarizer cube and a half-wave plate were also added in the optical path of the pump beam. Therefore, this setup permits the control of polarization and energy of both pulses.

The pump pulse is sent through a mechanical delay line (100 nm step, corresponding to a 0.67 fs resolution), where a retroreflector cube is mounted, to control the path length of the pump with respect to the fixed probe path.

The spots of the pump and probe beams at the sample position should have different sizes to assure that the probe spot hits a homogeneous pump-illuminated area of the sample. In particular, the spot size pump/probe ratio was adjusted to be 4:1.5 using lenses. The relatively long focal length of these lenses minimizes chromatic aberrations. Such as in any optical pump-probe experiment, these spots must be accurately focused and overlapped on the sample surface. This key point has been performed with the help of a CCD (charged coupled device) camera, which allows us to determine the spots sizes and positions by directly imaging the beams after attenuation with neutral density filters.

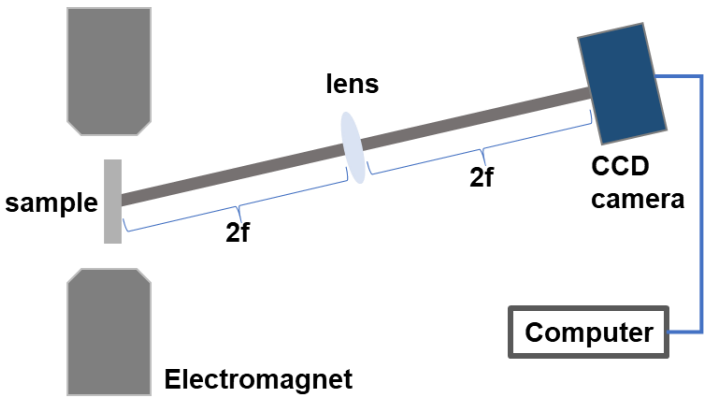

Figure 4.3: Experimental setup used to measure the pump and probe spots: a 2f-2f imaging system to create a 1:1 image of the spots at the sample surface.

To determine the diameter of the pump and probe spots, we measured the scattered light from the beam spots by implementing a 2f-2f imaging system to create a 1:1 image of the spots at the sample surface (Figure 4.3). The analysis of the spot image, obtained from the CCD camera, is fitted using Gaussian functions both in the vertical and horizontal directions (see Figure 4.4).

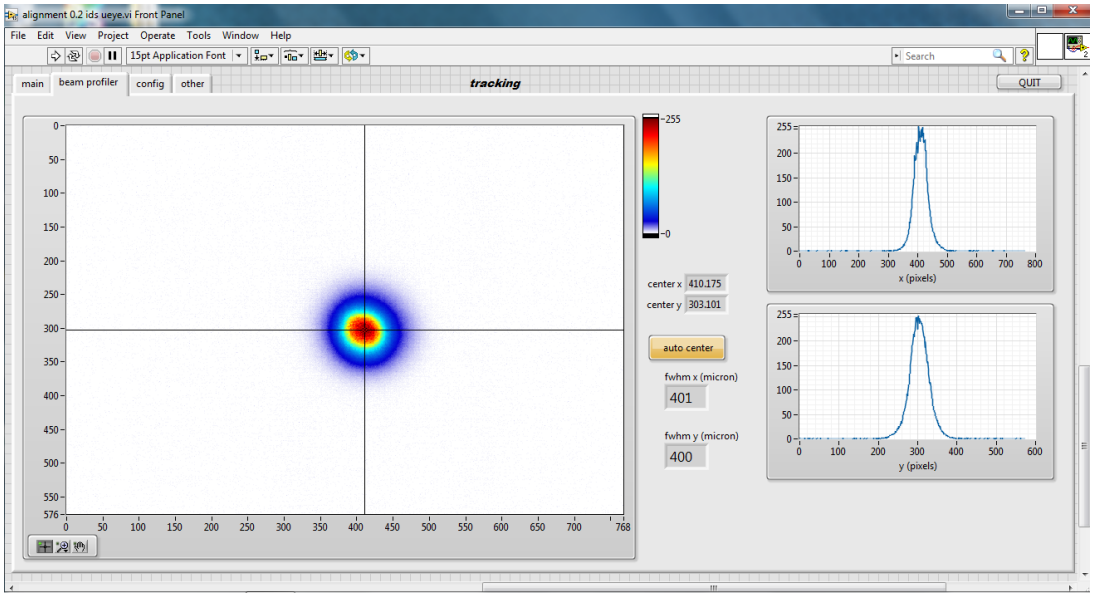

Figure 4.4: Pump spot size measurements in X and Y axis. The data is fitted using a Gaussian function and the width is measure at $1/e^2$ of the maximum, since we are measuring intensity.

It is well known that the fluence of the pump pulse plays a crucial role to perturb or excite a magnetic sample [140]. Therefore, it is essential to know the fluence provided by the pump beam, which can be estimated using:

$$Fluence = \frac{Energy}{\pi r^2} \tag{4.1}$$

where r is the $1/e^2$ pump spot radius at the sample surface. The energy of the pump pulse is obtained by the average power of the pump beam divided by the repetition rate. The conventional unit of the fluence is mJ/cm^2. We have chosen the pump and probe lenses according to each setup and with the idea of guaranteeing the highest possible fluence (always bellow the sample damage threshold) and keeping constant the spot ratio to 4:1.5. In case the fluence should be reduced, the beam intensity can be attenuated by moving away the pump lens from the maximum focus position. This lens displacement generates a larger spot at the sample plane and hence leads to a smaller fluence.

In the setups based on both the amplifier and the hollow-fiber laser sources, we have placed lenses with 400 and 200 mm focal length to focus the pump and probe beams, respectively. This configuration produces focused spots with diameters of about 400 (pump beam) and 150 μm (probe beam).

Regarding the external applied magnetic field, the sample was mounted between the poles of a water-cooled electromagnet which can generate up to 1 T at the sample plane.

The electromagnet is connected to a bipolar power supply which is automatically controlled.

As described in sub-section 3.5.1, a degenerate pump-probe setup can show some issues related to the pump contamination of the signal. In order to avoid these contaminations, we used several strategies. First, we should note that all measurements are usually carried out at both positive and negative field polarities. By taking the difference between these two measurements, one can eliminate any non-magnetic contributions to the signal. Moreover, we have crossed the polarization of the probe and pump pulses to remove the effects of both the coherent artifact and the transient grating in materials. Finally, we also used beam-blockers to prevent that the light scattered and reflected (or transmitted) from the sample surface and/or other components of the setup from reaching the detectors.

However, we should highlight that the coherent artifact, which is usually problematic in actual TR-MO measurements, can actually be used to confirm the temporal overlap position of the pump and the probe beams.

4.3. TR-MOKE System Based on the Oscillator

First, we built the setup based on a CEP-stabilized ultrafast oscillator (Femtolasers Rainbow) and a chirped-mirror-based Kerr-lens mode-locked laser (see section 2.3.1). As mentioned above, this laser source generates pulses with sub-7-fs duration, a spectral bandwidth centered at 800 nm, a repetition rate of 78 MHz and energy per pulse of 2 nJ. The choice of the optical components (beamsplitter, half-wave plates, Glan-Taylor polarizer, lenses and glass wedges) used had into account the bandwidth of the oscillator pulses (640-1000 nm).

4.3.1. Pulse Dispersion Compensation

After defining the setup design and choosing the required optical components, we dedicated our attention to the pulse temporal compression. To compress the oscillator pulses, ultra-broadband double chirped mirrors (DCM) with a working spectral bandwidth between 650 and 1150 nm (DCM7 from Venteon Optics, see the reflectivity and group delay dispersion curves on Figure 4.5) were used for the compensation of the positive dispersion affecting the femtosecond laser pulses.

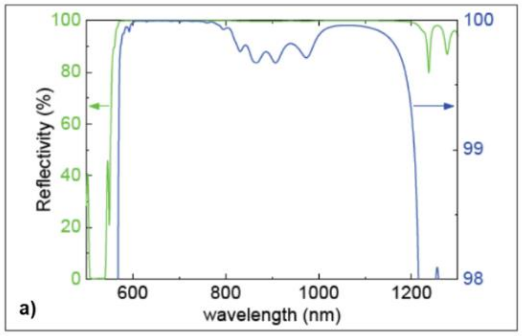

DCM7 Reflectivity: DCM7 reflectivity for p-polarized light under 7° angle of incidence for one bounce on both mirrors (green/ left full range, blue/right zoom-in to 98 to 100%).

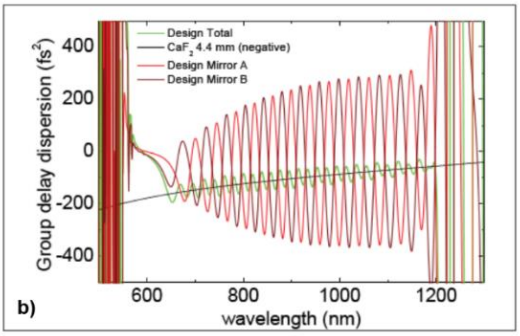

DCM7 Group delay dispersion: DCM7 reflected group delay dispersion for p-polarized light under 7° angle of incidence for one bounce on both mirrors (green, sum of mirror A (red) and mirror B (dark red)) and compensation target (black, 4.4 mm CaF2).

Figure 4.5: a), b) The reflectivity and group delay dispersion curves for the double chirped mirrors, DCM7, used in the experimental setup based on our oscillator. Each green/blue mirror pair provides a net GDD of -120 fs^2 per bounce (at 800 nm) with high reflectivity and minimized dispersion oscillations over the 650-1150 nm range (green curves). From Reference [254].

The estimation of the group delay dispersion (GDD) at 800 nm (see Tables 4.1 and 4.2) permitted us to identify the minimum number of reflection bounces needed with the DCM7 mirrors to ensure the optimal pulse compression. In particular, and for each reflection bounce on a pair of DCM7s, a negative dispersion of -120 fs^2 (at 800 nm) is introduced.

Components (+ material)	**GVD[1] (fs^2/mm)**	**Component Thickness (mm)**	**GDD (fs^2)**
Air path	0,02	3500,00	70,00
Beamsplitter FemtoOptics			20,00[2]
Half-wave Plate (quartz +sapphire)	40,355+64,57	0,80+0,80	83,94
Glan-Taylor Polarizer (Calcite)	44	7,50	330,00
Lens (BK7)	44,651	2,80	125,02
Total positive dispersion			628,96

Table 4.1: Estimate of the GDD introduced by the optical components and air in the pump beam path considering a center wavelength of 800 nm.

[1] Group Velocty Dispersion (GVD) data from https://refractiveindex.info/
[2] Data from FemtoOptics.

According to Tables 4.1 and 4.2, six reflection bounces, introducing a negative dispersion of -720 fs^2, are required to overcome the positive dispersion introduced by the optical components and air in both pump and probe paths.

Components (+ material)	GVD[3] (fs^2/mm)	Component Thickness (mm)	GDD (fs^2)
Air path	0,02	3500,00	70,00
Half-wave Plate (quartz +sapphire)	40,355+64,57	0,80+0,80	83,94
Glan-Taylor Polarizer (Calcite)	44	7,50	330,00
Lens (BK7)	44,651	3,10	138,42
Total positive dispersion			622.36

Table 4.2: Estimate of the GDD introduced by the optical components and air in the probe beam path considering a center wavelength of 800 nm.

Finally, a fine-tuning of the dispersion was performed by inserting a pair of BK7 glass wedges (FemtoOptics; antireflection (AR) coated for 650 - 1050 nm) into the probe and pump beam paths.

4.3.2. Longitudinal TR-MOKE Setup with the Oscillator

The initial setup, using the oscillator as the light source, was implemented in a longitudinal TR-MOKE configuration (see Figure 4.6). All optical components used in the pump and probe beam paths, namely the half-wave plates, the polarizers and lenses, have an AR coating with a bandwidth of 650 - 1050 nm, which was chosen in order to avoid, as much as possible, both the partial reflection beams and power losses.

Great attention was payed to the reduction of the power losses since the oscillator provides pulses with low energy (around 2 nJ). An alternative to overcome this limitation would be based on the use of microscope objectives which should provide higher fluence by reducing the pump spot size up to few tens of nanometers. Nevertheless, we cannot easily maintain the few-cycle temporal duration as it is very difficult to properly compensate the dispersion introduced by these objectives.

[3] Group Velocty Dispersion (GVD) data from https://refractiveindex.info/

Then, the main challenge was to achieve the maximum possible fluence without losing the pulse compression and keeping the sub-7 fs temporal duration.

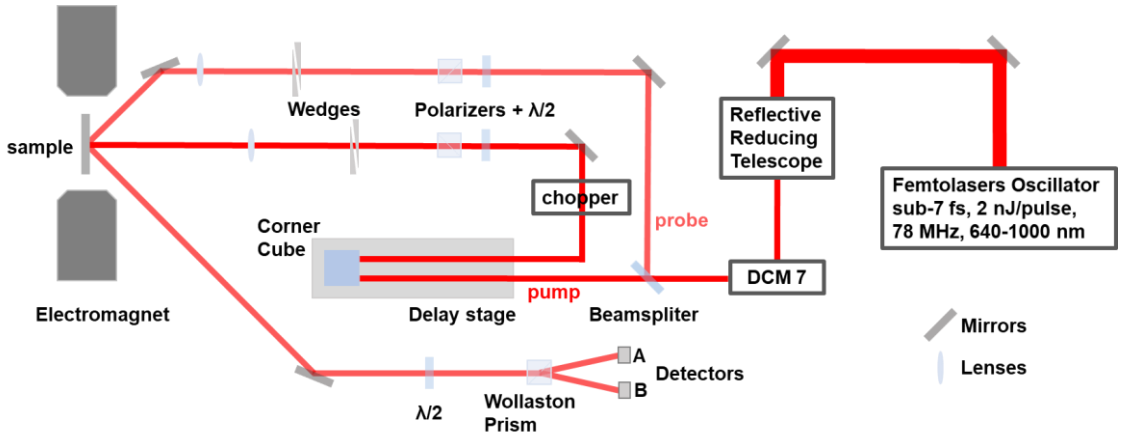

Figure 4.6: Schematic of our pump-probe TR-MOKE with a longitudinal configuration based on the oscillator laser source.

After the setup of our experimental system, we first checked and optimized its behaviour by performing several static measurements, namely hysteresis loops, of different nanostructured magnetic materials such as Permalloy (Py) line and antidot arrays. These measurements were done with our system in the longitudinal MOKE configuration.

Figure 4.7 shows the scanning electron microscopy (SEM) images of both kinds of nanostructures.

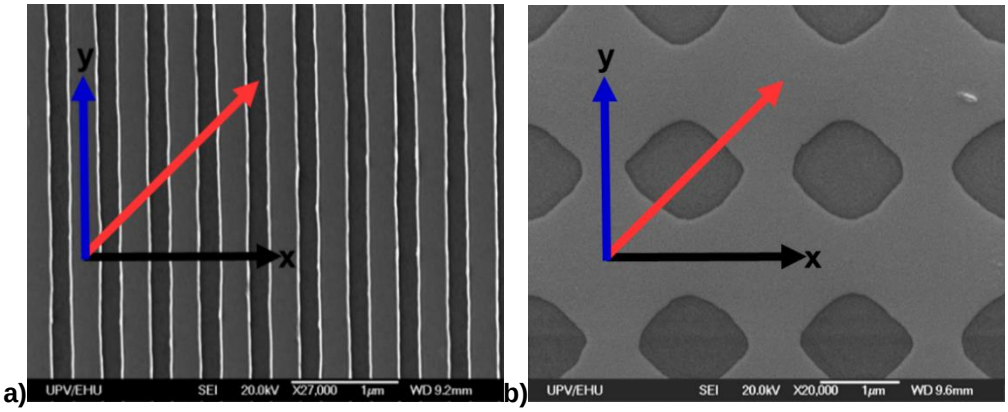

Figure 4.7: SEM images of the Py line array **a)** and antidot array **b)**. The black, blue and red arrows mark the directions in which the external magnetic field was applied during the measurements of the hysteresis loops.

Regarding the magnetic characterization, we measured the in-plane hysteresis loops along the x- (black arrow in Figure 4.7) and y-axis (blue arrow in Figure 4.7) as well as at 45º (red arrow in Figure 4.7). As expected, the hysteresis loops of the Py line array (Figure 4.8) show an easy magnetization axis along the line's direction and a hard axis along the perpendicular direction. Then, this clear in-plane uniaxial effective anisotropy along the line axis is mainly due to the contribution of the shape anisotropy energy. Our measurements were compared with the hysteresis loops measured in a commercial MOKE (Figures 4.7 (c) and (d)) magnetometer (NanoMOKE2 from Durham Magneto Optics Ltd's) employing a narrowband continuous-wave (CW) laser (660nm, <5mW) at the Spectroscopy Group of the Physical Chemistry Department at the University of the Basque Country (UPV/EHU, Leioa, Spain). Based on the excellent agreement observed in these measurements, the performance of our home-built system was fully validated. We should note that divergences observed in the hysteresis loops along the y-axis or hard magnetic axis (Figure 4.8 (b) and (d)) were related to the fact that the sample seems to be not fully saturated in the hysteresis loops measured in the commercial NanoMOKE2.

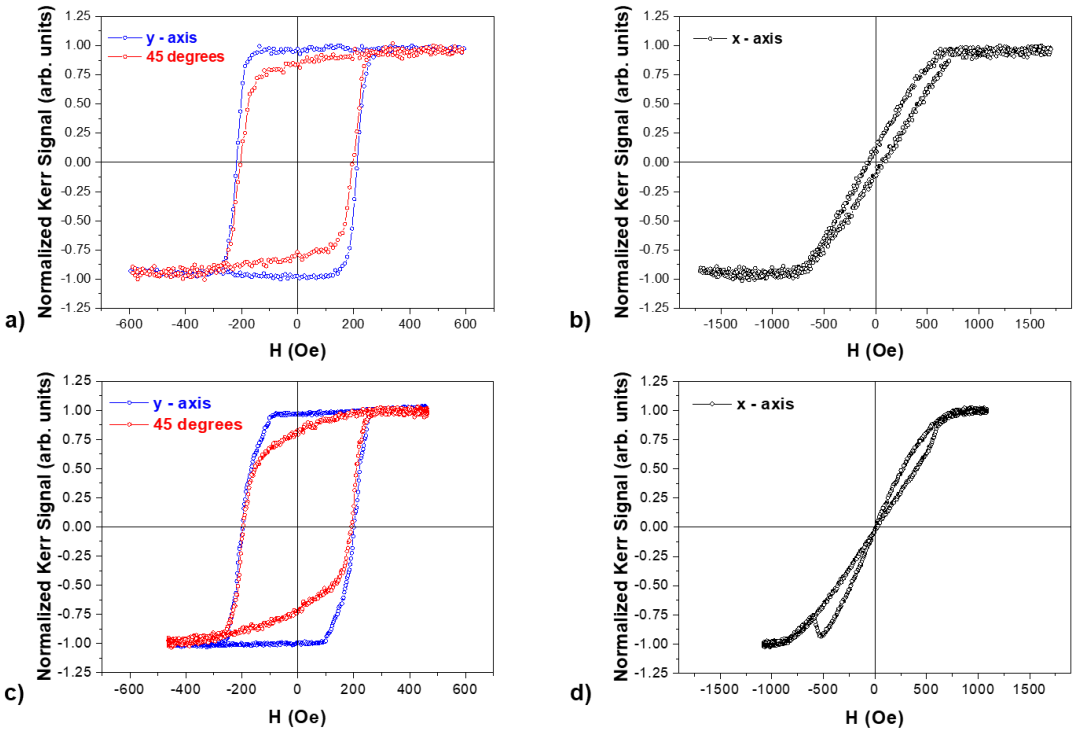

Figure 4.8: Hysteresis loops measured in our system based on a few-cycle femtosecond laser oscillator (**a)** and **b)**) and in a commercial MOKE (**c)** and **d)**) on two orthogonal directions (x- and y-axis) and 45º between them, marked on the SEM images (Figure 4.7) by the black, blue and red arrows, respectively.

On the other hand, the 10 nm thick Py antidot array with a square lattice symmetry show a four-fold anisotropic behavior with similar hysteresis loops when the external magnetic field was applied along the x- and y-axis, and an easy magnetization axis at 45º (Figure 4.9) [225].

In order to understand this behaviour, we performed 2-Dimensional micromagnetic simulations using MuMax3 software (Version 3.9.1) [255]. We used 2D periodic boundary conditions (PBC) with an exchange coupling constant A_{exch} = 13×10^{-7} erg/cm and saturation magnetization of M_{sat} = 810 emu/cm^3. SEM micrographs were used in order to resemble the real shape of the antidots in the simulations. Assuming that the magnetization is thickness homogeneous, cell size was chosen to be (5×5×10) nm^3, which was smaller than Py characteristic exchange length [256] (6 nm). A detailed description of this analysis can be found in Reference [225].

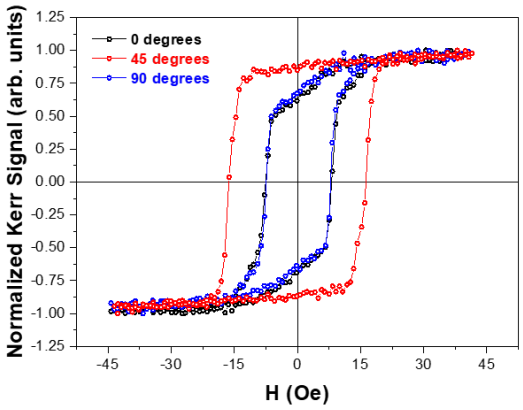

Figure 4.9: Hysteresis loops of the Py antidot array on two orthogonal directions and 45º between them, marked on the SEM image by the black, blue and red arrows, respectively.

Figure 4.10 shows the simulated hysteresis loops in combination with snapshots of the magnetization states at different points on the hysteresis curve with the external magnetic field applied along the x-axis, or θ = 0º, (Figure 4.10 (a)) and at θ = 45º (Figure 4.10 (b)). The simulated hysteresis loops, like the experimental ones (Figure 4.9), are also different when the external magnetic field is applied along either x- (θ = 0º) or y-axis (θ = 90º), and with an easy magnetization axis at θ = 45º. While the antidot array is well saturated for large applied magnetic fields, different magnetization configurations can be achieved due to the presence of the antidots in the unsaturated states. As soon as the external magnetic field is reduced, holes act as well-defined magnetization pinning centers affecting the nucleation and movement of domain walls. At remanence, the magnetization snapshot for θ = 0º shows two main magnetic domains with magnetization pointed along the x-axis

and at 45º. Moreover, an extra magnetic domain, pointed along the y-axis, shows up just before the magnetization switching (H = -30 Oe). On the other hand, the magnetization snapshots for θ = 45º already show these 3 kinds of domains under an applied field of 25 and 0 Oe. Before the magnetization switching (H = -50 Oe), a more complex magnetic configuration is observed.

Therefore, we have confirmed the good performance of our home-built MOKE by comparing our data with results obtained from a very different commercial system based on a CW laser as well as from micromagnetic simulations. Moreover, we can highlight some advantages of using a broadband femtosecond oscillator as the laser source. As the oscillator has a high stability and high repetition rate, a high signal-to-noise ratio in the hysteresis loop measurements can be achieved. Then, a smaller number of averages should be required and faster measurements can be carried out. In particular, between 10 and 30 averages were performed in our system in comparison with the 50-100 averages typically required by commercial systems).

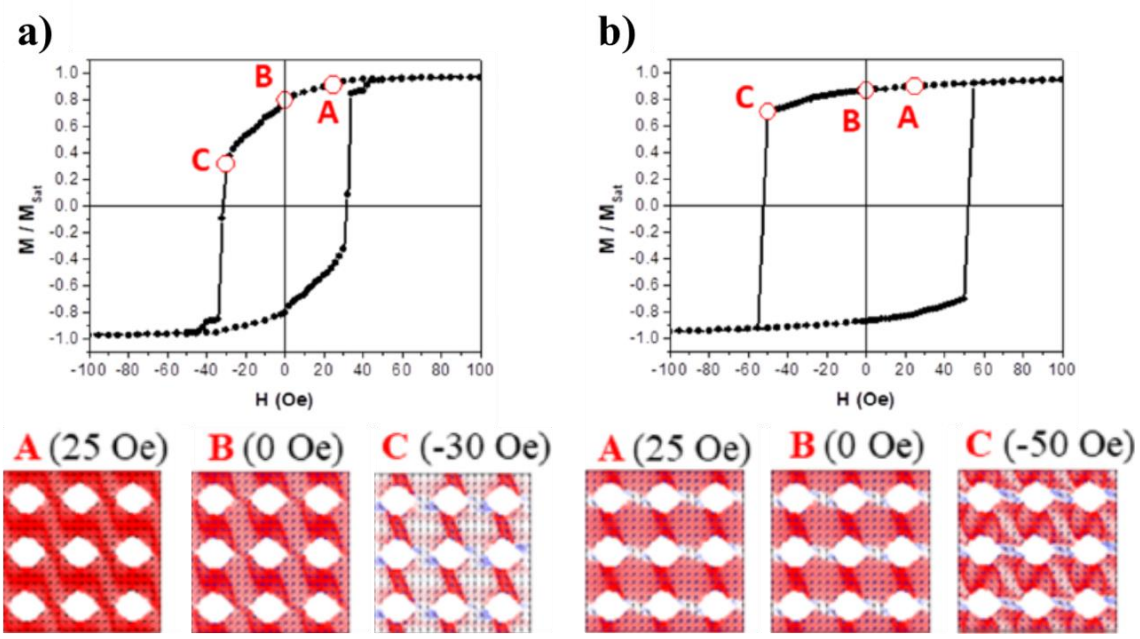

Figure 4.10: Simulated hysteresis loops of 10-nm-thick Py antidot array and snapshots of the magnetization when the external magnetic field was applied along the **a)** x- axis (θ = 0º) and **b)** at θ = 45º. The images of the magnetization were recording with different external applied fields **a)** A = 25 Oe, B = 0 Oe and C = -30 Oe, and **b)** A = 25 Oe, B = 0 Oe and C = -50 Oe. [225]

In the next step, we tested our apparatus by performing TR-MOKE measurements in the Py line array with the magnetic field applied along the hard axis (perpendicular direction with respect to the direction of the lines).

As the oscillator light source can only provide low fluence values, samples should be maintained in a magnetic state that could be easily excited, or removed from the equilibrium state, without the application of a large amount of energy. In order to overcome this limitation, we chose to fix the external magnetic applied field to the minimum value required to saturate the sample along the hard axis direction.

In particular, TR-MOKE signals were recorded with an external magnetic field of 605 Oe and applied in opposite directions (+H in black and -H in red) are shown in Figure 4.11 (a). By subtracting both TR-MOKE signals, the resulting demagnetization curve is obtained (Figure 4.11 (b)).

These curves present the coherent artifact which has been marked by blue ellipses in Figure 4.11. Although we have used its presence to confirm the zero time-delay position between the pump and probe pulses, this artifact can be eliminated by crossing the pump and probe pulse polarizations.

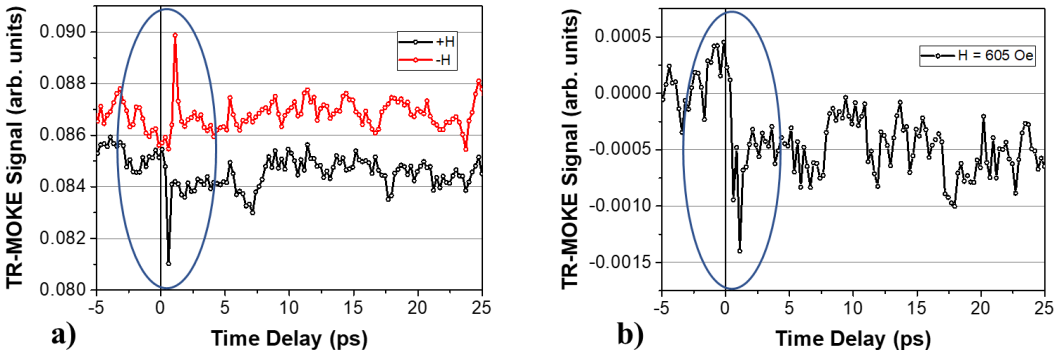

Figure 4.11: TR-MOKE curves of the Py line array using the oscillator as the light source, and applying the external magnetic field in the hard axis direction or perpendicular to the line axis. **a)** Curves measured with the magnetic field applied in opposite directions (+H in black and –H in red). **b)** The resulting demagnetization curve measured with an applied magnetic field of 605 Oe. These curves present the coherent artifact marked by blue ellipses in both figures.

Even when the maximum available fluence was used, the amplitude of the induced demagnetization was so small and the signal was so noisy that it was impossible to properly perform any systematic studies of the magnetization dynamics. Then, and although the use of an oscillator has shown some advantages, such as the stability and high repetition rate that increases the signal-to-noise ratio, it has important disadvantages as well, since the low energy pulses are not able to properly excite the samples. As previously commented, the pulse fluence can be increased by focusing the pump beam using microscope objectives, but the pulse temporal duration would be broadened and a worse temporal resolution would be achieved (potentially far from the original 7 fs).

4.4. TR-MOKE System Based on the Amplifier

One way to overcome this fluence limitation consists in using an ultrafast amplifier (referred in section 4.2) as the laser source for our TR-MOKE setup. Our amplifier system makes use of the chirped-pulse amplification (CPA) technique (described in section 2.3.2) to amplify the oscillator pulses in a multipass configuration. The pulses are stretched by a glass stretcher, up to about 20 ps, after passing through a Faraday rotator for optical isolation. A set of specially designed chirped mirrors are used to pre-compensate for the third-order dispersion mismatch between the total amplifier dispersion (mostly due to the glass stretcher) and the prism compressor dispersion [205]. Afterwards, the pulses are sent to a multipass amplifier. It is a nine-pass amplifier, and the beam is focused on the gain medium at each pass (focusing length of 50 cm) with spherical mirrors [205]. At the end of the first four passes, a Pockels cell pulse-picker selects pulses at a 1 kHz repetition rate. These pulses are sent back into the amplifier for more five passes after they are extracted and compressed with a Proctor-Wise prism compressor [194], [195]. The output pulses have up to 1 mJ of energy per pulse with duration of sub-30-fs.

4.4.1. Longitudinal TR-MOKE Setup with the Amplifier

For the initial measurements using the amplifier as the laser source, the longitudinal MOKE configuration was selected again. The main difference between this setup and the previous one (based on the oscillator) is the absence of the DCM compressor and the wedge pairs. No extra chirped mirror compressor is needed because the amplifier compressor is enough to compensate the dispersion introduced by the optical components and the air in the optical path (Figure 4.12). The rest of the optical components were kept the same since the smaller bandwidth of the amplifier is easily accommodated by the optics chosen for the oscillator, except for the lenses that we have changed for ones with a longer focal distance. There is no need to use lenses with small focal distance which provide smaller beam spots, since we have plenty of energy per pulse.

The compression of the pulses was verified by checking the second harmonic generation (SHG) signal at the sample plane. First, an SHG crystal in the sample position was installed. Using a spectrometer to visualize the SHG spectra, we then moved the pair of prisms in the amplifier compressor until the maximum SHG signal was obtained.

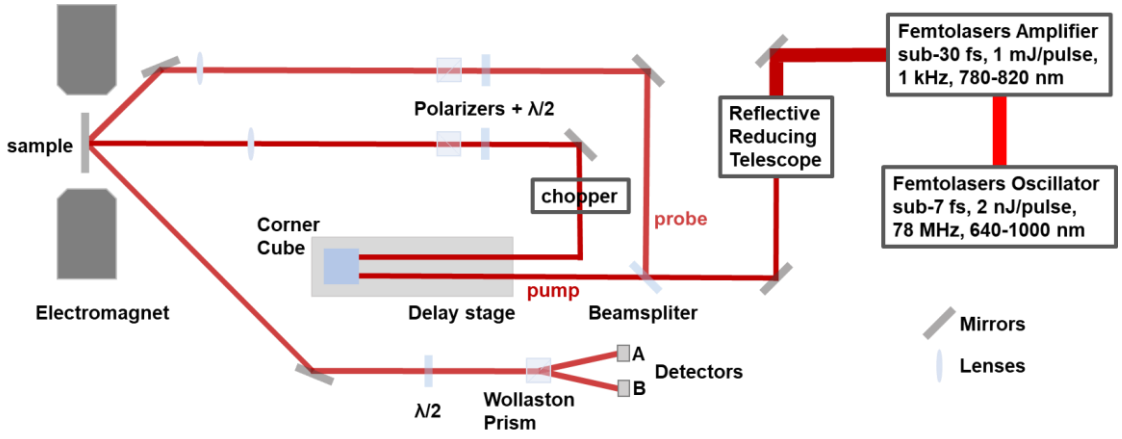

Figure 4.12: Schematic of our pump-probe TR-MOKE in longitudinal configuration based on the amplifier laser source.

As previously done with the oscillator, the hysteresis loop of the Py line array with the external magnetic field applied along the line axis was measured (Figure 4.13). The hysteresis loops, measured using the oscillator and the amplifier, are quite similar. The main difference is the reduced signal-to-noise ratio observed in the loops obtained with the amplifier. This was expected since the pulse repetition rate is smaller (1 kHz for the amplifier vs. 78 MHz for the oscillator). The signal-to-noise ratio, when the amplifier is used, can be improved by increasing the number of averaged loops. The hysteresis loops obtain with the oscillator and the amplifier, shown in Figure 4.13, have 15 and 50 averaged loops, respectively.

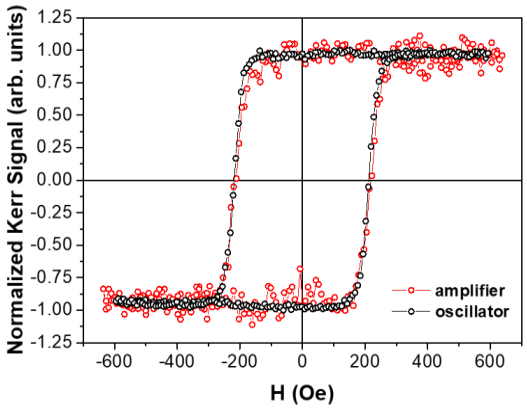

Figure 4.13: In-plane hysteresis loops of the Py line array along the easy axis and measured using oscillator pulses (black symbols; experimental setup shown in Figure 4.6) and the amplifier pulses (red symbols; experimental setup shown in Figure 4.12).

Once we have concluded that our system allows us to properly carry out static magnetic measurements, we tested this setup in a longitudinal MOKE configuration by performing magnetic dynamic measurements in the Py line array. For this purpose, we have maintained the same measurement conditions that we used previously with the oscillator. Again, we recorded the TR-MOKE signals (Figure 4.14 (a) with an external magnetic field of 605 Oe and applied in opposite directions (+H in black and -H in red). By subtracting both TR-MOKE signals, the resulting demagnetization curve is shown if Figure 4.14 (b). Although the signal to noise ratio is better with the amplifier than with the oscillator, and the magnetization precession can start to be observed in the resulting demagnetization curve (Figure 4.14 (b)), we should note that the signal is not good enough yet to perform systematic studies. Then, we decided to use the polar MOKE configuration instead of the longitudinal one since it is known that the signal from the polar effect is significantly larger than the one from the longitudinal measurements [233].

On the other hand, we confirmed again the presence of the coherent artifact before crossing the pump and probe pulse polarizations (see blue ellipses in Figure 4.14) and this effect was used to determine the position of the zero time-delay.

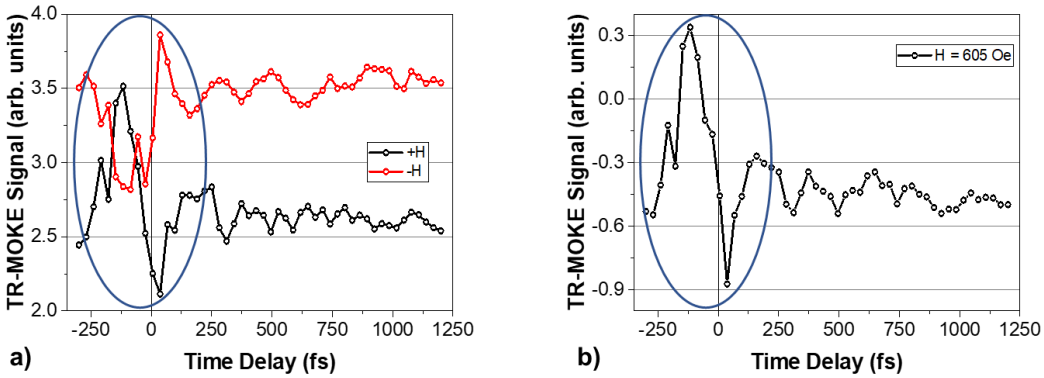

Figure 4.14: TR-MOKE curves of the Py line array using the amplifier as the light source and applying the external magnetic field in the hard axis direction or perpendicular to the line axis. **a)** Curves measured with the magnetic field applied in opposite directions (+H in black and –H in red). **b)** The resulting demagnetization curve measured with an applied magnetic field of 605 Oe. These curves also present the coherent artifact marked by blue ellipses in both figures.

4.4.2. Polar TR-MOKE Setup with the Amplifier

As one of the main aims of this thesis was the development of versatile TR-MOKE setup, we have used it in different configurations. In this sense, we modified the incidence angle of the probe beam (from around 45º to approximately 7º) and the MOKE system was transformed from the Longitudinal to the Polar configuration (see Figure 4.15). Besides

the rearrangement of the reflected beam to the detection system, the rest of the setup was maintained as in the longitudinal configuration.

The polar MOKE was mainly used for the study of the magnetization dynamics response of $[CoFeB/Pd]_N$ multilayers stack with perpendicular magnetic anisotropy and $[CoFeB/Pd]_5/Co$ exchange spring structures. These studies are presented in detail in Chapters 5 and 6.

Moreover, and according to literature [257], the signal-to-noise ratio of samples with perpendicular anisotropy and using the polar TR-MOKE configuration can be significantly increased when the external magnetic field is applied with an angle outside the sample plane. Therefore, measurements were performed by applying the magnetic field at an angle of 12º away from the sample plane.

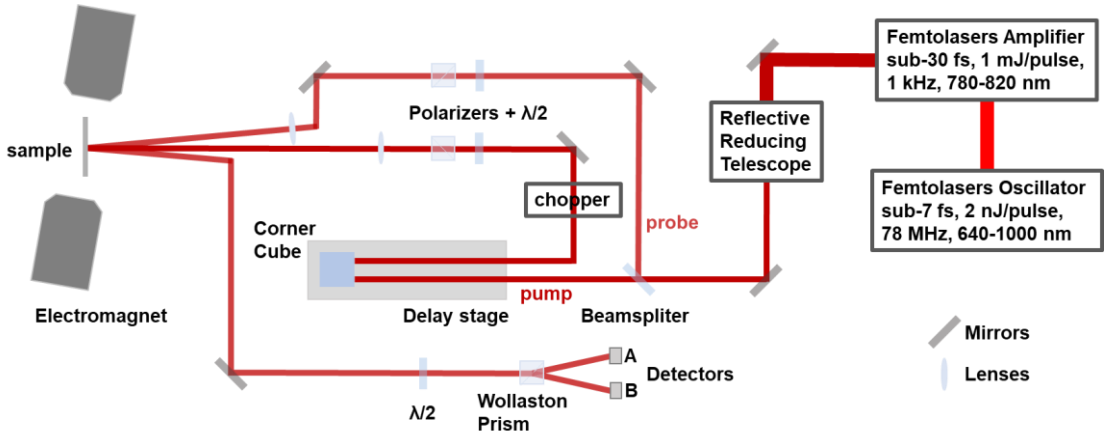

Figure 4.15: Schematic of our pump-probe TR-MOKE in a polar configuration and based on the amplifier laser source.

As an example, the dynamical response of the multilayers stack with perpendicular magnetic anisotropy ($[CoFeB$ (3 Å) / Pd (10 Å)$]_5$) and an applied magnetic field of 4310 Oe is shown in Figure 4.16 (a). In addition, Figure 4.16 (b) shows the ultrafast demagnetization curve of $[CoFeB$ (3 Å) / Pd (10 Å)$]_5$ / Co (7 Å) exchange spring structure and under an applied magnetic field of 2610 Oe. In both cases, measurements were performed with a fluence of around 2 mJ/cm^2 induced by the amplifier pulses. Magnetization in Figure 4.16 a) shows a sudden drop within the first picosecond after the pump pulse, a fast recovery (remagnetization) within a few picoseconds, followed by a clear oscillation, or precession, during a slower magnetization recovery, which is characterized by the ferromagnetic resonance frequency f_{res} and the Gilbert damping parameter α (detailed analysis will be provided along Chapters 5 and 6).

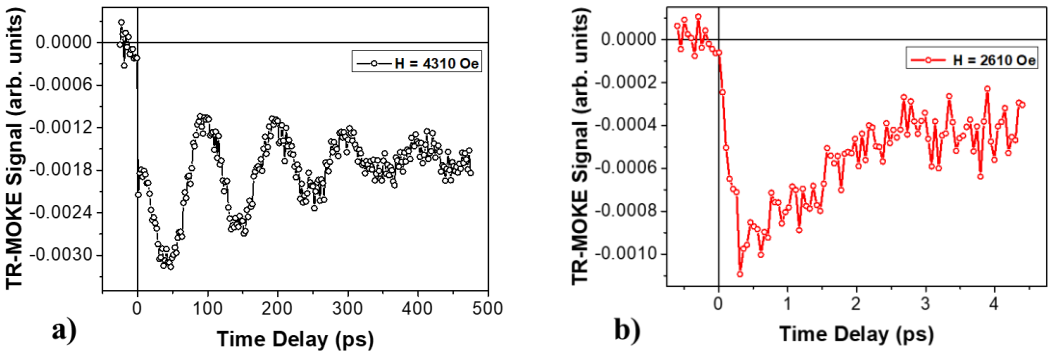

Figure 4.16: TR-MOKE curves of **a)** [CoFeB (3 Å) / Pd (10 Å)]$_5$ multilayer stack under an applied magnetic field of 4310 Oe and **b)** [CoFeB (3 Å) / Pd (10 Å)]$_5$ / Co(7 Å) exchange spring structure under an applied magnetic field of 2610 Oe, with a fluence of around 2 mJ/cm^2 induced by the amplifier pulses.

To conclude this section, the use of amplified laser pulses has shown some advantages such as the high available fluence, and the fact that a less number of optical components are required. However, the temporal resolution of the measurements is limited by the duration of the pulses (sub-30-fs). Therefore, the amplifier is the most suitable approach to perform studies which do not require a high temporal resolution, like the case of precession studies or other phenomena at longer temporal scales.

4.5. TR-MOKE System Based on the Hollow-fiber Compressor

In the previous sections, it was described that both high fluences and high temporal resolutions are required to carry out a complete study of the ultrafast demagnetization process. Then, the described laser sources are not adequate and show some limitations. With this in mind, we have developed our next pump-probe apparatus which is based on a state-of-art home-built hollow-core fiber and chirped mirror compressor.

4.5.1. Hollow-core Fiber and Chirped-mirror Compressor[4]

In order to generate intense radiation, with pulse energies of hundreds of μJ, and durations in the sub-4-fs regime, a high-energy pulse compression technique based on pulses initially created by CPA has been employed. This technique is composed of two steps: i) nonlinear spectral broadening and ii) broadband dispersion compensation [207]–[210] (shown in Figure 4.17).

[4] Based on [258]

In the first step, the optical pulse spectrum, delivered by the laser amplifier, is broadened inside a gas-filled hollow core fiber by nonlinear self-phase modulation (SPM). The hollow-core fiber (HCF) compressor used in this setup comprises a standard 1 m long hollow-core fiber with a diameter of 250 µm and placed in a static pressure chamber with 1 atm of Argon. This is a quite standard configuration of HCF compressor in terms of fiber parameters and nominal gas pressure. The choice of Argon gas was motivated by its higher Kerr-nonlinearity compared to lighter noble gases such as Neon. We found that Argon gas was more effective for generating broadband, octave-spanning spectra with a well-behaved spectral phase when pumped with the sub-mJ and sub-30-fs pulses of our laser amplifier [208]. For higher energy and/or shorter pulse laser systems, other gases, such as Neon, can be used too [209].

However, as the pulse spectrum broadens during nonlinear propagation along the hollow fiber, the pulse itself acquires a chirp due to SPM as well as due to the dispersion in the gas and the optical windows of the chamber containing the hollow fiber. This chirp needs to be compensated for in order to obtain pulses with the shortest possible temporal duration. Dispersion compensation can be achieved in many ways; among the most common are prism pairs or chirped mirrors [196].

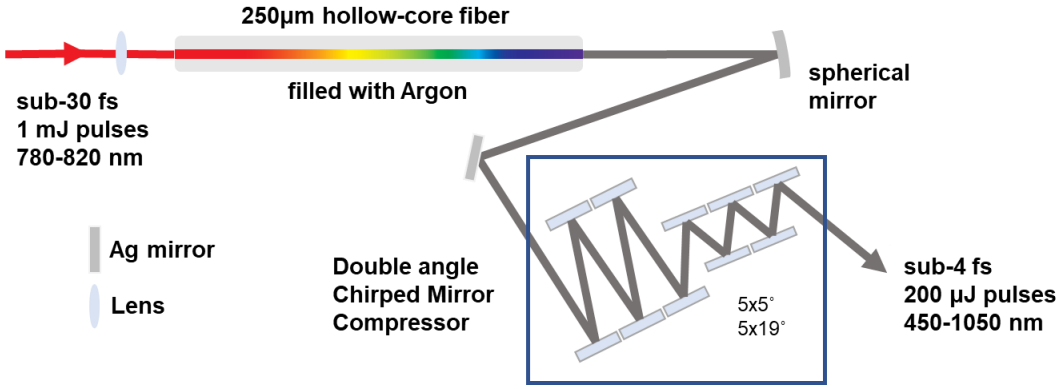

Figure 4.17: Simplified set-up of our hollow fiber and chirped mirror compressor. Into the blue rectangle is represented the double angle chirped mirrors which should be placed at two different angles (5° and 19°). Adapted from References [208], [258].

In our particular case, the 1 mJ, 27 fs pulses from the CPA amplifier are coupled into a hollow fiber through a lens with a focal length of 1.5 m (Figure. 4.17). It was determined that for an input pulse energy of 500–700 µJ, the fiber transmission is approximately 40% and the dispersion compensation was performed using a set of ultra-broadband chirped mirrors (CMs). The CMs (Ultrafast Innovations GmbH) have been designed in such a way that when two reflections are combined, with incidence angles of 5° and 19°, respectively,

the residual group delay oscillations are minimized [208], [221]. This compressor consistently delivers sub-4-fs pulses, with 200–300 µJ energy and a stabilized carrier-envelope phase (in case CEP stabilization is activated in the oscillator and amplifier). Its output is extremely broadband, spanning from 450 to 1050 nm, and with a Fourier-limit below 3 fs [208].

4.5.2. Pulse Characterization (d-scan technique)

The time domain waveform and pulse width are key parameters in any study involving ultrashort optical pulses, since they determine the timescale of the excitation, and hence the interaction regime, as well as the achievable temporal resolution.

The d-scan technique was invented in our group, in collaboration with Lund University, and is described in detail in References [208], [219]–[222], where it was used to successfully characterize the ultrashort laser pulses produced by the oscillator of our CPA system, as well as the output of the broadband hollow-core fiber compressor. In this work, d-scan was used to measure both the pump and probe pulses of our TR-MOKE system based on the hollow-core-fiber source at the plane of the sample.

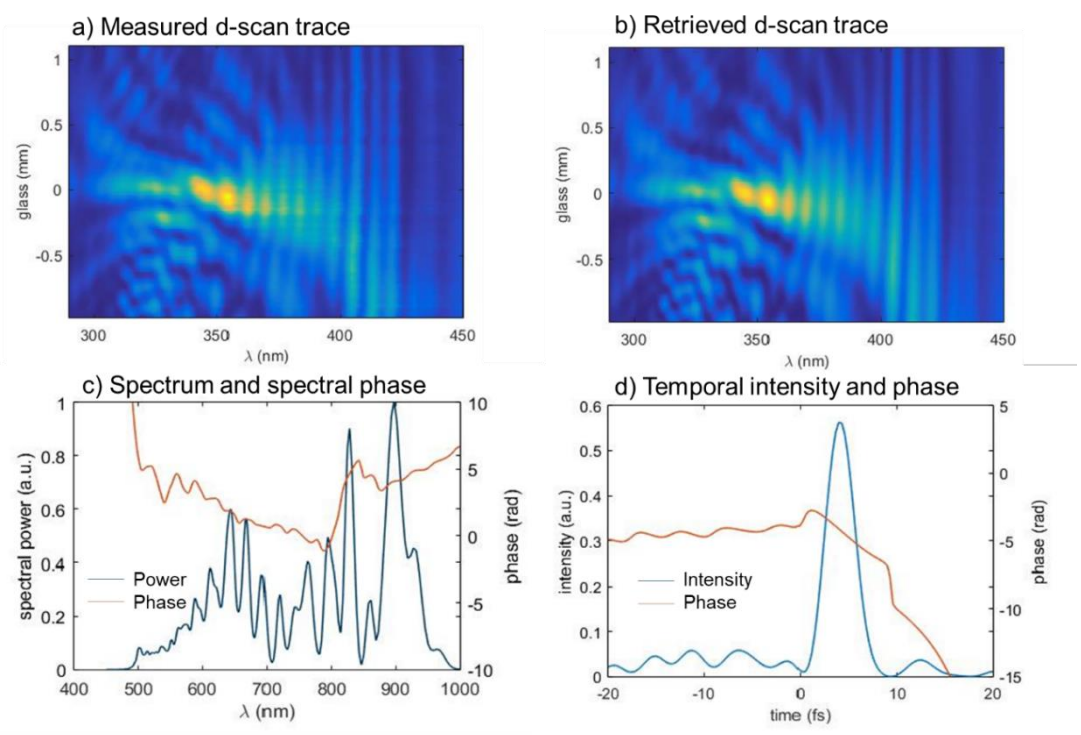

Figure 4.18: Measured **(a)** and retrieved **(b)** d-scan traces for the probe pulse; retrieved probe pulse in the spectral **(c)** and temporal **(d)** domains. **Probe pulse full width at half maximum (FWHM) is 3.6 fs**.

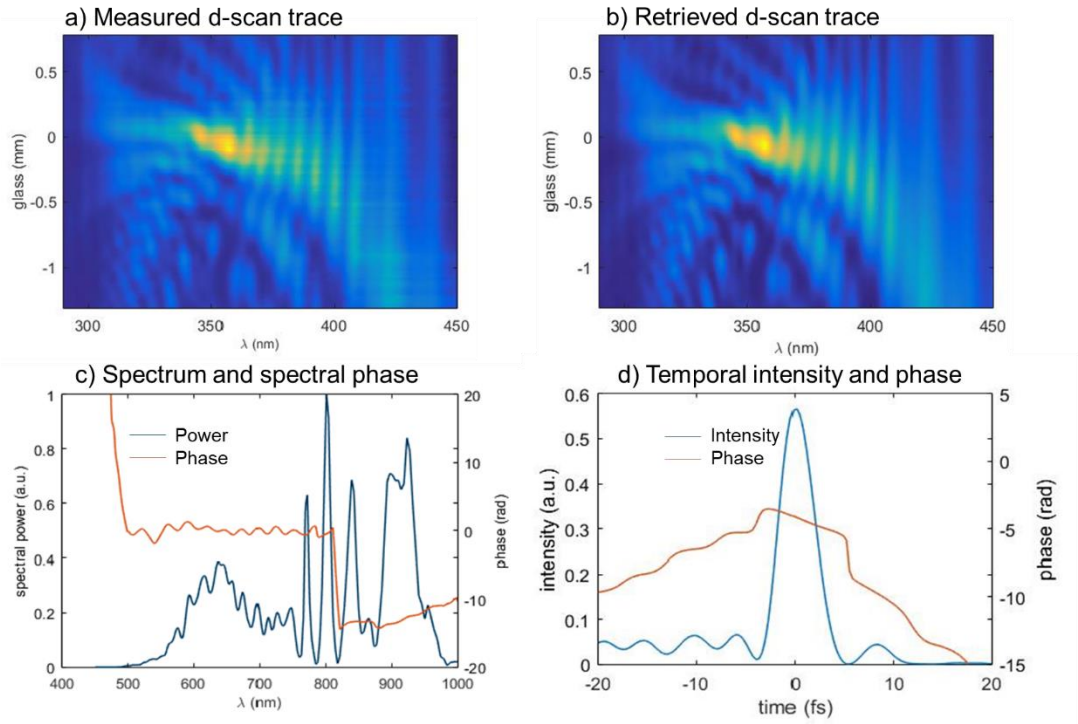

Figure 4.19: Measured **(a)** and retrieved **(b)** d-scan traces for the pump pulse; retrieved pump pulse in the spectral **(c)** and temporal **(d)** domains. **Pump pulse full width at half maximum (FWHM) is 4.0 fs**.

The experimental implementation of d-scan consists in measuring the second-harmonic generation (SHG) spectrum of the pulse (or the spectrum of another nonlinear process) while the dispersion is varied via the insertion of one of two glass wedges around the point of maximum compression (minimum pulse duration). As a result, a spectrally resolved SHG trace as a function of wedge insertion (dispersion) is obtained (shown in Figures 4.18 (a) and 4.19 (a)). Retrieval of the complete electric field related to the pulses is then performed with an iterative numerical algorithm [219], [220], [222], [223] (Figures. 4.18 (b) and 4.19 (b)).

In the present set-up, we focused the pump (probe) pulses using a lens with focal length of 400 mm (150 mm) on a nonlinear crystal (Beta Barium Borate BBO, 20 μm thick, cut for type I SHG at 800 nm) placed in the position where the pump and probe pulses are overlapped on the sample. The SHG signal is collimated with a lens, and a blue filter is used to remove the remaining fundamental frequency signal before the signal detection with an optical spectrometer (HR4000, Ocean Optics Inc.). Figures 4.18 and 4.19 show the d-scan results obtained for the probe and pump pulses with the measured temporal durations of 3.6 and 4 fs, respectively. We would like to thank Miguel Miranda for doing the d-scan retrieval of the pump and probe pulses presented in Figures 4.18 and 4.19.

4.5.3. Polar TR-MOKE Setup with the Sub-5-fs Hollow-fiber Compressor

The setup based on the hollow-fiber is described in Figure 4.20. As described in sub-section 4.5.1, the pulse dispersion compensation is accomplished by the hollow-fiber compressor itself by using a set of ultra-broadband chirped mirrors and a wedge pair.

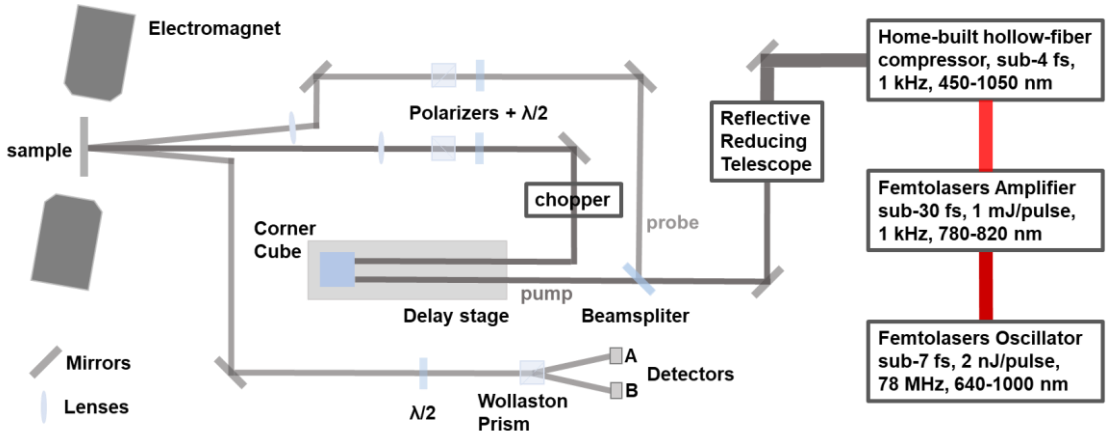

Figure 4.20: Schematic of our pump-probe TR-MOKE in a polar configuration and based on the hollow-fiber compressor as the laser source and before any extra changes required to compress the hollow fiber pulses to sub-5-fs durations.

In order to validate the performance of this last design, we first compared the dynamical response of a thin film with perpendicular magnetic anisotropy when measurements were carried out using the hollow-fiber or the amplifier as the laser sources (Figure 4.21). For this purpose, we measured the ultrafast demagnetization curves using the amplifier (black symbols in Figure 4.21). Then, we repeated this measurement after changing the laser source (from the amplifier to the hollow-fiber compressor) and making minor alignments (see red symbols in Figure 4.21). Both ultrafast demagnetization curves in Figure 4.21 seem to be identical. This result is not a complete surprise since we should highlight that the hollow fiber pulses were not yet compressed and larger pulse widths (similar to the ones provided by the amplifier) should be expected.

Therefore, the next step should be focused on achieving the full compression of the hollow-fiber pulses. In order to reach pulses with the smallest time duration at the sample plane, we have reduced to the minimum the amount of optical components in our setup. After removing several elements, we should have to compensate for the dispersion of the pump and probe lenses, the beamsplitter, the probe polarizer (used to “clean” the probe polarization), and the neutral density (ND) filters used to control the intensity of the beams (see Figure 4.22).

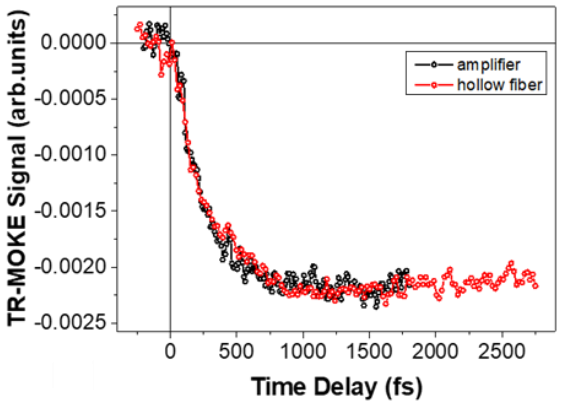

Figure 4.21: Ultrafast demagnetization curves of the sample $[CoFeB(3Å)/Pd(10Å)]_5$ measured with both laser sources, amplifier (black symbols; setup Figure 4.14) and hollow-fiber compressor (red symbols; setup Figure 4.20). The hollow fiber pulses were not yet compressed.

The optical components were chosen to take into account the ultrabroad bandwidth of the hollow fiber pulses (450 to 1050 nm). Then, we used a fused silica (FS) plate without any AR coating as the beamsplitter. The pump and probe lenses, with 400 and 200 mm of focal length, respectively, do not have any AR coating either. The polarizer is an ultra-broadband wire grid (250 nm to 4 μm). Its 2.2 mm FS substrate introduces much less dispersion than a conventional polarizer cube. The half-wave plate used in the detection is a superachromatic one with an ultrabroad wavelength range from 420 to 1100 nm. Afterwards, the d-scan technique was used to verify that both the pump and probe pulses provided by the hollow-fiber compressor were well compressed for the same insertion position of the wedges used for fine-tuning the dispersion.

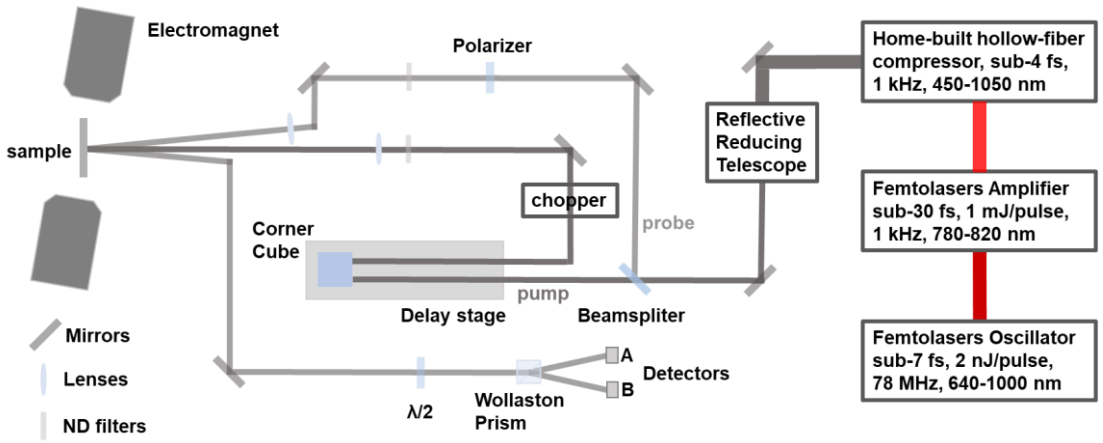

Figure 4.22: Schematic of our pump-probe TR-MOKE in a polar configuration based on the hollow-fiber compressor and delivering pulses with sub-5-fs duration at the sample plane.

To verify the proper operation of our setup with the sub-5-fs hollow fiber pulses in the sample plane, we measured the ultrafast demagnetization curve of the sample [CoFeB (3 Å) / Pd (10 Å)]$_5$ and compared with the one taken before the hollow fiber pulses were compressed (shown in Figure 4.23). In this particular case, we used time delay steps of 6 fs, applied a magnetic field of 4695 Oe and a fluence of ~2 mJ/cm^2. Comparing both curves presented in Figure 4.23, it is clear that the demagnetization reaches a maximum faster when for the sub-5-fs pulses. This difference will be addressed in Chapter 7.
All measurements presented in Chapter 7 have been performed using the setup based on the hollow core fiber with sub-5-fs pulse duration at the sample plane.

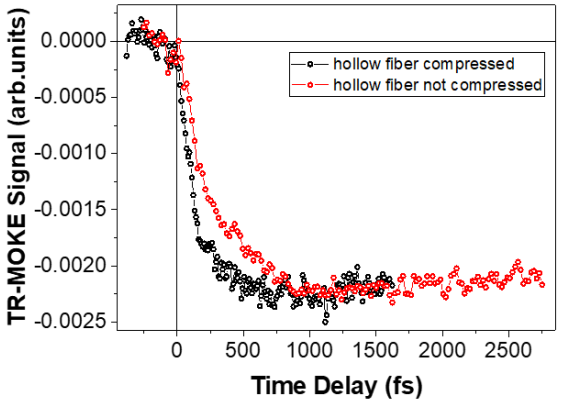

Figure 4.23: Ultrafast demagnetization curve of the sample [CoFeB (3 Å) / Pd (10 Å)]$_5$ measured with an applied field of 4695 Oe, a fluence of ~2 mJ/cm^2, measured with the hollow fiber pulses not yet compressed (red symbols; using the setup described in Figure 4.20) and with hollow fiber pulses with sub-5-fs duration (black symbols; using the setup described in Figure 4.22).

In summary, we should note that the last configuration of our setup has the advantage of being able to use any laser source just by adjusting the right dispersion compressor. Depending on the required studies, the apparatus can be easily modified and adapted.
The present pump-probe system, when operating in a degenerate configuration with sub-5-fs CEP stabilized pulses, enables us to further explore this temporal regime limit. We believe that it will be an important aim for future developments in the femtomagnetism research field. The first results obtained using this ultra-high resolution setup, will be presented in Chapter 7.

4.6. Detection and Acquisition System

4.6.1. Balanced Detection

In all time-resolved measurements, the basic idea is the detection of any pump-induced modification of the system. In particular, the detection of the magnetic state in a ferromagnetic sample is performed via the measurement of magneto-optical effects, which result in a rotation or modification of the ellipticity of an incident probe beam of polarized light.

In our system, the detection of the magneto-optic Kerr effect (MOKE) signal was performed by a balanced detection scheme. Figure 4.24 presents the elements of our balanced detection system: a half-wave plate, a Wollaston prism, and two photodetectors (A and B). The reflected beam is guided through a broadband half-wave-plate and a Wollaston prism then separates the two orthogonally polarized (s and p) components. Then, the intensities of both components are measured using two amplified photodetectors (Thorlabs PDA100A2, Si Switchable Gain Detector, 320 - 1100).

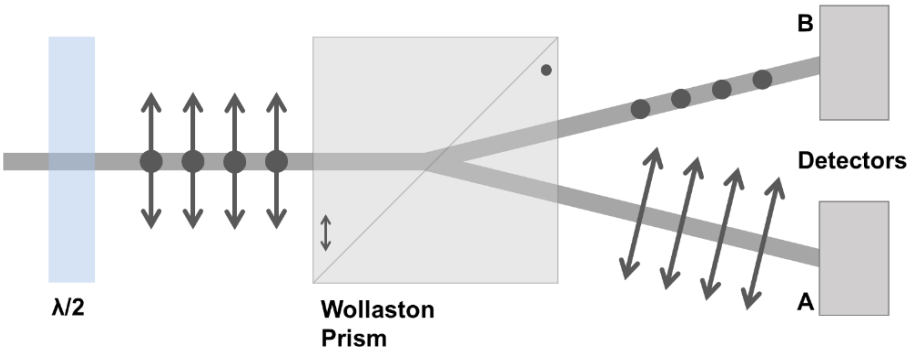

Figure 4.24: Schematic of our balanced detection system.

Before starting the measurement, we have to rotate the half-wave-plate until the difference of the intensities between the two orthogonally (s and p) polarized components results in a null signal. This procedure is called balancing the detector. It means that the electric field $\boldsymbol{E}$ of the linearly polarized beam passes through the Wollaston prism at an angle of α = 45º (see Figure 4.25) concerning the optical axis of the prism and the two output beams should be equal in intensity, as given by:

$$E_A = E \sin\frac{\pi}{4} = E \cos\frac{\pi}{4} = E_B \ . \tag{4.2}$$

Consequently, the signal measured by the two photodetectors, which is proportional to the intensities of the two beams ($I_{A;B} \propto |E_A; E_B|^2$), should be identical and the difference would be null: $I_A - I_B = 0$.

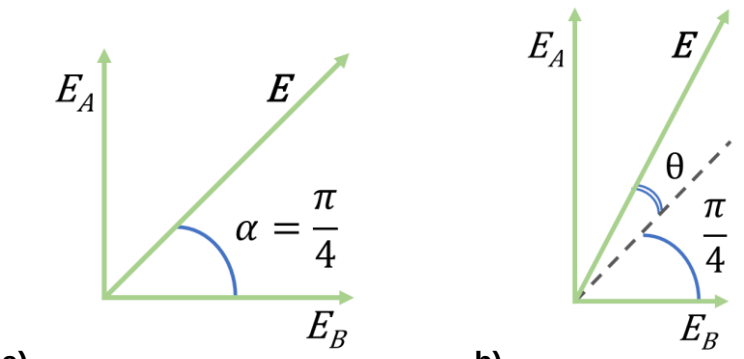

Figure 4.25: (a) If the incoming beam is linearly polarized along a direction 45º away from the optical axis of the Wollaston prism, it is split into two beams with the same intensity. (b) If the beam that passes through by the Wollaston prism is polarized differently from 45º, the electric fields of the two output beams are not equivalent. Adapted from [259].

Scanning the difference of these two signals allows us to evaluate the relative magnetization state of the sample as a function of the external applied magnetic field and the time delay introduced between the pump and the probe beams. In this way, if the polarization of the incoming beam is rotated by an angle θ, the electric fields of the two components become:

$$E_A = E \sin\left(\frac{\pi}{4} + \theta\right) \qquad E_B = E \cos\left(\frac{\pi}{4} + \theta\right) \quad . \tag{4.3}$$

The difference of the output photodetector signals, $I_A - I_B$, could be obtained by calculating the difference of the optical intensities and it could be expressed by:

$$I_A - I_B \propto E^2 \sin^2\left(\frac{\pi}{4} + \theta\right) - E^2 \cos^2\left(\frac{\pi}{4} + \theta\right) = E^2 \sin(2\theta). \tag{4.4}$$

Therefore, the balanced-detection scheme provides a signal which is proportional to the polarization rotation angle θ. Since the Kerr rotation angles are usually considerably smaller than one degree and detectors operate in a linear regime, Eq. (4.4) can be simplified to:

$$I_A - I_B \propto 2\theta E^2 \tag{4.5}$$

4.6.2. Acquisition System

We already emphasize that, in general, the measured polarization rotation angles are very small. This fact leads to a significant problem related to the signal to noise ratio (SNR). Mainly, the noise sources are the laser intensity fluctuations, the stray light that can reach the detector, and the dark current (current in the absence of light) of the photodiodes. As demonstrated in the literature, a signal modulation technique can significantly increase the signal to noise ratio [260], and this was used to improve the quality of our measurements with the addition of a lock-in amplifier.

In most of our measurements, we used the amplifier or the hollow-fiber as the laser sources. Both systems produce by default a modulation of the signal based on its internal repetition rate of 1 kHz. Then, one can use this signal, that synchronizes the laser system, as the trigger to the lock-in. Under this assumption, the lock-in should compare the situation when no pulse reaches the detector with the situation when a probe pulse reaches the detector (probe modulation). Therefore, the resulting signal should be proportional to the absolute values of the probe A and B signals in the detectors.

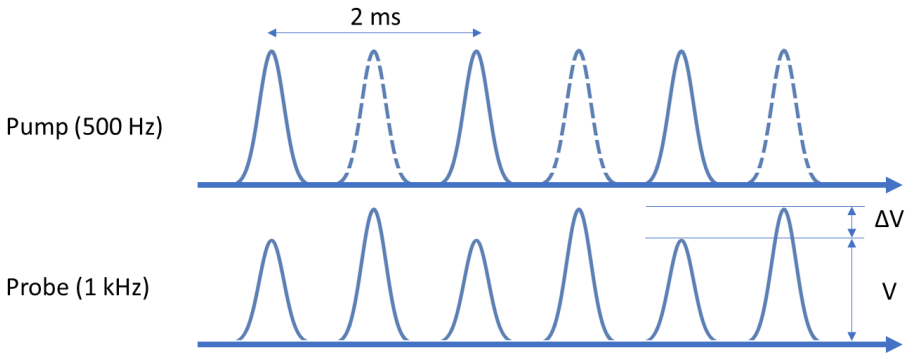

Figure 4.26: Induced probe modulation: probe beam in the presence and in the absence (dashed blue line) of the pump pulses.

However, another approach has been suggested [260] and it is based on a modulation in the probe signal by using an optical chopper in the pump path and operating at half the repetition rate of the laser system, 500 Hz (see Figure 4.26). It is known as a pump-on – pump-off pulse situation, i.e., every second pump pulse is blocked and does not reach the sample. The reference frequency sent to the lock-in is the chopper one (500 Hz). This kind of measurement is substantially more sensitive than the probe modulation. In this last case, the lock-in signal is proportional to the pump induced change rather than the absolute signal. The resulting signal is equivalent to the difference between the detected probe beam in the presence and the absence of the pump pulses.

If the oscillator is the chosen laser source, it is possible to modulate the probe by chopping the pump as well. The chopper is not synchronized with the high-repetition-rate of the oscillator, but it will work at any chosen frequency since the laser essentially behaves as a continuous source. It is equivalent to the pump pulse “on” and pump pulse “off” situation, but in this case, “on” will transmit many pump pulses and “off” will block many pump pulses, which induces a modulation in the probe signal at the chopper chosen frequency. The output signal of the chopper controller is used for triggering the lock-in.

During the development of our pump-probe system, we also explored other signal acquisition options. Namely, we tested the system with the laser amplifier using a gated integrator & boxcar averager (Stanford Research Systems SR250, referred to as boxcar in the following) combined with a lock-in amplifier (Stanford Research Systems SR850). In this case, the modulated probe signal (Figure 4.26) is first sent to the boxcar, which integrates the signal of each pulse separately within a given time window (gate) set around the pulse [261], while the rest of the signal is ignored, and hence avoiding any noise occurring between pulses. This adjustable-width gate is synchronized with the amplifier laser pulses (1 kHz).

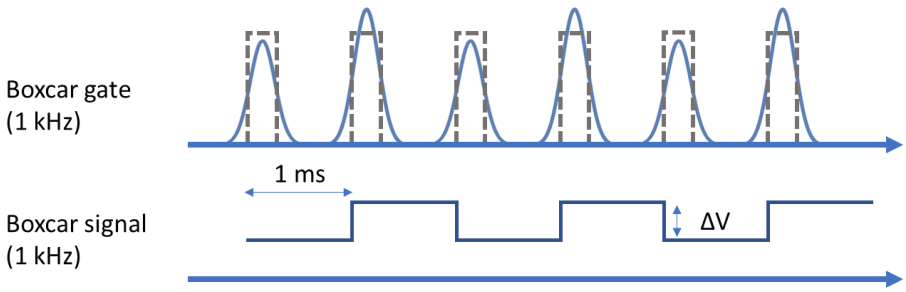

Figure 4.27: Schematic of the gate (dashed grey lines) synchronized with the modulated probe signal and the resulting boxcar signal of the sample-and-hold circuit.

Figure 4.27 shows a schematic representing the gate synchronized with the modulated probe signal and the resulting boxcar signal for the sample-and-hold circuit, i.e., the integrated signal of one pulse is held until the gate opens again and the signal of the next pulse is acquired. Each sample corresponds to the integrated signal of only one pulse, and no averages were made over the samples. This signal is then sent to the lock-in, which is trigged at 500 Hz (the frequency of the chopper), and averaged over several tens of samples (pulses), e.g., 50 if a time constant of 100 ms is chosen on the lock-in.

The configuration of the data acquisition system evolved until reaching a compromise between the achievable SNR and the complexity of the system (e.g., number of different modules/components, where each new module is also a source of additional noise), time

required to perform a measurement, and ease of use. In the following, the discussion refers to the system without the boxcar.

Our acquisition system includes two photodetectors (Thorlabs PDA100A2), one chopper (Thorlabs MC2000B), a home-made amplifier box (which performs the difference (A-B) and the sum (A+B) of the photodetector signals), two lock-in amplifiers (Stanford Research Systems SR850) (see Figure 4.28).

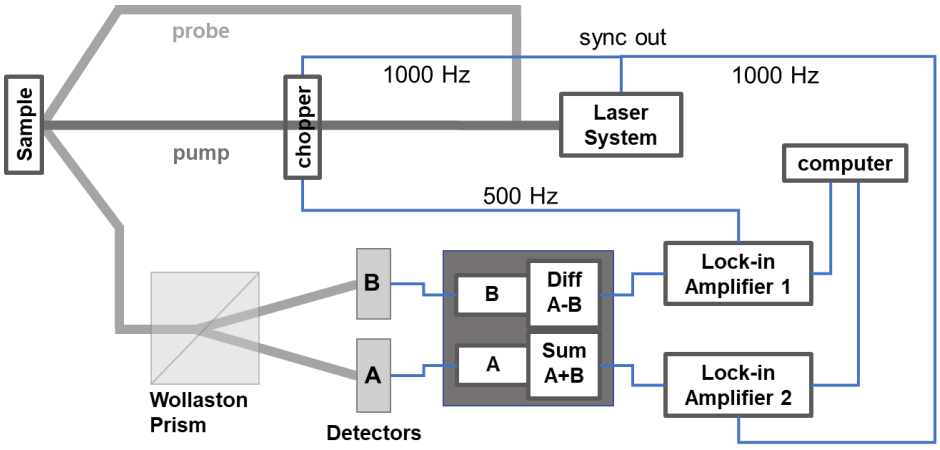

Figure 4.28: Schematic of our acquisition system used when the laser source is the amplifier or the hollow-fiber.

The amplified outputs of the A and B photodetectors are sent to the home-made amplifier box. The amplifier box outputs provide the difference signal ($A - B$) and the sum signal ($A + B$). Both signals are then sent to two lock-in amplifiers, which detect only components at the frequency of the reference signal [262]. In order to remove any noise in the detected signal produce by possible fluctuations of the laser intensity, the difference signal, $I_A - I_B$, is finally normalized by the sum signal $I_A + I_B$.

Next, we show how the detected voltages can be converted into degrees of the polarization rotation. Using Eq. (4.3), we can obtain that the sum $I_A + I_B$ is described by:

$$I_A + I_B \propto E^2 \sin^2\left(\frac{\pi}{4} + \theta\right) + E^2 \cos^2\left(\frac{\pi}{4} + \theta\right) = E^2 = \frac{2\sqrt{2}}{P.B_{A+B}} \frac{S^{Lock-in_{A+B}}}{A_{A+B}} \qquad (4.6)$$

where the factor $2\sqrt{2}$ takes into account the root mean square signal from the lock-in used for the photodetectors A and B, $P_A = P_B = P$ are the pre-amplification factors of the signals A and B of our photodetectors, B_{A+B} is the pre-amplification factor of the signal $A + B$ of our home-made amplifier box, $S^{Lock-in_{A+B}}$ is the output signal of the lock-in used

for the signal $A+B$ and A_{A+B} is the corresponding amplification factor. Here, we have considered the total reflected optical intensity of the probe beam, so the signal at the repetition rate of the laser (1 kHz) and not the frequency component at the modulation frequency. We can now express the output of the difference $I_A - I_B$ as:

$$I_A - I_B = \frac{2\sqrt{2}}{P.B_{A-B}} \frac{S^{Lock-in_{A-B}}}{A_{A-B}}. \tag{4.7}$$

Combining Eq. (4.5), (4.6) and (4.7) we can now express the output of the difference channels in degrees as:

$$\sin(2\theta) = \frac{2\sqrt{2}}{P.B_{A-B}} \frac{S^{Lock-in_{A-B}}}{A_{A-B}} \Big/ \frac{2\sqrt{2}}{P.B_{A+B}} \frac{S^{Lock-in_{A+B}}}{A_{A+B}} \tag{4.8}$$

from which it is straightforward to derive the angle of rotation of the probe polarization

$$\theta = \frac{1}{2}\sin^{-1}\left(\frac{S^{Lock-in_{A-B}}}{B_{A-B}.A_{A-B}} \Big/ \frac{S^{Lock-in_{A+B}}}{B_{A+B}.A_{A+B}}\right). \tag{4.9}$$

4.7. Summary

We have developed a unique compact versatile time-resolved magneto-optical system to study ultrafast magnetization dynamics processes. We have demonstrated that our final setup can be used with any laser source just adjusting the right dispersion compressor and allowing us to achieve a fine control of the time-resolution. Depending on the required studies, it was confirmed that the configuration of our apparatus can be easily modified and adapted.

As our main aim, we should highlight that we were well succeeded in the built of a TR-MOKE setup based on the hollow core fiber. Our set-up uses state-of-the-art ultrafast optical methods to deliver ultrashort laser pump and probe sub-5-fs carrier-envelope phase (CEP) stabilized pulses and at the sample position, permitting the observation of ultrafast magnetization dynamics at unprecedented temporal resolutions.

This few-cycle regime is also highly promising for the direct excitation and observation of coherent ultrafast magneto dynamic behavior. Furthermore, CEP-stabilized sub-5-fs pulses have opened the way for exploring the dependence of the induced magnetization dynamics on the electric field of the excited optical pulses. We believe that this is an important aim for future developments in ferromagnetism.

Chapter 5

Magnetization Dynamics of $[CoFeB(t)/Pd]_N$ Multilayers with Perpendicular Anisotropy

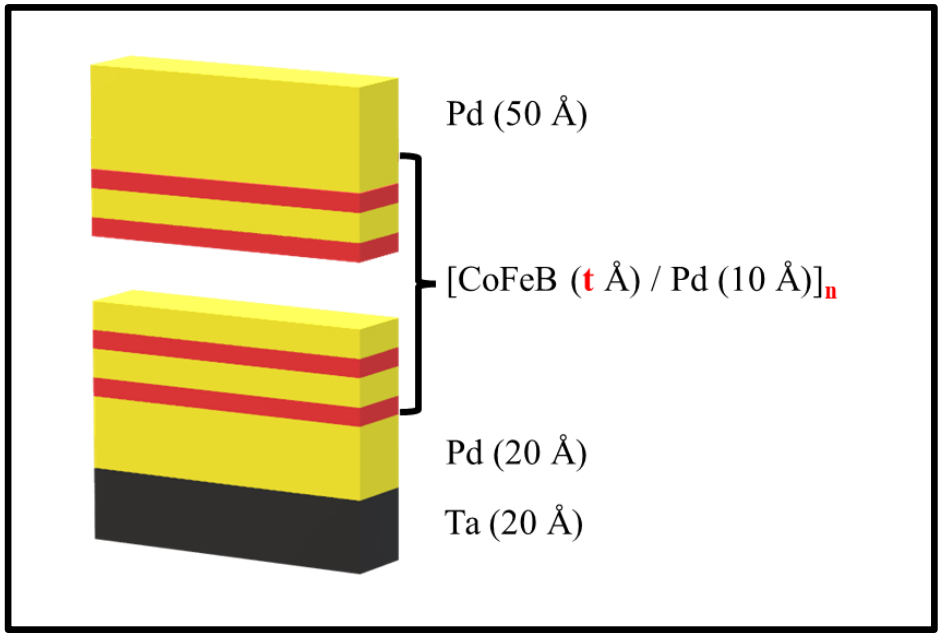

Chapter 5

Magnetization Dynamics of [CoFeB(t)/Pd]$_N$ Multilayers with Perpendicular Anisotropy

5.1. Introduction

CoFeB-based ultrathin films with perpendicular magnetic anisotropy are promising systems for different technological applications such as the development of nonvolatile memories with low power consumption and high-speed performance [31]. Therefore, the understanding of the magnetic dynamical behavior of those CoFeB-based structures is crucial for future applications. A deeper overview of this kind of materials was described in subsection 1.2.1.

In this chapter, we present the study of the dynamical properties of [CoFeB(t_{CoFeB})/Pd]$_N$ multilayer ultrathin films, ranging the CoFeB layer thickness (t_{CoFeB}) between 1 and 5 Å, as well as the number of bilayers (N), ranged between 3 and 15 and for the set of samples with t_{CoFeB} = 3 and 4 Å. In both cases, we used two complementary and independent techniques: Time-Resolved Magneto-Optical Kerr Effect (TR-MOKE) measurements with Vector Network Analyzer Ferromagnetic Resonance (VNA-FMR) analysis.

Although the used experimental methods were presented in Chapter 3, they are also briefly introduced in section 5.2. Regarding the sample preparation, the process was addressed in section 3.2.

In section 5.3, our work studies the magnetic response of [CoFeB(t_{CoFeB})/Pd]$_5$ multilayer ultrathin films and ranging t_{CoFeB} between 1 and 5 Å. We focused our attention on understanding its related magnetic moment, the anisotropy terms as well as the effective damping. In addition, we have defined the t_{CoFeB} values which are required to achieve thin films with effective perpendicular magnetic anisotropy.

In the second part of this chapter (section 5.4), the static and dynamical properties of the [CoFeB/Pd]$_N$ multilayer ultrathin films with N = 3, 5, 10 and 15 are described. According to the results shown in the previous study (section 5.3), multilayer thin films with a t_{CoFeB} = 3 and 4 Å have been analyzed. The main aim is based on understanding the effect of the number of bilayers N on the effective perpendicular magnetic anisotropy. In addition, the *N* dependence of the magnetic moment and the effective damping parameter have been also explored. Finally, the chapter is summarized with an overview of the completed study presented in previous sections.

5.2. Experimental Methods

Room temperature magnetic hysteresis loops were measured in a vibrating sample magnetometer (VSM), and the dynamical behaviour was studied by comparing time-resolved magneto-optical Kerr effect (TR-MOKE) measurements with ferromagnetic resonance analysis (VNA-FMR). VNA-FMR measurements were carried out at room temperature using a coplanar waveguide (CPW) connected to a vector network analyzer. The samples were placed film down on the CPW, and the complex S_{21} parameter was measured as a function of the external magnetic field over a frequency range up to 20 GHz. The external DC magnetic field (H) was applied along (θ_H = 90º) or perpendicular (θ_H = 0º) to the sample plane for in-plane and perpendicular measurements, respectively, and was always perpendicular to the ac field generated by the CPW. On the other hand, the dynamical response of the magneto-optical signals was obtained by an ultrafast pump-probe system based on a commercial Titanium:sapphire laser amplifier (Femtolasers Compact Pro CE-phase) delivering sub-30-fs laser pulses (approximately 40 nm bandwidth centered at 800 nm) with ~1 mJ of energy at a repetition rate of 1 kHz and with carrier-envelope phase (CEP) stabilization capability, seeded by a CEP-stabilized ultrafast laser oscillator (Femtolasers Rainbow). Time-resolved measurements were performed in polar MOKE configuration using 0.7% and 99.3% of the pulse energy for the probe and pump pulses, respectively. The spot size ratio between the pump and probe beams was adjusted to be 4:1 to assure that the probe spot hits a homogeneous pump illuminated area of the sample. The pump fluence used was ~ 1 mJ/cm^2. In order to increase the signal-to-noise ratio of the TR-MOKE signal amplitude, the external DC magnetic field was applied at an angle of θ_H = 78°, with 0º and 90º corresponding to the out-of-plane and in-plane measurements, respectively [257]. This angle was restricted to this maximum value due to space constraints. All optical measurements were performed under ambient conditions.

5.3. Results and Discussion of [CoFeB(t_{CoFeB})/Pd]$_5$ Multilayers Study

In this study, we have investigated the dynamical behaviour of ultrathin [CoFeB (t_{CoFeB}) / Pd (10 Å)]$_5$ films with the CoFeB thicknesses ranging from 1 to 5 Å by using both Vector Network Analyzer based Ferromagnetic Resonance (VNA-FMR) and Time-Magneto-Optical Kerr Effect (TR-MOKE) measurements.

The CoFeB / Pd multilayers with strong PMA were first reported in 2010 [64], [65]. Since then, subsequent works have been mainly focused on study the contributions of the

volumetric (K_{vol}) and surface (K_{sur}) anisotropy terms to the PMA and as a function of the CoFeB layer thickness and the number of CoFeB / Pd bilayers [67], [90], [263]. In this thesis, PMA was confirmed for multilayers with t_{CoFeB} ≤ 4 Å and reaches a clear maximum at t_{CoFeB} = 3 Å. Further increase of CoFeB layer thickness reduces the perpendicular magnetic anisotropy and the magnetization became in-plane oriented for t_{CoFeB} ≥ 5 Å. This behaviour is explained by considering competing contributions from surface and magnetoelastic anisotropies and both K_{vol} and K_{sur} were estimated. In addition, we have performed a systematic study of previously unreported characteristic magnetic parameters such as the CoFeB saturation magnetization and the damping parameter in ultrathin CoFeB/Pd films. Although it was reported that the Gilbert damping for $Co_{40}Fe_{40}B_{20}$ alloy is as low as 0.004 [115], [116], the estimated effective damping (α_{eff}) increases substantially at low thickness [31] which is detrimental to the development of STT- or MTJs-based devices. For example, it was reported that 1 or 1.3 nm thick CoFeB layers with PMA show α_{eff} parameters of 0.012 [92] or 0.027 [31], respectively. This rise has been associated with the fact that the α_{eff} parameter contains contributions from both intrinsic and extrinsic terms [113]. Therefore, the effective damping parameter and its related intrinsic and extrinsic contributions were analyzed as a function of t_{CoFeB}. It is suggested that in our case the main additional contribution to α_{eff} is spin-pumping.

5.3.1. Static Properties

Magnetic Moment

Figure 5.1 (a) and (b) show the in-plane and out-of-plane hysteresis loops of the [CoFeB (t_{CoFeB}) / Pd (10 Å)]$_5$ multilayer stacks, respectively. The loops indicated that our samples show PMA when the CoFeB thickness (t_{CoFeB}) ranged from 1 to 4 Å. However, the easy magnetization axis lays in-plane for the largest t_{CoFeB} (5 Å).

Moreover, hysteresis loops were used to obtain the values of the saturation magnetization (M_{Sat}) which are shown in Figure 5.2 (a). We observed that M_{Sat} increases with the CoFeB film thickness from (280 ± 50) to (700 ± 50) emu/cm^3 for t_{CoFeB} = 1 and 5 Å, respectively. This behavior was already observed in ultrathin films, for example in Pt / Co / Pt [264], Ta / CoFeB (t nm) / SiO_2 (t = 1, 2, 3, 4, 6, 10 13 nm) [265], [Co (t nm) / Pd]$_8$ [266], and [CoFeB (t nm) / Pd (1.0 nm)]$_{10}$ (t = 0.4, 0.6, 0.8, 1.0 and 1.2 nm) multilayer films [67] with perpendicular anisotropy.

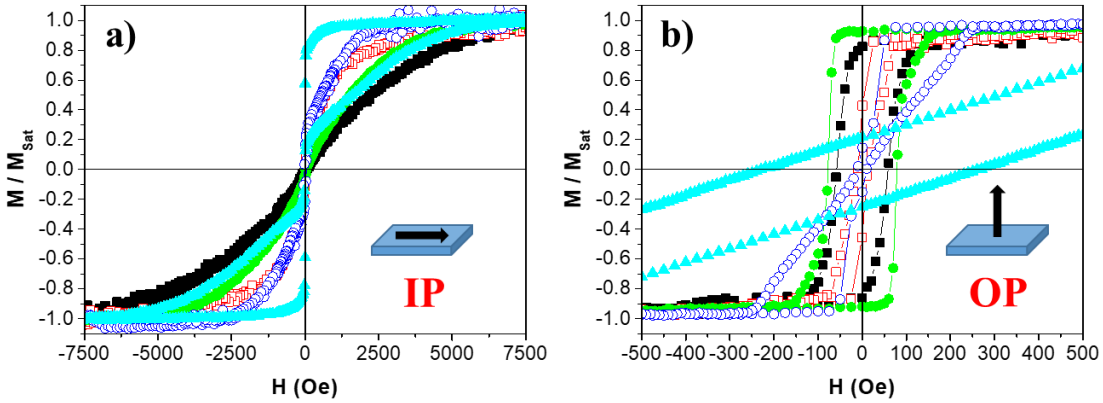

Figure 5.1: In-plane (a) and out-of-plane (b) hysteresis loops of [CoFeB (t_{CoFeB}) / Pd (10 Å)]$_5$ multilayer thin films with t_{CoFeB} = 1 (■), 2 (□), 3 (●), 4 (○) and 5 Å (▲).

As the CoFeB thickness was varied and both the Pd thickness (1 nm) and number of CoFeB / Pd bilayers (5) were kept constant, it can be suggested that the observed M_{Sat} increase with the CoFeB film thickness could be associated with the increase of the volume magnetic moment contribution while the surface/interface magnetization term should remain constant [67]. Therefore, the experimental magnetization data can be fitted by a linear dependence (continuous line in Figure 5.2 (a)) and the surface/interfacial magnetization term can be estimated from the extrapolation of this linear dependence to zero thickness. Our analysis determined that the surface/interfacial magnetization of CoFeB / Pd interfaces is (170 ± 60) emu/cm^3, which is in agreement with the value of (180 ± 10) emu/cm^3 reported by Ngo *et al.* [67].

In addition, the magnetization per unit area (M_{sat_sheet}) vs the CoFeB film thickness (t_{CoFeB}) is shown in Figure 5.2 (b). As described by Engel *et al.* [267], M_{sat_sheet} in superlattices can be estimated from

$$M_{sat\_sheet} = I/(N \times A) = M_{eff\_CoFeB} \times t_{CoFeB} + M_{eff\_Pd} \times t_{Pd} \qquad (5.1)$$

where I is the measured magnetic moment, N is the number of bilayers and A the area of the films (determined from the analysis of digital photographs of the samples), M_{eff_CoFeB} is the effective CoFeB saturation magnetization, t_{CoFeB} is the CoFeB layer thickness, M_{eff_Pd} is the effective magnetization of the polarized Pd induced by the ferromagnetic proximity effect [268]–[271], and t_{Pd} is the Pd layer thickness (10 Å). A linear fit of (M_{sat_sheet} vs t_{CoFeB}) is also plotted in Figure 5.2 (b). Assuming that the magnetic moment is uniformly induced in the entire Pd layer, M_{eff_Pd} = (120 ± 20) emu/cm^3 was estimated from the extrapolation of the linear fit to zero CoFeB layer thickness (t_{CoFeB} = 0 Å). This

saturation magnetization is in good agreement with previous studies on Co/Pd multilayers [268]–[271]. Additionally, an effective CoFeB saturation magnetization value of M_{eff_CoFeB} = (1760 ± 80) emu/cm^3 was obtained from the linear fit slope.

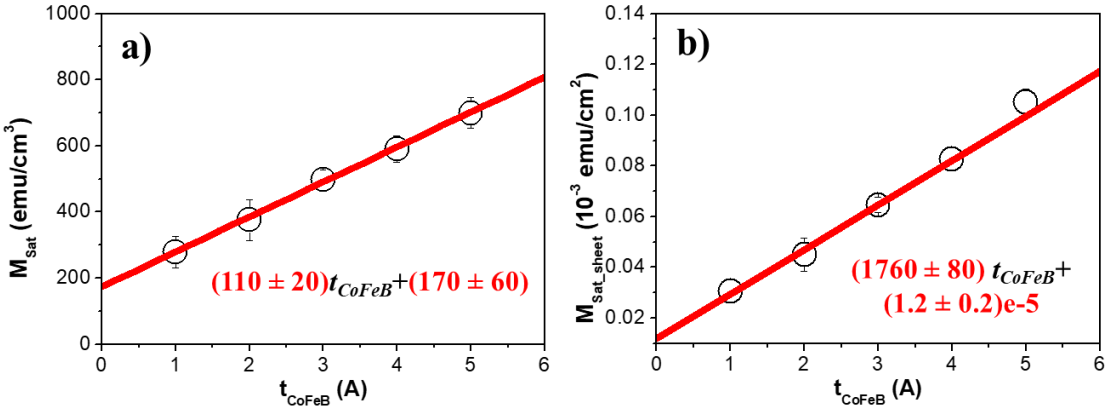

Figure 5.2: (a) Saturation magnetization, M_{Sat} as a function of the CoFeB layer thickness (t_{CoFeB}). (b) M_{Sat_sheet} as a function of the CoFeB layer thickness (t_{CoFeB}). The red continuous lines are linear fits.

This value seems to be too large in comparison with the values previously reported for $Co_{40}Fe_{40}B_{20}$ thin films estimated from the hysteresis loops (1000 [65] or 1034 emu/cm^3 [64], [272]), ferromagnetic resonance measurements (1019 emu/cm^3 [273]) or the linear fit of the magnetization per unit area (M_{eff_sheet}) vs the CoFeB film thickness (1120 [274], 1150 [83] or 1200 emu/cm^3 [84]). Usually, such large M_{sat} values are only reported for CoFeB alloys fabricated with lower B concentration, such as ≈ 1670 and 1830 emu/cm^3 for $(Co_{35}Fe_{65})_{90}B_{10}$ and $(Co_{35}Fe_{65})_{87.5}B_{12.5}$ respectively [275], or in CoFeB multilayers in which the boron atoms diffused out of the CoFeB alloy due to the application of an annealing process (1900 emu/cm^3 for Ta/$Co_{40}Fe_{40}B_{20}$/MgO multilayers) [58]. However, in 2013, Sinha *et al.* [276] studied the perpendicular magnetic anisotropy in Ta/CoFeB (t nm)/MgO multilayers and with CoFeB thickness ranging from 0.8 to 5 nm. In agreement with literature, they reported that the linear fit slope of (M_{sat_sheet} vs t_{CoFeB}) provides an effective CoFeB saturation magnetization of M_{eff_CoFeB} = 1210 emu/cm^3 for thicker samples (t ≥ 2.2 nm). But large M_{eff_CoFeB} values, such as 1790 emu/cm^3, were determined for the thinnest CoFeB layers (t ≤ 2.2 nm). Therefore, it was suggested that the effective saturation magnetization increases from its bulk value below a certain magnetic layer thickness. This behaviour was confirmed in our work as well as by Ngo *et al.* [67] who reported M_{eff_CoFeB} = 1550 emu/cm^3 in CoFeB (t nm) / Pd.

5.3.2. Dynamical Properties

Anisotropy Energy Terms

The origin of the PMA in ultrathin and multilayers stacks, such as (CoFeB/Noble metal) bilayers, is based on the competition between the volumetric (K_{vol}) and surface (K_{sur}) terms of the anisotropy energy [57]. In order to resolve both contributions, we have performed ferromagnetic resonance measurements when the DC external field was perpendicular to the sample plane.

In general, the FMR spectrum of a thin film depends significantly on the presence of different anisotropies, such as the magnetocrystalline, shape, magnetoelastic and surface contributions.

Figure 5.3 (a), (b), (c) and (d) shows the out-of-plane VNA-FMR spectra of the [CoFeB (t Å) / Pd (10 Å)]$_5$ multilayer thin film (t ranging from 2 to 5 Å) with PMA. In all cases, the black lines correspond to the fits using the Kittel formula [134] (Eq. (5.2)) which was discussed in subsection 3.7.1:

$$f_{res} = \frac{\gamma}{2\pi}\left(H + H_{eff}\right) \tag{5.2}$$

However, we should note that we were not able to achieve a good signal to noise ratio from samples with the thinnest CoFeB thicknesses (t_{CoFeB} = 1 - 3 Å). Then, our analysis was complemented by performing TR-MOKE measurements for the samples with t_{CoFeB} ≤ 4 Å. Figure 5.4 (a), (b), (c) and (d) shows the TR-MOKE signals for the samples with a t_{CoFeB} = 1, 2, 3 and 4 Å, respectively, as a function of the external applied magnetic field. An ultrafast demagnetization process on the subpicosecond timescale is observed after the application of the pump pulse, followed by first a quick remagnetization stage and subsequent slower one that shows a precessional response. Both the ferromagnetic resonance frequency (f_{res}) and the damping parameter (α) characterize the oscillatory response of the magnetization and it can be fitted by Eq. (5.3) [249], [250]:

$$\theta = \theta_0 + A \times e^{-t/t_0} + B \times \sin\left(2\pi f_{res}\, t + \varphi\right) \times e^{-t/\tau} \tag{5.3}$$

where θ_0 and A are the background magnitudes and t_0 is the background recovery time. The final term represents the precessional motion where B, f_{res}, φ and τ are the amplitude, frequency, phase, and relaxation time, respectively.

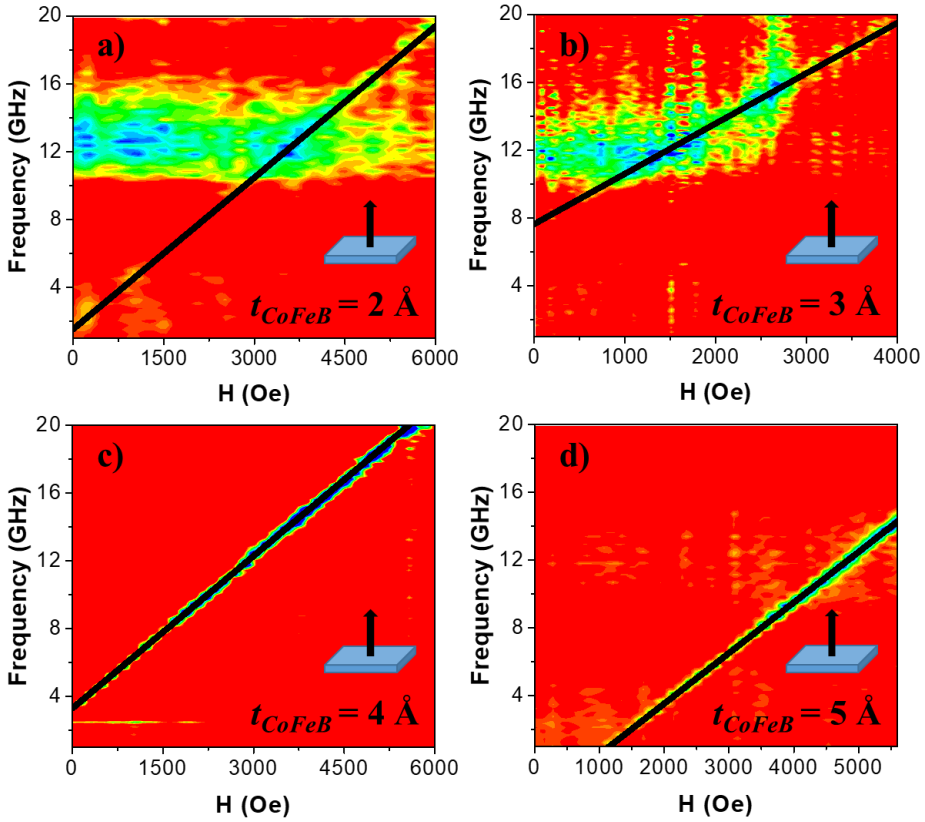

Figure 5.3: (a), (b), (c) and (d) VNA-FMR spectra of the [CoFeB (t Å) / Pd (10 Å)]$_5$ multilayer thin film, with t ranging from 2 to 5 Å, with the external magnetic field applied perpendicularly to the sample plane. The black lines correspond to the fits using the Kittel formula (Eq. (5.2)).

Fits, using Eq. (5.3), are plotted as solid curves in Figure 5.4 revealing a good agreement between the model and the experimental data. Therefore, the resonance frequency (f_{res}) can be determined and its field-dependence is shown in Figure 5.5 (a) for t_{CoFeB} = 1 and 2 Å and Figure 5.5 (b) for t_{CoFeB} = 3 and 4 Å, respectively. The fit of (f_{res} vs. H) can be performed through the set of Eq. (5.4) and (5.5) [78], [134], [249], as addressed in subsection 3.7.1:

$$f_{res} = \frac{\gamma}{2\pi}\sqrt{H_1 \times H_2} \tag{5.4}$$

with $$H_1 = H\cos(\theta_0 - \theta_H) + H_{eff}\cos^2(\theta_0) \tag{5.4 (a)}$$

and $$H_2 = H\cos(\theta_0 - \theta_H) + H_{eff}\cos(2\theta_0) \tag{5.4 (b)}$$

where $(\gamma/2\pi) = (g\mu_B/h)$ is the gyromagnetic ratio, g is the g-factor, μ_B is the Bohr magneton, h is Planck´s constant, H is the external applied DC magnetic field and H_{eff}

is the effective anisotropy field, θ_H is the angle of the external applied magnetic field and θ_0 is the equilibrium angle of the sample magnetization. As described in subsection 3.7.1, the equilibrium angle θ_0 is calculated using:

$$H\sin(\theta_H - \theta_0) = \frac{1}{2}H_{eff}\sin(2\theta_0) \tag{5.5}$$

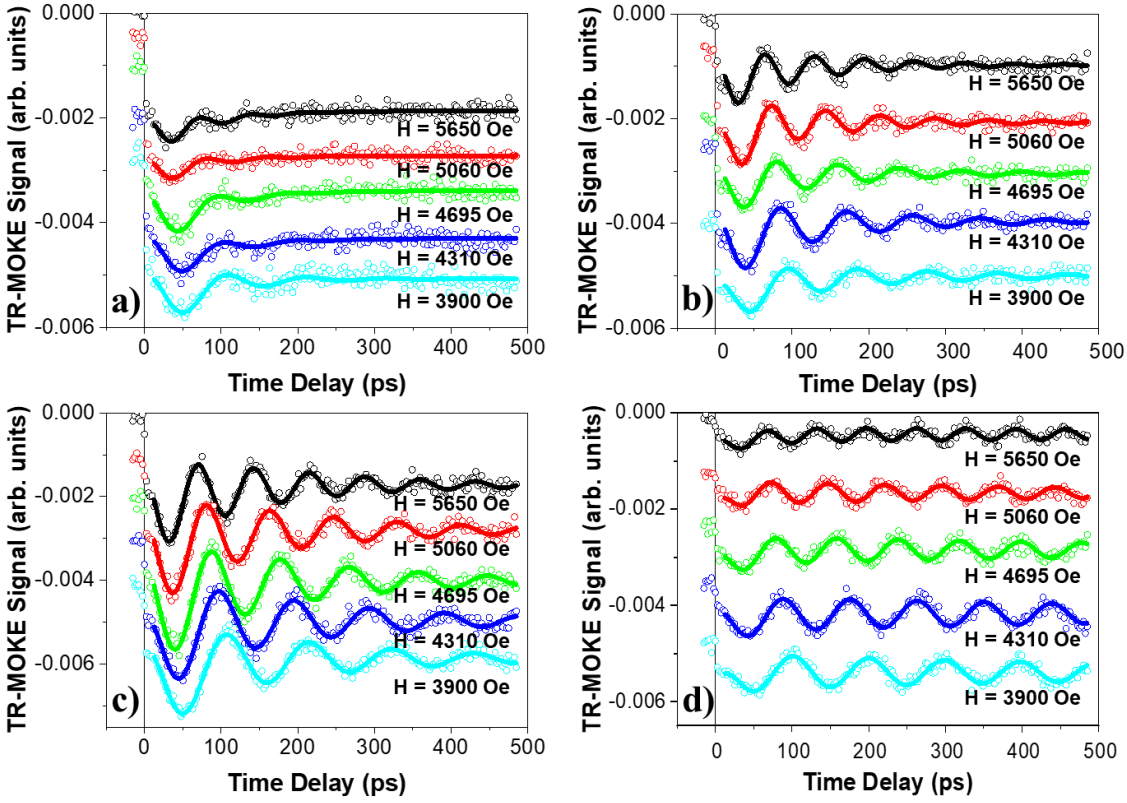

Figure 5.4: (a), (b), (c) and (d) Time-resolved magneto-optical Kerr effect (TRMOKE) signals for the samples with a CoFeB thicknesses of 1, 2, 3 and 4 Å, respectively, under different external applied fields (H = 5650, 5060, 4695, 4310 and 3900 Oe) and when H was applied at 78º. Theoretical curves (solid curves) are fits to the experimental data (open symbols) using Eq. (5.3).

The main results of our VNA-FMR and TR-MOKE fits are summarized in Table 5.1. The gyromagnetic ratio and g-factor did not show any significant dependence with the CoFeB thickness, and we obtained average values of (2.98 ± 0.03) GHz/kOe and (2.14 ± 0.03) for the VNA-FMR results and (2.96 ± 0.10) GHz/kOe and (2.12 ± 0.08) for the TR-MOKE results, respectively, in agreement with the literature [81], [92], [273], [277]. Although the gyromagnetic ratio and g-factor values obtained from the TR-MOKE data present higher errors, we should highlight that these parameters are in agreement with the VNA-FMR data, even taking into account that our fits were performed using only 5 experimental points.

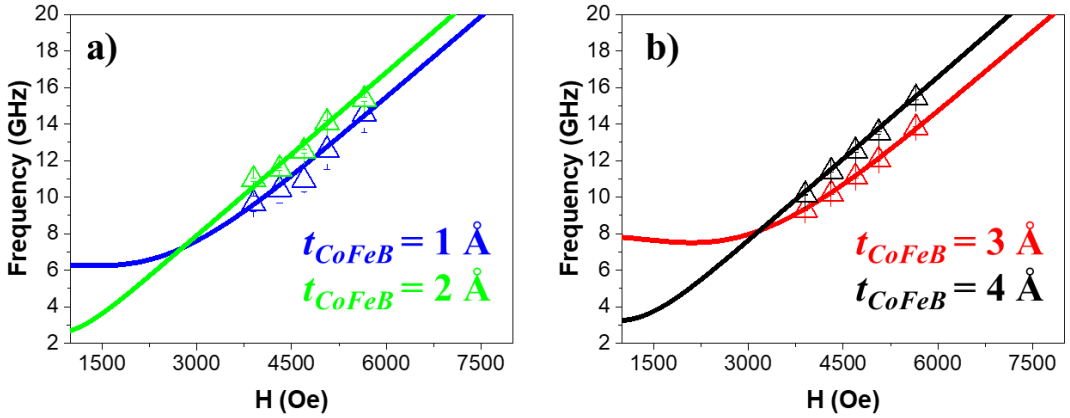

Figure 5.5: (a) and (b) Experimental data of the resonance frequency vs. the external magnetic field of [CoFeB (t Å) / Pd (10 Å)]$_5$ multilayer thin film (Δ). Solid lines are theoretical curves, calculated using Eq. (5.4) and (5.5), when the external magnetic fields were applied at 78º.

t_{CoFeB} (Å)	M_{sat} (emu/cm³)	$\gamma/2\pi$ (GHz/kOe)	g	H_{eff} (Oe)	K_{eff} (10^5 erg/cm³)	$N*t_{CoFeB+Pd}*K_{eff}$ (erg/cm²)	α_{eff}	ΔH_0 (Oe)	α
1	280 ± 50	*2.99 ± 0.19*	*2.14 ± 0.14*	*2005 ± 605*	*2.8 ± 1.3*	*0.15 ± 0.07*	*0.20 ± 0.04*	--	--
2	375 ± 60	*2.939 ± 0.097*	*2.10 ± 0.07*	*805 ± 330*	*1.51 ± 0.86*	*0.09 ± 0.04*	*0.083 ± 0.006*	380 ± 130	0.04 ± 0.02
		2.98 ± 0.04	2.147 ± 0.029	510 ± 50	0.96 ± 0.25	0.057 ± 0.015	0.08 ± 0.03		
3	500 ± 30	*2.91 ± 0.09*	2.08 ± 0.07	*2460 ± 330*	*6.2 ± 1.2*	*0.40 ± 0.08*	*0.075 ± 0.004*	230 ± 375	0.02 ± 0.02
		2.96 ± 0.08	2.12 ± 0.06	2575 ± 150	6.4 ± 0.8	0.42 ± 0.05	0.059 ± 0.02		
4	590 ± 40	*3.004 ± 0.062*	*2.146 ± 0.044*	*1230 ± 190*	*3.6 ± 0.8*	*0.25 ± 0.05*	*0.020 ± 0.004*	103 ± 10	0.009 ± 0.001
		3.001 ± 0.006	2.144 ± 0.006	1095 ± 10	3.2 ± 0.2	0.23 ± 0.02	0.019 ± 0.001		
5	700 ± 50	2.985 ± 0.005	2.133 ± 0.004	-410 ± 30	-1.4 ± 0.3	-0.11 ± 0.02	0.018 ± 0.001	22 ± 7	0.018 ± 0.001

Table 5.1: Summary of the results for [CoFeB/Pd]$_N$ multilayer systems (N = 5 bilayers) as a function of the CoFeB thickness (t_{CoFeB}): the saturation magnetization (M_{sat}) extracted from VSM; the gyromagnetic ratio ($\gamma/2\pi$), the g-factor (g) and the effective anisotropy field (H_{eff}) determined by VNA-FMR (Eq. (5.2)) and TR-MOKE (Eq. (5.3), (5.4) and (5.5)); the effective anisotropy energy (K_{eff}) determined from M_{sat} and H_{eff} using Eq. 5.6; the effective damping (α_{eff}) determined by VNA-FMR (Eq. (5.12)) and TR-MOKE (Eq. (5.13)). The inhomogeneity contribution (ΔH_0) and damping parameter (α) determined by VNA-FMR (Eq. (5.14) and (5.15)). Data extracted from the VNA-FMR measurements is shown in black. Data extracted from the TR-MOKE measurements is written in *italics* and *red*.

On the other hand, and as it was observed in the hysteresis loops, the fitted data of the effective anisotropy field (H_{eff}) shows a transition from positive values for t_{CoFeB} ≤ 4 Å, meaning that the multilayer films show PMA, to negative ones (with in-plane easy magnetization) for t_{CoFeB} = 5 Å (see Figure 5.6 (a)). The sample with PMA and the larger positive H_{eff} values corresponds to the multilayer thin film with t_{CoFeB} = 3 Å. Also, we should note that the H_{eff} value for t_{CoFeB} = 1 Å is larger than for 2 Å. This behaviour in combination with the fact that $Co_{20}Fe_{60}B_{20}$, with a body-centered-cubic (bcc) crystalline structure, has a lattice parameter of 2.86 Å [278] leads us to believe that both the 1 and 2 Å thick CoFeB layers is are not a continuous thin films, so theses samples was were excluded in the subsequent analysis.

From the fitted H_{eff} data, the effective anisotropy energy (K_{eff}) can be estimated, as introduced in section 1.3, according to Eq. (5.6) (see Table 5.1):

$$K_{eff} = \frac{1}{2}\left(H_{eff} \times M_{sat}\right) \tag{5.6}$$

Moreover, K_{eff} can be phenomenologically separated into a volume contribution K_{vol} (erg/cm^3) and a contribution from the interfaces K_{sur} (erg/cm^2), and it can be approximately described by the Néel model [279]:

$$K_{eff} = K_{vol} + (2K_{sur}/t) \tag{5.7}$$

where the origin of the factor of 2 in the last term is due to the presence of two identical interfaces per magnetic layer and t is the magnetic layer thickness. Therefore, both K_{vol} and K_{sur} can be obtained by plotting ($t \times K_{eff}$) versus t. According to the Néel model [279], ($t \times K_{eff}$) should show a linear dependence on t, where K_{vol} is the linear dependence slope and $2K_{sur}$ corresponds to the intercept with the vertical axis. However, our data shows a deviation from the expected linear behavior at small CoFeB thicknesses (see Figure 5.6 (b)). This behaviour was already observed in different systems such as Co/Au [280] and Ni/Cu [281]–[283] multilayer thin films. This deviation was explained using a phenomenological model that includes the shape anisotropy term, the bulk magnetocrystalline and magnetoelastic anisotropy energies, the surface magnetocrystalline and surface magnetoelastic anisotropy terms [282] or the second order term of the magnetoelastic contribution [283].

More recently, this non linearity was also reported for NM/CoFeB/MgO thin films (where NM was Ta [274] or Hf [81]) and it was fitted using the equation proposed by Gowtham *et al.* [274]:

$$K_{eff} \times t = K_{vol}^{eff} \times t + K_{sur}^{eff} + (K_3/t) \tag{5.8}$$

where K_{vol}^{eff} is the effective volumetric contribution that should include the shape anisotropy term and both the bulk magnetocrystalline and bulk magnetoelastic anisotropy energy contributions; K_{sur}^{eff} is the effective surface term that includes the surface magnetocrystalline and magnetoelastic anisotropy terms as well as the second order term of the bulk magnetoelastic contribution; and coefficient K_3 is related with the second order term of the surface magnetoelastic contribution.

In agreement with Engel *et al.* [267], we have estimated that ($t_{CoFeB} \times K_{eff\_CoFeB}$) = (N × $t_{CoFeB+Pd} \times K_{eff}$) where N is the number of bilayers, $t_{CoFeB+Pd}$ (t_{CoFeB}) is the thickness of the CoFeB/Pd bilayer (CoFeB layer), K_{eff} is the measured effective anisotropy energy of the [CoFeB/Pd]$_5$ system and K_{eff_CoFeB} the effective anisotropy energy of a CoFeB thin film. Therefore, both K_{vol_CoFeB} and K_{sur_CoFeB} can be obtained by plotting (t_{CoFeB} x K_{eff_CoFeB}) versus t_{CoFeB} (shown in Figure 5.6 (b)). Using Eq. (5.8) to fit the experimental data, we have estimated that K_{vol_CoFeB} = (-5.4 ± 0.1) x 10^7 erg/cm^3, K_{sur_CoFeB} = (1.71± 0.06) erg/cm^2 and K_3 = (-4.2 ± 0.2) x 10^{-8} erg/cm. Our values are in agreement with the data previously reported in the bibliography literature for Hf/CoFeB/MgO [81] and Ta/CoFeB/MgO [274] thin films.

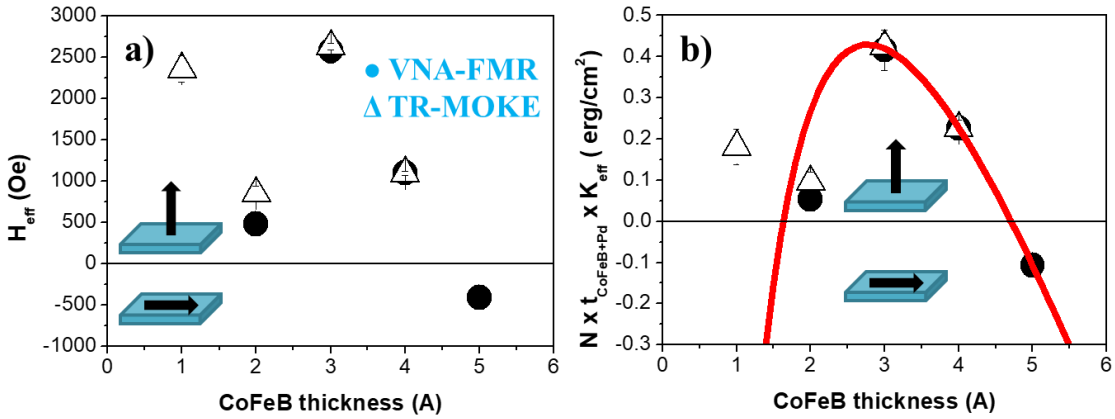

Figure 5.6: (a) H_{eff} and (b) (N x $t_{CoFeB+Pd}$ x K_{eff_CoFeB}) as a function of the CoFeB layer thickness (t_{CoFeB} = 1 – 5 Å) for [CoFeB (t_{CoFeB}) / Pd (10 Å)]$_5$ multilayer thin films. While ● are the experimental data determined from the VNAFMR measurements, Δ were determined from the TR-MOKE studies. The red solid line in (b) is the fitting to the model described by Eq. (5.8).

Assuming that the CoFeB layer is amorphous, the bulk magneto-crystalline anisotropy energy contribution should be null. Therefore, we suggest that the volumetric term could be formed by:

$$K_{vol\_CoFeB} = K_{dem\_CoFeB} + K_{elas\_CoFeB} = (-5.4 \pm 0.1) \times 10^7 \ erg/cm^3 \quad (5.9)$$

where $K_{dem\_CoFeB} = -2\pi M_{eff\_CoFeB}^2$ = (-1.95 ± 0.2) x 10^7 erg/cm^3 is the shape anisotropy term and K_{elas_CoFeB} = (-3.4 ± 0.2) x 10^7 erg/cm^3 (= (-3.4 ± 0.2) x 10^6 J/m^3) is the magneto-elastic anisotropy contribution.

As thin films are generally in a state of biaxial stress ($\sigma_x = \sigma_y = \sigma_{in\_plane}$ and $\sigma_z = \sigma_{out\_of\_plane} = 0$), the magnetoelastic anisotropy term can be defined by [57], [97]:

$$K_{elas\_CoFeB} = \frac{3}{2}\lambda_{sat}\sigma_{in\_plane} \quad (5.10)$$

with λ_{sat} and σ_{in_plane}, the saturation magnetostriction coefficient and the applied stresses, respectively. Moreover, σ_{in_plane} is related with the in plane strain ε_{in_plane}, via the Young's modulus (E) and the Poisson ratio (ν) [98]:

$$\sigma_{in\_plane} = \frac{E\varepsilon_{in\_plane}}{(1-\nu)} \quad (5.11)$$

As the magnetoelastic anisotropy term favors that the effective anisotropy energy lies in the sample plane and the saturation magnetostriction coefficient of amorphous $Fe_{40}Co_{40}B_{20}$ is positive λ_{sat} = 20 x 10^{-6} [284], the magnetic layer should be under tensile stress with σ_{in_plane} ≈ (110 ± 20) x 10^{10} dyne/cm^2 (= (110 ± 20) GPa). Using the Young's modulus E = 160 x 10^{10} dyne/cm^2 (= 160 GPa) for CoFeB and the Poisson ratio ν = 1/3 [285], the analysis indicates a tensile in plane strain of ε_{in_plane} = (0.46 ± 0.08). However, this value is one order of magnitude larger than the strains reported by Gowtham *et al.* [274] in Hf/$Co_{20}Fe_{60}B_{20}$/MgO heterostructures with thicker CoFeB layers. Although, a deeper analysis should be required in order to be able understand such a large in plane tensile strain in our ultrathin films, it should be related with the large lattice mismatch (≈36%) [57] between Pd (3.88 Å) [286] and CoFeB (2.86 Å for bcc) [278] lattice parameters.

Effective Damping

Afterwards, we studied the behaviour of the damping parameter (α) as a function of the CoFeB thin film thickness and extracted it from the frequency linewidths (Δf_{res}) in the VNA-FMR spectra. However, it was experimentally observed that the measured frequency linewidths (Δf_{res}) are broadened by extrinsic contributions which affect the calculations of the damping parameter [104]. Then, we have used the frequency linewidths (Δf_{res}) to determine an apparent damping by using Eq. (5.12) (shown in subsection 3.7.1) [104]:

$$\alpha_{app} = \frac{\Delta f_{res}}{\left(\frac{\gamma}{2\pi}\right)\left(2H + H_{eff}\right)} \tag{5.12}$$

where $(\gamma/2\pi) = (g\mu_B/h)$ is the gyromagnetic ratio, g is the g-factor, μ_B is the Bohr magneton, h is Planck´s constant, H is the external applied DC magnetic field and H_{eff} is the effective anisotropy field.

Although α_{app} and the intrinsic damping may be different, we should note that α_{app} should be an upper limit for the intrinsic or Gilbert damping ($\alpha_{Gilbert}$). Figures 5.7 (a) and (b) show the apparent damping versus the external applied magnetic field for multilayers with t_{CoFeB}= 4 and 5 Å, respectively. Albeit we cannot distinguish between the different extrinsic contributions to the linewidth, it is observed that α_{app} approaches a constant value for large applied fields and we have defined it as the effective damping α_{eff} (red lines in Figures 5.7 (a) and (b)).

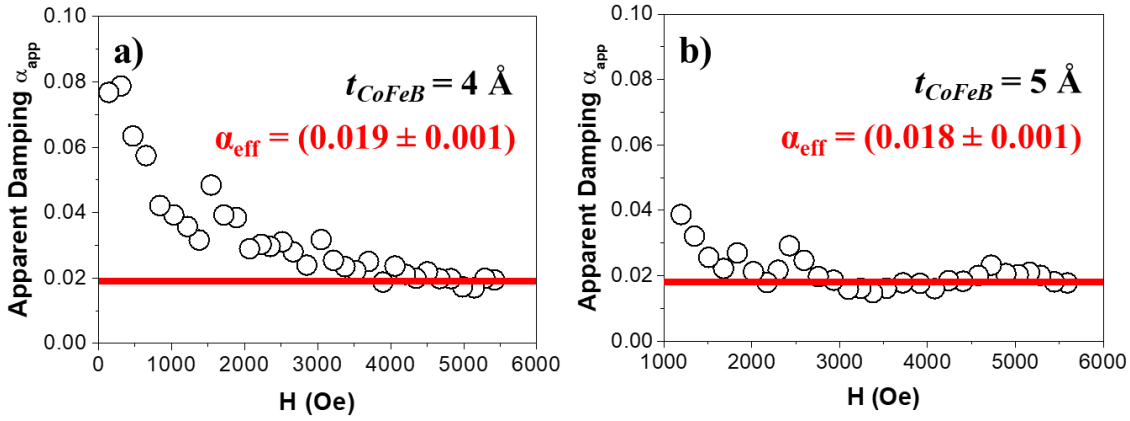

Figure 5.7: Apparent damping α_{app} as a function of the external applied magnetic field for CoFeB layer thickness of t_{CoFeB} = 4 (a) and 5 Å (b). The red solid lines are the average of α_{app} for large applied fields and correspond to the α_{eff} .

Again, we should note that the signal-to-noise ratio is significantly low for those samples with the thinnest CoFeB thicknesses (t_{CoFeB} ≤ 3 Å) so optical studies were required to complete our analysis. From the pump-probe measurements, α_{app} can be determined using Eq. (5.13) (see subsection 3.7.1) [249]:

$$\alpha_{app} = \frac{1}{2\pi \times f_{res} \times \tau} \tag{5.13}$$

where f_{res} is the resonance frequency and τ is the relaxation time. Figures 5.8 (a) and (b) show the apparent damping versus the external applied magnetic field for multilayers with t_{CoFeB} = 2 to 3 Å, respectively. Again, it was observed that α_{app} approaches a constant value for large applied fields and we assumed that this value is α_{eff} .

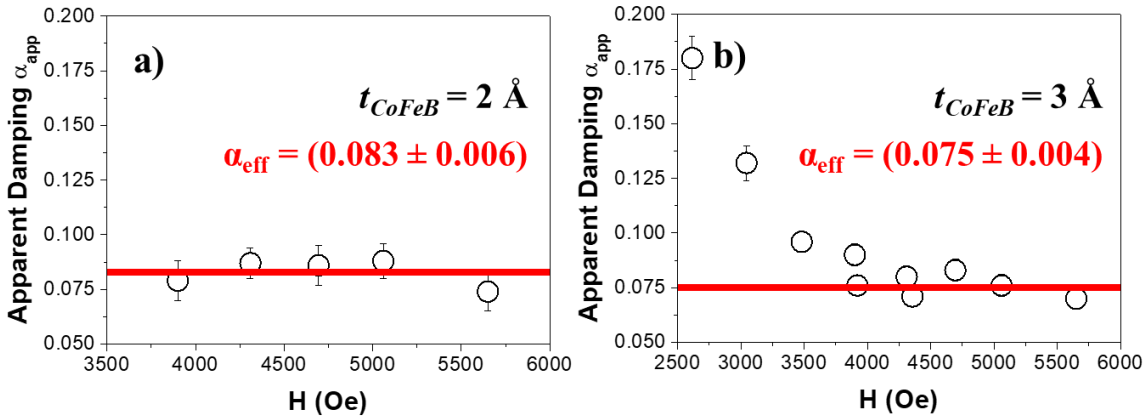

Figure 5.8: Apparent damping α_{app} as a function of the external applied magnetic field for CoFeB layer thickness of t_{CoFeB} = 2 (a) and 3 Å (b, and extracted from the pump-probe measurements. The red solid lines are the average of α_{app} for large applied fields and correspond to the α_{eff} .

The evolution of the effective damping (α_{eff}) vs the CoFeB film thicknesses (t_{CoFeB}) obtained by combining both types of measurements is summarized in Table 5.1 and is shown in Figure 5.9 (a). We should note that both VNA-FMR and pump-probe have provided the same α_{eff} parameters for t_{CoFeB} = 4 Å, and similar values for t_{CoFeB} = 2 and 3 Å. On the other hand, the large α_{eff} = (0.20 ± 0.04) for t_{CoFeB} = 1 Å was not considered in the following analysis because this sample is not a continuous thin film. In agreement with the literature [31], α_{eff} increased (up to 4-times) when the magnetic layer was reduced from 4 (0.020 ± 0.004) to 2 Å (0.083 ± 0.006).

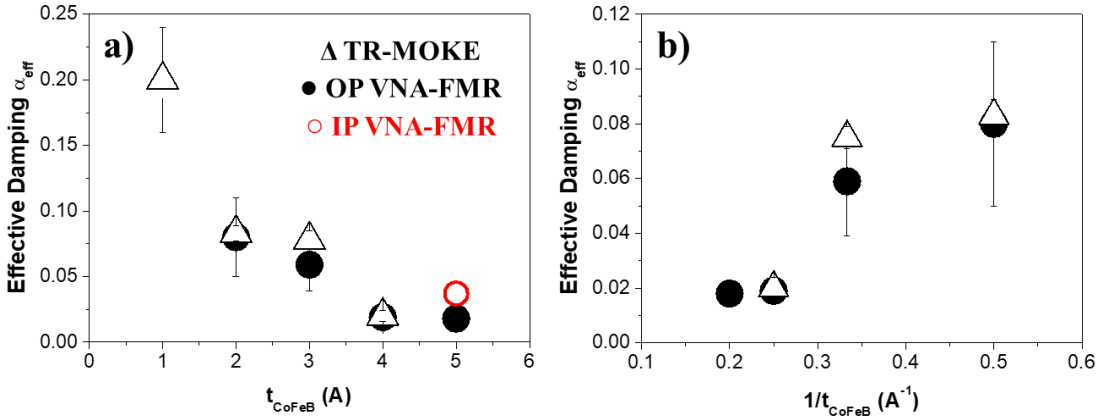

Figure 5.9: (a) Evolution of the effective damping α_{eff} vs t_{CoFeB} (a) and ($1/t_{CoFeB}$) (b) as determined from the TR-MOKE measurements (Δ), the perpendicular VNA-FMR (●) and the in-plane VNA-FMR (○) measurements.

As we introduced in subsection 3.7.1, the damping parameter from FMR measurements is usually determined by another approach which is based on the linear relationship between the field swept linewidth (ΔH) and the resonance frequency (f_{res}) [251].

Figures 5.10 (a) and (b) show the field swept linewidth (ΔH) vs frequency for multilayers with t_{CoFeB} = 4 and 5 Å, respectively, and according to (more details in subsection 3.7.1):

$$\Delta H = (\Delta f_{res})/(\gamma/2\pi). \tag{5.14}$$

The continuous red lines are the fits of the experimental data using Eq (3.16):

$$\Delta H = \Delta H_0 + \frac{4\pi\alpha f_{res}}{\gamma} \tag{5.15}$$

where ΔH_0 corresponds to ΔH at f_{res} = 0 and is a measure of the inhomogeneity term , the damping parameter (α) is the slope of this curve and is formed by the sum of the different contributions to α (described in section 1.5.2).

The value of the damping parameter α, obtained by this second method, is expected to be in agreement with the effective damping value α_{eff} . For the multilayered thin film with t_{CoFeB} = 5 Å, it was determined an α = (0.018 ± 0.001) which is identical to α_{eff} = (0.018 ± 0.001) obtained with the first approach. However, the agreement between α and α_{eff} is not verified for the multilayers with t_{CoFeB} ≤ 4 Å (see Table 5.1). One possible explanation is that for lower thickness samples, our VNA-FMR spectra are too noisy and reliable measurements of the field swept linewidth, and consequently the damping parameter, cannot be performed.

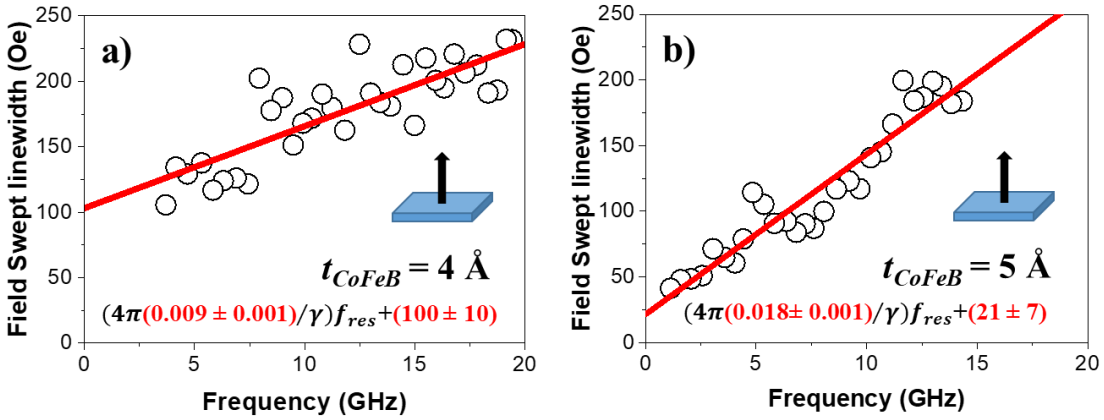

Figure 5.10: Field swept linewidth (ΔH) as a function of the frequency for CoFeB layer thickness of t_{CoFeB} = 4 (a) and 5 Å (b). The red solid lines are the best fits using Eq. (3.16).

Even considering this assumption, we have observed that thicker samples show a smaller inhomogeneity contribution (ΔH_0= (21 ± 7) for t_{CoFeB} = 5 Å). The inhomogeneity contribution increases with the decrease of the t_{CoFeB} (see Table 5.1). This behavior could be related to the fact the thinner films are more sensitive to inhomogeneities such as structural defects, thickness variations, strains, variations of the surface anisotropies, etc [88], [113], [287].

Since results seem to be reasonable only for the thicker sample, this method has not been excluded and it was not considered in the studies presented along this thesis.

Finally, we have focused our attention on distinguish between the different contributions to the damping parameter that we already described in the subsection 1.4.3. Remembering that eddy currents becomes important when the magnetic film thickness is comparable to or greater than the skin depth [104] and the radiative damping is proportional to the magnetic layer thickness [129], neither α_{eddy} nor α_{rad} should have significant contributions in our ultrathin films and they could be ignored. On the other hand, in the literature it has been suggested that the two-magnon scattering contribution is minimized in the perpendicular geometry such as the one used in this work [288]. In particular, Liu *et al.* [115] studied the angular dependence of the two-magnon scattering contribution in a CoFeB thin film and confirmed that this effect is suppressed in the perpendicular configuration. They determined that the two-magnon contribution is significant when the sample magnetization angle, relative to the perpendicular direction or 0º, is pointed out to an angle larger than 45º. Even, α_{TMS} can achieve a value as large as the intrinsic damping in the in-plane configuration. Therefore, the α_{TMS} contribution

could be also disregarded, and the total measured damping should be mainly composed of the intrinsic term and spin-pumping contribution:

$$\alpha_{eff} = \alpha_{Gilbert} + \alpha_{s-p} \tag{5.16}$$

The estimated damping values α_{eff} versus (1 / t_{CoFeB}) are summarized in Figure 5.9 (b). It is observed that α_{eff} is inversely proportional to the CoFeB thickness. This variation can be explained by an interface effect such as the spin pumping contribution (α_{s-p}) [78], [121], [122] and it can be defined by [289]–[291]:

$$\alpha_{s-p} = 2g\mu_B \frac{g^{\uparrow\downarrow}}{4\pi M_{eff\_CoFeB}} \frac{1}{t_{CoFeB}} \left(1 - e^{-2t_{Pd}/\lambda_{Pd}}\right) \tag{5.17}$$

where g is the g-factor; μ_B = (9.27400915 x 10^{-21}) erg/Oe is the Bohr magneton; M_{eff_CoFeB} = (1760 ± 80) emu/cm^3 and t_{CoFeB} are the effective saturation magnetization moment and thickness of the CoFeB layer, respectevily; $g^{\uparrow\downarrow}$ is the CoFeB/Pd interface spin mixing conductance; t_{Pd} = 0.5 nm is half the Pd layer thickness and λ_{Pd} = 9 nm [89] is the spin diffusion length for Pd layer. The factor of 2 is related with the fact that the CoFeB layer is sandwiched by two Pd layers.

Considering the damping value for t_{CoFeB} = 4 Å (α_{eff} = 0.019 ± 0.001) and assuming that $\alpha_{Gilbert}$ = 0.004 [115]–[117], we have estimated α_{s-p} ≈ (0.015 ± 0.001). From Eq. (5.8), the CoFeB/Pd interface spin mixing conductance value should be $g^{\uparrow\downarrow}$ ≈ 3 x 10^{15} cm^{-2}. Although this is a basic estimation and deeper analysis should be required, our calculated $g^{\uparrow\downarrow}$ is of the same order of magnitude than the values already reported in literature, such as 2.21 x 10^{15} cm^{-2} for a CoFeB/Pd interface [292] or (0.722 ± 0.005) x 10^{15} cm^{-2} for a b-Ta/CoFeB interface [265].

Finally, we focus our attention on the two-magnon term (α_{TMS}). As it was already described, α_{TMS} is negligible in the perpendicular geometry but can have an important contribution in the in-plane geometry. Therefore, we have also analyzed the damping parameter of the multilayer with t_{CoFeB} = 5 Å and when it was determined from the in-plane VNA-FMR measurement (see red open symbol in Figure 5.9 (a)). While the perpendicular damping is $\alpha_{eff}{}^{OP}$ = (0.018 ± 0.001), the measured in-plane value is $\alpha_{eff}{}^{IP}$ = (0.037 ± 0.008). Then, and assuming that the difference between both values is due to the two-magnon contribution, we can estimated that α_{TMS} = (0.019 ± 0.005), confirming the important of α_{TMS} in the in-plane configuration and in agreement with literature [115].

5.3.3. Conclusions of the [CoFeB (t Å) / Pd]$_5$ Multilayers Study

In summary, we have studied the magnetic static and dynamical behaviour of [CoFeB/Pd]$_5$ multilayer thin films. Up to now, the thicknesses of the CoFeB films reported in literature have usually ranged between 0.5 nm to few tens of nm. Here, we focused our attention in multilayers where t_{CoFeB} was varied between 1 and 5 Å. First, our analysis determined a negligible magnetic dead layer thickness and an increase of the effective saturation magnetization from its bulk value to M_{eff_CoFeB} = (1760 ± 80) emu/cm^3. PMA was observed in the as-cast samples for CoFeB layer thickness ≤ 4 Å. This behaviour was modeled by considering volumetric and surface anisotropy contributions. Then, we confirmed the presence of a strong surface anisotropy contribution as well as a magnetoelastic anisotropy term. This last term suggests that our ultrathin CoFeB films are under a large in plane tensile strain.

Finally, we studied the damping parameter and we observed that α_{eff} increases when the CoFeB film thickness is reduced from 5 to 2 Å. We obtained an effective damping parameter as low as α_{eff} = (0.019 ± 0.001) for the multilayer with 4 Å CoFeB thickness. Moreover, we posit that α_{eff} is formed by the Gilbert term ($\alpha_{Gilbert}$ = 0.004) plus a spin-pumping contribution α_{s-p} ≈ (0.015 ± 0.001) in the perpendicular configuration, while α_{TMS} = (0.019 ± 0.005) should be also considered in the in-plane configuration.

5.4. Results and Discussion of [CoFeB(3 or 4 Å)/Pd]$_N$ Multilayers Study

In this section, we present the study of the magnetic behaviour of ultrathin [CoFeB/Pd]$_N$ films ranging the number of bilayers N between 3 and 15. According to the previous analysis, we have fixed both t_{CoFeB} (3 or 4 Å) and t_{Pd} = 10 Å in order to can achieve PMA. Then, we have focused our analysis on understanding the evolution of PMA as a function of N. In general, we have observed that PMA improves with N.

In addition, we were also interested on understanding the dependence of the damping parameter (α) with the number of CoFeB/Pd repeats (N). Up today, literature in superlattices with PMA reported some works showing that α is proportional to N [293], inversely proportional to N [45], [294], [295] or even, independent of N [46], [250]. Therefore, the reported relationship between the damping parameter and N in superlattices with PMA is not well stablished yet. Moreover, and as this evolution was not previously reported in CoFeB/Pd superlattices, we have studied (α vs N) by combining

both ferromagnetic resonance (VNA-FMR) and time-resolved magneto-optical Kerr effect (TR-MOKE) measurements. The evolution of α with N shows a complex response and we have suggested that the value of the effective damping could be correlated with the magnetization process: large α for samples with square hysteresis loops and independent of N for samples with bow-tie-shaped hysteresis loops.

5.4.1. Static Properties

Magnetic Moment

While typical out-of-plane and in-plane hysteresis loops of the multilayer stacks with t_{CoFeB} = 3 Å and as a function of the number of (CoFeB/ Pd) bilayers (N = 3, 5, 10 and 15) are plotted in Figures 5.11 (a) and (b), respectively, Figures 5.12 (a) and (b) shows the hysteresis loops for t_{CoFeB} = 4 Å. Although the loops suggest that PMA is well defined for both CoFeB thickness (t_{CoFeB} = 3 and 4 Å) when N ≥ 5, the out-of-plane hysteresis loops exhibit rather different shapes at different N [67], [89], [91], [296].

In general, the out-of-plane reversal processes of ferromagnetic thin films with PMA can be described by the nucleation of reverse domains when the magnetic field reaches the switching field (H_{sw}), followed by an avalanche-like growth until residual unreversed or bubble domains are finally annihilated at the annihilation field (H_a) [296].

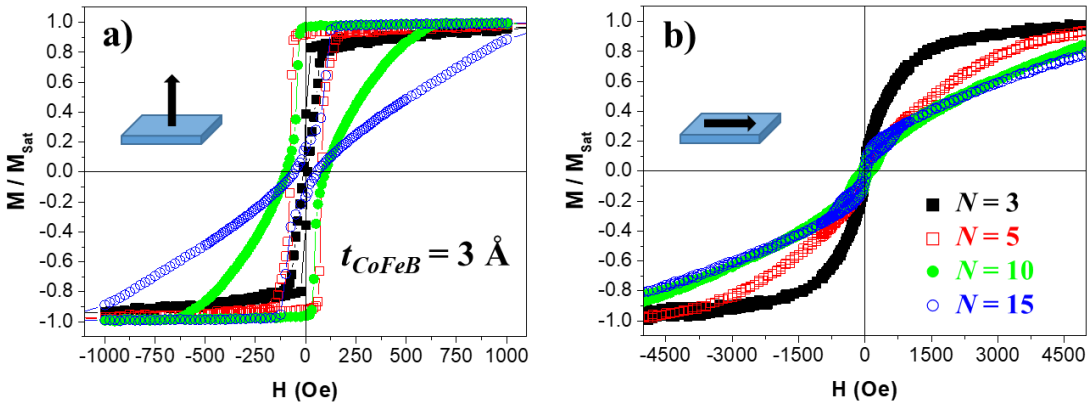

Figure 5.11: Out-of-plane (a) and in-plane (b) hysteresis loops of [CoFeB (3 Å) / Pd (10 Å)]$_N$ multilayer thin films with N = 3 (■), 5 (□), 10 (●) and 15 (○).

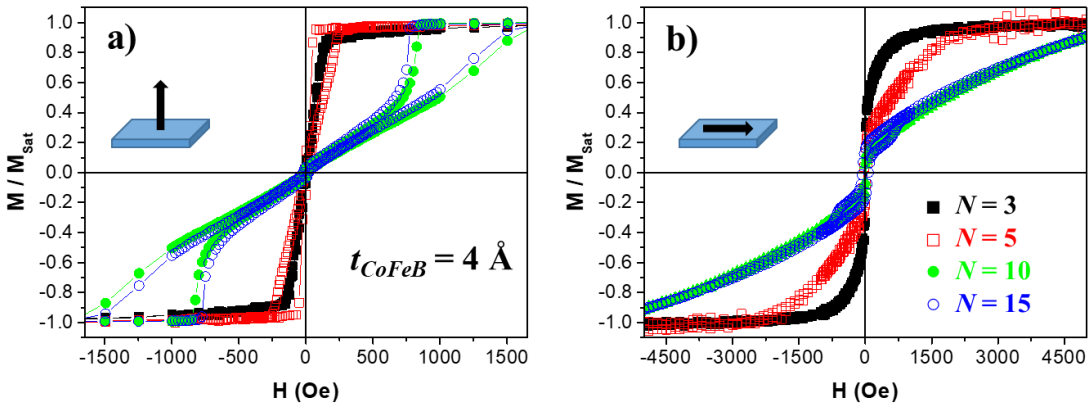

Figure 5.12: Out-of-plane (a) and in-plane (b) hysteresis loops of [CoFeB (4 Å) / Pd (10 Å)]$_N$ multilayer thin films with N = 3 (■), 5 (□), 10 (●) and 15 (○).

In our case, the perpendicular hysteresis loops of the multilayer stacks with t_{CoFeB} = 3 Å (Figure 5.11 (a)) show a gradually increase of the PMA with the number of layers until almost square hysteresis loops, with reduced remanence ratios close to 1 (See Figure 5.13 (b)), were achieved for N = 5 and 10. In these loops with squared shape, the magnetization is fully or almost fully inverted after a sharp reversal transition when the switching field (H_{sw}) was reached. Therefore, this means that a reverse magnetic domain is nucleated and quickly growth to take over the whole or almost the whole sample [296]. On the other hand, thicker layers (N = 15) shows a bow-tie-shaped hysteresis loop with low reduced remanence (See Figure 5.13 (b)), which is also characteristic of magnetic thin films with PMA [297]. The sharp reversal transition at H_{sw} leads only to a partial inversion of the sample magnetization that requires a further change of the external field to complete the reversal process. Regarding its related magnetic domain configuration, this reversal process starts by the nucleation of several domains which expand into stripes at the coercive field (H_c) and covering the whole film by a labyrinth pattern [298]. The slow approach to saturation corresponds to the growth in size of the stripe domains until unreversed isolated domains are annihilated at the annihilation field (H_a). This multidomain configuration is usually generated in order to reduce the sample magnetostatic energy term [52] which increases with the magnetic layers thickness or the number of bilayers [299].

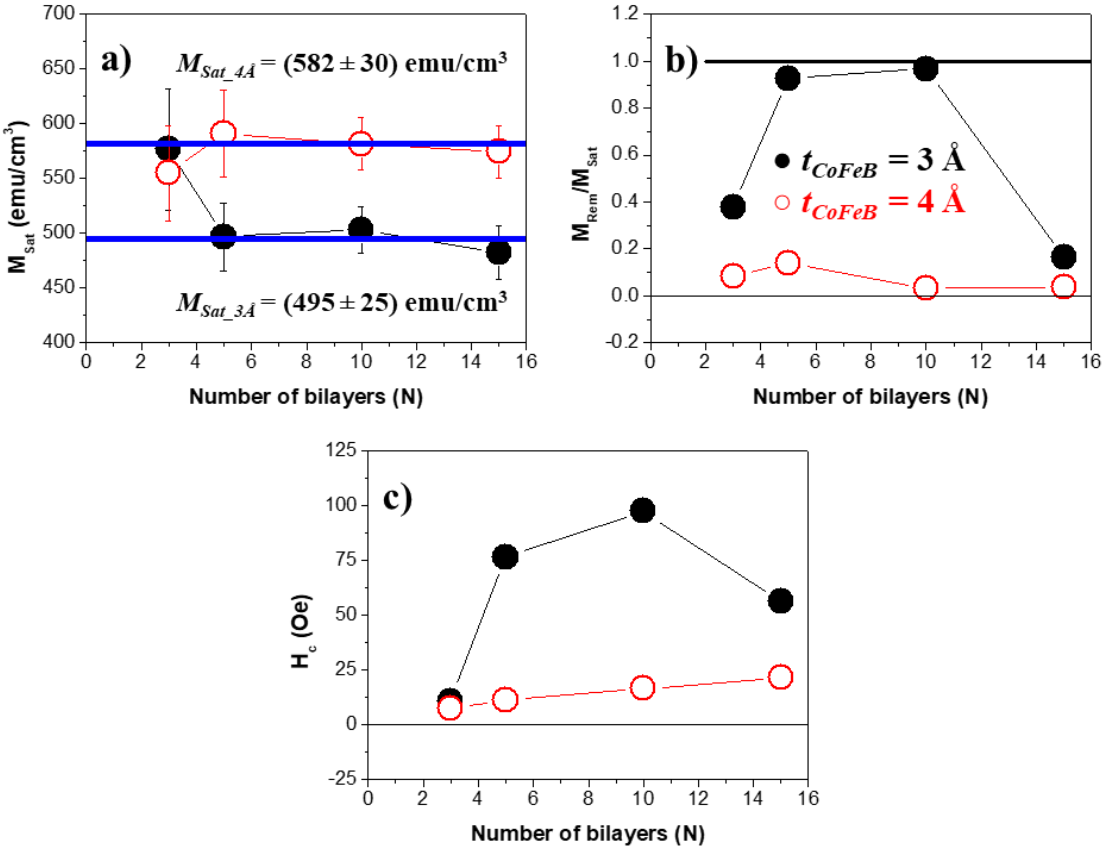

Figure 5.13: Saturation magnetization (a), reduced remanence (b) and coercivity fields (c) of thin films with t_{CoFeB} = 3 Å (●) and t_{CoFeB} = 4 Å (○) as a function of N.

Multilayers with t_{CoFeB} = 4 Å also confirmed a gradually increase of the PMA with the number of layers but no square hysteresis loops were observed (Figure 5.12 (a)). Bow-tie-shaped hysteresis loops with low reduced remanence (Figure 5.12 (b)) were obtained for N ≥ 5 which becomes more evident as N increases.

From the in-plane hysteresis loops (Figures 5.11 (b) and 5.12 (b)), we should note that a small in-plane component was observed for thicker layers (N ≥ 5) for both t_{CoFeB} = 3 and 4 Å, and it is again more evident as N increases.

Saturation magnetization (M_{sat}), reduced remanence (M_{rem}/M_{sat}) and coercivity fields (H_c) of thin films with t_{CoFeB} = 3 and 4 Å were extracted from the out-of-plane hysteresis loops and they are summarized in Figure 5.13 as a function of N.

M_{sat} (Figure 5.13 (a)) increase with N and stays almost constant, M_{sat} = (580 ± 30) emu/cm^3, for N ≥ 5 in multilayers with t_{CoFeB} = 4 Å. While the non-dependence of M_{sat} with N was reported for different systems with PMA such as Co/Ni [45]–[47], Co/Pt [49]–[51], Co/Pd [52] or CoFe/Pt [53] multilayered thin films, the increase of M_{sat} with N was also observed in Co/Ni [295] and (CoFeB/Pd) [67], [91] multilayers. In the latter case, it

was claimed that the M_{sat} rise could be attributed to the existence of a magnetic dead layer with constant thickness [295] or to the surfaces roughness which could enhance the surface/interface magnetization and leading to the increase of the volume magnetic moment [91]. However, we believe that the lower M_{sat} values for N = 3 could be related to the idea that the bottom Pd/CoFeB interface is slightly different than the remaining interfaces as it was suggested in Reference [90]. This fact should be more evident for those samples with the lowest N.

Regarding the multilayers with t_{CoFeB} = 3 Å, M_{sat} = (495 ± 25) emu/cm^3 stays also constant for $N \geq 5$ but a higher value for N = 3 was observed. We must note that until now, and although we could speculate that it could be also related to differences at the bottom Pd/CoFeB interface, we are not able to provide a clear explanation for this value and more and detailed microstructural and magnetic analysis should be required.

As it was already described in subsection 5.3.1, when a material, such Pd, is in contact with a ferromagnet, a spontaneous magnetic polarization in the interfacial region arises and magnetism in Pd is induced [268]–[271]. The induced magnetic moment in Pd can be estimated from Eq. (5.1) [267], M_{eff_CoFeB} = (1760 ± 80) emu/cm^3 is the effective CoFeB saturation magnetization (obtained in the study presented in previous section), t_{CoFeB} is the CoFeB layer thickness (3 or 4 Å), M_{eff_Pd} is the effective magnetization of the polarized Pd and t_{Pd} is the Pd layer thickness (10 Å). Assuming that the magnetic moment is uniformly induced in the entire Pd layer, M_{eff_Pd} = (110 ± 60) emu/cm^3 (in agreement with the value obtain in last section) was determined from Eq. (5.1). This value is also in good agreement with previous studies on Co/Pd [268]–[271] and CoFeB/Pd [67] multilayers (and value obtained in the previous section).

The evolution of the coercivity fields (H_c) of thin films with t_{CoFeB} = 3 and 4 Å as a function of N are plotted in Figure 5.13 (c). While H_c of thin films with t_{CoFeB} = 4 Å increases with N, H_c of thin films with t_{CoFeB} = 3 increases with N for $N \leq 10$ following by the H_c reduction for thicker layers (N = 15). Knepper *et al.* [300] suggested that H_c is proportional to the interlayer coupling between ferromagnetic layers. Then, the H_c rise could be explained by the increase of the interlayer coupling contribution with N. On the other hand, the slight H_c decrease may be related to the degradation of PMA with increasing N [301]. Moreover, Rozatian *et al.* [302] claimed that roughness increases with N and the loss of conformity between layers can appear. This loss of conformity leads to the observed coercivity reduction for large N. Similar dependence was reported for different ferromagnetic heterostructures such as Co/Pt [300], [303], CoFe/Pt [53], Co/Pd [304], [305], Ni/Co [301] and CoFeB/Pd [91] multilayer thin films.

5.4.2. Dynamical Properties

Anisotropy Energy Terms

In order to determine the effective anisotropy fields as well as the effective anisotropy energies and the damping parameters, we have performed VNA-FMR and TR-MOKE measurements.

In the VNA-FMR measurements the DC external field was applied perpendicular to the sample plane. Figures 5.14 (a) and (b) show the N dependence of the experimental resonance frequencies, extracted from the VNA-FMR spectra in perpendicular geometry, for multilayer thin films with t_{CoFeB} = 3 and 4 Å, respectively. Continuous lines on Figures 5.14 (a) and (b) correspond to the fits using the Kittel formula [134] (Eq. (5.2)).

However, we should note again that the signal to noise ratios are pretty low for the thinnest multilayer films (N = 3 and 5) and our analyses were complemented by performing TR-MOKE measurements. Figures 5.15 (a) and 5.16 (a) shows the typical TR-MOKE signals for [CoFeB (t_{CoFeB} Å) / Pd (10 Å)]$_3$, with t_{CoFeB} = 3 and 4 Å, respectively, as a function of the external applied magnetic field. Magnetization shows a sudden drop within the first picosecond after the pump pulse, a fast recovery (remagnetization) within a few picoseconds, followed by a precessional magnetization recovery. These precessional processes can be fitted using a damped-harmonic function superposed with an exponential decay background [249], [250] (Eq (5.3)).

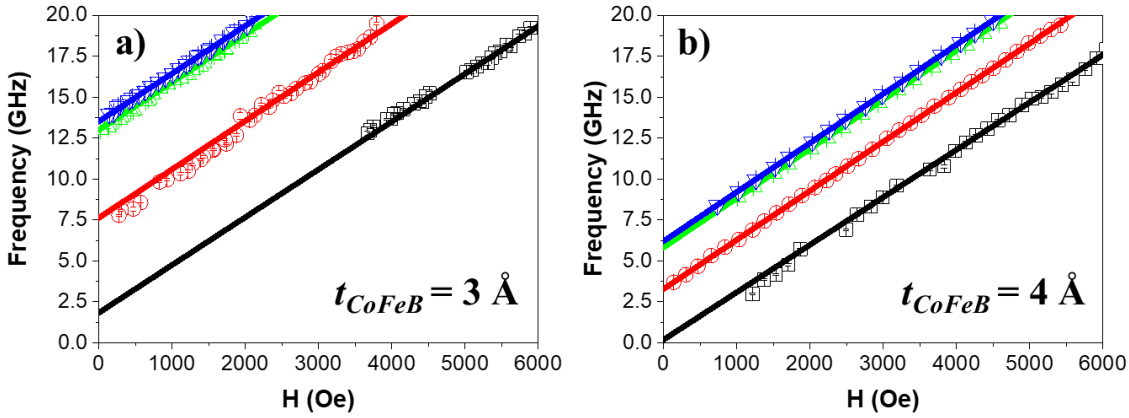

Figure 5.14: Experimental data of the resonance field (open symbols) and fits (continuous lines) using the Kittel formula (Eq. (5.2)) of [CoFeB (t_{CoFeB}) / Pd (10 Å)]$_N$ thin films with t_{CoFeB} = 3 (a) and 4 Å (b) and as a function of N: 3 (□), 5 (○), 10 (Δ) and 15 (∇).

A good agreement between the model, using the Eq. (5.3), and the experimental data was achieved (Figures 5.15 (a) and 5.16 (a)). Next, the evolution of the estimated

resonance frequency (f_{res}) versus H was analyzed through Eq. (5.4) and (5.5) [78], [134], [249]. Figures 5.15 (b) and 5.16 (b) shows the fits of f_{res} vs. H for N = 3 and 5 to t_{CoFeB} = 3 and 4 Å, respectively.

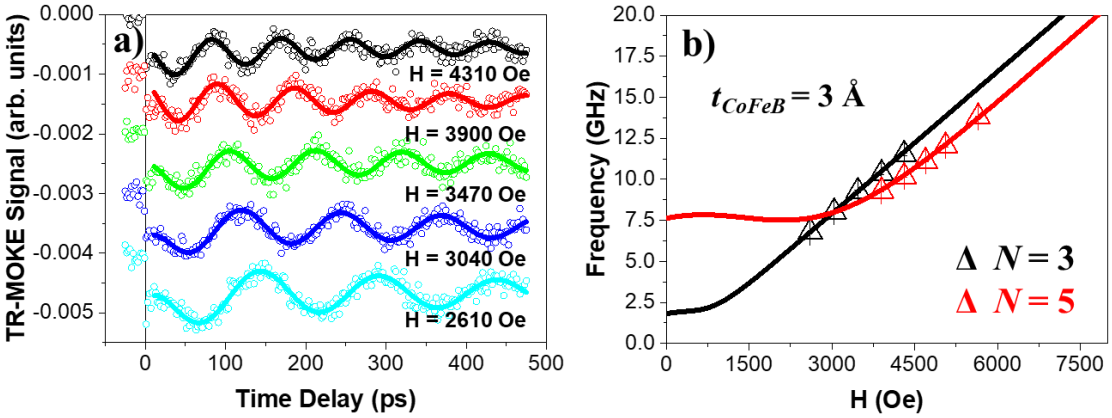

Figure 5.15: (a) Time-resolved magneto-optical Kerr effect (TRMOKE) signals of [CoFeB (3 Å) / Pd (10 Å)]$_3$ multilayer thin film under different external applied fields and when H was applied at 78º. Theoretical curves (solid curves) are fits to the experimental data (open symbols) using Eq. (5.3). (b) Experimental data of the resonance frequency vs. the external magnetic field for the same multilayer thin film (Δ). Solid lines are theoretical curves, calculated using Eq. (5.4) and (5.5) (black line for *N* = 3 and red line for *N* = 5).

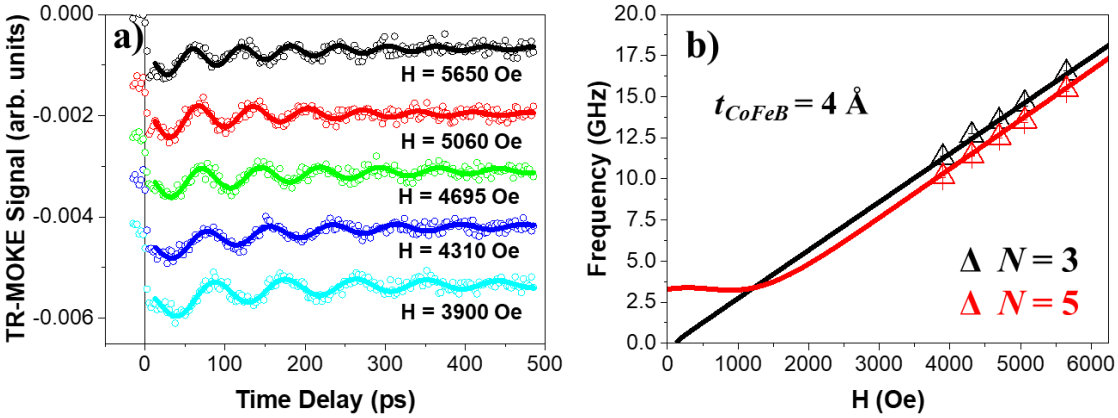

Figure 5.16: (a) Time-resolved magneto-optical Kerr effect (TRMOKE) signals of [CoFeB (4 Å) / Pd (10 Å)]$_3$ multilayer thin film under different external applied fields and when H was applied at 78º. Theoretical curves (solid curves) are fits to the experimental data (open symbols) using Eq. (5.3). (b) Experimental data of the resonance frequency vs. the external magnetic field for the same multilayer thin film (Δ). Solid lines are theoretical curves, calculated using Eq. (5.4) and (5.5) (black line for *N* = 3 and red line for *N* = 5).

The main results of our VNA-FMR and TR-MOKE studies are summarized in Table 5.2. The gyromagnetic ratio and g-factor did not show a significant dependence with N for

t_{CoFeB} = 3 Å. While no dependence was observed either for t_{CoFeB} = 4 Å when $N \geq 5$, smaller values were determined for the thinnest sample (N = 3). In agreement with bibliography [81], [92], [273], [277], we have estimated from the VNA-FMR analysis that the average gyromagnetic ratio and g-factor are (2.93 ± 0.06) GHz/kOe and (2.10 ± 0.05) for t_{CoFeB} = 3 Å, while (2.99 ± 0.04) GHz/kOe and (2.14 ± 0.02) for t_{CoFeB} = 4 Å. The TR-MOKE results are in agreement with these VNA-FMR values.

t_{CoFeB} (3 Å)	M_{sat} (emu/cm^3)	$\gamma/2\pi$ (GHz/kOe)	g	H_{eff} (Oe)	K_{eff} (10^5 erg/cm^3)	α_{eff}
3	580 ± 60	*2.89 ± 0.02*	*2.07 ± 0.01*	*625 ± 40*	*1.8 ± 0.3*	*0.038 ± 0.007*
		2.92 ± 0.07	2.09 ± 0.05	630 ± 150	1.8 ± 0.6	0.055 ± 0.01
5	500 ± 30	*2.91 ± 0.09*	*2.08 ± 0.07*	*2460 ± 330*	*6.2 ± 1.2*	*0.075 ± 0.004*
		2.96 ± 0.08	2.12 ± 0.06	2575 ± 150	6.4 ± 0.8	0.059 ± 0.02
10	505 ± 20	2.93 ± 0.06	2.09 ± 0.04	4440 ± 120	11.21 ± 0.7	0.048 ± 0.01
15	485 ± 25	2.92 ± 0.02	2.09 ± 0.01	4630 ± 40	11.23 ± 0.7	0.043 ± 0.02
t_{CoFeB} (4 Å)						
3	555 ± 45	*2.93 ± 0.07*	*2.09 ± 0.05*	*150 ± 250*	*0.4 ± 0.7*	*0.050 ± 0.008*
		2.90 ± 0.06	2.08 ± 0.04	65 ± 100	0.2 ± 0.3	0.034 ± 0.006
5	590 ± 40	*3.004 ± 0.062*	*2.146 ± 0.044*	*1230 ± 190*	*3.6 ± 0.8*	*0.020 ± 0.004*
		3.001 ± 0.006	2.144 ± 0.006	1095 ± 10	3.2 ± 0.2	0.019 ± 0.001
10	580 ± 25	3.006 ± 0.009	2.148 ± 0.006	1940 ± 15	5.6 ± 0.3	0.020 ± 0.001
15	575 ± 25	2.999 ± 0.006	2.143 ± 0.004	2070 ± 10	5.9 ± 0.3	0.019 ± 0.002

Table 5.2: Summary of the results for [CoFeB(t_{CoFeB} = 3 and 4 Å)/Pd]$_N$ multilayer systems ranging N from 3 to 15 bilayers: the saturation magnetization (M_{sat}) extracted from VSM; the gyromagnetic ratio ($\gamma/2\pi$), the g-factor (g) and the effective anisotropy field (H_{eff}) determined *by* VNA-FMR (Eq. (5.2)) and TR-MOKE (Eq. (5.3), (5.4) and (5.5)); the effective anisotropy energy (K_{eff}) determined from M_{sat} and H_{eff} using Eq. (5.6); the effective damping (α_{eff}) determined *by* VNA-FMR (Eq. (5.12)) and TR-MOKE (Eq. (5.13)). Data extracted from the VNA-FMR measurements is shown in black. Data extracted from the TR-MOKE measurements is written in *italics* and *red*.

On the other hand, the effective anisotropy energy (K_{eff}) can be estimated from the fitted H_{eff} data and the saturation magnetization (M_{Sat}) by using Eq. (5.6). The K_{eff} values are summarized in Table 5.2. Both H_{eff} and K_{eff} are plotted as function of the number of bilayers N in Figures 5.17 (a) and (b), respectively. The evolution of both terms with N behaves in similar fashion to that for coercivity (see Figure 5.13 (c)). First, they increase when N is ranged between 3 and 10, and then reach saturated values for $N \geq 10$. As PMA in this kind of multilayers is mainly supported by the presence of a strong surface anisotropy contribution, the initial rise can be related to the increase in the number of CoFeB/Pd interfaces (N). It means that samples with larger N seem to have a much better PMA stability. However, and as the magnetostatic energy [52] and the sample roughness [302] also increase with N, the reduction of PMA in samples with larger N ≥ 10 has been associated with the rise of both effects. A similar trend has been reported in Co/Pd [302], CoFe/Pt [53], Co/Ni [45]–[47], [301] and CoFeAlSi/Pt [306] multilayer thin films.

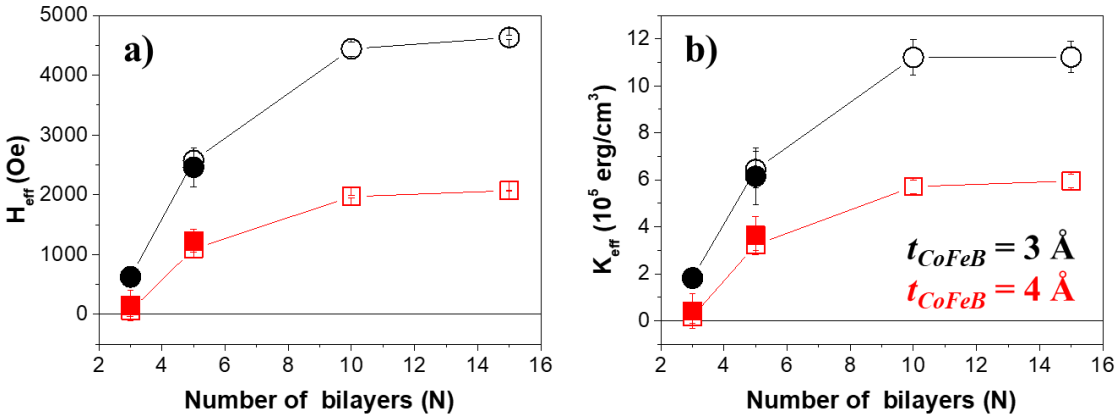

Figure 5.17: (a) H_{eff} and (b) K_{eff} as a function of the number of bilayers (N) for multilayer thin films with t_{CoFeB} = 3 (○) and 4 Å (□). While empty symbols (○ and □) correspond to the data extracted from VNA-FMR, full symbols are data from TR-MOKE measurements (● and ■).

Effective Damping

Finally, we have studied the behaviour of the damping parameter (α) as a function of N. First of all, the apparent damping (α_{app}) was estimated from the frequency linewidths (Δf_{res}) and according to Eq. (5.12) [104].

Empty symbols in Figure 5.18 (a), and (b) shows the typical field dependence behaviour of α_{app} for N = 15 multilayer thin films with t_{CoFeB} = 3 and 4 Å thickness, respectively. α_{app} approaches a constant value for large applied external magnetic fields and this value has been defined as the effective damping α_{eff} (red lines in Figures 5.18).

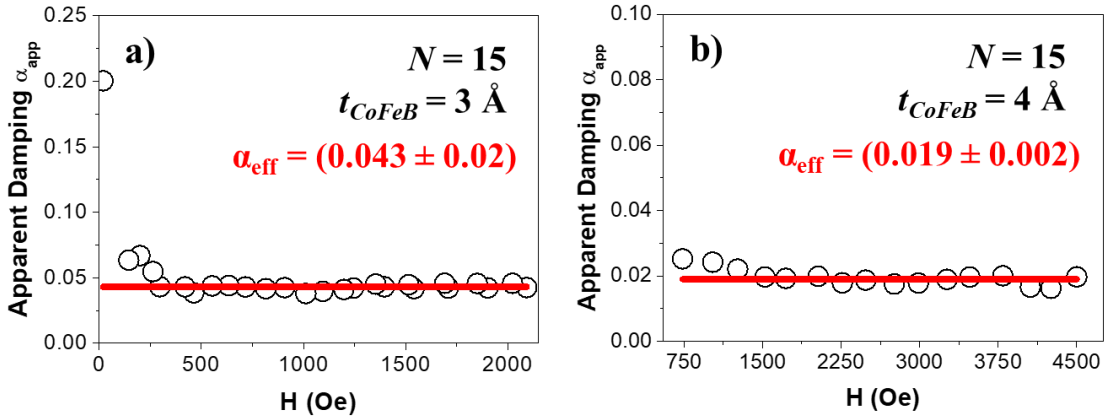

Figure 5.18: Apparent damping α_{app} (o) as a function of the external applied magnetic field for CoFeB layer thickness of t_{CoFeB} = 3 (a) and 4 (b) Å with N = 15, respectively, extracted from the VNA-FMR measurements. The red solid lines are the average of α_{app} for large applied fields and correspond to the α_{eff} .

Our analysis was completed by performing optical studies in the thinnest samples ($N \leq 5$) with t_{CoFeB} = 3 and 4 Å. We should note that optical studies could not be performed in the thickest samples ($N \geq 10$) since the available magnetic applied field in our pump-probe system is not enough to fully saturate these samples. From the TR-MOKE measurements, α_{app} can be also determined using Eq. (5.13) [249].

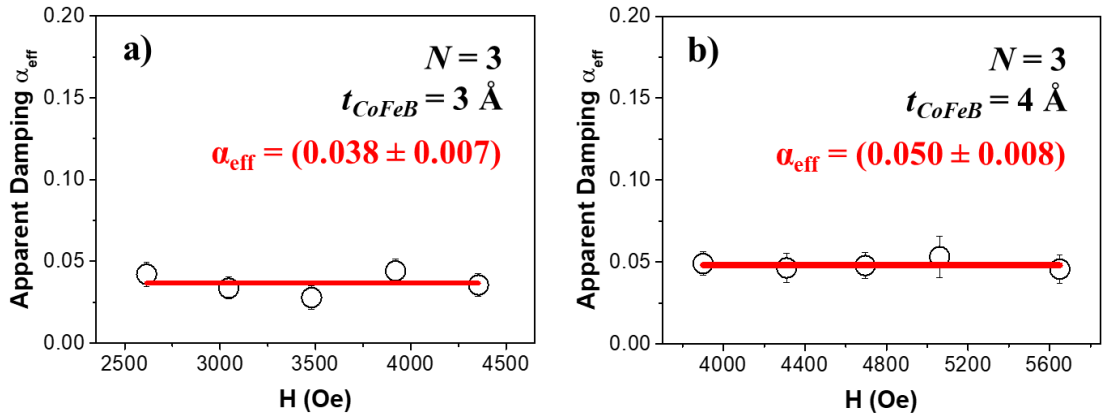

Figure 5.19: Apparent damping α_{app} as a function of the external applied magnetic field for t_{CoFeB} = 3 (a) and 4 Å (b) with N = 3 extracted from the TR-MOKE measurements. The red solid lines are the average of α_{app} for large applied fields and correspond to the α_{eff} .

Open symbols in Figures 5.19 (a) and (b) shows the field dependence behaviour of α_{app} in multilayer thin films with N = 3 and for t_{CoFeB} = 3 and 4 Å, respectively. Again, it was

observed that α_{app} approaches a constant value for large applied fields and we have assumed that this value is α_{eff}.

The evolution of the effective damping (α_{eff}) vs the number of bilayers (N) for both CoFeB film thicknesses (t_{CoFeB} = 3 and 4 Å) is summarized in Table 5.2 and shown in Figure 5.20. From a general point of view and in agreement with bibliography [31], we can claim that α_{eff} increases when the magnetic layer was reduced from t_{CoFeB} = 4 to 3 Å regardless of the number of bilayers (N).

Focusing our attention on the multilayer thin films with well-defined PMA ($N \geq 5$) a complex behaviour can be observed and two different trends have been distinguished. While CoFeB multilayer thin films with t_{CoFeB} = 4 Å shows almost a constant value regardless of N, VNA-FMR and TR-MOKE measurements of the samples with t_{CoFeB} = 3 Å show the larger α_{eff} for N = 5 which is reduced for both N = 10 and 15.

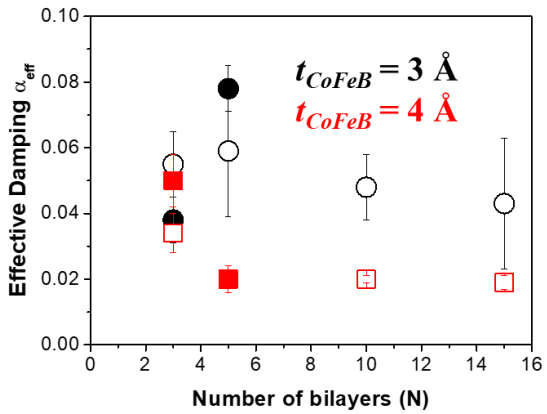

Figure 5.20: Effective Damping (α_{eff}) as a function of N determined from the VNA-FMR (open symbols) and the TR-MOKE measurements (full symbols). Black and red symbols for t_{CoFeB} = 3 and 4 Å, respectively.

According to this behaviour, we have suggested that the value of the effective damping could be correlated with the magnetization process. As it was previously described, the magnetization process of CoFeB/Pd multilayer thin films varies with N from square to bow-tie-shaped hysteresis loops, or from a single to a multidomian configuration. Therefore, we have observed that α_{eff} is larger for samples with square hysteresis loops and it is reduced when N increases and bow-tie-shaped hysteresis loops or multidomian configurations were achieved. Afterwards, α_{eff} reach an almost constant value without any significant dependence with the number of bilayers as soon as N is enough to observe the multidomian configuration. According to this suggestion, the different behaviours, described in the bibliography, of the damping parameter with N could be mainly explained.

For example, Barman *et al.* [293] reported that α_{eff} is proportional to N in [Co/Pt]$_N$ multilayers. In this work, the hysteresis loops showed squared/almost squared shapes for any N and PMA becomes more evident as N increases confirming that these samples were in the first regime with larger damping parameters. On the other hand, Sabino *et al.* [45] and Liu *et al.* [295] studied [Co/Ni]$_N$ multilayers and they observed that α_{eff} was inversely proportional to N. As hysteresis loops in both publications evolved with N from square to bow-tie-shaped hysteresis loops, the reduction of α_{eff} when N was increased could be related to our suggestion when the magnetization process changes from a single to a multidomain configuration.

Finally, we want to notice that the VNA-FMR spectra of the [CoFeB (4 Å) / Pd (10 Å)]$_5$ multilayer thin film with N = 10 and 15, in perpendicular geometry, present a secondary ferromagnetic resonance mode (open symbols in Figure 5.21 (a) and (b)). While the black lines correspond to the fits of the main mode using the Kittel formula (Eq. (5.2)), the open symbols (○) are the ferromagnetic resonances f_{res} related to this secondary mode. The origin for this secondary ferromagnetic resonance mode is not clear yet, and an explanation for what is behind it requires further studies and analysis.

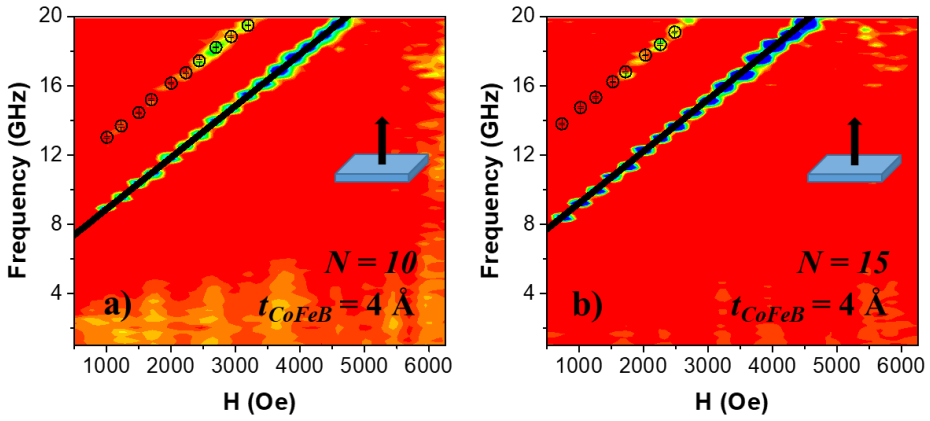

Figure 5.21: (a) and (b) VNA-FMR spectra of the [CoFeB (4 Å) / Pd (10 Å)]$_5$ multilayer thin film with N = 10 and 15, respectively, and the external magnetic field applied perpendicularly to the sample plane. The black lines correspond to the fits using the Kittel formula (Eq. (5.2)). A secondary ferromagnetic resonance mode can be also observed at higher frequencies (○).

5.4.3. Conclusions of the [CoFeB (3 and 4 Å)/Pd]$_N$ multilayers study

In summary, we have studied the magnetic behaviour of ultrathin [CoFeB/Pd]$_N$ multilayer films showing PMA and ranging N between 3 and 15 bilayers. Our analysis determined that the saturation magnetization depends on the ferromagnetic layer thickness but it is

mainly independent of N. Although all samples show PMA ($N \geq 5$) and it is improved by N, the perpendicular hysteresis loops exhibit different shapes at different N: a transition from square to bow-tie-shaped hysteresis loops with the increase of N. Finally, the damping parameter was studied. As it was expected, α_{eff} increases when the CoFeB film thickness is reduced from 4 to 3 Å mainly due to the spin-pumping contribution (as discussed in previous section). Regarding the evolution of α_{eff} with N, it was suggested that square hysteresis loops provides larger α that increase with the PMA stability, while α_{eff} is independent of N for samples with bow-tie-shaped hysteresis loops. Within this general assumption, we have tried to explain the different dependences which were observed in literature such as that α_{eff} is proportional to N [293], inversely proportional to N [45], [294], [295] or independent of N [46], [250].

5.5. Summary

Summing up, along this chapter we have studied the magnetic dynamical behaviour of CoFeB/Pd-based multilayer systems with different configurations.

First, the CoFeB layer thickness (t_{CoFeB}) was ranging between 1 and 5 Å, and the number of bilayers (N) was fixed to 5. The main purpose of this study was to determine the range of t_{CoFeB} where thin films show perpendicular magnetic anisotropy (PMA). We confirmed that the CoFeB/Pd-based multilayers show PMA for $t_{CoFeB} \leq 4$ Å. The multilayer stacks that presented the highest effective anisotropy field (H_{eff}) were $t_{\mathrm{CoFeB}} = 3$ and 4 Å. Then, we studied the PMA as a function of the number of bilayers (N) which was ranged between 3 and 15, for multilayers with $t_{\mathrm{CoFeB}} = 3$ and 4 Å. In this case, all samples of both sets of multilayers presents PMA, which increases for $N \leq 5$ and then reach saturated values for $N \geq 10$.

Regarding the evolution of the damping parameter (α_{eff}) with the t_{CoFeB}, it is observed that increases when t_{CoFeB} is reduced from 5 to 2 Å. Furthermore, we posit different contributions, intrinsic and extrinsic, for α_{eff}. Beside the Gilbert term ($\alpha_{Gilbert}$) plus a spin-pumping contribution ($\alpha_{\mathrm{s-p}}$) in the perpendicular configuration, a two-magnon scattering term (α_{TMS}) should also be considered in the in-plane configuration. Considering the behavior exhibit by α_{eff} with N for multilayers with $t_{\mathrm{CoFeB}} = 3$ and 4 Å, in agreement with literature, α_{eff} increases when the t_{CoFeB} is reduced from 4 to 3 Å. In addition, to explain the dependence of α_{eff} with N we suggest that samples with square hysteresis loops provides larger α_{eff}, that increase with the PMA stability, while damping is independent of N in films with bow-tie-shaped hysteresis loops.

Chapter 6

Magnetization Dynamics of [CoFeB/Pd]/Co-based Exchange Spring Structures

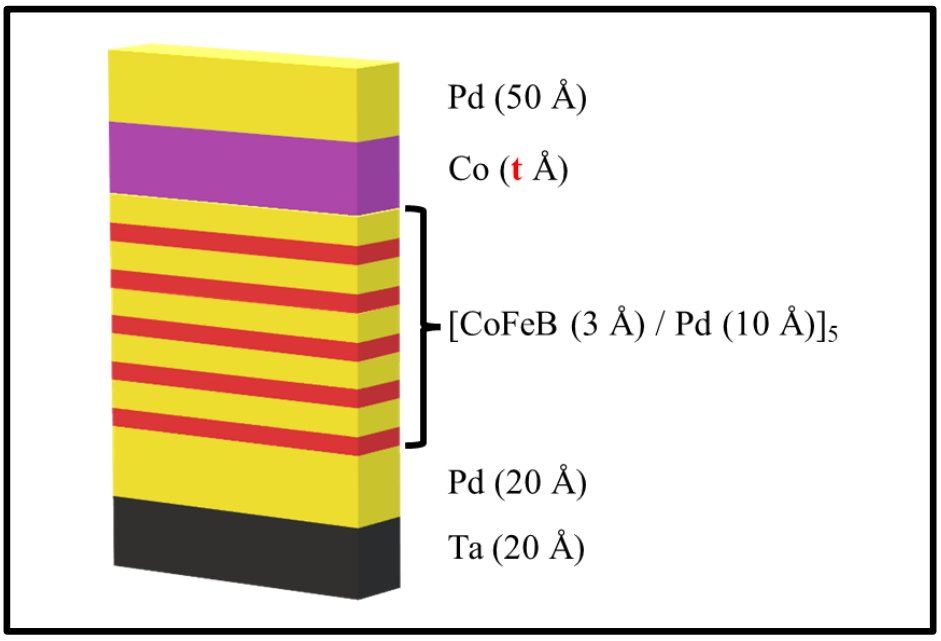

Chapter 6

Magnetization Dynamics of [CoFeB/Pd]/Co-based Exchange Spring Structures

6.1. Introduction

In the sequence of the studies presented in previous chapter, the CoFeB/Pd-based multilayer system with PMA was magnetically coupled to a Co layer with in-plane magnetic anisotropy. As in standard perpendicular exchange spring magnets, this system consisting of a hard (CoFeB/Pd multilayered stack) exchange-coupled with a soft phase (Co/Pd bilayer), and with perpendicular and in-plane effective anisotropy energy, respectively.

Ferromagnetic thin films with perpendicular magnetic anisotropy (PMA) have been widely studied for recording media applications [19], [307]. These systems can be designed with high thermal stability to avoid superparamagnetic behavior [308] and with good writability [19], but this may raise the switching field above that which can be produced by currently available write heads. In order to overcome this limitation, other alternatives, such as perpendicular exchange coupled composite or exchange spring media, have been explored [309]–[313]. While the magnetically hard film provides thermal stability, the soft layer reduces the reversal field. When an external magnetic field is applied, the soft layer reverses, first which creates an additional effective field applied to the hard phase through exchange coupling, lowering the switching field of the whole system [314].

Over the last years, exchange-spring systems have been widely studied, and the coupling of the hard multilayer with a soft layer allows broad control of the magnetic properties of the composite film by varying the layer thickness, layer composition, number of repeats, interfacial anisotropy, and exchange coupling strength. Numerous studies have been devoted to investigating the static and dynamic magnetic properties of these systems with mixed anisotropies where the exchange coupling can be used to tailor their properties ([Co/Pd]-NiFe [247], [315]–[317], [Co/Pd]-Co-Pd-NiFe [318], [Co/Ni]-NiFe [319], $[Co/Pd]_8$-NiFe [320], [Co/Pd]/Co [321], [Co/Pd]/CoFeB [321]–[323], and CoCrPt-Ni [314]).

The damping parameter of the materials is also relevant to spintronic applications [315], and plays a key role in optimizing writing speeds and controlling power consumption [247].

In this chapter, we present the study the magnetic response of $[CoFeB(t_{CoFeB})/Pd]_3/Co(t_{Co})$ exchange-spring structure, ranging the Co film thickness

(t_{Co}) between 0 and 25 Å and keeping constant both the CoFeB (t_{CoFeB} = 3 Å) and Pd (t_{Pd} = 10 Å) thicknesses, as well as the number of (CoFeB/Pd) bilayers (N = 5). We used two complementary and independent techniques: Time-Resolved Magneto-Optical Kerr Effect (TR-MOKE) measurements with Vector Network Analyzer Ferromagnetic Resonance (VNA-FMR) analysis.

Although the used experimental methods were presented in Chapter 3, they are also briefly introduced in section 6.2. Regarding the sample preparation, the process was addressed in section 3.2.

In section 6.3, we start with the static properties of [CoFeB(t_{CoFeB})/Pd]$_3$/Co(t_{Co}), followed by the dynamical properties, focusing our attention on understanding its dependence of the magnetic moment, the anisotropy terms as well as the effective damping on the Co film thickness (t_{Co}).

The main aim is based on understanding the effect of Co film thickness (t_{Co}) on the effective perpendicular magnetic anisotropy, we have defined the t_{Co} values which are required to the exchange spring change from perpendicular magnetic anisotropy to in-plane anisotropy.

6.2. Experimental Methods

Room temperature magnetic hysteresis loops were measured in a vibrating sample magnetometer (VSM), and the dynamical behaviour was studied by comparing time-resolved magneto-optical Kerr effect (TR-MOKE) measurements with ferromagnetic resonance analysis (VNA-FMR). VNA-FMR measurements were carried out at room temperature using a coplanar waveguide (CPW) connected to a vector network analyzer and over a frequency range up to 20 GHz. The external DC magnetic field (H) was applied along (θ_H = 90º) or perpendicular (θ_H = 0º) to the sample plane for in-plane and perpendicular measurements. On the other hand, the dynamical response of the magneto-optical signals was obtained by an ultrafast pump-probe system in polar MOKE configuration. The pump fluence used was ~ 1 mJ/cm^2. In order to increase the signal-to-noise ratio of the TR-MOKE signal amplitude, the external DC magnetic field was applied at an angle of θ_H = 78°, with 0º and 90º corresponding to the out-of-plane and in-plane measurements, respectively [257]. All optical measurements were performed under ambient conditions (more details are described in Section 5.2).

6.3. Results and Discussion

6.3.1. Static Properties

Magnetic Moment

The out-of-plane and in-plane hysteresis loops of the [CoFeB (3 Å) / Pd (10 Å)]$_5$ / Co (t_{Co}) exchange spring structures, with t_{Co} ranging from 0 to 25 Å, are shown in Figure 6.1 (a) and (b), respectively. The loops confirm the reorientation of the effective magnetization from the out-of-plane to the in-plane configuration with increasing the Co thickness. Therefore, the hysteresis loops indicate that our samples show PMA when t_{Co} ≤ 11 Å, as well as an increase of the in-plane anisotropy component with the increase of t_{Co}. In particular, the loops suggest that the easy magnetization axis lays in-plane for t_{Co} ≥ 13 Å. Reduced remanence (M_{rem}/M_{sat}) and coercivity fields (H_c) of the exchange spring system were also extracted from the out-of-plane (●) and in-plane (○) hysteresis loops and they are summarized in Figure 6.2 as a function of the Co layer thickness t_{Co}.

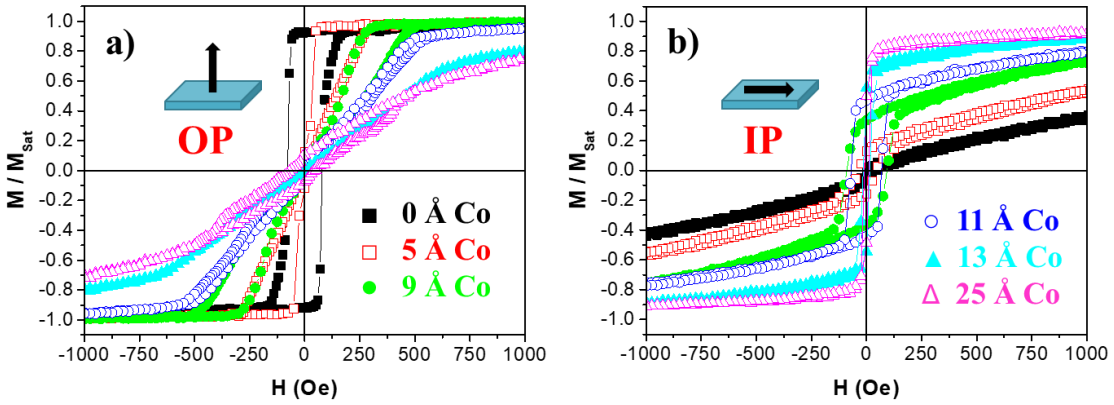

Figure 6.1: Out-of-plane (a) and in-plane (b) hysteresis loops of [CoFeB (3 Å) / Pd (10 Å)]$_5$ / Co (t_{Co}) exchange springs with t_{Co} = 0 (■), 5 (□), 9 (●), 11 (○), 13 (▲) and 25 Å (Δ).

The perpendicular hysteresis loops of the [CoFeB (3 Å) / Pd (10 Å)]$_5$ / Co (t_{Co}) (Figure 6.1 (a)) show different shapes at different t_{Co} and confirming a decrease of the PMA with the increase of the Co layer thickness.

In the absence of the Co layer ($t_{Co} = 0$ Å), the perpendicular hysteresis loop exhibits a squared shape loop with a reduced remanence (M_{rem}/M_{sat}) close to 1 (see Figure 6.2 (a)). On the other hand, the M_{rem}/M_{sat}value, obtained from the in-plane hysteresis loop (Figure 6.2 (a)), is almost zero, confirming a clear PMA. As it was described in section

5.4.1, the magnetization, in samples with a squared shape loops, is fully or almost fully inverted after a sharp reversal transition when the switching field (H_{sw}) was reached. Therefore, this means that a reverse magnetic domain is nucleated and quickly growth to take over the whole or almost the whole sample [296].

On the other hand, the out-of-plane hysteresis loops of thicker layers ($5\ Å \leq t_{Co} \leq 11\ Å$) show a bow-tie-shape (Figure 6.1 (a)) with low reduced remanence (See Figure 6.2 (a)), which is also characteristic of magnetic thin films with PMA [297]. This kind of loops has been related to a reversal process that starts by the nucleation of several domains which expand into stripes at the coercive field (H_c) and covering the whole film by a labyrinth pattern [298]. From the in-plane hysteresis loops (Figures 6.1 (b)), the observed increase of the M_{rem}/M_{sat} values (Figure 6.2 (a)) and coercivity fields (Figure 6.2 (b)) could suggest a small in-plane component of the magnetization that it is present for thicker layers ($5\ Å \leq t_{Co} \leq 11\ Å$). Moreover, this in-plane magnetization component is more evident for the thicker Co layers.

Finally, the magnetic behaviour of the exchange spring systems is controlled by the soft magnetic phase, or the Co sub-system, and the hysteresis loops (Figure 6.1) confirm an in-plane effective anisotropy energy for those samples with the thickest Co layers ($t_{Co} \geq 13\ Å$).

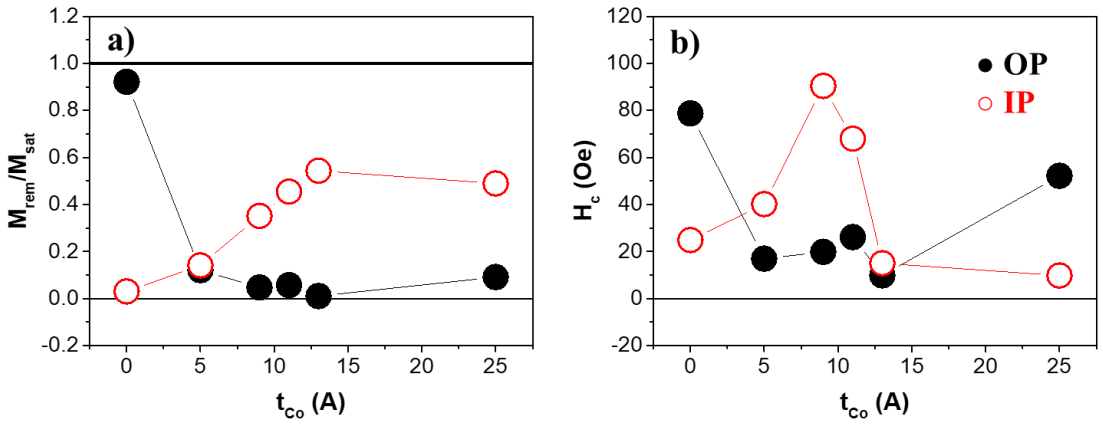

Figure 6.2: Reduced remanence (a) and coercivity fields (b) of the out-of-plane (●) and the in-plane (○) hysteresis loops as function of the Co layer thickness (t_{Co}).

From the hysteresis loops, the effective saturation magnetization (M_{sat_total}) values were also extracted and they are summarized in Figure 6.3. Assuming that the effective magnetic moment of our exchange spring magnets can be determined by using the following equation [267]

$$M_{sat\_total} = \frac{\left(M^{eff}_{sat\_CoFeB/Pd} \times t^{eff}_{CoFeB/Pd}\right) + \left(M^{eff}_{sat\_Co/Pd} \times t^{eff}_{Co/Pd}\right)}{\left(t^{eff}_{CoFeB/Pd} + t^{eff}_{CoFeB/Pd}\right)}$$

with $$t^{eff}_{CoFeB/Pd} = (t_{CoFeB} + t_{Pd}) \times N \quad (6.1\ (a))$$

$$t^{eff}_{Co/Pd} = (t_{Co} + t_{Pd}) \quad (6.1\ (b))$$

and where $M^{eff}_{sat\_CoFeB/Pd} = (500 \pm 30)\ emu/cm^3$ (obtained from the analysis described in Chapter 5) and $M^{eff}_{sat\_Co/Pd}$ are the effective saturation magnetization values of the (CoFeB/Pd) and (Co/Pd) subsystems, respectively. While $t^{eff}_{CoFeB/Pd}$ and $t^{eff}_{Co/Pd}$ are the effective thicknesses of the hard (CoFeB/Pd) and soft (Co/Pd) magnetic parts of the system, t_{CoFeB}, t_{Pd} and t_{Co} are the CoFeB, Pd and Co layer thickness, respectively. Therefore, the observed increase of the M_{sat_total} with the Co film thickness (Figure 6.3) suggests that $M^{eff}_{sat\_CoFeB/Pd} < M^{eff}_{sat\_Co/Pd}$. This suggestion will be confirm in the following section (see section 6.3.2) where the $M^{eff}_{sat_Co/Pd}$value will be calculated from the study of the dynamical responses.

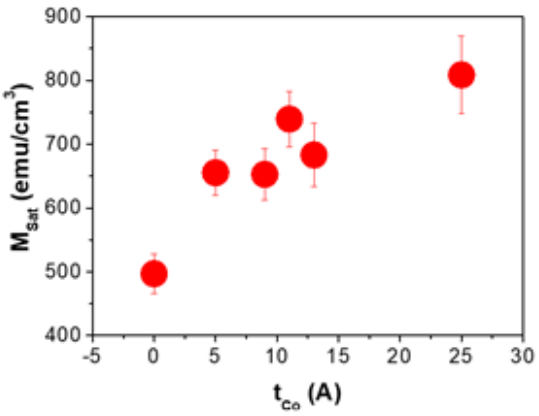

Figure 6.3: (a) Saturation magnetization, M_{sat} as a function of the Co layer thickness (t_{Co}).

6.3.2. Dynamical Properties

Anisotropy Energy Terms

Figure 6.4 (a)-(e) shows the in-plane VNA-FMR spectra of the [CoFeB (3 Å) / Pd (10 Å)]$_5$ / Co (t_{Co} Å) system with t_{Co} ranging from 5 to 25 Å, respectively. In all cases, the black

dashed lines correspond to the fits using the Kittel formula [134] (more details were addressed in subsection 3.7.1):

$$f_{res} = \frac{\gamma}{2\pi}\sqrt{H \times \left(H - H_{eff}\right)} \tag{6.2}$$

where $(\gamma/2\pi) = (g\mu_B/h)$ is the gyromagnetic ratio, g is the g-factor, μ_B is the Bohr magneton, h is Planck´s constant, H is the external applied DC magnetic field and H_{eff} is the effective anisotropy field.

Our analyses were complemented by performing TR-MOKE measurements. Figure 6.5 shows the typical TR-MOKE signals for our exchange spring system ranging t_{Co} from 0 to 25 Å, and as a function of the external applied magnetic field. Magnetization shows the typical behaviour with a sudden drop within the first picosecond after the pump pulse, followed by first a quick remagnetization stage and subsequent slower one precessional magnetization recovery. Both the ferromagnetic resonance frequency (f_{res}) and the damping parameter (α) characterize the oscillatory response of the magnetization and can be fitted by [249], [250]:

$$\theta = \theta_0 + A \times e^{-t/t_0} + B \times \sin\left(2\pi f_{res}\, t + \varphi\right) \times e^{-t/\tau} \tag{6.3}$$

In Figures 6.5, the fits using Eq. (6.3) are plotted as solid lines and exhibit a good agreement between the model and the experimental data. Therefore, the resonance frequencies (f_{res}) have been determined and they have been plotted in Figures 6.4 (see circular open symbols). As it was discussed in subsection 3.7.1, the behaviour of (f_{res} vs. H) can be fitted by using the set of Eq. (6.4) and (6.5) [78], [134], [249]:

$$f_{res} = \frac{\gamma}{2\pi}\sqrt{H_1 \times H_2} \tag{6.4}$$

with $$H_1 = H\cos(\theta_0 - \theta_H) + H_{eff}\cos^2(\theta_0) \tag{6.4 (a)}$$

and $$H_2 = H\cos(\theta_0 - \theta_H) + H_{eff}\cos(2\theta_0) \tag{6.4 (b)}$$

where $(\gamma/2\pi) = (g\mu_B/h)$ is the gyromagnetic ratio, g is the g-factor, μ_B is the Bohr magneton, h is Planck´s constant, H is the external applied DC magnetic field and H_{eff} is the effective anisotropy field, θ_H is the angle of the external applied magnetic field and θ_0 is the equilibrium angle of the sample magnetization.

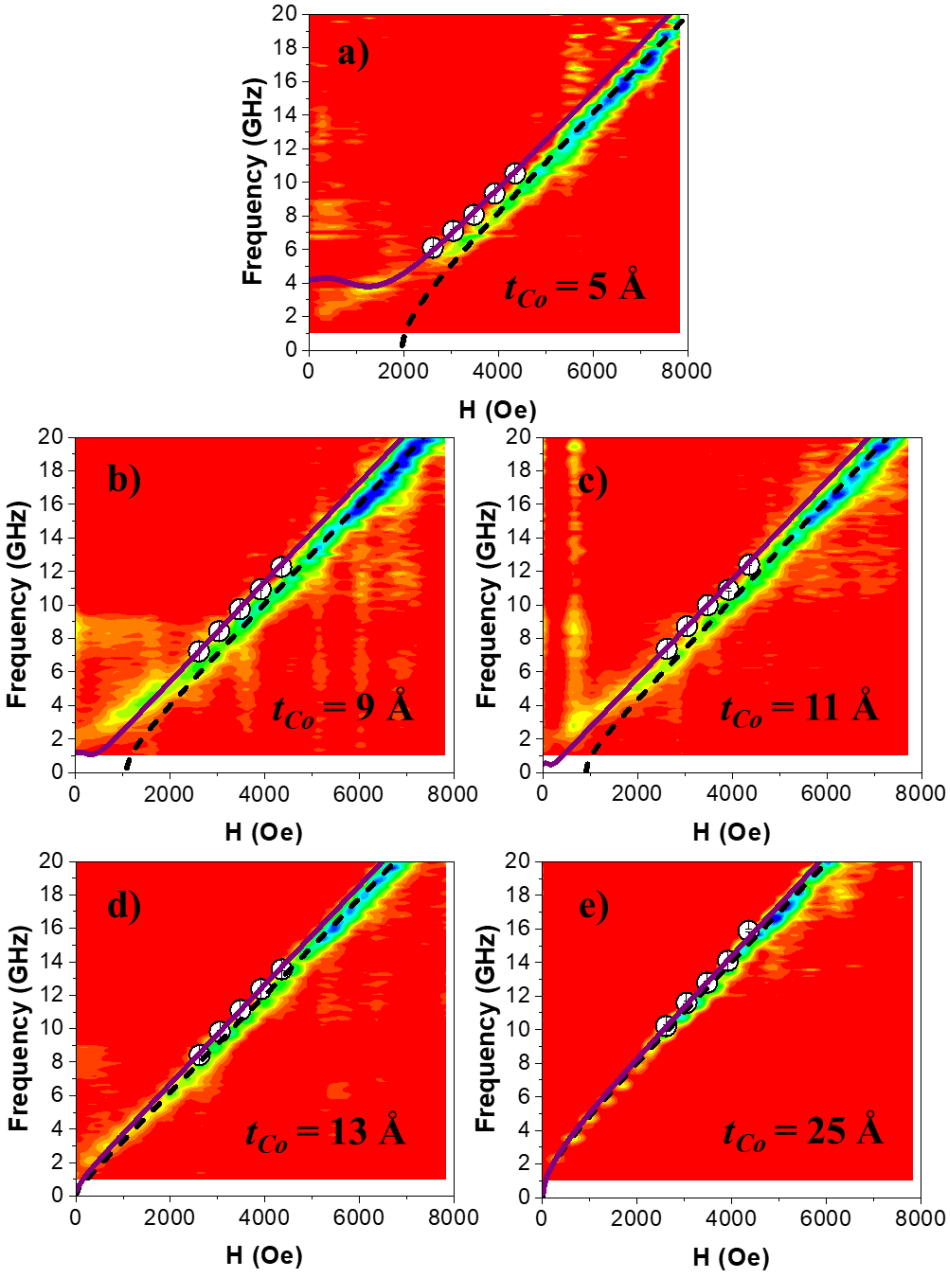

Figure 6.4: (a), (b), (c), (d) and (e) VNA-FMR spectra of the [CoFeB (3 Å) / Pd (10 Å)]$_5$ /Co (t_{Co}) multilayer thin film, with t_{Co} ranging from 5 to 25 Å, with the external magnetic field applied perpendicularly to the sample plane. The black dashed lines correspond to the fits using the Kittel formula (Eq. (6.2)). The open symbols represent the f_{res} obtain from the fit of TR-MOKE curves (see Figures 6.5) using Eq. (6.3). The purple solid lines correspond to fits using de Eq. (6.4) and (6.5).

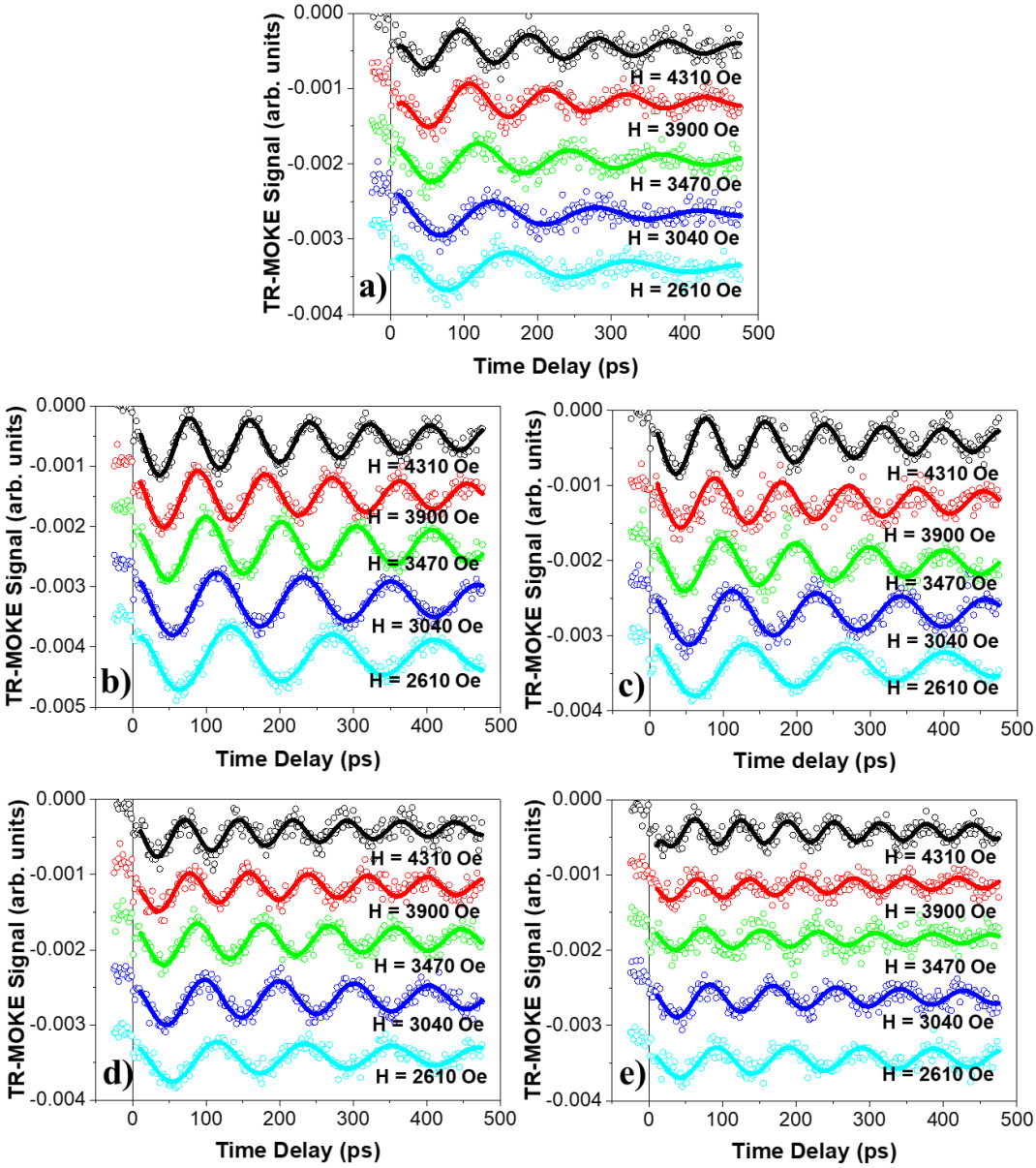

Figure 6.5: (a), (b), (c), (d) and (e) TR-MOKE signals for the samples with a Co thicknesses of 5, 9, 11, 13 and 25 Å, respectively, under different external applied fields (H = 4310, 3900, 3470, 3040 and 2610 Oe) and when H was applied at 78º. Theoretical curves (solid curves) are fits to the experimental data (open symbols) using Eq. (6.3).

As it was described in subsection 3.7.1, the equilibrium angle θ_0 can be calculated using the following relation:

$$H\sin(\theta_H - \theta_0) = \frac{1}{2}H_{eff}\sin(2\theta_0) \tag{6.5}$$

Therefore, the fits of the f_{res} field-dependence are plotted in Figures 6.4 as purple solid lines. Experimental values (open symbols) and fits also show a good agreement.

t_{Co} (Å)	M_{sat} (emu/cm³)	$\gamma/2\pi$ (GHz/kOe)	g	H_{eff} (Oe)	K_{eff} (10^5 erg/cm³)	α_{eff}
0	500 ± 30	*2.91 ± 0.09*	*2.08 ± 0.07*	*2460 ± 330*	*6.15 ± 1.19*	*0.075 ± 0.005*
		2.96 ± 0.08	2.12 ± 0.06	2575 ± 150	6.44 ± 0.76	0.059 ± 0.02
5	655 ± 40	*2.88 ± 0.11*	*2.06 ± 0.08*	*1450± 240*	*4.75 ± 1.08*	-- --
		2.87 ± 0.02	*2.05 ± 0.02*	*1965 ± 60*	6.44 ± 1.10	0.037 ± 0.008
9	653 ± 40	*2.97 ± 0.02*	*2.12 ± 0.01*	*395 ± 40*	*1.29 ± 0.21*	*0.030± 0.003*
		2.95 ± 0.04	2.10 ± 0.03	*1080 ± 120*	3.53 ± 0.61	0.036 ± 0.007
11	740 ± 40	*2.94 ± 0.04*	*2.10 ± 0.03*	*180 ± 95*	*0.70 ± 0.37*	*0.031 ± 0.006*
		2.90 ± 0.02	*2.08 ± 0.02*	*910 ± 70*	3.37 ± 0.49	0.035 ± 0.009
13	685 ± 50	*2.96 ± 0.05*	*2.11 ± 0.04*	*-575 ± 160*	*-1.96 ± 0.40*	*0.024 ± 0.005*
		2.90 ± 0.02	2.07 ± 0.02	-285 ± 75	-0.98 ± 0.33	0.036 ± 0.005
25	810 ± 60	*2.99 ± 0.07*	*2.13 ± 0.05*	*-1970 ± 270*	*-8.87 ± 1.71*	*0.016 ± 0.007*
		2.94 ± 0.03	2.10 ± 0.02	-1695 ± 100	-6.86 ± 0.91	-- --

Table 6.1: Summary of the results for [CoFeB (3 Å) / Pd]$_5$ / Co (t_{Co}) multilayer systems ranging t_{Co} from 0 to 25 Å: the saturation magnetization (M_{sat}) extracted from VSM; the gyromagnetic ratio ($\gamma/2\pi$), the g-factor (g) and the effective anisotropy field (H_{eff}) determined by VNA-FMR (Eq. (6.2)) and TR-MOKE (Eq. (6.3), (6.4) and (6.5)); the effective anisotropy energy (K_{eff}) determined from M_{sat} and H_{eff} using Eq. (6.6); the effective damping (α_{eff}) determined by VNA-FMR (Eq. (6.10)) and TR-MOKE (Eq. (6.11)). Data extracted from the VNA-FMR measurements is shown in black. Data extracted from the TR-MOKE measurements is written in *italics* and *red*.

Main results, obtained from our VNA-FMR and TR-MOKE fits, are summarized in Table 6.1. The gyromagnetic ratio and g-factor did not show any significant dependence with the Co thickness, and we have obtained average values of (2.92 ± 0.03) GHz/kOe and (2.09 ± 0.03) from the VNA-FMR studies and (2.94 ± 0.06) GHz/kOe and (2.10 ± 0.06) for the TR-MOKE measurements, respectively. We should highlight, albeit present higher errors, the gyromagnetic ratio and g-factor values obtained from the TR-MOKE data are in agreement with the VNA-FMR data, even taking into account that our fits were performed using only 5 experimental points.

Besides, and as it was observed in the hysteresis loops, the estimated effective anisotropy field (H_{eff}) shows a transition from positive values for t_{Co} ≤ 11 Å, meaning that the multilayer films show PMA, to negative ones (with in-plane easy magnetization) for t_{Co} ≥ 13 Å (see Figure 6.6 (a)).

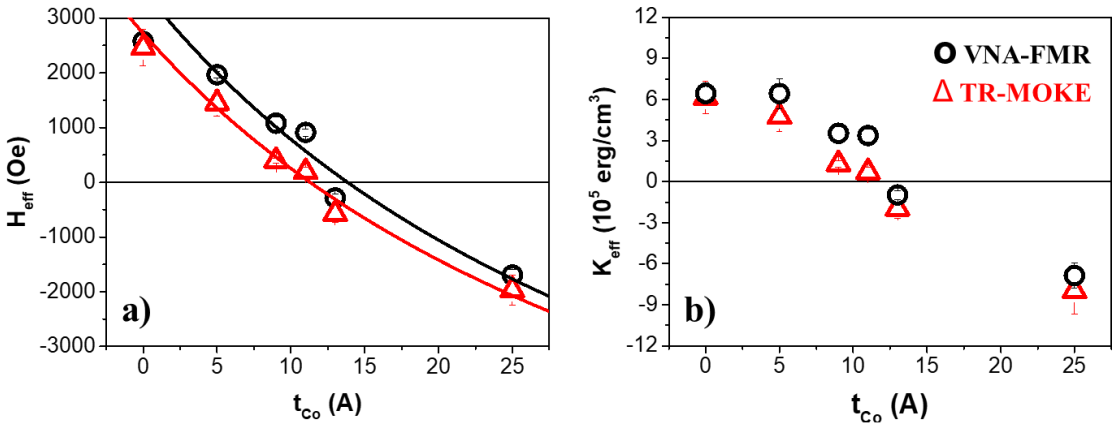

Figure 6.6: (a) H_{eff} and (b) K_{eff} as a function of the Co layer thickness ranging from 0 to 25 Å. While empty symbols (**o**) correspond to the data extracted from VNA-FMR, the empty symbols (**Δ**) are data from TR-MOKE measurements. The black and red lines correspond to fits using de Eq. (6.8) using the data extracted from VNA-FMR and TR-MOKE measurements, respectively.

As it was introduced in section 1.3, the effective anisotropy energy (K_{eff}) can be estimated from H_{eff} by using the following equation (summarized in Table 6.1):

$$K_{eff} = \frac{1}{2}\left(H_{eff} \times M_{sat}\right) \tag{6.6}$$

Figure 6.6 (b) shows the estimated K_{eff}values as function of the Co layer thickness (t_{Co} ranging from 0 to 25 Å). The sample with t_{Co} = 5 Å show a K_{eff}value similar to the sample without Co meaning that the behaviour of the exchange spring magnet is mainly controlled by the hard phase. In other words, the magnetic moments of the (Co/Pd) phase are forced by the hard phase (CoFeB/Pd) to point in the out-of-plane direction (see diagram in Figure 6.7 (a)).

However, and although our multilayers still shows an effective PMA (positive values of K_{eff}), it is reduced when t_{Co} is increased (9 Å ≤ t_{Co} ≤ 11 Å). Then, the magnetic moment of the soft phase should start to rotate to the in-plane direction (see diagram in Figure 6.7 (b)).

Finally, the transition to thin films with an effective in-plane easy magnetization axis (negative values of K_{eff}) is observed for t_{Co} ≥ 13 Å. In this situation, the response of the

multilayers is governed by the soft phase forcing the magnetic moment of the hard phase to point in-plane (diagram in Figure 6.7 (c)).

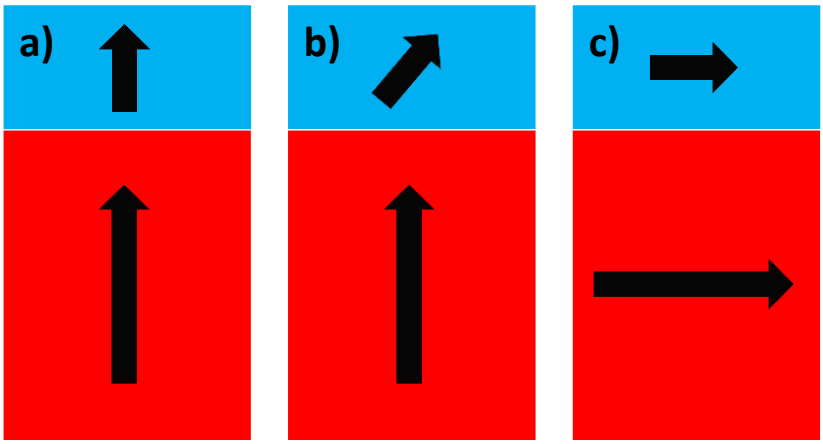

Figure 6.7: Diagram of the hard magnetic phase [CoFeB/Pd] in red, soft phase (Co/Pd) in blue and the direction of the effective magnetic moments (black arrows) in each phase when the multilayer shows (a) a very strong PMA (t_{Co} = 5 Å), (b) PMA (9 Å $\leq$ t_{Co} $\leq$ 11 Å) and (c) in-plane effective magnetization axis (t_{Co} ≥ 13 Å).

Next, we focus our attention on trying to determine the interlayer exchange coupling J_{inter} that can be estimated according to [324]:

$$H_{ex} = 2\,J_{inter}\left[1/\left(\left(M^{eff}_{sat\_CoFeB/Pd} \times t^{eff}_{CoFeB/Pd}\right) + \left(M^{eff}_{sat\_Co/Pd} \times t^{eff}_{Co/Pd}\right)\right)\right] \quad (6.7)$$

where H_{ex} is the exchange field, $M^{eff}_{sat\_CoFeB/Pd} = (500 \pm 30)\ emu/cm^3$ (obtained in the analysis described in Chapter 5) and $M^{eff}_{sat\_Co/Pd}$ are the effective saturation magnetization values of the (CoFeB/Pd) and (Co/Pd) subsystems, respectively. $t^{eff}_{CoFeB/Pd}$ and $t^{eff}_{Co/Pd}$ are the effective thickness of the hard and soft magnetic parts, and they are defined by Eq. 6.1 (a) and 6.1 (b), respectively.

On the other hand, the effective field of the whole system can be defined as the sum of the contributions from the soft and hard phases plus an exchange term:

$$H_{eff} = H^{eff}_{sat\_CoFeB/Pd} + H^{eff}_{sat\_Co/Pd} + H_{ex} \quad (6.8)$$

where the $H^{eff}_{sat\_CoFeB/Pd} = (2575 \pm 150)\ Oe$ and $H^{eff}_{sat\_Co/Pd}$ are the effective fields of the (CoFeB/Pd) and (Co/Pd) subsystems.

Assuming that the contribution of the soft magnetic part (Co/Pd sub-system) with in-plane anisotropy is mainly attributed to the shape anisotropy energy contribution, $K_{sat\_Co/Pd}^{eff} = K_{dem} = -2\pi\left(M_{sat\_Co/Pd}^{eff}\right)^2$, the effective field of the soft magnetic phase can be described by

$$H_{sat\_Co/Pd}^{eff} = H_{dem} = -4\pi M_{sat\_Co/Pd}^{eff} \quad (6.9)$$

Therefore, the (H_{eff} vs t_{Co}) values can be fitted by Eq. (6.8) (See black and red lines in Figure 6.6 (a)) and using $M_{sat\_Co/Pd}^{eff}$ and J_{inter} as the fitting parameters. From our fits, we have estimated that

$J_{inter} = (3.0 \pm 0.3)\ erg/cm^2$

and $M_{sat\_Co/Pd}^{eff} = (1040 \pm 70)\, emu/cm^3$ from the VNA-FMR data,

as well as $J_{inter} = (2.7 \pm 0.2)\ erg/cm^2$

and $M_{sat\_Co/Pd}^{eff} = (1010 \pm 40)\, emu/cm^3$ from the TR-MOKE data.

These values are in good agreement with the data reported in Reference [90].

Effective Damping

In this last section, we have studied the behaviour of the damping parameter (α) as a function of the Co thin film thickness. First, we have used the frequency linewidths (Δf_{res}) from the VNA-FMR spectra to determine an apparent damping by using Eq. (6.10) (shown in subsection 3.7.1) [104]:

$$\alpha_{app} = \frac{\Delta f_{res}}{\left(\frac{\gamma}{2\pi}\right)(2H + H_{eff})} \quad (6.10)$$

where $(\gamma/2\pi) = (g\mu_B/h)$ is the gyromagnetic ratio, g is the g-factor, μ_B is the Bohr magneton, h is Planck´s constant, H is the external applied DC magnetic field and H_{eff} is the effective anisotropy field.

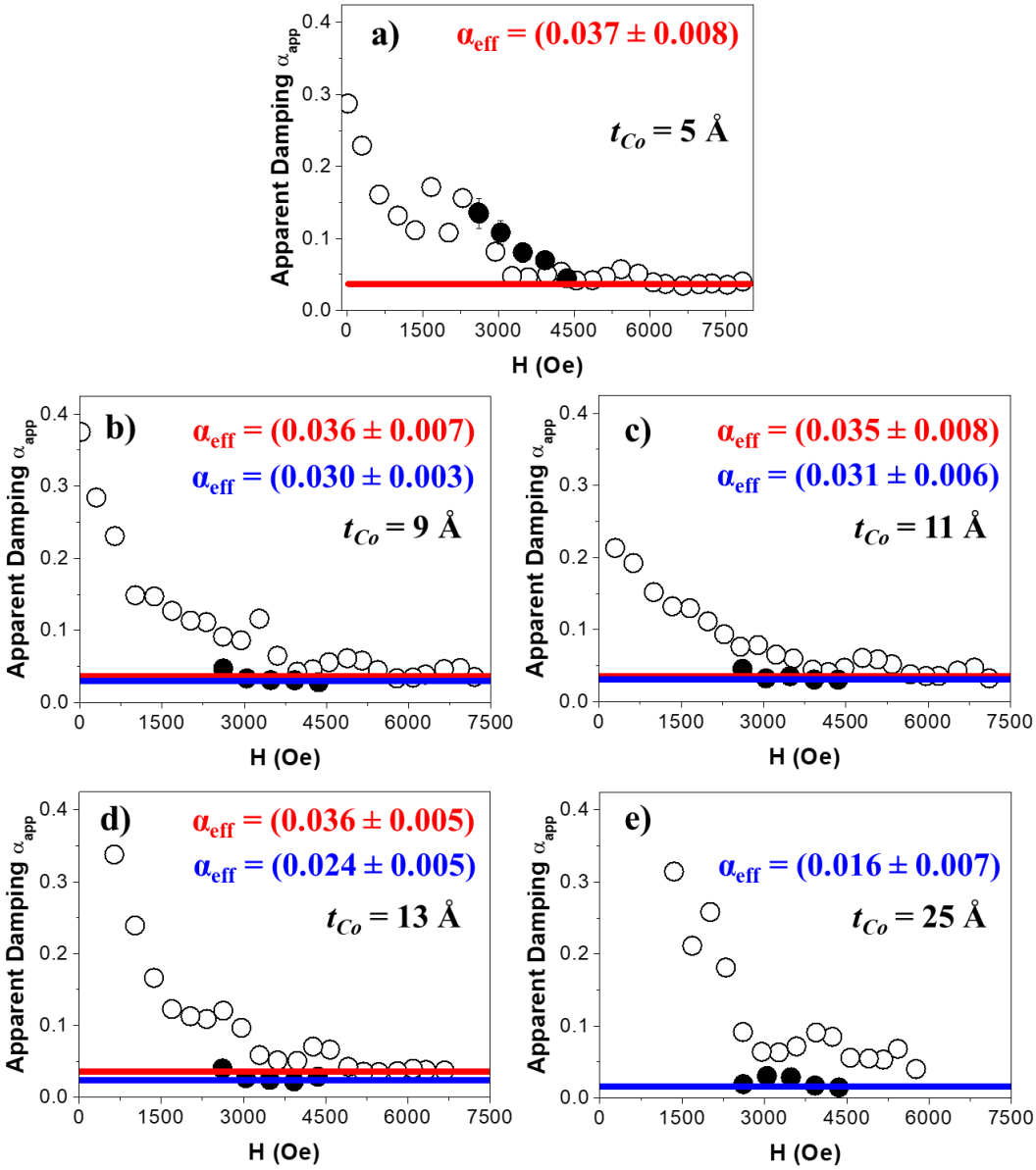

Figure 6.8: (a), (b), (c), (d) and (e) apparent damping α_{app} (o) as a function of the external applied magnetic field for Co layer thickness of t_{Co} = 5 , 9, 11, 13 and 25 Å, respectively, data from VNA-FMR measurements (Eq. (6.10)), and the red solid lines are the average of α_{app} for large applied fields corresponding to the α_{eff}. The full symbols correspond to the apparent damping α_{app} as a function of the external applied magnetic field for t_{Co} = 5 (a), 9 (b), 11 (c), 13 (d) and 25 (e) Å extracted from the pump-probe measurements (Eq. (6.11)), and the blue solid lines are the average of α_{app} for large applied fields corresponding to the α_{eff}.

Although α_{app} and the intrinsic damping may be different, we should note that α_{app} should be an upper limit for the intrinsic or Gilbert damping ($\alpha_{Gilbert}$). Figures 6.8 (a)-(e) show the apparent damping versus the external applied magnetic field for exchange coupled multilayers with t_{Co}= 5, 9, 11, 13 and 25 Å, respectively. Albeit we cannot distinguish

between the different extrinsic contributions to the linewidth, it is observed that α_{app} approaches a constant value for large applied fields and we have defined it as the effective damping α_{eff} (red solid lines in Figures 6.7). However, we should highlight that α_{app} for exchange coupled multilayers with the thicker Co layer (t_{Co}= 25 Å) do not approach a constant value. Then, data for large applied fields should be required to can properly define an effective damping α_{eff} .

From the TR-MOKE measurements, α_{app} can be determined using Eq. (6.11) (see subsection 3.7.1) [249]:

$$\alpha_{app} = \frac{1}{2\pi \times f_{res} \times \tau} \tag{6.11}$$

where f_{res} is the resonance frequency and τ is the relaxation time. Figure 6.7 also shows the apparent damping from the TR-MOKE data (black full symbols) versus the external applied magnetic field for hard-soft magnetic system with t_{Co} ranging from 5 to 25 Å. Again, it was observed that α_{app} approaches a constant value for large applied fields and we assumed that this value is α_{eff} (blue solid lines in Figures 6.7)., for all Co layer thickness except for the t_{Co} = 5 Å. In this particular case, experimental data for larger applied magnetic fields should be required to can properly define an effective damping α_{eff} .

Figure 6.9 shows the evolution of the effective damping (α_{eff}) vs the Co film thicknesses (t_{Co}) obtained by combining both types of measurements. All set of data is summarized in Table 6.1.

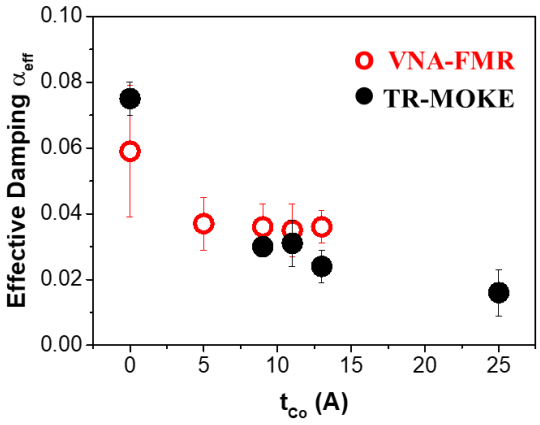

Figure 6.9: Effective Damping (α_{eff}) as a function of t_{Co} determined from the VNA-FMR (open symbols **o**) and the TR-MOKE measurements (open symbols ●).

We should note that when the Co layer (soft phase) is coupled to the [CoFeB/Pd] system (hard phase) the α_{eff} decreases to roughly half of its value, for both VNA-FMR and TR-MOKE techniques.

In the case of the VNA-FMR results, the α_{eff} of the for hard-soft magnetic system the is basically constant not showing dependence on the Co layer thickness. On the other hand, the TR-MOKE results presents a decrease of the α_{eff} parameter as the t_{Co} increases. Nevertheless, both VNA-FMR and TR-MOKE techniques have provided the similar α_{eff} parameters for a Co layer thickness t_{Co} = 9 and 11 Å. For evaluate this discrepancy, further measurements should be done.

6.4. Summary

To summarize, along this chapter we have studied the magnetic static and dynamical properties of $[CoFeB/Pd]_3$/Co exchange spring structures. We focused our attention in Co layer thickness influence in the magnetic behaviour of the exchange couple system when the t_{Co} was varied between 0 and 25 Å, and the hard phase was kept unchanged.

The magnetic behaviour of the exchange spring systems is controlled by the soft phase, and the hysteresis loops confirm an in-plane effective anisotropy energy for those samples with the thickest Co layers ($t_{Co} \geq 13$ Å), as well the dynamical response by the K_{eff} values. Our systems shows an effective PMA (positive values of K_{eff}) for $t_{Co} \leq 11$ Å, which is reduced when t_{Co} is increased (9 Å $\leq t_{Co} \leq 11$ Å), and transition to an effective in-plane anisotropy (negative values of K_{eff}) for t_{Co} ≥ 13 Å.

The observed increase of the M_{sat_total} with the Co film thickness suggests that $M^{eff}_{sat\_CoFeB/Pd} < M^{eff}_{sat\_Co/Pd}$., which was confirmed by the evaluation of the $M^{eff}_{sat_Co/Pd}$value done by the study of the dynamical responses. From the fit of effective field as function of the Co thickness (H_{eff} vs t_{Co}), we were able to determine interlayer exchange coupling J_{inter} and the $M^{eff}_{sat\_Co/Pd}$. From the VNA-FMR data, $J_{inter} = (3.0 \pm 0.3)\ erg/cm^2$ and $M^{eff}_{sat\_Co/Pd} = (1040 \pm 70)\, emu/cm^3$, and from the TR-MOKE data, $J_{inter} = (2.7 \pm 0.2)\ erg/cm^2$ and $M^{eff}_{sat\_Co/Pd} = (1010 \pm 40)\, emu/cm^3$.

Finally, we studied the damping parameter and we observed that α_{eff} decreases to roughly half of its value. From the VNA-FMR and TR-MOKE results different behaviour of α_{eff} as function of t_{Co} was observed, further measurements must be done.

Chapter 7

Ultrafast Magnetization Dynamics in the Sub-5 fs regime (with CEP stabilized pulses)

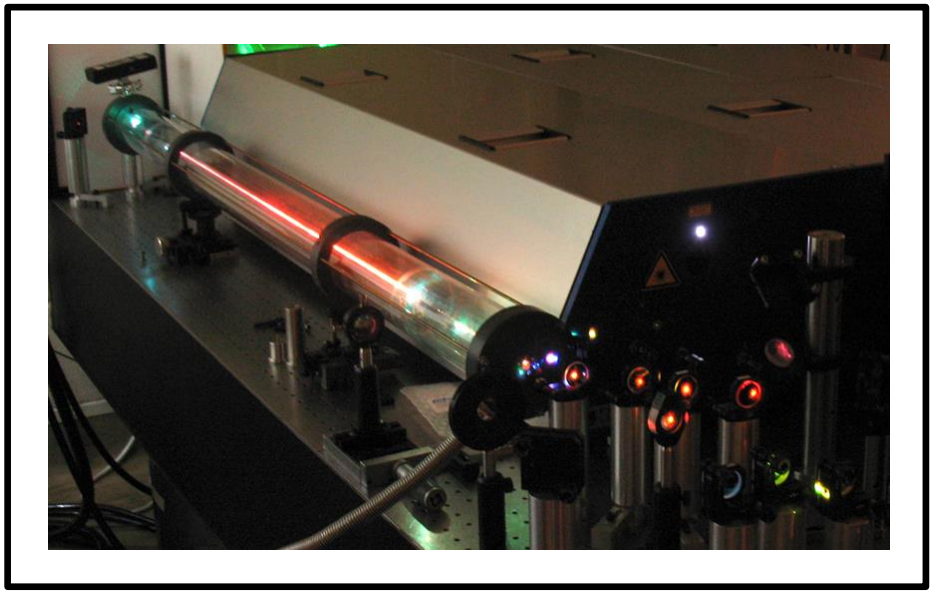

Chapter 7

Ultrafast Magnetization Dynamics in the Sub-5 fs Regime (with CEP stabilized pulses)

7.1. Introduction

Ultrafast coherent control of magnetism, as introduced in section 1.6, implies the interaction of the light electric-field directly with the spin system, which is only possible using few-cycle laser pulses.

In the few-cycle regime, the laser pulse duration approaches the period of its electric field oscillation (e.g. 2.7 fs for λ_0 = 800 nm). A few-cycle pulse typically has only 3-4 periods of light within its envelope (e.g. less than 10 fs in duration for a central wavelength of 800 nm).

The time dependence of the electric field of a light pulse can be described as a rapidly sinusoidal oscillation, the so-called carrier, multiplied by a more slowly varying envelope function [325], as introduced in section 2.2. The offset between the position of the carrier wave and the peak of the pulse envelope is called the carrier-envelope phase (CEP), ϕ_0 (see Figure 7.1).

In few cycle laser pulses, the CEP starts to play an important role since there are electric-field-sensitive processes where a ϕ_0 variation means a different result, e.g. high-harmonic generation (HHG) [326]. For pulses with many optical cycles the effect of the CEP is negligible.

When a pulse propagates inside a dispersive medium through a distance L, the CEP changes due to the chromatic dispersion, because of the differences between the phase velocity v_ϕ and the group velocity v_g, and is shifted by an amount defined by [327]:

$$\Delta\phi = \left(\frac{1}{v_\phi} - \frac{1}{v_g}\right) L. \tag{7.1}$$

In Figure 7.1 two pulses with shifted CEP are shown, where the CEP difference between the two pulses is $\Delta\phi$ = -π/2 rad.

In general, this phase is not constant from pulse to pulse because the group and phase velocities differ inside the laser cavity [328] (where the pulses are generated via mode-locking) due to the intracavity dispersion. Since the CEP is an important parameter for the

interaction between the optical pulse and matter in the few-cycle regime, it is necessary to stabilize it from shot to shot (this is addressed in subsection 7.3.1.).

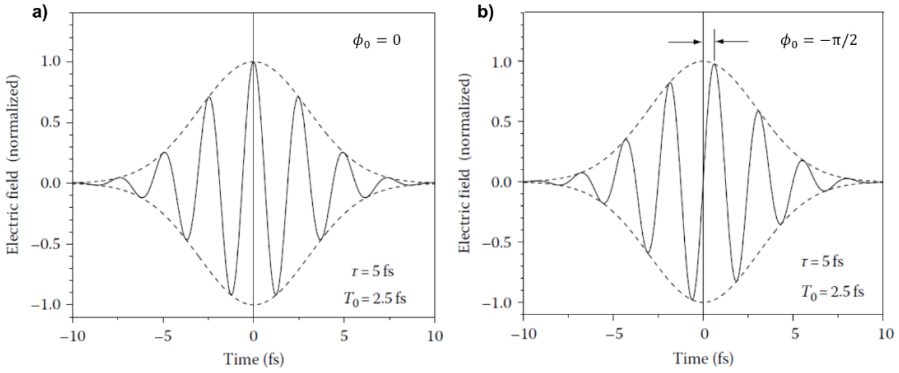

Figure 7.1: Electric field and envelope of two pulses with a duration of 5 fs with a carrier-envelope phase of 0 rad (a) and -π/2 rad (b). From Reference [327].

After the initial publications on ultrafast coherent magnetism [154], [178], several works, both theoretical [167], [168], [182] and experimental [181], [183]–[185], were done in the few-cycle pulse regime (see section 1.6).

Work with single-cycle terahertz transient phase-stable pulses done by C. Vicario *et al.* [180] reported magnetization dynamics of ferromagnetic Cobalt films following the temporal terahertz field oscillation tightly locked to the terahertz phase.

In 2019, F. Siegrist *et al.* [181] showed the first experimental evidence of ultrafast control of the magnetic properties of a ferromagnetic layer stack by the electric-field oscillations of light. They combined simultaneously attosecond transient extreme ultraviolet (XUV) absorption spectroscopy detection (attosecond XAS) with attosecond time-resolved magnetic circular dichroism (attosecond MCD).

The stabilization of the CEP in the few-cycle regime is essential to measure the interaction of the spin system with the light electric field. To the best of our knowledge, magneto-dynamical measurements using both pump and probe few-cycle CEP-stabilized pulses in the visible region, and varying the CEP, were not done until now.

With the aim of accessing the ultrafast coherent magnetization regime with few-cycle visible pulses, we developed a time-resolved magneto-optical setup based on a hollow-fiber compressor with CEP-stabilized sub-5-fs pulse durations at the sample plane (described in Section 4.5).

In the following section, with the purpose of testing our setup in this time regime, we present a comparison of fluence dependent ultrafast demagnetization performed using pulses coming from the laser amplifier with a duration of ~30 fs and the hollow-fiber

compressor pulses with sub-5-fs pulse durations, used both as pump and probe pulses, at the sample plane.

In section 7.3, we start by describing the CEP stabilization (subsection 7.3.1). The preliminary results obtained by our all-optical pump-probe setup using sub-two cycle CEP-stabilized pulses are addressed in subsection 7.3.2.

7.2. Ultrafast Demagnetization by Multi-cycle (Amplifier) Pulses *vs*. Few-cycle (Hollow-fiber) Pulses

The measurements presented here were performed to test our pump-probe setup in the few-cycle pulse regime, i.e. with the hollow-fiber compressor as the laser source (described in section 4.5), and comparing it with the system using the laser amplifier, already validated in the studies presented in the previous Chapters 5 and 6.

We compared fluence-dependent ultrafast demagnetization using amplifier pulses with a duration of ~30 fs and the hollow-fiber compressor pulses with sub-5-fs pulse durations (few-cycle regime) at the sample plane, without CEP-stabilization.

We carried out the pump-probe measurements in a polar TR-MOKE configuration, at different fluences, ranging from 0.8 to 2.1 mJ/cm^2, with an external magnetic field of 4695 Oe applied at 78º from the surface normal, in the [CoFeB (3 Å) / Pd (10 Å)]$_5$ multilayer structure. Figure 7.2 shows the ultrafast demagnetization curves with both (a) laser amplifier and (b) hollow-fiber compressor. As the pump fluence increases, one can observe a gradual increase of the demagnetization.

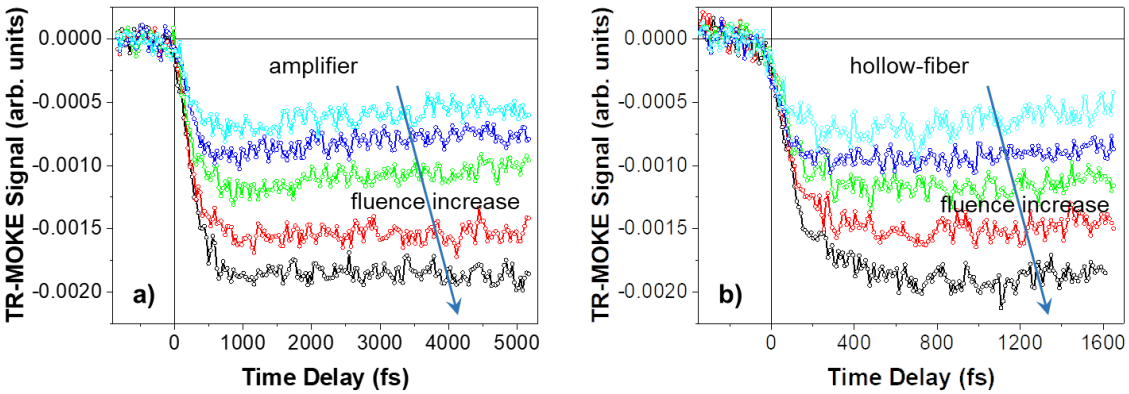

Figure 7.2: Ultrafast Demagnetization curves using amplifier 30fs pulses (a) and hollow-fiber compressor suf-5-fs pulses (b) with different fluences: 0.8 mJ/cm^2 (o), 1.3 mJ/cm^2 (o),1.7 mJ/cm^2 (o), 1.9 mJ/cm^2 (o) and 2.1 mJ/cm^2 (o).

We also measured hysteresis loops with and without the presence of the pump beam. Figure 7.3 shows the hysteresis loops for both (a) laser amplifier and (b) hollow-fiber compressor, for the higher fluence used (2.1 mJ/cm^2). The hysteresis loops have a similar shape for both laser sources. From the normalization of the hysteresis loops, we can observe that applying a fluence of 2.1 mJ/cm^2 there is drop in the magnetization of around 50% in both cases.

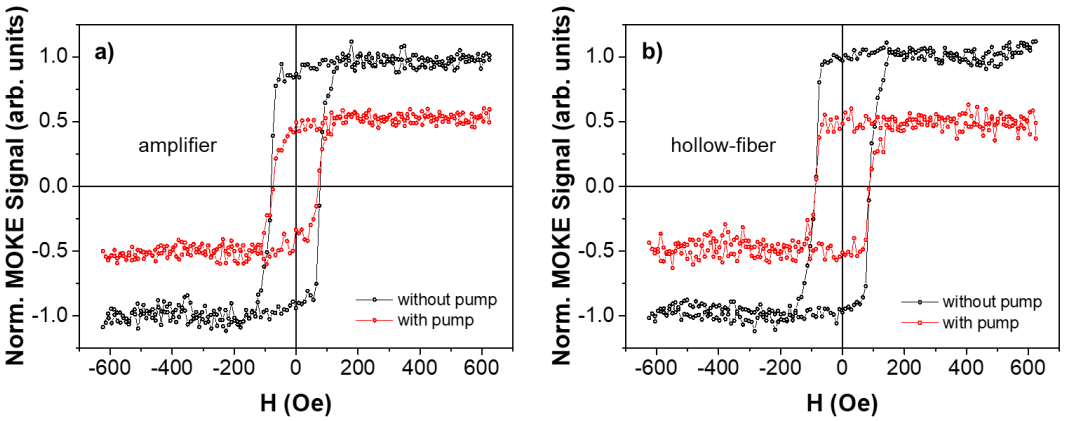

Figure 7.3: Hysteresis loops of the [CoFeB (3 Å) / Pd (10 Å)]$_5$ multilayer stack took using the amplifier (a) and the hollow-fiber compressor (b) as laser source, with a fluence of 2.1 mJ/cm^2 in both cases. The black symbols (**o**) refer to the loops without pump pulses, and red symbols (**o**) to the loops with the pump pulses, with a time delay corresponding to the maximum demagnetization for each case.

Figure 7.4 shows the normalized demagnetization as a function of pump fluence for both laser amplifier and hollow-fiber compressor.

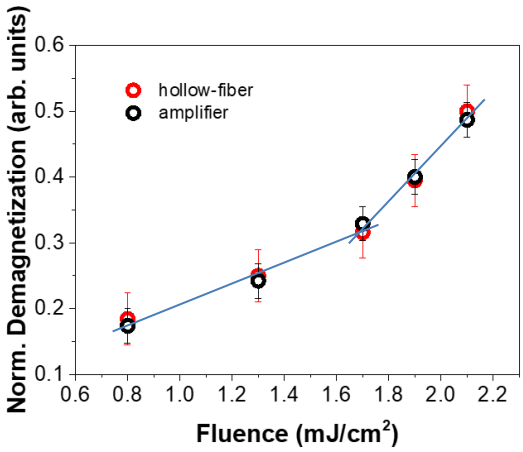

Figure 7.4: Normalized demagnetization as a function of pump fluence. The solid blue lines are a guide to the eye to easily identify what can be two possible regimes of demagnetization depending on pump fluence.

The demagnetization dependence on pump fluence seems nonlinear. We can observe what appear to be two possible regimes of demagnetization vs. pump fluence, above and below 1.7 mJ/cm^2 (solid blue lines in Figure 7.4), respectively. Moreover, the recovery of demagnetization, in the first picoseconds after the demagnetization drop (Figure 7.2 (a)) starts earlier in the case of the three lower fluences (up to 1.7 mJ/cm^2) compared to the higher ones. The fluence of 1.7 mJ/cm^2 seems to be a threshold value for the demagnetization behavior. Further measurements will be made to clarify this possible nonlinear dependence.

In our experiments, the achieved demagnetization is similar for both pulses (provided they have the same fluence). However, we can observe a different slope of the magnetization drop in the first tens of fs for the few-cycle pulses (hollow-fiber) and the multi-cycle (amplifier) (see Figure 7.5). The demagnetization will depend on the laser power density absorbed by the sample, which is related to the fluence and pump pulse width, among other factors [329]. For an understanding of the observed behavior, further data analysis is being conducted.

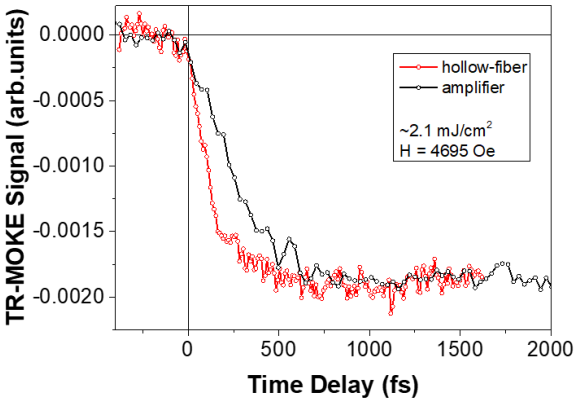

Figure 7.5: Ultrafast demagnetization curves taken with laser amplifier pulses (**o**) and hollow-fiber compressor pulses (**o**) for the same fluence (~2.1 mJ/cm^2). It is clear that the drop in magnetization is much faster for the measurements using the hollow-fiber compressor pulses.

7.3. Ultrafast Magnetization Dynamics with CEP-stabilized Pulses

In the previous section we tested and validated our setup with the hollow-fiber compressor as the laser source, obtaining few-cycle pulses with sub-5-fs duration at sample plane. In this section we present preliminary ultrafast demagnetization measurements as a function of the relative carrier-envelope phase (CEP) of the pulses.

7.3.1. Carrier Envelope Phase (CEP) Stabilization

Our work is based on a CEP-stable laser oscillator-amplifier (Femtolasers Femtopower Compact Pro – CEP). The pulses from the ultrafast laser oscillator are CEP-stabilized (fast-loop) using a monolithic scheme based on difference-frequency generation and self-phase modulation in a periodically-poled lithium niobate crystal (PPNL).
We control the CEP of the laser amplifier pulses using a stabilization system (slow-loop) from MenloSystem GmbH, which is based on a Fourier analysis of the interference pattern generated in an $f:2f$ interferometer [328].
From the properties of the Fourier transform, we know that a shift in time corresponds to a phase shift that is linear with frequency (Figure 7.6), and the phase at angular frequency ω is ωt for a time shift of t [328].

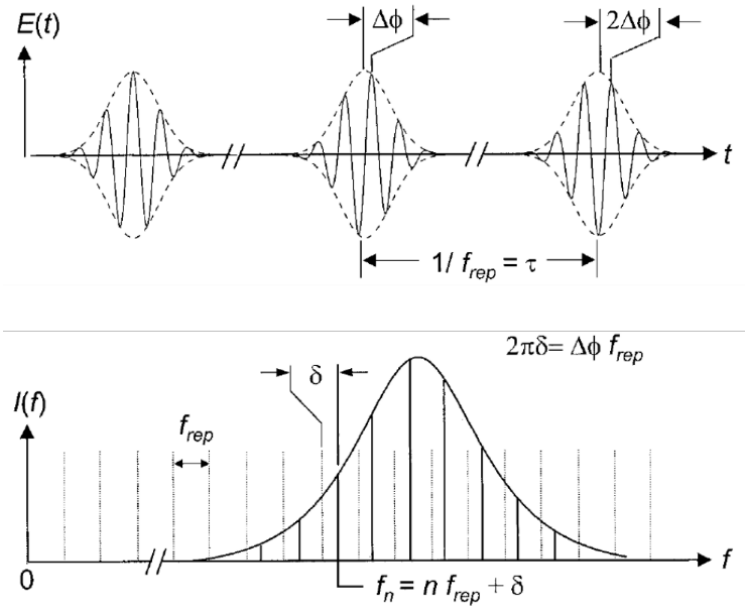

Figure 7.6: Time-frequency correspondence and relation between $\Delta\phi$ and δ. (a) In the time domain, the relative phase between the carrier (solid) and the envelope (dotted) evolves from pulse to pulse by the amount $\Delta\phi$. (b) In the frequency domain, the elements of the frequency comb of a mode-locked pulse train are spaced by f_{rep}. The entire comb (solid) is offset from integer multiples (dotted) of f_{rep} by an offset frequency $\delta = \Delta\phi f_{rep}/2\pi$. From Reference [328].

For a mode-locked pulse train with a τ between pulses, the frequency spectrum consist of a comb of frequencies $f_n = n/\tau = nf_{rep}$, where n is an integer, and $f_{rep} = 1/\tau$ is the repetition frequency of the pulse train. Introducing a pulse-to-pulse phase shift $\Delta\phi$, the phase difference between successive pulses at angular frequency ω is now $\omega\tau - \Delta\phi$, which for constructive interference is set equal to $2n\pi$, and the frequencies are $f_n = nf_{rep} + \delta$, where $2\pi\delta = \Delta\phi f_{rep}$ (Figure 7.6) [328].

For the laser amplifier, with a kHz repetition rate, the relative CEP is only possible to measure by spectral interference (see the fringe pattern in spectrum box in Figure 7.7).

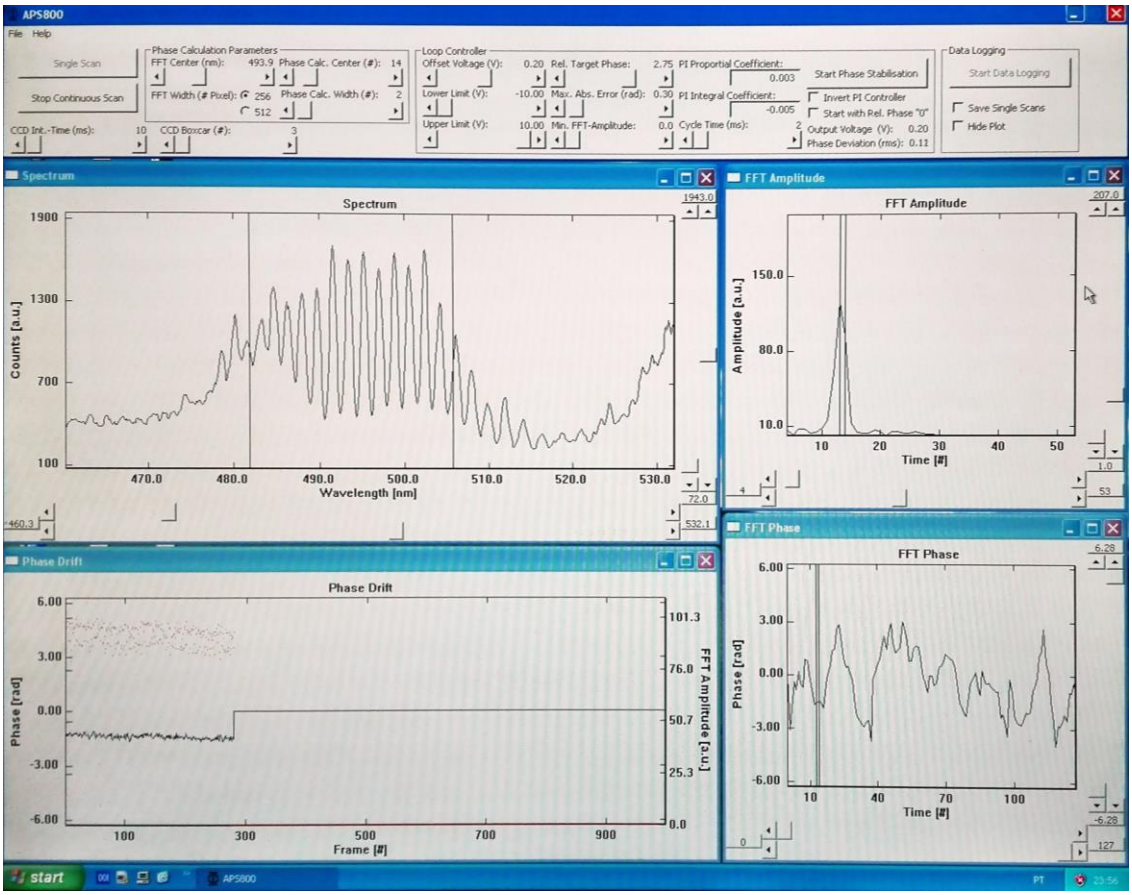

Figure 7.7: The CEP is stabilized using a commercial system from MenloSystems GmbH (APS800) and its measurement is done inside the oscillator/amplifier enclosure. Screenshot of the software APS800 used in the laser system to stabilize the CEP of the amplifier output pulses. The f-to-2f scheme is used and fringes are found at λ = 494 nm, where there is an overlap between the spectrum of the fundamental field and its second harmonic. These fringes must be stabilized in order to have CEP-stabilized output pulses.

First, the spectrum of the amplifier pulses is broadened to obtain an octave-spanning spectrum (meaning that it covers at least a given frequency ω and its second harmonic 2ω), which can be done by nonlinear effects, e.g. self-phase modulation in a sapphire window. Then, the SHG of the spectrally broadened pulse is generated, which will have a frequency of $2f_n = 2nf_{rep} + 2\delta$. In the octave-spanning spectrum, there is an existing frequency component at around $2nf_{rep}$, and the fundamental and SHG spectra will overlap at the wings. The interference of the pulse and its second harmonic is measured in an $f\!:\!2f$ scheme, and the resulting fringe pattern (see spectrum box in Figure 7.7) gives information about the CEP [330], since the fringe position on the wavelength axis depends

on the CEP. Changes in the CE phase inside the amplifier lead to shifts in the fringe pattern over time, which are analyzed in a PC by a Fourier-transform algorithm [326].

A common technique to achieve CEP stabilization, keeping the fringes pattern as much stable as possible, is to act directly on the laser oscillator, whose stabilized ultrashort pulses feed the laser amplifier.

To correct the additional CEP drift emerging from the process of amplification, a slow signal is sent to the oscillator CEP controller, effectively changing its CEP to stabilize the CEP at the amplifier output, the so-called slow loop. Another feedback loop, called fast loop, acts to keep the oscillator pulses CEP stabilized, and both loops modulate the oscillator pump power [326]. When the feedback loops are both activated, the root mean square (rms) of the phase deviation (Figure 7.7) is minimized. During the measurements, presented in the section (see Figure 7.9; each curve took ~10 min to be measured), the rms was kept between 100 and 150 mrad.

We would like to notice that an increase in the rms of the phase deviation is perceived in the TR-MOKE signal with an increase of its noise.

To prevent CEP instability due to air flows in the path of the pulses from the output of the laser to the experiment, an enclosure system was designed and built to cover all the beam paths from the sources to the setup and sample.

7.3.2. Ultrafast Demagnetization Dependence on CEP stabilized

Here we present the preliminary results of the ultrafast demagnetization measurements for the [CoFeB (3 Å) / Pd (10 Å)]$_5$ multilayer system as a function of the relative CEP (ϕ) of the sub-5-fs pulses. The pulse temporal characterization was obtained with the d-scan technique. We obtained 3.6 fs and 4.0 fs pulse durations (FWHM) for the probe and pump pulse, respectively, as already presented in section 4.5.

The magnetodynamic measurements were done in a polar TR-MOKE configuration, with a pump fluence of 2.1 mJ/cm^2 and an external magnetic field of 4695 Oe applied at 78º from the sample surface normal in the [CoFeB (3 Å) / Pd (10 Å)]$_5$ multilayer structure. In Figure 7.8, we show the ultrafast demagnetization curves with a relative CEP (a) ϕ = -π, -3π/4, -π/2 and -π/4, and (b) ϕ = -π, -π/2 and zero.

We plotted the achieved level of demagnetization as a function of the relative phase in Figure 7.9, which provides additional insight on these results.

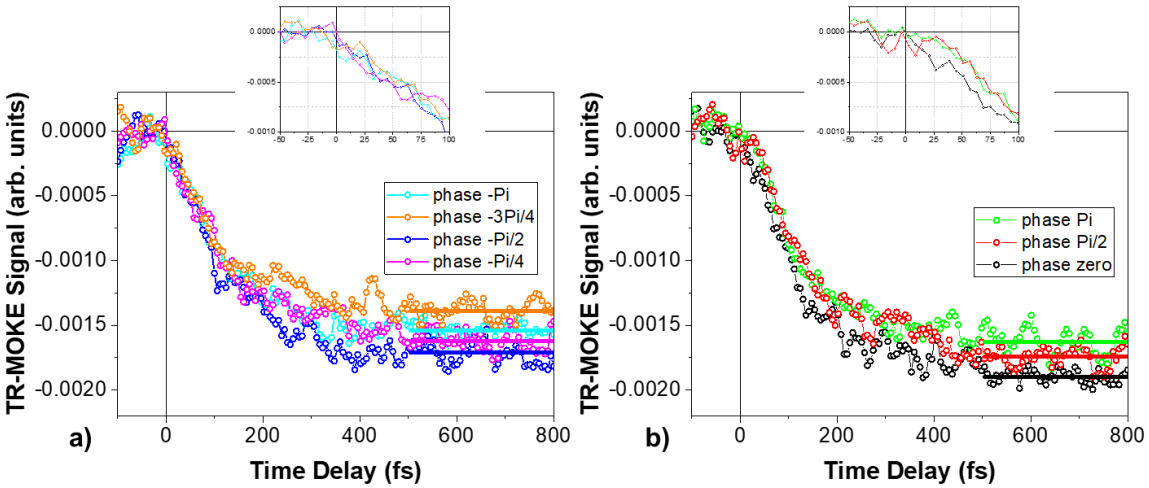

Figure 7.8: Ultrafast demagnetization curves using hollow-fiber compressor sub-5-fs pulses with the CEP stabilized at different values of relative phase: (a) ϕ = -π, -3π/4, -π/2 and -π/4, and (b) ϕ = π, π/2 and zero. The colored solid lines in the right side of the curves are a guide to the eye to visualize the level of demagnetization depending on the ϕ value. The insets highlight the first tens of fs where the initial behavior of the magnetization seems to be different to ϕ = π and π/2 when compared to the one observed to the other values of ϕ.

The observed ultrafast magnetization drop seems to be sensitive to the complete electric field of the pulses, amplitude and sign phase, which is related to the CEP and appears to have the same periodicity of 2π.

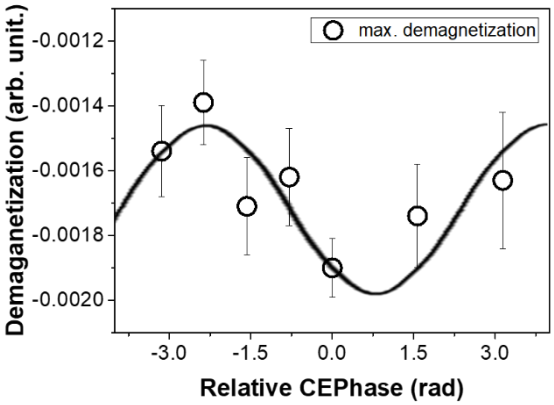

Figure 7.9: Maximum value attained for the demagnetization using hollow-fiber compressor sub-5-fs pulses with the CEP stabilized, as a function of relative CEP. The solid line is a guide to the eye for easier visualization of the demagnetization behavior.

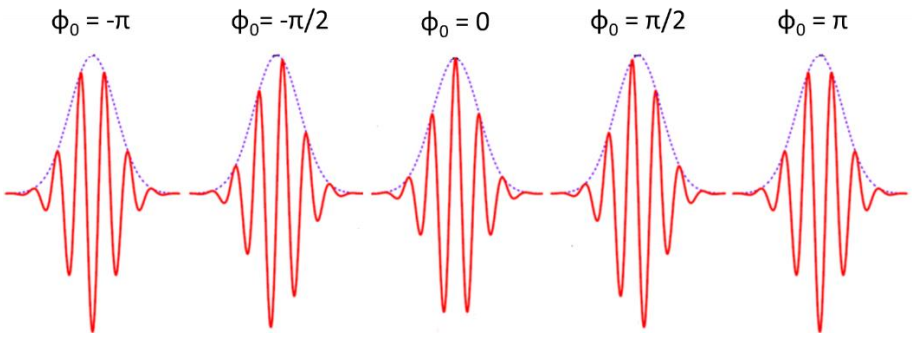

Figure 7.10: Envelope (blue dashed curve), electric field (red curves) of few-cycle laser pulses with variable CEP phase. Adapted from Reference [331].

These results show that it is easier to demagnetize the sample using a cosine-like pulse (ϕ_0 = 0 rad), whereas for a sine-like pulse (ϕ_0 = ±π rad) it is harder. We should stress that, apart from the sign, 0 rad CEP and ±π rad CEP pulses exhibit the same peak power (Figure 7.10). On the other hand, for values of around ϕ_0 = ±π/2 the demagnetization shows similar behavior, seems not sensitive to the phase sign only to the amplitude. However, it seems that in the first tens of fs, the demagnetization appears to behave differently to ϕ = π and π/2 when compared to the one observed to the other values of ϕ (see insets Figure 7.8). Could this mean that the demagnetization is sensitive to the sign of the phase? If it is the case, this behavior is different from other known CEP dependent effects as HHG, which has a π periodicity [326] since it is only sensitive to the intensity and not to the sign of the amplitude of the field (Figure 7.10). Further studies must be performed for understanding magnetism on the few-cycle pulse regime, and clarify this possible dependence on the complete electric field, not only on ultrashort temporal scales (first tens of fs) but also if the coupling between the light electric field and the spin system continues on longer time scales (hundreds of fs or more) .

7.4. Summary

To summarize, our time-resolved magneto optical setup was tested and validated using hollow-fiber compressor pulses with a duration of sub-5-fs at the sample plane. Ultrafast demagnetization measurements were performed for different fluences using both the laser amplifier and hollow-fiber compressor as sources. For the same fluence, the same percentage of demagnetization was reached for both sources. A different slope of the magnetization drop in the first tens of fs is observed for few-cycle pulses (hollow-fiber) compered to multi-cycle (amplifier).

Once we tested the setup, we made ultrafast demagnetization measurements where we varied the relative phase of the CEP-stabilized pulses, observing a demagnetization behavior that appears to correlate with the CEP variation.

CEP-stabilized few-cycle pulses are a highly promising tool for observing and exploring the dependence of the induced magnetization dynamics on the electric field of the light pulses and should help us gain a deeper understanding of the underlying fundamental processes.

Chapter 8

Summary

8.1. Summary

During this thesis work, we have addressed the measurement and characterization of ultrafast magnetization dynamics of multilayer ultrathin films. For this purpose, we have developed a unique compact and versatile time-resolved magneto-optical (TR-MO) system to study ultrafast magnetization dynamics processes using different magneto-optical configurations (Chapter 4). It was confirmed that the configuration of our apparatus can be easily modified and adapted. We have demonstrated that our setup can be used with different laser sources just adjusting the right dispersion compressor and allowing us to achieve a fine control of the time-resolution.

Our TR-MO system was used to study the static and dynamical magnetic behaviour of CoFeB/Pd-based multilayer ultrathin films with different configurations with perpendicular magnetic anisotropy (PMA) and exchange spring structures (Chapter 5). First, the CoFeB layer thickness (t_{CoFeB}) was ranging between 1 and 5 Å, and the number of bilayers (N) was fixed to 5. Please note that up to now, the thicknesses of the CoFeB films (t_{CoFeB}) reported in literature has usually ranged between 0.5 nm to few tens of nm. The main purpose of this study was to determine the range of t_{CoFeB} where thin films show perpendicular magnetic anisotropy (PMA). We confirmed that the CoFeB/Pd-based multilayers show PMA for t_{CoFeB} ≤ 4 Å. The multilayer stacks that presented the highest effective anisotropy field (H_{eff}) were t_{CoFeB} = 3 and 4 Å. Then, we studied the PMA as a function of the number of bilayers (N) which was ranged between 3 and 15, for multilayers with t_{CoFeB} = 3 and 4 Å. In this case, all samples of both sets of multilayers present PMA, which increases as N rises until saturating when N ≥ 10. Regarding the evolution of the damping parameter (α_{eff}) with the t_{CoFeB}, it is observed that it increases when t_{CoFeB} is reduced from 5 to 2 Å. Furthermore, we posit different contributions, intrinsic and extrinsic, for α_{eff}. Beside the Gilbert term ($\alpha_{Gilbert}$) plus a spin-pumping contribution ($\alpha_{\mathrm{s-p}}$) in the perpendicular configuration, a two-magnon scattering term (α_{TMS}) should also be considered in the in-plane configuration. Considering the behavior exhibited by α_{eff} with N for multilayers with t_{CoFeB} = 3 and 4 Å, in agreement with the literature, α_{eff} grows

when the t_{CoFeB} is reduced from 4 to 3 Å. In addition, to explain the dependence of α_{eff} with N we suggest that samples with square hysteresis loops provides larger α_{eff}, that increase with the PMA stability, while damping is independent of N in films with bow-tie-shaped hysteresis loops.

Next, we have studied the magnetic static and dynamical properties of [CoFeB($t_{CoFeB} = 3$ Å)/Pd]$_5$ exchange spring structures (Chapter 6). We focused our attention in Co layer thickness influence in the magnetic behaviour of the exchange couple system when the t_{Co} was varied between 0 and 25 Å, and the hard phase was kept unchanged. The magnetic behaviour of the exchange spring systems is controlled by the soft phase. Our systems shows an effective PMA for $t_{Co} \leq 11$ Å, which is reduced when t_{Co} is increased (9 Å $\leq t_{Co} \leq 11$ Å), and transition to an effective in-plane anisotropy for $t_{\mathrm{Co}} \geq 13$ Å. We also determined the interlayer exchange coupling J_{inter} and the effective saturation magnetization of the (Co/Pd) subsystem $M^{eff}_{sat\_Co/Pd}$ that are in agreement with the literature. Finally, we studied the damping parameter and observed that α_{eff} decreases to roughly half of its value.

In order to highlight the potential of our TR-MO setup, we show its performance under few cycle pulse conditions (Chapter 7). Our setup uses state-of-the-art ultrafast optical methods to deliver ultrashort laser pump and probe sub-5-fs carrier-envelope phase (CEP) stabilized pulses at the sample position, permitting the observation of ultrafast magnetization dynamics at unprecedented temporal resolutions. We present the preliminary results of ultrafast demagnetization measurements made when the CEP of the laser electric field is varied. We observed a demagnetization behavior that appears to correlate with the CEP variation. This few-cycle regime is highly promising for the direct excitation and observation of coherent ultrafast magneto dynamic behavior. Furthermore, CEP-stabilized few-cycle pulses are opening the way for exploring the dependence of the induced magnetization dynamics on the electric field of light pulses and should help us gain a deeper understanding of the underlying fundamental processes behind. We believe that this is an important aim for future developments in magnetism.

8.2. Conclusiones

En la presente Tesis Doctoral se ha desarrollado un sistema original de medidas magnetoópticas resueltas en el tiempo (TR-MO), compacto y versátil para estudiar la dinámica de procesos de magnetización ultrarrápida empleando diferentes configuraciones magnetoópticas. Se ha confirmado que la configuración del aparato presentado puede ser fácilmente modificada y adaptada. Se ha demostrado, asimismo,

que el montaje experimental puede ser empleado para diferentes fuentes láser con tan solo ajustar la dispersión del compresor, permitiendo la obtención de un control fino de la resolución temporal.

Nuestro sistema TR-MO ha sido empleado para el uso de comportamiento estático y dinámico de películas ultrafinas basadas en multicapas de CoFeB/Pd con anisotropía perpendicular (PMA) y presencia de fenómenos de *exchange spring structures*. Hasta el presente, el grosor de las multicapas de CoFeB (t_{CoFeB}) mencionadas en la literatura habitualmente se encuentra en el rango de entre 0.5 nm hasta algunas pocas docenas de nm. En el presente trabajo, nos hemos centrado en multicapas en las que su grosor t_{CoFeB} se ha variado entre 1 y 5 Å.

En el capítulo 5 hemos estudiado el comportamiento magnético dinámico de sistemas de multicapas [CoFeB(t_{CoFeB})/Pd]$_N$ en diferentes configuraciones. En primer lugar, el espesor de la capa de CoFeB (t_{CoFeB}) se ha modificado entre 1 y 5 Å mientras que el número de bicapas (N) quedó fijado en 5. El principal propósito de este estudio ha sido determinar el rango de valores de t_{CoFeB} en los que las películas ultrafinas presentan PMA. Se ha confirmado que las multicapas basadas en CoFeB/Pd presentan PMA para gorsores de CoFeB t_{CoFeB} ≤ 4 Å. En particular, los sistemas que presentan mayor campo efectivo de anisotripía (H_{eff}) son aquellos en los que t_{CoFeB} = 3 y 4 Å. A continuación, se ha estudiado la PMA en función del número de bicapas (N), abarcando los casos de entre 3 y 15, para muestras de multicapas con t_{CoFeB} = 3 y 4 Å. En estos casos, todas las muestras han presentado PMA, que incrementa para N ≤ 5 presenta valores saturados para N ≥ 10. En relación a la evolución del parámetro de amortiguamiento (α_{eff}) en función del espesor t_{CoFeB}, se ha observado un incremento cuando t_{CoFeB} se reduce de 5 a 2 Å. Así, proponemos diferentes contribuciones, intrínsecas y extrínsecas, para α_{eff}. Además del término de Gilbert ($\alpha_{Gilbert}$) y de una contribución *spin-pumping* ($\alpha_{\mathrm{s-p}}$) en la configuración perpendicular, se debería tener en consideración un término de *scattering* a dos magnones (α_{TMS}) en la configuración en el plano. Cuando se estudia el comportamiento del amortiguamiento α_{eff} con respect al número N de multicapas para grosores de estas de t_{CoFeB} = 3 and 4 Å, se observa que α_{eff} aumenta cuando t_{CoFeB} pasa de 4 to 3 Å, lo que concuerda con la bibliografía. Además, para explicar la dependencia de α_{eff} con N, proponemos que las muestras que presentan ciclos de histéresis cuadrados manifiestan mayores amortiguamientos α_{eff}, algo que aumenta con la estabilidad PMA, al tiempo que el amortiguamiento es independiente de N en películas ultrafinas con ciclos de histéresis con forma de pajatira.

En el capítulo 6 se ha estudiado el comportamiento magnético estático y dinámico de estructuras de *exchange spring* en [CoFeB(t_{CoFeB} = 3 Å)/Pd]$_5$. No hemos concentrado en

la influencia del gosor de las capas de Co sobre el comportamiento magnético y el sistema acoplado de intercambio cuando t_{Co} se modifica entre 0 y 25 Å y la fase *dura* no es modificada. El comportamiento magnético del sistema *exchange spring* es modificado a través de la fase *blanda*. Nuestros sistemas presentan una PMA efectiva para $t_{Co} \leq 11$ Å, la cual se reduce cuando se incrementa t_{Co} ($9\ \text{Å} \leq t_{Co} \leq 11$ Å), y aparece una transición hacia una anisotropía efectiva en plano para $t_{\mathrm{Co}} \geq 13$ Å. Igualmente, hemos determinado el acoplamiento de intercambio intracapas J_{inter} y la saturación efectiva de magnetización $M_{sat\_Co/Pd}^{eff}$ del subsistema Co/Pd, obteniendo resultados concordantes con la bibliografía. También se ha estudiado el parámetro de amortiguamiento y se ha observado que α_{eff} disminuye aproximadamente la mitad de su valor.

Se ha logrado el desarrollo de un montaje TR-MOKE aplicado a pulsos comprimidos mediante la técnica de la fibra hueca (capítulo 7). Dicho montaje emplea métodos de vanguardia para obtener pulsos en el plano de la muestra con duraciones inferiores a 5 fs y fase portadora-envolvente (CEP) estabilizada. Esto permite la observación de la dinámica de magnetización ultrarrápida con resoluciones sin precedentes. En el capítulo 7 se presentan los resultados de la desmagnetización ultrarrápida empleando dicho montaje. Se ha observado que esta parece presentar una correlación con la CEP. Este régimen de pulsos de pocos ciclos (< 5 fs) es muy prometedor para la excitación directa y observación de comportamientos de dinámica ultrarrápida coherente. Los pulsos de pocos ciclos y CEP estabilizada están abriendo el camino a la exploración de la dependencia de la dinámica de magnetización inducida por el campo eléctrico de dichos pulsos y podría ser de ayuda para obtener un conocimiento más profundo de los procesos fundamentales subyacentes. Esto constituye, en nuestra opinión, un objetivo importante para futuros desarrollos en el campo del magnetismo.

List of Publications

A. S. Silva, S. P. Sá, S. A. Bunyaev, C. Garcia, I. J. Sola, G. Kakazei, H. Crespo, and D. Navas, “Dynamical behaviour of ultrathin [CoFeB (t_{CoFeB})/Pd] films with perpendicular magnetic anisotropy”, Submitt. to Sci. Reports, 2020.

A. S. Silva, S. A. Bunyaev, C. Garcia, G. Kakazei, H. Crespo, and D. Navas, “PMA and damping in ultrathin [CoFeB (t_{CoFeB})/Pd]$_N$ films as a function of the number of bilayers”, In preparation.

A. S. Silva, S. A. Bunyaev, C. Garcia, G. Kakazei, H. Crespo, and D. Navas, “Dynamical behaviour of [CoFeB/Pd]/Co exchange spring structure as function of the soft layer”, In preparation.

A. S. Silva, A. Hierro-Rodriguez, S. A. Bunyaev, G. N. Kakazei, O. V. Dobrovolskiy, C. Redondo, R. Morales, H. Crespo, and D. Navas, “Magnetic properties of permalloy antidot array fabricated by interference lithography”, AIP Advances 9, 035136 (2019) https://doi.org/10.1063/1.5080111

M. Miranda, F. Silva, L. Neoričić, C. Guo, V. Pervak, M. Canhota, A. S. Silva, Í. J. Sola, R. Romero, P. T. Guerreiro, A. L’Huillier, C. L. Arnold, and H. Crespo, "All-optical measurement of the complete waveform of octave-spanning ultrashort light pulses", Opt. Lett. 44, 191-194 (2019) https://doi.org/10.1364/OL.44.000191

C. S. Goncalves, A. S. Silva, D. Navas, M. Miranda, F. Silva, Helder Crespo, D. S. Schmool, “A Dual-Colour Architecture for Pump-Probe Spectroscopy of Ultrafast Magnetization Dynamics in the Sub-10-femtosecond Range”, Sci. Rep. 6, 22872 (2016) https://doi.org/10.1038/srep22872

Bibliography

[1] M. Fowler, “Historical Beginnings of Theories of Electricity and Magnetism.” [Online]. Available: http://galileoandeinstein.physics.virginia.edu/more_stuff/E&M_Hist.html. [Accessed: 30-Aug-2020].

[2] U. Häfeli, “The History of Magnetism in Medicine,” in *Magnetism in Medicine: A Handbook: Second Edition*, Weinheim, Germany: Wiley-VCH Verlag GmbH & Co. KGaA, pp. 1–25., 2007

[3] J. Vardalas, “History Lesson: The Magnetic Compass.” [Online]. Available: http://theinstitute.ieee.org/tech-history/technology-history/a-history-of-the-magnetic-compass. [Accessed: 30-Aug-2020].

[4] A. Barman and A. Haldar, “Time-Domain Study of Magnetization Dynamics in Magnetic Thin Films and Micro- and Nanostructures,” in *Solid State Physics - Advances in Research and Applications*, vol. 65, Academic Press Inc., pp. 1–108, 2014.

[5] J. Stöhr and H. C. Siegmann, *Magnetism: From fundamentals to nanoscale dynamics*, vol. 152. Berlin, Heidelberg: Springer Berlin Heidelberg, 2006.

[6] A. P. Guimarães, *Principles of Nanomagnetism*, 2nd ed. Cham: Springer International Publishing, 2017.

[7] D. Sander *et al.*, “The 2017 Magnetism Roadmap,” *J. Phys. D. Appl. Phys.*, vol. 50, no. 36, p. 363001, Sep. 2017.

[8] R. L. Stamps *et al.*, “The 2014 Magnetism Roadmap,” *J. Phys. D. Appl. Phys.*, vol. 47, no. 33, p. 333001, Aug. 2014.

[9] E. Y. Vedmedenko *et al.*, “The 2020 magnetism roadmap,” *J. Phys. D. Appl. Phys.*, vol. 53, no. 45, p. 453001, Nov. 2020.

[10] A. Fernández-Pacheco, R. Streubel, O. Fruchart, R. Hertel, P. Fischer, and R. P. Cowburn, “Three-dimensional nanomagnetism,” *Nat. Commun.*, vol. 8, no. 1, p. 15756, Aug. 2017.

[11] F. Hellman *et al.*, “Interface-induced phenomena in magnetism,” *Rev. Mod. Phys.*, vol. 89, no. 2, p. 025006, Jun. 2017.

[12] R. A. Lukaszew, *Handbook of Nanomagnetism: Applications and Tools*. Boca Raton: CRC Press, Taylor & Francis Group, 2016.

[13] J. E. Greene, “Review Article: Tracing the recorded history of thin-film sputter deposition: From the 1800s to 2017,” *J. Vac. Sci. Technol. A Vacuum, Surfaces, Film.*, vol. 35, no. 5, p. 05C204, Sep. 2017.

[14] M. Benelmekki and A. Erbe, Eds., “Nanostructured Thin Films: Fundamentals and Applications,” in *Frontiers of Nanoscience vol. 14*, Elsevier, 2019, pp. 1–34.

[15] K. Seshan, Ed., *Handbook of Thin-Film Deposition Processes and Techniques*, 2nd ed. Norwich, New York, U.S.A.: William Andrew Publishing, 2002.

[16] K. Barmak and K. Coffey, Eds., *Metallic Films for Electronic, Optical and Magnetic Applications*, 1st ed. Woodhead Publishing, 2014.

[17] M. Benelmekki, M. Torrell, E. Xuriguera, F. Vaz, and V. Teixeira, “Structure and Properties of Silver Clusters Implanted in PET by PVD Sputtering for Active Packaging Applications,” *J. Nano Res.*, vol. 18–19, pp. 105–116, Jul. 2012.

[18] M. H. Kryder, “Magnetic thin films for data storage,” *Thin Solid Films*, vol. 216, no. 1, pp. 174–180, Aug. 1992.

[19] H. J. Richter, “The transition from longitudinal to perpendicular recording,” *J. Phys. D. Appl. Phys.*, vol. 40, no. 9, pp. R149–R177, May 2007.

[20] S. N. Piramanayagam and K. Srinivasan, “Recording media research for future hard disk drives,” *J. Magn. Magn. Mater.*, vol. 321, no. 6, pp. 485–494, Mar. 2009.

[21] D. Wang, “Magnetoresistive Thin Film Materials and Their Device Applications,” in *Handbook of Advanced Magnetic Materials*, Y. Liu, D. J. Sellmyer, and D. Shindo, Eds. Boston, MA: Springer US, 2006, pp. 1635–1666.

[22] X. Liang *et al.*, “A Review of Thin-Film Magnetoelastic Materials for Magnetoelectric Applications,” *Sensors*, vol. 20, no. 5, p. 1532, Mar. 2020.

[23] B. Heinrich and J.A.C. Bland, *Ultrathin Magnetic Structures III*. Berlin/Heidelberg: Springer-Verlag, 2005.

[24] L. Néel, “Anisotropie magnétique superficielle et surstructures d’orientation,” *J. Phys. le Radium*, vol. 15, no. 4, pp. 225–239, Apr. 1954.

[25] S. Iwasaki and Y. Nakamura, “The magnetic field distribution of a perpendicular recording head,” *IEEE Trans. Magn.*, vol. 14, no. 5, pp. 436–438, Sep. 1978.

[26] S. Iwasaki, Y. Nakamura, and K. Ouchi, “Perpendicular magnetic recording with a composite anisotropy film,” *IEEE Trans. Magn.*, vol. 15, no. 6, pp. 1456–1458, Nov. 1979.

[27] B. D. Terris and T. Thomson, “Nanofabricated and self-assembled magnetic structures as data storage media,” *J. Phys. D. Appl. Phys.*, vol. 38, no. 12, pp. R199–R222, Jun. 2005.

[28] A. Moser, O. Hellwig, D. Kercher, and E. Dobisz, “Off-track margin in bit patterned media,” *Appl. Phys. Lett.*, vol. 91, no. 16, p. 162502, Oct. 2007.

[29] A. V. Khvalkovskiy *et al.*, “Basic principles of STT-MRAM cell operation in memory arrays,” *J. Phys. D. Appl. Phys.*, vol. 46, no. 8, p. 074001, Feb. 2013.

[30] S. Mangin, D. Ravelosona, J. A. Katine, M. J. Carey, B. D. Terris, and E. E. Fullerton, “Current-induced magnetization reversal in nanopillars with perpendicular anisotropy,” *Nat. Mater.*, vol. 5, no. 3, pp. 210–215, Mar. 2006.

[31] S. Ikeda *et al.*, “A perpendicular-anisotropy CoFeB-MgO magnetic tunnel junction,” *Nat. Mater.*, vol. 9, no. 9, pp. 721–724, Sep. 2010.

[32] A. Fert, V. Cros, and J. Sampaio, “Skyrmions on the track,” *Nat. Nanotechnol.*, vol. 8, no. 3, pp. 152–156, Mar. 2013.

[33] C. Moreau-Luchaire *et al.*, “Additive interfacial chiral interaction in multilayers for stabilization of small individual skyrmions at room temperature,” *Nat. Nanotechnol.*, vol. 11, no. 5, pp. 444–448, May 2016.

[34] S. Woo *et al.*, “Observation of room-temperature magnetic skyrmions and their current-driven dynamics in ultrathin metallic ferromagnets,” *Nat. Mater.*, vol. 15, no. 5, pp. 501–506, May 2016.

[35] R. Mansell *et al.*, “Magnetic particles with perpendicular anisotropy for mechanical cancer cell destruction,” *Sci. Rep.*, vol. 7, no. 1, p. 4257, Dec. 2017.

[36] T. Vemulkar, R. Mansell, D.C.M.C. Petit, R. P. Cowburn, and M. S. Lesniak, “Highly tunable perpendicularly magnetized synthetic antiferromagnets for biotechnology applications,” *Appl. Phys. Lett.*, vol. 107, no. 1, p. 012403, Jul. 2015.

[37] L. Peixoto *et al.*, “Magnetic nanostructures for emerging biomedical applications,” *Appl. Phys. Rev.*, vol. 7, no. 1, p. 011310, Mar. 2020.

[38] N. Inaba, Y. Uesaka, and M. Futamoto, “Compositional and temperature dependence of basic magnetic properties of CoCr-alloy thin films,” *IEEE Trans. Magn.*, vol. 36, no. 1, pp. 54–60, 2000.

[39] D. Navas *et al.*, “Microscopic reversal magnetization mechanisms in CoCrPt thin films with perpendicular magnetic anisotropy: Fractal structure versus labyrinth stripe domains,” *Phys. Rev. B*, vol. 96, no. 18, p. 180403, Nov. 2017.

[40] M. L. Yan, N. Powers, and D. J. Sellmyer, “Highly oriented nonepitaxially grown L10 FePt films,” *J. Appl. Phys.*, vol. 93, no. 10 3, pp. 8292–8294, May 2003.

[41] J. U. Thiele, L. Folks, M. F. Toney, and D. K. Weller, “Perpendicular magnetic anisotropy and magnetic domain structure in sputtered epitaxial FePt (001) L10 films,” *J. Appl. Phys.*, vol. 84, no. 10, pp. 5686–5692, Nov. 1998.

[42] M. Futamoto, M. Nakamura, M. Ohtake, N. Inaba, and T. Shimotsu, “Growth of L 1 0 -ordered crystal in FePt and FePd thin films on MgO(001) substrate,” *AIP Adv.*, vol. 6, no. 8, p. 085302, Aug. 2016.

[43] H. Sato *et al.*, “Fabrication of L11 type Co-Pt ordered alloy films by sputter deposition,” *J. Appl. Phys.*, vol. 103, no. 7, p. 07E114, Apr. 2008.

[44] G. C. Hermosa and A. C. Sun, “Sputtered high perpendicular magnetic anisotropy CoPt thin film on flexible substrate at low temperature,” *AIP Adv.*, vol. 10, no. 1, p. 015132, Jan. 2020.

[45] M. P. R. Sabino, M. Tran, C. Hin Sim, Y. Ji Feng, and K. Eason, “Seed influence on the ferromagnetic resonance response of Co/Ni multilayers,” *J. Appl. Phys.*, vol. 115, no. 17, p. 17C512, May 2014.

[46] M. Tang, W. Li, Y. Ren, Z. Zhang, and Q. Y. Jin, “Lack of dependence between intrinsic magnetic damping and perpendicular magnetic anisotropy in Cu(tCu)/[Ni/Co]N multilayers,” *J. Magn. Magn. Mater.*, vol. 428, pp. 269–273, Apr. 2017.

[47] M. Arora, R. Hübner, D. Suess, B. Heinrich, and E. Girt, “Origin of perpendicular magnetic anisotropy in Co/Ni multilayers,” *Phys. Rev. B*, vol. 96, no. 2, p. 024401, Jul. 2017.

[48] J. M. Shaw, H. T. Nembach, and T. J. Silva, “Measurement of orbital asymmetry and strain in Co90Fe 10/Ni multilayers and alloys: Origins of perpendicular anisotropy,” *Phys. Rev. B - Condens. Matter Mater. Phys.*, vol. 87, no. 5, p. 054416, Feb. 2013.

[49] C. J. Tatnall, J. P. Schille, P. J. Grundy, and D. G. Lord, “A magnetic study of Co/Pt multilayer thin films using magnetic X-ray circular dichroism (MXCD),” *J. Magn. Magn. Mater.*, vol. 165, no. 1–3, pp. 391–393, Jan. 1997.

[50] C. J. Tatnall, D. E. Joyce, P. J. Grundy, J. P. Schille, and G. Van Der Laan, “Anisotropy, orbital moments and microstructure in Co/Pt multilayer films,” *J. Magn. Magn. Mater.*, vol. 177–181, no. PART 2, pp. 1181–1182, Jan. 1998.

[51] B. D. Fulthorpe, D. E. Joyce, T. P. A. Hase, A. S. H. Rozatian, B. K. Tanner, and P. J. Grundy, “The progression of interface structure through sputtered Co/Cu and Co/Pt multilayer films,” *J. Phys. Condens. Matter*, vol. 11, no. 43, pp. 8477–8487, Nov. 1999.

[52] R. Sbiaa *et al.*, “Effect of magnetostatic energy on domain structure and magnetization reversal in (Co/Pd) multilayers,” *J. Appl. Phys.*, vol. 107, no. 10, p. 103901, May 2010.

[53] J. Qiu, Z. Meng, Y. Yang, J. F. Ying, Q. J. Yap, and G. Han, “Effect of roughness on perpendicular magnetic anisotropy in (Co90Fe10/Pt)n superlattices,” *AIP Adv.*, vol. 6, no. 5, p. 056123, May 2016.

[54] D. C. Worledge *et al.*, “Spin torque switching of perpendicular Ta|CoFeB|MgO-based magnetic tunnel junctions,” *Appl. Phys. Lett.*, vol. 98, no. 2, p. 022501, Jan. 2011.

[55] M. Bersweiler, H. Sato, and H. Ohno, “Magnetic and Free-layer Properties of MgO/(Co)FeB/MgO Structures: Dependence on CoFeB Composition,” *IEEE Magn. Lett.*, vol. 8, pp. 1–3, Sep. 2017.

[56] M. Endo, S. Kanai, S. Ikeda, F. Matsukura, and H. Ohno, “Electric-field effects on thickness dependent magnetic anisotropy of sputtered MgO/Co40Fe40B20/Ta structures,” *Appl. Phys. Lett.*, vol. 96, no. 21, p. 212503, May 2010.

[57] M. T. Johnson, P. J. H. Bloemen, F. J. A. Den Broeder, and J. J. De Vries, “Magnetic anisotropy in metallic multilayers,” *Reports Prog. Phys.*, vol. 59, no. 11, pp. 1409–1458, Nov. 1996.

[58] S. Fukami *et al.*, “Current-induced domain wall motion in perpendicularly magnetized CoFeB nanowire,” *Appl. Phys. Lett.*, vol. 98, no. 8, p. 082504, Feb. 2011.

[59] K. Mizunuma *et al.*, “MgO barrier-perpendicular magnetic tunnel junctions with CoFe/Pd multilayers and ferromagnetic insertion layers,” *Appl. Phys. Lett.*, vol. 95, no. 23, p. 232516, Dec. 2009.

[60] H. Meng, W. H. Lum, R. Sbiaa, S. Y. H. Lua, and H. K. Tan, “Annealing effects on CoFeB-MgO magnetic tunnel junctions with perpendicular anisotropy,” *J. Appl. Phys.*, vol. 110, no. 3, p. 033904, Aug. 2011.

[61] J. Y. Bae, W. C. Lim, H. J. Kim, T. D. Lee, K. W. Kim, and T. W. Kim, “Compositional change of MgO barrier and interface in CoFeB⁄MgO⁄CoFeB tunnel junction after annealing,” *J. Appl. Phys.*, vol. 99, no. 8, p. 08T316, Apr. 2006.

[62] A. K. Rumaiz *et al.*, “Boron migration due to annealing in CoFeB/MgO/CoFeB interfaces: A combined hard x-ray photoelectron spectroscopy and x-ray absorption studies,” *Appl. Phys. Lett.*, vol. 99, no. 22, p. 222502, Nov. 2011.

[63] Y. P. Wang *et al.*, “Tunnel magnetoresistance effect and interface study in magnetic tunnel junctions using epitaxial Fe 2 CrSi Heusler alloy electrode,” *J. Appl. Phys.*, vol. 114, no. 1, p. 013910, Jul. 2013.

[64] J. H. Jung, S. H. Lim, and S. R. Lee, “Strong perpendicular magnetic anisotropy in thick CoFeB films sandwiched by Pd and MgO layers,” *Appl. Phys. Lett.*, vol. 96, no. 4, p. 042503, Jan. 2010.

[65] C. Fowley, N. Decorde, K. Oguz, K. Rode, H. Kurt, and J. M. D. Coey, “Perpendicular Magnetic Anisotropy in CoFeB/Pd Bilayers,” *IEEE Trans. Magn.*, vol. 46, no. 6, pp. 2116–2118, Jun. 2010.

[66] J. H. Jung, S. H. Lim, and S. R. Lee, “Perpendicular magnetic anisotropy properties of CoFeB/Pd multilayers,” *J. Nanosci. Nanotechnol.*, vol. 11, no. 7, pp. 6233–6236, Jul. 2011.

[67] D. T. Ngo, D. T. Quach, Q. H. Tran, K. Møhave, T. L. Phan, and D. H. Kim, “Perpendicular magnetic anisotropy and the magnetization process in CoFeB/Pd multilayer films,” *J. Phys. D. Appl. Phys.*, vol. 47, no. 44, p. 445001, Nov. 2014.

[68] P. V. Paluskar *et al.*, “Spin tunneling in junctions with disordered ferromagnets,” *Phys. Rev. Lett.*, vol. 100, no. 5, p. 057205, Feb. 2008.

[69] S. X. Huang, T. Y. Chen, and C. L. Chien, “Spin polarization of amorphous CoFeB determined by point-contact Andreev reflection,” *Appl. Phys. Lett.*, vol. 92, no. 24, p. 242509, Jun. 2008.

[70] D. Wang, C. Nordman, J. M. Daughton, Z. Qian, and J. Fink, “70% TMR at room temperature for SDT sandwich junctions with CoFeB as free and reference layers,” *IEEE Trans. Magn.*, vol. 40, no. 4 II, pp. 2269–2271, Jul. 2004.

[71] A. T. G. Pym, A. Lamperti, B. K. Tanner, T. Dimopoulos, M. Rührig, and J. Wecker, “Interface sharpening in CoFeB magnetic tunnel junctions,” *Appl. Phys. Lett.*, vol. 88, no. 16, p. 162505, Apr. 2006.

[72] Y. Luo *et al.*, “Co-rich magnetic amorphous films and their application in magnetoelectronics,” *Phys. Rev. B - Condens. Matter Mater. Phys.*, vol. 72, no. 1, p. 014426, Jul. 2005.

[73] S. Li, H. Nakamura, T. Kanazawa, X. Liu, and A. Morisako, “Current-induced domain wall motion in TbFeCo wires with perpendicular magnetic anisotropy,” *IEEE Trans. Magn.*, vol. 46, no. 6, pp. 1695–1698, Jun. 2010.

[74] D. T. Ngo, K. Ikeda, and H. Awano, “Direct observation of domain wall motion induced by low-current density in TbFeCo wires,” *Appl. Phys. Express*, vol. 4, no. 9, p. 093002, Aug. 2011.

[75] D.-T. Ngo, K. Ikeda, and H. Awano, “Modulation of domain wall dynamics in TbFeCo single layer nanowire,” *J. Appl. Phys.*, vol. 111, no. 8, p. 083921, Apr. 2012.

[76] M. Ding and S. J. Poon, “Tunable perpendicular magnetic anisotropy in GdFeCo amorphous films,” *J. Magn. Magn. Mater.*, vol. 339, pp. 51–55, Aug. 2013.

[77] B. Dieny and M. Chshiev, “Perpendicular magnetic anisotropy at transition metal/oxide interfaces and applications,” *Rev. Mod. Phys.*, vol. 89, no. 2, p. 025008, Jun. 2017.

[78] S. Iihama, S. Mizukami, H. Naganuma, M. Oogane, Y. Ando, and T. Miyazaki, “Gilbert damping constants of Ta/CoFeB/MgO(Ta) thin films measured by optical detection of precessional magnetization dynamics,” *Phys. Rev. B - Condens. Matter Mater. Phys.*, vol. 89, no. 17, p. 174416, May 2014.

[79] K. Watanabe *et al.*, “Dependence of magnetic properties of MgO/CoFeB/Ta stacks on CoFeB and Ta thicknesses,” *Jpn. J. Appl. Phys.*, vol. 54, no. 4S, p. 04DM04, Apr. 2015.

[80] T. Liu, J. W. Cai, and L. Sun, “Large enhanced perpendicular magnetic anisotropy in CoFeB/MgO system with the typical Ta buffer replaced by an Hf layer,” *AIP Adv.*, vol. 2, no. 3, p. 032151, Sep. 2012.

[81] J. Lourembam, A. Ghosh, M. Zeng, S. K. Wong, Q. J. Yap, and S. Ter Lim, “Thickness-Dependent Perpendicular Magnetic Anisotropy and Gilbert Damping in Hf/Co20Fe60 B20/Mg O Heterostructures,” *Phys. Rev. Appl.*, vol. 10, no. 4, p. 044057, Oct. 2018.

[82] T. Liu, Y. Zhang, J. W. Cai, and H. Y. Pan, “Thermally robust Mo/CoFeB/MgO trilayers with strong perpendicular magnetic anisotropy,” *Sci. Rep.*, vol. 4, no. 1, p. 5895, Jul. 2014.

[83] K. Watanabe, S. Fukami, H. Sato, F. Matsukura, and H. Ohno, “Magnetic Properties of CoFeB–MgO Stacks With Different Buffer-Layer Materials (Ta or Mo),” *IEEE Trans. Magn.*, vol. 52, no. 7, pp. 1–4, Jul. 2016.

[84] A. Natarajarathinam, Z. R. Tadisina, T. Mewes, S. Watts, E. Chen, and S. Gupta, “Influence

of capping layers on CoFeB anisotropy and damping," *J. Appl. Phys.*, vol. 112, no. 5, p. 053909, Sep. 2012.

[85] D. S. Lee, H. T. Chang, C. W. Cheng, and G. Chern, "Perpendicular Magnetic Anisotropy in MgO/CoFeB/Nb and a Comparison of the Cap Layer Effect," *IEEE Trans. Magn.*, vol. 50, no. 7, pp. 1–4, Jul. 2014.

[86] G. Malinowski, K. C. Kuiper, R. Lavrijsen, H. J. M. Swagten, and B. Koopmans, "Magnetization dynamics and Gilbert damping in ultrathin Co48 Fe32 B20 films with out-of-plane anisotropy," *Appl. Phys. Lett.*, vol. 94, no. 10, p. 102501, Mar. 2009.

[87] D. Y. Lee, T. H. Shim, and J. G. Park, "Effects of Pt capping layer on perpendicular magnet anisotropy in pseudo-spin valves of Ta/CoFeB/MgO/CoFeB/Pt magnetic-tunneling junctions," *Appl. Phys. Lett.*, vol. 102, no. 21, p. 212409, May 2013.

[88] P. Kuświk, H. Głowiński, E. Coy, J. Dubowik, and F. Stobiecki, "Perpendicularly magnetized Co20Fe60B20 layer sandwiched between Au with low Gilbert damping," *J. Phys. Condens. Matter*, vol. 29, no. 43, p. 435803, Nov. 2017.

[89] J. H. Jung, B. Jeong, S. H. Lim, and S. R. Lee, "Strong perpendicular magnetic anisotropy in CoFeB/Pd multilayers," *Appl. Phys. Express*, vol. 3, no. 2, p. 023001, Jan. 2010.

[90] A. F. Franco, C. Gonzalez-Fuentes, J. Åkerman, and C. Garcia, "Anisotropy constant and exchange coupling strength of perpendicularly magnetized CoFeB/Pd multilayers and exchange springs," *Phys. Rev. B*, vol. 95, no. 14, p. 144417, Apr. 2017.

[91] D. T. Quach, "Magnetic Properties and Domain Structure of CoFeB/Pd Multilayers with Perpendicular Magnetic Anisotropy," *Vietnam J. Sci. Technol.*, vol. 57, no. 6, p. 685, Nov. 2019.

[92] T. Devolder *et al.*, "Damping of CoxFe80-xB20 ultrathin films with perpendicular magnetic anisotropy," *Appl. Phys. Lett.*, vol. 102, no. 2, p. 022407, Jan. 2013.

[93] A. Aharoni, *Introduction to the theory of ferromagnetism*. Oxford University Press, 2000.

[94] C. Kittel, *Introduction to Solid State Physics*, 8th Editio. John Wiley & Sons, Inc., 1966.

[95] A. Hubert and R. Schäfer, *Magnetic Domains - The Analysis of Magnetic Microstructures*. Berlin, Heidelberg: Springer Berlin Heidelberg, 1998.

[96] S. Chikazumi and C. D. Graham, *Physics of Ferromagnetism (International Series of Monographs on Physics)*. Oxford University Press, 1997.

[97] B. D. Cullity and C. D. Graham, *Introduction to Magnetic Materials*, 2nd ed. Hoboken, NJ: John Wiley & Sons, Inc., 2009.

[98] R. C. O'Handley, *Modern magnetic materials : principles and applications*. New York: John Wiley & Sons, Inc., 1999.

[99] A. Arora, "Optical and electric field control of magnetism," Ph.D. Thesis, University of

Potsdam, 2018.

[100] L. D. Landau and E. M. Lifshitz, “On the Theory of the Dispersion of Magnetic Permeability in Ferromagnetic Bodies,” *Phys. Z. Sowjetunion*, vol. 8, pp. 153–169, 1935.

[101] T. L. Gilbert, “A Lagrangian formulation of the gyromagnetic equation of the magnetic field,” *Phys Rev*, vol. 100, p. 1243, 1955.

[102] T. L. Gilbert, “A phenomenological theory of damping in ferromagnetic materials,” *IEEE Trans. Magn.*, vol. 40, no. 6, pp. 3443–3449, Nov. 2004.

[103] A. Barman and J. Sinha, *Spin Dynamics and Damping in Ferromagnetic Thin Films and Nanostructures*. Cham: Springer International Publishing, 2018.

[104] C. Bilzer, “Microwave susceptibility of thin ferromagnetic films: metrology and insight into magnetization dynamics,” Ph.D. thesis, Universite Paris-Sud - Paris XI, 2007.

[105] J. Smit and H. G. Beljers, “Ferromagnetic resonance absorption in BaFe12O19, a highly anisotropic crystal,” *Philips Res. Rep*, vol. 10, p. 113, 1955.

[106] H. Suhl, “Ferromagnetic Resonance in Nickel Ferrite Between One and Two Kilomegacycles,” *Phys. Rev.*, vol. 97, no. 2, pp. 555–557, Jan. 1955.

[107] M. D. Kaufmann, “Magnetization dynamics in all-optical pump-probe experiments: spin-wave modes and spin-current damping,” Ph.D. thesis, Georg-August-Universität Göttingen, 2006.

[108] I. Tudosa, J. A. Katine, S. Mangin, and E. E. Fullerton, “Perpendicular spin-torque switching with a synthetic antiferromagnetic reference layer,” *Appl. Phys. Lett.*, vol. 96, no. 21, p. 212504, May 2010.

[109] A. Conca *et al.*, “Low spin-wave damping in amorphous Co40Fe40B 20 thin films,” *J. Appl. Phys.*, vol. 113, no. 21, p. 213909, Jun. 2013.

[110] A. Ruiz-Calaforra *et al.*, “The role of the non-magnetic material in spin pumping and magnetization dynamics in NiFe and CoFeB multilayer systems,” *J. Appl. Phys.*, vol. 117, no. 16, p. 163901, Apr. 2015.

[111] M. A. Correa *et al.*, “Exploring the magnetization dynamics, damping and anisotropy in engineered CoFeB/(Ag, Pt)multilayer films grown onto amorphous substrate,” *J. Magn. Magn. Mater.*, vol. 485, pp. 75–81, Sep. 2019.

[112] Z. Duan *et al.*, “Spin-wave modes in permalloy/platinum wires and tuning of the mode damping by spin Hall current,” *Phys. Rev. B - Condens. Matter Mater. Phys.*, vol. 90, no. 2, p. 024427, Jul. 2014.

[113] M. Farle, “Ferromagnetic resonance of ultrathin metallic layers,” *Reports Prog. Phys.*, vol. 61, no. 7, pp. 755–826, Jul. 1998.

[114] S. M. Bhagat and P. Lubitz, “Temperature variation of ferromagnetic relaxation in the 3 d

transition metals," *Phys. Rev. B*, vol. 10, no. 1, pp. 179–185, Jul. 1974.

[115] X. Liu, W. Zhang, M. J. Carter, and G. Xiao, "Ferromagnetic resonance and damping properties of CoFeB thin films as free layers in MgO-based magnetic tunnel junctions," *J. Appl. Phys.*, vol. 110, no. 3, p. 033910, Aug. 2011.

[116] A. Okada *et al.*, "Magnetization dynamics and its scattering mechanism in thin CoFeB films with interfacial anisotropy," *Proc. Natl. Acad. Sci.*, vol. 114, no. 15, pp. 3815–3820, Apr. 2017.

[117] N. Sato, K. P. O'Brien, K. Millard, B. Doyle, and K. Oguz, "Investigation of extrinsic damping caused by magnetic dead layer in Ta-CoFeB-MgO multilayers with perpendicular anisotropy," *J. Appl. Phys.*, vol. 119, no. 9, p. 093902, Mar. 2016.

[118] V. Kamberský, "On ferromagnetic resonance damping in metals," *Czechoslov. J. Phys.*, vol. 26, no. 12, pp. 1366–1383, Dec. 1976.

[119] K. Lenz, H. Wende, W. Kuch, K. Baberschke, K. Nagy, and A. Jánossy, "Two-magnon scattering and viscous Gilbert damping in ultrathin ferromagnets," *Phys. Rev. B - Condens. Matter Mater. Phys.*, vol. 73, no. 14, p. 144424, Apr. 2006.

[120] J. Lindner *et al.*, "Two-magnon damping in thin films in case of canted magnetization: Theory versus experiment," *Phys. Rev. B - Condens. Matter Mater. Phys.*, vol. 80, no. 22, p. 224421, Dec. 2009.

[121] Y. Tserkovnyak, A. Brataas, and G. E. W. Bauer, "Enhanced Gilbert Damping in Thin Ferromagnetic Films," *Phys. Rev. Lett.*, vol. 88, no. 11, p. 117601, Feb. 2002.

[122] Y. Tserkovnyak, A. Brataas, and G. E. W. Bauer, "Spin pumping and magnetization dynamics in metallic multilayers," *Phys. Rev. B - Condens. Matter Mater. Phys.*, vol. 66, no. 22, pp. 1–10, Dec. 2002.

[123] L. Berger, "Emission of spin waves by a magnetic multilayer traversed by a current," *Phys. Rev. B - Condens. Matter Mater. Phys.*, vol. 54, no. 13, pp. 9353–9358, Oct. 1996.

[124] S. Mizukami, Y. Ando, and T. Miyazaki, "Ferromagnetic resonance linewidth for NM/80NiFe/NM films (NM = Cu, Ta, Pd and Pt)," *J. Magn. Magn. Mater.*, vol. 226–230, no. PART II, pp. 1640–1642, May 2001.

[125] S. Mizukami, Y. Ando, and T. Miyazaki, "Effect of spin diffusion on Gilbert damping for a very thin permalloy layer in Cu/permalloy/Cu/Pt films," *Phys. Rev. B - Condens. Matter Mater. Phys.*, vol. 66, no. 10, pp. 1044131–1044139, Sep. 2002.

[126] J. M. Lock, "Eddy current damping in thin metallic ferromagnetic films," *Br. J. Appl. Phys.*, vol. 17, no. 12, pp. 1645–1647, Dec. 1966.

[127] E. Van De Riet and F. Roozeboom, "Ferromagnetic resonance and eddy currents in high-permeable thin films," *J. Appl. Phys.*, vol. 81, no. 1, pp. 350–354, Jan. 1997.

[128] M. A. W. Schoen, J. M. Shaw, H. T. Nembach, M. Weiler, and T. J. Silva, "Radiative

damping in waveguide-based ferromagnetic resonance measured via analysis of perpendicular standing spin waves in sputtered permalloy films," *Phys. Rev. B - Condens. Matter Mater. Phys.*, vol. 92, no. 18, p. 184417, Nov. 2015.

[129] M. A. W. Schoen *et al.*, "Ultra-low magnetic damping of a metallic ferromagnet," *Nat. Phys.*, vol. 12, no. 9, pp. 839–842, Sep. 2016.

[130] Z. Zhang, P. C. Hammel, and P. E. Wigen, "Observation of ferromagnetic resonance in a microscopic sample using magnetic resonance force microscopy," *Appl. Phys. Lett.*, vol. 68, no. 14, pp. 2005–2007, Apr. 1996.

[131] P. E. Wigen, M. L. Roukes, and P. C. Hammel, "Ferromagnetic resonance force microscopy," in *Spin Dynamics in Con ned Magnetic Structures III*, B. Hillebrands and A. Thiaville, Eds. Berlin: Springer, 2006, p. 105{136.

[132] H. Pinkvos, H. Poppa, E. Bauer, and J. Hurst, "Spin-polarized low-energy electron microscopy study of the magnetic microstructure of ultra-thin epitaxial cobalt films on W(110)," *Ultramicroscopy*, vol. 47, no. 4, pp. 339–345, Dec. 1992.

[133] J. H. E. Griffiths, "Anomalous High-frequency Resistance of Ferromagnetic Metals," *Nature*, vol. 158, pp. 670–671, Nov. 1946.

[134] C. Kittel, "On the theory of ferromagnetic resonance absorption," *Phys. Rev.*, vol. 73, no. 2, pp. 155–161, Jan. 1948.

[135] B. Hillebrands, "Progress in multipass tandem Fabry-Perot interferometry: I. A fully automated, easy to use, self-aligning spectrometer with increased stability and flexibility," *Rev. Sci. Instrum.*, vol. 70, no. 3, pp. 1589–1598, Mar. 1999.

[136] S. Demokritov, "Brillouin light scattering studies of confined spin waves: linear and nonlinear confinement," *Phys. Rep.*, vol. 348, no. 6, pp. 441–489, Jul. 2001.

[137] T. J. Silva, C. S. Lee, T. M. Crawford, and C. T. Rogers, "Inductive measurement of ultrafast magnetization dynamics in thin-film Permalloy," *J. Appl. Phys.*, vol. 85, no. 11, pp. 7849–7862, Jun. 1999.

[138] A. B. Kos, T. J. Silva, and P. Kabos, "Pulsed inductive microwave magnetometer," *Rev. Sci. Instrum.*, vol. 73, no. 10, p. 3563, Oct. 2002.

[139] J. Hohlfeld, E. Matthias, R. Knorren, and K. H. Bennemann, "Nonequilibrium Magnetization Dynamics of Nickel," *Phys. Rev. Lett.*, vol. 78, no. 25, pp. 4861–4864, Jun. 1997.

[140] A. Kirilyuk, A. V. Kimel, and T. Rasing, "Ultrafast optical manipulation of magnetic order," *Rev. Mod. Phys.*, vol. 82, no. 3, pp. 2731–2784, Sep. 2010.

[141] M. van Kampen *et al.*, "All-optical probe of coherent spin waves," *Phys. Rev. Lett.*, vol. 88, no. 22, pp. 227201/1-227201/4, May 2002.

[142] M. Vomir, L. H. F. Andrade, L. Guidoni, E. Beaurepaire, and J. Y. Bigot, "Real Space Trajectory of the Ultrafast Magnetization Dynamics in Ferromagnetic Metals," *Phys. Rev.*

Lett., vol. 94, no. 23, p. 237601, Jun. 2005.

[143] E. Beaurepaire, J. C. Merle, A. Daunois, and J. Y. Bigot, “Ultrafast spin dynamics in ferromagnetic nickel,” *Phys. Rev. Lett.*, vol. 76, no. 22, pp. 4250–4253, May 1996.

[144] T. Kampfrath, R. G. Ulbrich, F. Leuenberger, M. Münzenberg, B. Sass, and W. Felsch, “Ultrafast magneto-optical response of iron thin films,” *Phys. Rev. B*, vol. 65, no. 10, p. 104429, Feb. 2002.

[145] M. Aeschlimann *et al.*, “Ultrafast spin-dependent electron dynamics in fcc Co,” *Phys. Rev. Lett.*, vol. 79, no. 25, pp. 5158–5161, Dec. 1997.

[146] J. Wang, Cywiński, C. Sun, J. Kono, H. Munekata, and L. J. Sham, “Femtosecond demagnetization and hot-hole relaxation in ferromagnetic Ga1-x Mnx As,” *Phys. Rev. B - Condens. Matter Mater. Phys.*, vol. 77, no. 23, p. 235308, Jun. 2008.

[147] A. V. Kimel, R. V. Pisarev, J. Hohlfeld, and T. Rasing, “Ultrafast Quenching of the Antiferromagnetic Order in FeBO3: Direct Optical Probing of the Phonon-Magnon Coupling,” *Phys. Rev. Lett.*, vol. 89, no. 28, p. 287401, Dec. 2002.

[148] G. M. Müller *et al.*, “Spin polarization in half-metals probed by femtosecond spin excitation,” *Nat. Mater.*, vol. 8, no. 1, pp. 56–61, Jan. 2009.

[149] J. Y. Bigot and M. Vomir, “Ultrafast magnetization dynamics of nanostructures,” *Ann. Phys.*, vol. 525, no. 1–2, pp. 2–30, Feb. 2013.

[150] A. Kirilyuk, A. V. Kimel, and T. Rasing, “Laser-induced magnetization dynamics and reversal in ferrimagnetic alloys,” *Reports Prog. Phys.*, vol. 76, no. 2, p. 026501, Feb. 2013.

[151] M. I. Kaganov, I. M. Lifshitz, and L. V. Tanatarov, “Relaxation between electrons and the crystalline lattice,” *Sov Phys J Exp Theor Phys*, vol. 4, no. 2, pp. 173–178, 1957.

[152] B. Koopmans, “Time-resolved Kerr-effect and Spin Dynamics in Itinerant Ferromagnets,” in *Handbook of Magnetism and Advanced Magnetic Materials*, Chichester, UK: John Wiley & Sons, Ltd, 2007.

[153] G. P. Zhang and W. Hübner, “Laser-induced ultrafast demagnetization in ferromagnetic metals,” *Phys. Rev. Lett.*, vol. 85, no. 14, pp. 3025–3028, Oct. 2000.

[154] J. Y. Bigot, M. Vomir, and E. Beaurepaire, “Coherent ultrafast magnetism induced by femtosecond laser pulses,” *Nat. Phys.*, vol. 5, no. 7, pp. 515–520, Jul. 2009.

[155] R. J. Elliott, “Theory of the effect of spin-Orbit coupling on magnetic resonance in some semiconductors,” *Phys. Rev.*, vol. 96, no. 2, pp. 266–279, Oct. 1954.

[156] Y. Yafet, “g Factors and Spin-Lattice Relaxation of Conduction Electrons,” in *Solid State Physics - Advances in Research and Applications*, vol. 14, no. C, Academic Press, 1963, pp. 1–98.

[157] B. Koopmans, J. J. M. Ruigrok, F. Dalla Longa, and W. J. M. De Jonge, “Unifying ultrafast

magnetization dynamics," *Phys. Rev. Lett.*, vol. 95, no. 26, p. 267207, Dec. 2005.

[158] B. Koopmans *et al.*, "Explaining the paradoxical diversity of ultrafast laser-induced demagnetization," *Nat. Mater.*, vol. 9, no. 3, pp. 259–265, Mar. 2010.

[159] M. Battiato, K. Carva, and P. M. Oppeneer, "Superdiffusive spin transport as a mechanism of ultrafast demagnetization," *Phys. Rev. Lett.*, vol. 105, no. 2, p. 027203, Jul. 2010.

[160] M. Battiato, K. Carva, and P. M. Oppeneer, "Theory of laser-induced ultrafast superdiffusive spin transport in layered heterostructures," *Phys. Rev. B - Condens. Matter Mater. Phys.*, vol. 86, no. 2, p. 024404, Jul. 2012.

[161] D. Rudolf *et al.*, "Ultrafast magnetization enhancement in metallic multilayers driven by superdiffusive spin current," *Nat. Commun.*, vol. 3, no. 1, p. 1037, Jan. 2012.

[162] A. Eschenlohr *et al.*, "Ultrafast spin transport as key to femtosecond demagnetization," *Nat. Mater.*, vol. 12, no. 4, pp. 332–336, Apr. 2013.

[163] B. Y. Mueller *et al.*, "Feedback Effect during Ultrafast Demagnetization Dynamics in Ferromagnets," *Phys. Rev. Lett.*, vol. 111, no. 16, p. 167204, Oct. 2013.

[164] R. Chimata, A. Bergman, L. Bergqvist, B. Sanyal, and O. Eriksson, "Microscopic model for ultrafast remagnetization dynamics," *Phys. Rev. Lett.*, vol. 109, no. 15, p. 157201, Oct. 2012.

[165] U. Atxitia, O. Chubykalo-Fesenko, N. Kazantseva, D. Hinzke, U. Nowak, and R. W. Chantrell, "Micromagnetic modeling of laser-induced magnetization dynamics using the Landau-Lifshitz-Bloch equation," *Appl. Phys. Lett.*, vol. 91, no. 23, p. 232507, Dec. 2007.

[166] N. Kazantseva, D. Hinzke, U. Nowak, R. W. Chantrell, U. Atxitia, and O. Chubykalo-Fesenko, "Towards multiscale modeling of magnetic materials: Simulations of FePt," *Phys. Rev. B - Condens. Matter Mater. Phys.*, vol. 77, no. 18, p. 184428, May 2008.

[167] W. Töws and G. M. Pastor, "Many-Body Theory of Ultrafast Demagnetization and Angular Momentum Transfer in Ferromagnetic Transition Metals," *Phys. Rev. Lett.*, vol. 115, no. 21, p. 217204, Nov. 2015.

[168] K. Krieger, J. K. Dewhurst, P. Elliott, S. Sharma, and E. K. U. Gross, "Laser-Induced Demagnetization at Ultrashort Time Scales: Predictions of TDDFT," *J. Chem. Theory Comput.*, vol. 11, no. 10, pp. 4870–4874, Oct. 2015.

[169] C. D. Stanciu *et al.*, "All-optical magnetic recording with circularly polarized light," *Phys. Rev. Lett.*, vol. 99, no. 4, p. 047601, Jul. 2007.

[170] K. Vahaplar *et al.*, "Ultrafast Path for Optical Magnetization Reversal via a Strongly Nonequilibrium State," *Phys. Rev. Lett.*, vol. 103, no. 11, p. 117201, Sep. 2009.

[171] A. R. Khorsand *et al.*, "Role of magnetic circular dichroism in all-optical magnetic recording," *Phys. Rev. Lett.*, vol. 108, no. 12, p. 127205, Mar. 2012.

[172] I. Radu *et al.*, “Transient ferromagnetic-like state mediating ultrafast reversal of antiferromagnetically coupled spins,” *Nature*, vol. 472, no. 7342, pp. 205–209, Apr. 2011.

[173] T. A. Ostler *et al.*, “Ultrafast heating as a sufficient stimulus for magnetization reversal in a ferrimagnet,” *Nat. Commun.*, vol. 3, no. 1, p. 666, Jan. 2012.

[174] S. Mangin *et al.*, “Engineered materials for all-optical helicity-dependent magnetic switching,” *Nat. Mater.*, vol. 13, no. 3, pp. 286–292, Mar. 2014.

[175] C. H. Lambert *et al.*, “All-optical control of ferromagnetic thin films and nanostructures,” *Science (80-.).*, vol. 345, no. 6202, pp. 1337–1340, Sep. 2014.

[176] G. P. Zhang, T. Latta, Z. Babyak, Y. H. Bai, and T. F. George, “All-optical spin switching: A new frontier in femtomagnetism - A short review and a simple theory,” *Mod. Phys. Lett. B*, vol. 30, no. 21, p. 16300052, Aug. 2016.

[177] A. V. Kimel and M. Li, “Writing magnetic memory with ultrashort light pulses,” *Nat. Rev. Mater.*, vol. 4, no. 3, pp. 189–200, Mar. 2019.

[178] G. P. Zhang, W. Hübner, G. Lefkidis, Y. Bai, and T. F. George, “Paradigm of the time-resolved magneto-optical Kerr effect for femtosecond magnetism,” *Nat. Phys.*, vol. 5, no. 7, pp. 499–502, Jul. 2009.

[179] J. Walowski and M. Münzenberg, “Perspective: Ultrafast magnetism and THz spintronics,” *J. Appl. Phys.*, vol. 120, no. 14, p. 140901, Oct. 2016.

[180] C. Vicario *et al.*, “Off-resonant magnetization dynamics phase-locked to an intense phase-stable terahertz transient,” *Nat. Photonics*, vol. 7, no. 9, pp. 720–723, Sep. 2013.

[181] F. Siegrist *et al.*, “Light-wave dynamic control of magnetism,” *Nature*, vol. 571, no. 7764, pp. 240–244, Jul. 2019.

[182] J. K. Dewhurst, P. Elliott, S. Shallcross, E. K. U. Gross, and S. Sharma, “Laser-Induced Intersite Spin Transfer,” *Nano Lett.*, vol. 18, no. 3, pp. 1842–1848, Mar. 2018.

[183] M. Hofherr *et al.*, “Ultrafast optically induced spin transfer in ferromagnetic alloys,” *Sci. Adv.*, vol. 6, no. 3, p. eaay8717, Jan. 2020.

[184] F. Willems *et al.*, “Optical inter-site spin transfer probed by energy and spin-resolved transient absorption spectroscopy,” *Nat. Commun.*, vol. 11, no. 1, p. 871, Feb. 2020.

[185] P. Tengdin *et al.*, “Direct light–induced spin transfer between different elements in a spintronic Heusler material via femtosecond laser excitation,” *Sci. Adv.*, vol. 6, no. 3, p. eaaz1100, Jan. 2020.

[186] D. Steil *et al.*, “Efficiency of ultrafast optically induced spin transfer in Heusler compounds,” *Phys. Rev. Res.*, vol. 2, no. 2, p. 023199, May 2020.

[187] C. Rullière, *Femtosecond Laser Pulses: Principles and Experiments*. New York, NY: Springer New York, 2003.

[188] F. Träger, Ed., *Springer Handbook of Lasers and Optics*. New York, NY: Springer New York, 2007.

[189] R. R. Thomson, C. Leburn, and D. Reid, *Ultrafast Nonlinear Optics*. Heidelberg: Springer International Publishing, 2013.

[190] M. Canhota, “Ultrashort light pulses over large spectral ranges: novel sources and dispersion-scan-based spatiotemporal diagnostics,” Ph.D. Thesis, Universidade do Porto, 2018.

[191] E. B. Treacy, “Optical Pulse Compression with Diffraction Gratings,” *IEEE J. Quantum Electron.*, vol. 5, no. 9, pp. 454–458, Sep. 1969.

[192] C. V. Shank, R. L. Fork, R. Yen, R. H. Stolen, and W. J. Tomlinson, “Compression of femtosecond optical pulses,” *Appl. Phys. Lett.*, vol. 40, no. 9, pp. 761–763, May 1982.

[193] R. L. Fork, O. E. Martinez, and J. P. Gordon, “Negative dispersion using pairs of prisms,” *Opt. Lett.*, vol. 9, no. 5, p. 150, May 1984.

[194] Z. Cheng, F. Krausz, and C. Spielmann, “Compression of 2 mJ kilohertz laser pulses to 17.5 fs by pairing double-prism compressor: analysis and performance,” *Opt. Commun.*, vol. 201, no. 1–3, pp. 145–155, Jan. 2002.

[195] B. Proctor and F. Wise, “Quartz prism sequence for reduction of cubic phase in a mode-locked Ti:Al_2O_3 laser,” *Opt. Lett.*, vol. 17, no. 18, p. 1295, Sep. 1992.

[196] R. Szipöcs, C. Spielmann, F. Krausz, and K. Ferencz, “Chirped multilayer coatings for broadband dispersion control in femtosecond lasers,” *Opt. Lett.*, vol. 19, no. 3, p. 201, Feb. 1994.

[197] G. Steinmeyer, D. H. Sutter, L. Gallmann, N. Matuschek, and U. Keller, “Frontiers in ultrashort pulse generation: Pushing the limits in linear and nonlinear optics,” 1999.

[198] F. X. Kärtner *et al.*, “Design and fabrication of double-chirped mirrors,” *Opt. Lett.*, vol. 22, no. 11, p. 831, Jun. 1997.

[199] N. Matuschek, F. X. Kärtner, and U. Keller, “Theory of double-chirped mirrors,” *IEEE J. Sel. Top. Quantum Electron.*, vol. 4, no. 2, pp. 197–208, 1998.

[200] V. Pervak, I. Ahmad, M. K. Trubetskov, A. V. Tikhonravov, and F. Krausz, “Double-angle multilayer mirrors with smooth dispersion characteristics,” *Opt. Express*, vol. 17, no. 10, p. 7943, May 2009.

[201] P. F. Moulton, “Spectroscopic and laser characteristics of Ti:Al_2O_3,” *J. Opt. Soc. Am. B*, vol. 3, no. 1, p. 125, Jan. 1986.

[202] C. S. L. Gonçalves, “Novel dual-colour architecture for ultrafast spin dynamics measurements in sub-8 fs regime,” Ph.D. Thesis, Universidade do Porto, 2015.

[203] S. Yefet and A. Pe’er, “A Review of Cavity Design for Kerr Lens Mode-Locked Solid-State

Lasers," *Appl. Sci.*, vol. 3, no. 4, pp. 694–724, Dec. 2013.

[204] D. Strickland and G. Mourou, "Compression of amplified chirped optical pulses," *Opt. Commun.*, vol. 56, no. 3, pp. 219–221, Dec. 1985.

[205] M. Miranda, "Sources and Diagnostics for Attosecond Science," Ph.D. thesis, Lund University and Porto University, 2012.

[206] M. Hentschel, Z. Cheng, F. Krausz, and C. Spielmann, "Generation of 0.1-TW optical pulses with a single-stage Ti:sapphire amplifier at a 1-kHz repetition rate," *Appl. Phys. B Lasers Opt.*, vol. 70, no. SUPPL. 1, pp. S161–S164, Jun. 2000.

[207] M. Nisoli *et al.*, "Compression of high-energy laser pulses below 5 fs," *Opt. Lett.*, vol. 22, no. 8, p. 522, Apr. 1997.

[208] F. Silva, M. Miranda, B. Alonso, J. Rauschenberger, V. Pervak, and H. Crespo, "Simultaneous compression, characterization and phase stabilization of GW-level 14 cycle VIS-NIR femtosecond pulses using a single dispersion-scan setup," *Opt. Express*, vol. 22, no. 9, p. 10181, May 2014.

[209] F. Silva *et al.*, "Strategies for achieving intense single-cycle pulses with in-line post-compression setups," *Opt. Lett.*, vol. 43, no. 2, p. 337, Jan. 2018.

[210] B. Schenkel *et al.*, "Generation of 38-fs pulses from adaptive compression of a cascaded hollow fiber supercontinuum," *Opt. Lett.*, vol. 28, no. 20, p. 1987, Oct. 2003.

[211] G. New, *Introduction to nonlinear optics*, vol. 9780521877. Cambridge: Cambridge University Press, 2011.

[212] R. W. Boyd, *Nonlinear Optics*, 3rd ed. Boston, MA: Academic Press, 2008.

[213] P. E. Powers and J. W. Haus, *Fundamentals of Nonlinear Optics*, 2nd ed. Boca Raton: CRC Press, 2017.

[214] A. M. Weiner, *Ultrafast Optics*. Hoboken, NJ, USA: John Wiley & Sons, Inc., 2009.

[215] F. X. Kartner, "Pulse Characterization," in *Ultrafast Optics Lectures Notes*, MIT OpenCourseWare, 2005.

[216] R. Trebino, *Frequency-Resolved Optical Gating: The Measurement of Ultrashort Laser Pulses*. Boston, MA: Springer US, 2000.

[217] C. Iaconis and I. A. Walmsley, "Spectral phase interferometry for direct electric-field reconstruction of ultrashort optical pulses," *Opt. Lett.*, vol. 23, no. 10, p. 792, May 1998.

[218] B. Xu, J. M. Gunn, J. M. Dela Cruz, V. V. Lozovoy, and M. Dantus, "Quantitative investigation of the multiphoton intrapulse interference phase scan method for simultaneous phase measurement and compensation of femtosecond laser pulses," *J. Opt. Soc. Am. B*, vol. 23, no. 4, p. 750, Apr. 2006.

[219] M. Miranda, T. Fordell, C. Arnold, A. L'Huillier, and H. Crespo, "Simultaneous compression

and characterization of ultrashort laser pulses using chirped mirrors and glass wedges," *Opt. Express*, vol. 20, no. 1, p. 688, Jan. 2012.

[220] M. Miranda *et al.*, "Characterization of broadband few-cycle laser pulses with the d-scan technique," *Opt. Express*, vol. 20, no. 17, p. 18732, Aug. 2012.

[221] B. Alonso *et al.*, "Characterization of sub-two-cycle pulses from a hollow-core fiber compressor in the spatiotemporal and spatiospectral domains," *Appl. Phys. B*, vol. 112, no. 1, pp. 105–114, Aug. 2013.

[222] M. Miranda *et al.*, "All-optical measurement of the complete waveform of octave-spanning ultrashort light pulses," *Opt. Lett.*, vol. 44, no. 2, p. 191, Jan. 2019.

[223] M. Miranda *et al.*, "Fast iterative retrieval algorithm for ultrashort pulse characterization using dispersion scans," *J. Opt. Soc. Am. B*, vol. 34, no. 1, p. 190, Jan. 2017.

[224] Y. Zhu, *Modern techniques for characterizing magnetic materials*. New York: Springer-Verlag, 2005.

[225] A. S. Silva *et al.*, "Magnetic properties of permalloy antidot array fabricated by interference lithography," *AIP Adv.*, vol. 9, no. 3, p. 035136, Mar. 2019.

[226] S. Foner, "Vibrating Sample Magnetometer," *Rev. Sci. Instrum.*, vol. 27, no. 7, pp. 548–548, Jul. 1956.

[227] S. Foner, "Versatile and sensitive vibrating-sample magnetometer," *Rev. Sci. Instrum.*, vol. 30, no. 7, pp. 548–557, Jul. 1959.

[228] J. Kerr, " XLIII. On rotation of the plane of polarization by reflection from the pole of a magnet ," *London, Edinburgh, Dublin Philos. Mag. J. Sci.*, vol. 3, no. 19, pp. 321–343, May 1877.

[229] Z. Q. Qiu and S. D. Bader, "Surface magneto-optic Kerr effect," *Rev. Sci. Instrum.*, vol. 71, no. 3, pp. 1243–1255, Mar. 2000.

[230] A. K. Zvezdin and V. A. Kotov, *Modern Magnetooptics and Magnetooptical Materials*. CRC Press, 1997.

[231] M. Faraday, "On the magnetization of light, and the illumination of magnetic lines of force," *Philos. Trans. R. Soc. London*, vol. 136, pp. 1–20, Dec. 1846.

[232] S. Višňovský, *Optics in magnetic multilayers and nanostructures*. CRC Taylor & Francis, 2006.

[233] V. Antonov, B. Harmo, and A. Yaresko, *Electronic Structure and Magneto-Optical Properties of Solids*. Dordrecht: Kluwer Academic Publishers, 2004.

[234] C. You and S. Shin, "Derivation of simplified analytic formulae for magneto-optical Kerr effects," *Appl. Phys. Lett.*, vol. 69, no. 9, pp. 1315–1317, Aug. 1996.

[235] M. V. Lebedev, O. V. Misochko, T. Dekorsy, and N. Georgiev, "On the nature of 'coherent

artifact,'" *J. Exp. Theor. Phys.*, vol. 100, no. 2, pp. 272–282, Feb. 2005.

[236] C. W. Luo, Y. T. Wang, F. W. Chen, H. C. Shih, and T. Kobayashi, "Eliminate coherence spike in reflection-type pump-probe measurements," *Opt. Express*, vol. 17, no. 14, p. 11321, Jul. 2009.

[237] C. La-O-Vorakiat *et al.*, "Ultrafast demagnetization measurements using extreme ultraviolet light: Comparison of electronic and magnetic contributions," *Phys. Rev. X*, vol. 2, no. 1, p. 011005, Jan. 2012.

[238] R. P. Prasankumar and A. J. Taylor, *Optical Techniques for Solid-State Materials Characterization*. CRC Press, 2016.

[239] I. Neudecker, G. Woltersdorf, B. Heinrich, T. Okuno, G. Gubbiotti, and C. H. Back, "Comparison of frequency, field, and time domain ferromagnetic resonance methods," *J. Magn. Magn. Mater.*, vol. 307, no. 1, pp. 148–156, Dec. 2006.

[240] C. Bilzer, T. Devolder, P. Crozat, C. Chappert, S. Cardoso, and P. P. Freitas, "Vector network analyzer ferromagnetic resonance of thin films on coplanar waveguides: Comparison of different evaluation methods," *J. Appl. Phys.*, vol. 101, no. 7, p. 074505, Apr. 2007.

[241] S. Sievers, J. Kurda, N. Liebing, F. Hohls, and H. W. Schumacher, "Microwave Interferometry for High Sensitivity VNA-FMR Measurements," *IEEE Trans. Magn.*, vol. 53, no. 4, pp. 1–4, Apr. 2017.

[242] N. Bloembergen, E. M. Purcell, and R. V. Pound, "Relaxation effects in nuclear magnetic resonance absorption," *Phys. Rev.*, vol. 73, no. 7, pp. 679–712, Apr. 1948.

[243] V. P. Denysenkov and A. M. Grishin, "Broadband ferromagnetic resonance spectrometer," *Rev. Sci. Instrum.*, vol. 74, no. 7, pp. 3400–3405, Jul. 2003.

[244] M. L. M. Lalieu, P. L. J. Helgers, and B. Koopmans, "Absorption and generation of femtosecond laser-pulse excited spin currents in noncollinear magnetic bilayers," *Phys. Rev. B*, vol. 96, no. 1, p. 014417, Jul. 2017.

[245] D. Bossini *et al.*, "Laser-driven quantum magnonics and terahertz dynamics of the order parameter in antiferromagnets," *Phys. Rev. B*, vol. 100, no. 2, p. 024428, Jul. 2019.

[246] D. Bossini *et al.*, "Macrospin dynamics in antiferromagnets triggered by sub-20 femtosecond injection of nanomagnons," *Nat. Commun.*, vol. 7, no. 1, p. 10645, Apr. 2016.

[247] C. Banerjee, S. Pal, M. Ahlberg, T. N. A. Nguyen, J. Åkerman, and A. Barman, "All-optical study of tunable ultrafast spin dynamics in [Co/Pd]/NiFe systems: The role of spin-twist structure on Gilbert damping," *RSC Adv.*, vol. 6, no. 83, pp. 80168–80173, 2016.

[248] S. S. Kalarickal *et al.*, "Ferromagnetic resonance linewidth in metallic thin films: Comparison of measurement methods," *J. Appl. Phys.*, vol. 99, no. 9, p. 093909, May 2006.

[249] S. Mizukami *et al.*, "Fast magnetization precession observed in L10-FePt epitaxial thin film,"

Appl. Phys. Lett., vol. 98, no. 5, p. 052501, Jan. 2011.

[250] H.-S. Song *et al.*, “Observation of the intrinsic Gilbert damping constant in Co/Ni multilayers independent of the stack number with perpendicular anisotropy,” *Appl. Phys. Lett.*, vol. 102, no. 10, p. 102401, Mar. 2013.

[251] B. Heinrich, J. F. Cochran, and R. Hasegawa, “FMR linebroadening in metals due to two-magnon scattering,” *J. Appl. Phys.*, vol. 57, no. 8, pp. 3690–3692, Apr. 1985.

[252] C. E. Patton, “Linewidth and relaxation processes for the main resonance in the spin-wave spectra of Ni-Fe Alloy Films,” *J. Appl. Phys.*, vol. 39, no. 7, pp. 3060–3068, Jun. 1968.

[253] P. Hello and C. N. Man, “Design of a low-loss off-axis beam expander,” *Appl. Opt.*, vol. 35, no. 15, p. 2534, May 1996.

[254] V. Optics, “DCM7.” [Online]. Available: https://www.laserquantum.com/download-ds.cfm?id=626. [Accessed: 04-Jun-2020].

[255] A. Vansteenkiste, J. Leliaert, M. Dvornik, M. Helsen, F. Garcia-Sanchez, and B. Van Waeyenberge, “The design and verification of MuMax3,” *AIP Adv.*, vol. 4, no. 10, p. 107133, Oct. 2014.

[256] G. S. Abo, Y. K. Hong, J. Park, J. Lee, W. Lee, and B. C. Choi, “Definition of magnetic exchange length,” *IEEE Trans. Magn.*, vol. 49, no. 8, pp. 4937–4939, Aug. 2013.

[257] D. M. Lattery, J. Zhu, D. Zhang, J.-P. Wang, P. A. Crowell, and X. Wang, “Quantitative analysis and optimization of magnetization precession initiated by ultrafast optical pulses,” *Appl. Phys. Lett.*, vol. 113, no. 16, p. 162405, Oct. 2018.

[258] C. S. Goncąlves *et al.*, “A Dual-Colour Architecture for Pump-Probe Spectroscopy of Ultrafast Magnetization Dynamics in the Sub-10-femtosecond Range,” *Sci. Rep.*, vol. 6, no. 1, p. 22872, Sep. 2016.

[259] D. Bossini, “Femtosecond Optical Excitation of Spins in Antiferromagnetic fluorides An opto-magnetic journey from the center to the edges of the Brillouin zone,” Ph.D. Thesis, Radboud Universiteit, 2016.

[260] R. P. Prasankumar and A. J. Taylor, *Optical Techniques for Solid-State Materials Characterization*. Boca Raton: CRC Press, 2012.

[261] S. R. Systems, “Model SR250 Gated Integrator and Bocar Averager Module, User’s Manual.” Stanford Research Systems, Sunnyvale, CA, U.S.A. (version 2.3 (1993)), 1993.

[262] S. R. Systems, “Model SR850 DSP Lock-In Amplifier, User’s Manual.” Stanford Research Systems, Sunnyvale, CA, U.S.A. (Revision 2.0 (01/2009)), 1992.

[263] A. F. Franco *et al.*, “Variable variance Preisach model for multilayers with perpendicular magnetic anisotropy,” *Phys. Rev. B*, vol. 94, no. 6, p. 064431, Aug. 2016.

[264] P. J. Metaxas *et al.*, “Creep and flow regimes of magnetic domain-wall motion in ultrathin

Pt/Co/Pt films with perpendicular anisotropy," *Phys. Rev. Lett.*, vol. 99, no. 21, p. 217208, Nov. 2007.

[265] S. N. Panda, S. Mondal, J. Sinha, S. Choudhury, and A. Barman, "All-optical detection of interfacial spin transparency from spin pumping in β-Ta/CoFeB thin films," *Sci. Adv.*, vol. 5, no. 4, p. eaav7200, Apr. 2019.

[266] S. Pal, B. Rana, O. Hellwig, T. Thomson, and A. Barman, "Tunable magnonic frequency and damping in [Co/Pd]8 multilayers with variable Co layer thickness," *Appl. Phys. Lett.*, vol. 98, no. 8, p. 082501, Feb. 2011.

[267] B. N. Engel, C. D. England, R. A. Van Leeuwen, M. H. Wiedmann, and C. M. Falco, "Interface magnetic anisotropy in epitaxial superlattices," *Phys. Rev. Lett.*, vol. 67, no. 14, pp. 1910–1913, Sep. 1991.

[268] F. J. A. Den Broeder, H. C. Donkersloot, H. J. G. Draaisma, and W. J. M. De Jonge, "Magnetic properties and structure of Pd/Co and Pd/Fe multilayers," *J. Appl. Phys.*, vol. 61, no. 8, pp. 4317–4319, Apr. 1987.

[269] W. R. Bennett, C. D. England, D. C. Person, and C. M. Falco, "Magnetic properties of Pd/Co multilayers," *J. Appl. Phys.*, vol. 69, no. 8, pp. 4384–4390, Apr. 1991.

[270] R. Wu, C. Li, and A. J. Freeman, "Structural, electronic and magnetic properties of Co/Pd(111) and Co/Pt(111)," *J. Magn. Magn. Mater.*, vol. 99, no. 1–3, pp. 71–80, Sep. 1991.

[271] A. Obinata *et al.*, "Electric-field control of magnetic moment in Pd," *Sci. Rep.*, vol. 5, no. 1, p. 14303, Nov. 2015.

[272] J. Hayakawa *et al.*, "Current-driven magnetization switching in CoFeB/MgO/CoFeB magnetic tunnel junctions," *Japanese J. Appl. Physics, Part 2 Lett.*, vol. 44, no. 37–41, pp. L1267–L1270, Sep. 2005.

[273] M. Ranjbar *et al.*, "CoFeB-based spin Hall nano-oscillators," *IEEE Magn. Lett.*, vol. 5, pp. 1–4, 2014.

[274] P. G. Gowtham, G. M. Stiehl, D. C. Ralph, and R. A. Buhrman, "Thickness-dependent magnetoelasticity and its effects on perpendicular magnetic anisotropy in Ta/CoFeB/MgO thin films," *Phys. Rev. B*, vol. 93, no. 2, p. 024404, Jan. 2016.

[275] M. Munakata, Shin-Ichi Aoqui, and M. Yagi, "B-concentration dependence on anisotropy field of CoFeB thin film for gigahertz frequency use," *IEEE Trans. Magn.*, vol. 41, no. 10, pp. 3262–3264, Oct. 2005.

[276] J. Sinha *et al.*, "Enhanced interface perpendicular magnetic anisotropy in Ta|CoFeB|MgO using nitrogen doped Ta underlayers," *Appl. Phys. Lett.*, vol. 102, no. 24, p. 242405, Jun. 2013.

[277] H. Q. Tu *et al.*, "Gilbert damping in CoFeB/GaAs(001) film with enhanced in-plane uniaxial

magnetic anisotropy," *Sci. Rep.*, vol. 7, no. 1, p. 43971, Apr. 2017.

[278] C. Park, J. G. Zhu, M. T. Moneck, Y. Peng, and D. E. Laughlin, "Annealing effects on structural and transport properties of rf-sputtered CoFeBMgOCoFeB magnetic tunnel junctions," *J. Appl. Phys.*, vol. 99, no. 8, p. 08A901, Apr. 2006.

[279] L. Neel, "L'approche à la saturation de la magnétostriction," *J. Phys. le Radium*, vol. 15, no. 5, pp. 376–378, May 1954.

[280] F. J. A. den Broeder, W. Hoving, and P. J. H. Bloemen, "Magnetic anisotropy of multilayers," *J. Magn. Magn. Mater.*, vol. 93, no. C, pp. 562–570, Feb. 1991.

[281] R. Jungblut, M. T. Johnson, J. Aan De Stegge, A. Reinders, and F. J. A. Den Broeder, "Orientational and structural dependence of magnetic anisotropy of Cu/Ni/Cu sandwiches: Misfit interface anisotropy," *J. Appl. Phys.*, vol. 75, no. 10, pp. 6424–6426, May 1994.

[282] G. Bochi *et al.*, "Perpendicular magnetic anisotropy, domains, and misfit strain in epitaxial Ni/Cu1-xNix/Cu/Si (001) thin films," *Phys. Rev. B*, vol. 52, no. 10, pp. 7311–7321, Sep. 1995.

[283] K. Ha and R. C. O'Handley, "Nonlinear magnetoelastic anisotropy in Cu/Ni/Cu/Si(001) films," *J. Appl. Phys.*, vol. 85, no. 8, pp. 5282–5284, Apr. 1999.

[284] R. C. O'Handley, "Magnetostriction of transition-metal-metalloid glasses: Temperature dependence," *Phys. Rev. B*, vol. 18, no. 2, pp. 930–938, Jul. 1978.

[285] Z. Tang *et al.*, "Magneto-mechanical coupling effect in amorphous Co40Fe40B20films grown on flexible substrates," *Appl. Phys. Lett.*, vol. 105, no. 10, p. 103504, Sep. 2014.

[286] J. W. Arblaster, "Crystallographic properties of palladium," *Platin. Met. Rev.*, vol. 56, no. 3, pp. 181–189, Aug. 2012.

[287] W. Platow, A. Anisimov, G. Dunifer, M. Farle, and K. Baberschke, "Correlations between ferromagnetic-resonance linewidths and sample quality in the study of metallic ultrathin films," *Phys. Rev. B - Condens. Matter Mater. Phys.*, vol. 58, no. 9, pp. 5611–5621, Sep. 1998.

[288] M. J. Hurben and C. E. Patton, "Theory of two magnon scattering microwave relaxation and ferromagnetic resonance linewidth in magnetic thin films," *J. Appl. Phys.*, vol. 83, no. 8, pp. 4344–4365, Apr. 1998.

[289] J. M. Shaw, H. T. Nembach, and T. J. Silva, "Determination of spin pumping as a source of linewidth in sputtered Co 90Fe 10/Pd multilayers by use of broadband ferromagnetic resonance spectroscopy," *Phys. Rev. B - Condens. Matter Mater. Phys.*, vol. 85, no. 5, p. 054412, Feb. 2012.

[290] J. Foros, G. Woltersdorf, B. Heinrich, and A. Brataas, "Scattering of spin current injected in Pd(001)," *J. Appl. Phys.*, vol. 97, no. 10, p. 10A714, May 2005.

[291] T. Kato *et al.*, "Perpendicular anisotropy and gilbert damping in sputtered Co/Pd

multilayers," *IEEE Trans. Magn.*, vol. 48, no. 11, pp. 3288–3291, Nov. 2012.

[292] D. J. Kim, S. Il Kim, S. Y. Park, K. D. Lee, and B. G. Park, "Ferromagnetic resonance spin pumping in CoFeB with highly resistive non-magnetic electrodes," *Curr. Appl. Phys.*, vol. 14, no. 10, pp. 1344–1348, Oct. 2014.

[293] A. Barman, S. Wang, O. Hellwig, A. Berger, E. E. Fullerton, and H. Schmidt, "Ultrafast magnetization dynamics in high perpendicular anisotropy [CoPt]n multilayers," *J. Appl. Phys.*, vol. 101, no. 9, p. 09D102, May 2007.

[294] S. Mizukami *et al.*, "Gilbert damping in Ni/Co multilayer films exhibiting large perpendicular anisotropy," *Appl. Phys. Express*, vol. 4, no. 1, p. 013005, Jan. 2011.

[295] Y. Liu *et al.*, "Effect of bilayer repeats on magnetic properties of Au-buffered Co/Ni multilayers with perpendicular magnetic anisotropy," *Phys. Lett. Sect. A Gen. At. Solid State Phys.*, vol. 383, no. 34, p. 125986, Dec. 2019.

[296] E. A. Jagla, "Hysteresis loops of magnetic thin films with perpendicular anisotropy," *Phys. Rev. B - Condens. Matter Mater. Phys.*, vol. 72, no. 9, p. 094406, Sep. 2005.

[297] C. Kooy and U. Enz, "Experimental and theoretical study of the domain configuration in thin layers of BaFe12O19," *Philips Res. Reports*, vol. 15, pp. 7–29, 1960.

[298] J. E. Davies, O. Hellwig, E. E. Fullerton, G. Denbeaux, J. B. Kortright, and K. Liu, "Magnetization reversal of Co/Pt multilayers: Microscopic origin of high-field magnetic irreversibility," *Phys. Rev. B - Condens. Matter Mater. Phys.*, vol. 70, no. 22, p. 224434, Dec. 2004.

[299] X. Su *et al.*, "Evolution of magnetic properties and domain structures in Co/Ni multilayers," *Jpn. J. Appl. Phys.*, vol. 55, no. 11, p. 110306, Nov. 2016.

[300] J. W. Knepper and F. Y. Yang, "Oscillatory interlayer coupling in Co Pt multilayers with perpendicular anisotropy," *Phys. Rev. B - Condens. Matter Mater. Phys.*, vol. 71, no. 22, p. 224403, Jun. 2005.

[301] S. M. Mohseni, M. Hamdi, S. Chung, S. R. Sani, and J. Åkerman, "Magnetostatically driven domain replication in Ni/Co based perpendicular pseudo-spin-valves," *J. Phys. D. Appl. Phys.*, vol. 49, no. 41, p. 415004, Oct. 2016.

[302] A. S. H. Rozatian, C. H. Marrows, T. P. A. Hase, and B. K. Tanner, "The relationship between interface structure, conformality and perpendicular anisotropy in CoPd multilayers," *J. Phys. Condens. Matter*, vol. 17, no. 25, pp. 3759–3770, Jun. 2005.

[303] D. Weller *et al.*, "Thickness dependent coercivity in sputtered Co/Pt multilayers," *IEEE Trans. Magn.*, vol. 28, no. 5, pp. 2500–2502, Sep. 1992.

[304] B. Hu, N. Amos, Y. Tian, J. Butler, D. Litvinov, and S. Khizroev, "Study of Co/Pd multilayers as a candidate material for next generation magnetic media," *J. Appl. Phys.*, vol. 109, no. 3, p. 034314, Feb. 2011.

[305] V. Garcia-Vazquez, Y. J. Chang, A. Canizo-Cabrera, A. Garzon-Roman, and T. H. Wu, “Perpendicular magnetic anisotropy in composite MgO/CoFeB/Ta/[Co/Pd]n structures,” *Jpn. J. Appl. Phys.*, vol. 55, no. 2, p. 023001, Feb. 2016.

[306] Y. Wu *et al.*, “Perpendicular magnetic anisotropy and thermal stability in Co2FeAl0.5Si0.5/Pt multilayers,” *Appl. Phys. A Mater. Sci. Process.*, vol. 117, no. 2, pp. 773–779, Nov. 2014.

[307] J. H. Judy, “Advancements in PMR thin-film media,” *J. Magn. Magn. Mater.*, vol. 287, no. SPEC. ISS., pp. 16–26, Feb. 2005.

[308] D. Weller and A. Moser, “Thermal effect limits in ultrahigh-density magnetic recording,” *IEEE Trans. Magn.*, vol. 35, no. 6, pp. 4423–4439, 1999.

[309] R. H. Victora and X. Shen, “Composite media for perpendicular magnetic recording,” *IEEE Trans. Magn.*, vol. 41, no. 2, pp. 537–542, Feb. 2005.

[310] D. Suess *et al.*, “Exchange spring media for perpendicular recording,” *Appl. Phys. Lett.*, vol. 87, no. 1, p. 012504, Jul. 2005.

[311] D. Suess *et al.*, “Exchange spring recording media for areal densities up to 10Tbit/in2,” *J. Magn. Magn. Mater.*, vol. 290–291, pp. 551–554, Apr. 2005.

[312] A. Y. Dobin and H. J. Richter, “Domain wall assisted magnetic recording,” *Appl. Phys. Lett.*, vol. 89, no. 6, p. 062512, Aug. 2006.

[313] H. J. Richter and A. Y. Dobin, “Analysis of magnetization processes in composite media grains,” *J. Appl. Phys.*, vol. 99, no. 8, p. 08Q905, Apr. 2006.

[314] D. Navas *et al.*, “Magnetization reversal and exchange bias effects in hard/soft ferromagnetic bilayers with orthogonal anisotropies,” *New J. Phys.*, vol. 14, no. 11, p. 113001, Nov. 2012.

[315] L. Tryputen *et al.*, “Magnetic structure and anisotropy of [Co/Pd]5/NiFe multilayers,” *Phys. Rev. B - Condens. Matter Mater. Phys.*, vol. 91, no. 1, p. 014407, Jan. 2015.

[316] T. N. A. Nguyen *et al.*, “[Co/Pd]-NiFe exchange springs with tunable magnetization tilt angle,” *Appl. Phys. Lett.*, vol. 98, no. 17, p. 172502, Apr. 2011.

[317] S. Tacchi *et al.*, “Spin wave excitations in exchange-coupled [Co/Pd]-NiFe films with tunable tilting of the magnetization,” *Phys. Rev. B*, vol. 87, no. 14, p. 144426, Apr. 2013.

[318] T. N. Anh Nguyen *et al.*, “[Co/Pd] 4-Co-Pd-NiFe spring magnets with highly tunable and uniform magnetization tilt angles,” *J. Magn. Magn. Mater.*, vol. 324, no. 22, pp. 3929–3932, Nov. 2012.

[319] S. Chung *et al.*, “Tunable spin configuration in [Co/Ni]-NiFe spring magnets,” *J. Phys. D. Appl. Phys.*, vol. 46, no. 12, p. 125004, Mar. 2013.

[320] G. Heldt *et al.*, “Topologically confined vortex oscillations in hybrid [Co/Pd] 8 -Permalloy

structures," *Appl. Phys. Lett.*, vol. 104, no. 18, p. 182401, May 2014.

[321] T. N. A. Nguyen *et al.*, "Investigation of the Tunability of the Spin Configuration Inside Exchange Coupled Springs of Hard/Soft Magnets," *IEEE Trans. Magn.*, vol. 50, no. 6, pp. 1–6, Jun. 2014.

[322] T. N. A. Nguyen *et al.*, "Depth-Dependent Magnetization Profiles of Hybrid Exchange Springs," *Phys. Rev. Appl.*, vol. 2, no. 4, p. 044014, Oct. 2014.

[323] S. Tacchi *et al.*, "[Co/Pd]-CoFeB exchange spring magnets with tunable gap of spin wave excitations," *J. Phys. D. Appl. Phys.*, vol. 47, no. 49, p. 495004, Dec. 2014.

[324] J. Lindner and K. Baberschke, "In situ ferromagnetic resonance: An ultimate tool to investigate the coupling in ultrathin magnetic films," *J. Phys. Condens. Matter*, vol. 15, no. 4, pp. R193–R232, Feb. 2003.

[325] R. Paschotta, "Carrier–envelope Offset," *RP Photonics Encyclopedia*. [Online]. Available: https://www.rp-photonics.com/carrier_envelope_offset.html.

[326] A. Baltuška *et al.*, "Attosecond control of electronic processes by intense light fields," *Nature*, vol. 421, no. 6923, pp. 611–615, Feb. 2003.

[327] Z. Chang, *Fundamentals of Attosecond Optics*, 1 st. Boca Raton: CRC Press, Taylor & Francis Group, 2011.

[328] D. J. Jones *et al.*, "Carrier-envelope phase control of femtosecond mode-locked lasers and direct optical frequency synthesis," *Science (80).*, vol. 288, no. 5466, pp. 635–639, Apr. 2000.

[329] U. Atxitia and U., "Modeling of ultrafast laser-induced magnetization dynamics within the Landau-Lifshitz-Bloch approach," PhD thesis, Universidad Autonoma de Madrid, 2012.

[330] H. R. Telle, G. Steinmeyer, A. E. Dunlop, J. Stenger, D. H. Sutter, and U. Keller, "Carrier-envelope offset phase control: A novel concept for absolute optical frequency measurement and ultrashort pulse generation," *Appl. Phys. B Lasers Opt.*, vol. 69, no. 4, pp. 327–332, Oct. 1999.

[331] P. Dombi *et al.*, "Direct measurement and analysis of the carrier-envelope phase in light pulses approaching the single-cycle regime," *New J. Phys.*, vol. 6, no. 1, pp. 39–39, Mar. 2004.